

Slow Pyrolysis Experiments for High Yields of Solid Carbon

By

Jeffrey LeBlanc

A dissertation submitted to the Graduate Faculty of Engineering
in partial fulfillment of the requirements for the degree of

Doctor of Philosophy

The City College of New York

2016

© 2016
Jeffrey R. LeBlanc
All Rights Reserved

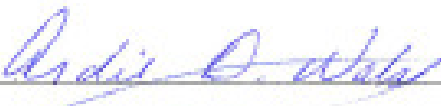
This manuscript has been read and accepted for the
Graduate Faculty in Engineering in satisfaction of the
dissertation requirement for the degree of Doctor of Philosophy.



Dr. Marco J. Castaldi, Chair of Examining Committee



Date



Ardie D. Walser, Associate Dean for Academic Affairs



Date

Examining Committee

Dr. Marco J. Castaldi, Professor of Chemical Engineering, The City College of New York

Dr. Ilana Kivitschman, Professor of Chemical Engineering, The City College of New York

Dr. David Rumschitzki, Professor of Chemical Engineering, The City College of New York

Dr. Gabriel Tardos, Professor of Chemical Engineering, The City College of New York

Dr. John F. Quanci, Vice President of Engineering and Technology, Suncoke Energy

THE CITY COLLEGE OF NEW YORK

Slow Pyrolysis Experiments for High Yields of Solid Carbon

by

Jeffrey LeBlanc

Adviser: Professor Marco J. Castaldi

Preface

Commercial coke and charcoal are precursors to metal production and fuels which are important to society. These carbon materials are produced from pyrolysis processes. To meet increasing demands and sustainability goals, future coke and charcoal production must achieve higher yield and low-emissions while maintaining a high-quality product. The feedstocks and pyrolysis reaction mechanisms are complex and therefore require scientific understanding to improve yields. Due the commercial demand and sustainability challenges, it is important for chemical engineers to obtain an understanding of complex pyrolysis mechanism. In this thesis, the complexity of the mechanism is discussed in a detailed summary of biomass and coal pyrolysis research. In general, pyrolysis is the thermal decomposition of these feedstocks in an inert environment. In this work, the mass balance was measured in the pyrolysis of three coals and one biomass to $\geq 99.2\%$. The product distribution was then quantified between H_2 , CH_4 , CO , CO_2 , C_2H_6 , C_2H_4 , tar and coke at various pyrolysis conditions. Furthermore, real-time mass loss and gas evolution profile measurements along with the corresponding tar collection enabled the process mass balance to be measured at every temperature. The various pyrolysis conditions included heating rates of 1, 3, and $10\text{ }^\circ\text{C min}^{-1}$, particle sizes between $40\text{ }\mu\text{m}$ to $1000\text{ }\mu\text{m}$, and

two reaction confinements. Reaction confinement refers to the physical geometry of the confined pyrolysis system such as bed depth, flux area, or aspect ratio. This parameter was used to vary the residence time of volatile products in the pyrolysis system. All of the investigated conditions varied in the degree of secondary reactions which enabled the quantitative description of the secondary char formation from volatile products to be realized. An important contribution from this work was the measurement of the extent of secondary reactions within the solid-gas interface. This work demonstrated that increasing the residence time of tar in the solid-gas interface by 0.35 seconds results in a 5.0 wt. % increase in solid yield with a commensurate 40 wt. % and 11 wt. % increase in CH₄ and H₂, respectively. The comparisons of time-resolved thermogravimetry-gas chromatography (TG-GC) measurements between two reaction confinements show that H₂, CH₄ and coke production increase between 510 and 575 °C from the secondary reaction in the solid-gas interface. This work includes investigation of the solid-state reactions up to 500 °C by TG-GC and Diffuse Reflectance Infrared Fourier-Transform Spectroscopy (DRIFTS). DRIFTS is an upcoming technique in the field of pyrolysis able to monitor loss of oxygenated functional groups as well as increases in aromaticity. The development of a partial least squares regression (PLS) calibration between TG-GC and DRIFTS data is presented as a chemometric technique for optimizing product distribution and char properties from pyrolysis processes. This technique was also used to explain the mechanistic relationship between functional groups and volatile pyrolysis products. Gas and tar production correspond to the loss of surface functional group and increase in char aromaticity. Ex-situ analysis of pyrolysis product was another important aspect of this work. The tar product was analyzed by gas chromatographic-mass spectrometry (GC-MS), laser desorption/ionization-time-of-flight mass spectrometry (LDI-TOF), and TG-GC. LDI-TOF measured the molecular weight

distribution (MWD) of the pyrolysis tar product to be between 200 and 550 amu. GC-MS was used to identify 120 distinct species in the tar product. TG-GC shows that 75-90% of coal tar products vaporize before 400 °C and 10-25% vaporizes by 1000 °C without producing secondary gas products or coke. The TG-GC of biomass tar produces a 40 wt. % char product plus CO₂, CO, CH₄, C₂H₄, C₂H₆, and H₂. The tar products of the different reaction confinements were analyzed and showed that extended residence time of pyrolysis tars in the solid-gas interface decreased the average MWD, decreased the H/C ratio, and resulted in a broader distribution of nitrogen and sulfur species of the tar. In regard to solid-phase products, two anomalous coke by-products were analyzed by scanning electron microscopy (SEM), energy dispersive spectroscopy (EDS), x-ray diffraction (XRD), and inductively coupled plasma-mass spectrometry (ICP-MS). The two coke specimens were referred as coke hair and silver coke. The nature of the formation of these structures was inferred from the characterization and analysis. Silver coke is a result of aluminum-iron mineral mobility within the char structure as a function of temperature. Coke hairs form from catalytic secondary reactions between volatile pyrolysis product and iron minerals. The experimentally measured mass closure enabled that the product distributions and profiles are absolute and the error may be directly calculated. We have estimations of the number of reactions which constitute the rate profiles of specific gas products, the accumulated tar, and the solid decomposition during pyrolysis.

Jeffrey R. LeBlanc

New York, New York

November 2016

| | |
|---|----|
| Preface..... | 2 |
| Table of Abbreviations and Notation..... | 16 |
| Chapter 1: Introduction..... | 18 |
| 1.1 Application for Solid Carbon Products..... | 18 |
| 1.1.1 Biochar Concept..... | 19 |
| 1.1.2 Carbothermic Reduction..... | 21 |
| 1.2 Commercial Production..... | 23 |
| Chapter 2: Fundamentals of Pyrolysis..... | 31 |
| 2.1 Biomass..... | 31 |
| 2.1.1 Biomass Constitution..... | 31 |
| 2.1.2 Biomass Pyrolysis Mechanism..... | 34 |
| 2.2 Coal..... | 43 |
| 2.2.1 Coal Constitution..... | 43 |
| 2.2.2 Coal Pyrolysis Mechanism..... | 48 |
| 2.3 Pyrolysis Models..... | 62 |
| Chapter 3: Experimental Procedure and Methods..... | 63 |
| 3.1 Samples and Sample Preparation..... | 63 |
| 3.2 Experiments..... | 64 |
| 3.2.1 Thermogravimetric-Gas Chromatography (TG-GC)..... | 64 |
| 3.2.1.1 Tar Capture..... | 67 |

| | |
|--|----|
| 3.2.1.2 Confinement..... | 68 |
| 3.2.2 Carbon, Hydrogen, Nitrogen, Sulfur, Oxygen (CHNSO) analyzer..... | 69 |
| 3.2.3 Gas Chromatography-Mass Spectroscopy (GC-MS)..... | 70 |
| 3.2.4 MALDI-Time of Flight (TOF)..... | 71 |
| 3.2.5 Diffuse Reflectance Infrared Fourier Transform Spectroscopy (DRIFTS)..... | 73 |
| 3.2.6 Scanning Electron Microscopy (SEM)/Energy Dispersive Spectroscopy (EDS)..... | 74 |
| 3.2.7 X-Ray Diffraction (XRD)..... | 74 |
| 3.2.8 Inductively Coupled Plasma (ICP)-Mass Spectroscopy..... | 75 |
| 3.3 Calculations..... | 75 |
| 3.3.1 Mass balance..... | 75 |
| 3.3.2 Stoichiometric Equations..... | 76 |
| 3.3.3 Energy Balance..... | 77 |
| 3.3.4 Gaussian Fits..... | 78 |
| 3.3.5 DRIFTS-GC Partial Least Squares (PLS) Calibration..... | 78 |
| Chapter 4: Investigation of Coal Pyrolysis..... | 80 |
| 4.1 Mass Balance..... | 80 |
| 4.2 Thermogravimetry of Jewel Coal Pyrolysis..... | 81 |
| 4.3 Gas Chromatography of Jewel Coal Pyrolysis..... | 83 |
| 4.4 Tar Analysis of Jewell Coal Pyrolysis..... | 87 |
| Chapter 5: Effect of Volatile Material Content..... | 96 |

| | |
|---|-----|
| Chapter 6: Investigation of Secondary Pyrolysis Reactions | 99 |
| 6.1 Effect of Confinement..... | 100 |
| 6.2 Effect of Particle Size..... | 109 |
| 6.3 Effect of Heating Rate..... | 111 |
| 6.4 Effect of Heating Rate and Confinement | 112 |
| Chapter 7: Investigation of Secondary Tar Products | 113 |
| Chapter 8: Investigation of Biomass Pyrolysis..... | 116 |
| 8.1 Thermogravimetry on Pecan Shell Pyrolysis | 117 |
| 8.2 Gas Chromatography on Pecan Shell Pyrolysis | 119 |
| 8.3 Tar and Gas Evolution Fits from Pecan Shell Pyrolysis | 120 |
| 8.4 Biomass Surface Functional Groups | 125 |
| 8.5 DRIFTs-TG-GC PLS Calibration | 129 |
| Chapter 9: Tar Thermal Treatment | 135 |
| Chapter 10: Coke Hairs and Silver Coke..... | 140 |
| 10.1 Silver Coke..... | 141 |
| 10.2 Coke hairs..... | 143 |
| Chapter 11: Analysis of Experimental Data | 150 |
| 11.1 Thermodynamics Analysis of Secondary Reactions..... | 151 |
| 11.2 Exercising the Measured Mass Closure | 156 |
| Chapter 12: Conclusions and Future Work..... | 159 |

| | |
|---|-----|
| Appendix..... | 162 |
| Lists of identified compounds from GC-MS analysis of tar | 162 |
| MALDI-TOF spectra of coal tar with various matrices | 179 |
| LDI-TOF spectra of coal tar using various degrees of laser power (No matrix) | 180 |
| Repeated LDI-TOF scans of High VM coal tar (two 0.5 μ L drops on target desorbed using 50% laser power)..... | 181 |
| Empirical correlations evaluated to estimate HHV from ultimate/proximate analysis results | 181 |
| Bibliography | 183 |

| | |
|--|----|
| Figure 1 Flow diagram from Woolf et al. illustrating how agricultural and agroforestry secondary biomass through pyrolysis may avoid greenhouse gas emissions and produce bio-oil, syngas, heat, and biochar. | 19 |
| Figure 2 Global productions of various metals from United States Geological Survey (USGS) and British Geological Survey (BGS)..... | 22 |
| Figure 3 Suncoke horizontal heat recovery oven design | 24 |
| Figure 4 Two edge-structures of aromatic carbon (a) zigzag and (b) armchair edge-structures of coke | 29 |
| Figure 5 Representative molecules of (a) cellulose (b) hemicellulose and (c) lignin, which are the main components of biomass..... | 33 |
| Figure 6 Two dehydration reactions in biomass pyrolysis (a) an intramolecular formation of anhydrocellulose and (b) an intermolecular formation of a glucose cross-link..... | 35 |

| | |
|--|----|
| Figure 7 Differential Scanning Calorimetry (DSC) from Areneau [43] of cellulose between 150 and 400 °C in three conditions (a-b) thin sample (c) reprocessed tar from cellulose (d) thick sample and (e) capped..... | 36 |
| Figure 8 Wood color change during retification; (a) untreated beechwood, (b) beechwood treated at 190 °C, and (c) beechwood treated at 200 °C (image public domain) | 36 |
| Figure 9 Decarboxylation reaction..... | 37 |
| Figure 10 Torrefied wood samples. Image from Heyl & Patterson..... | 38 |
| Figure 11 Gas evolution plots from (a) cellulose (b) hemicellulose and (c) lignin heated at 10 °C min ⁻¹ accredited to Yang et al. | 41 |
| Figure 12 Solid-state ¹³ C NMR spectra of pecan shells showing spectra from slow pyrolysis biochars at final temperatures of 300, 500, and 700°C ⁴⁵ | 41 |
| Figure 13 The coalification sequence along with geological pressure, temperature and evolution of gaseous products..... | 45 |
| Figure 14 Coal macerals categorized and defined. Low-rank coals have huminite macerals and higher rank coals have vitrinite macerals. Liptinite and inertinite are present in all types of coal. | 46 |
| Figure 15 Representative bituminous coal molecule | 47 |
| Figure 16 Representative bond breaking and formation sequences illustrating the free radical mechanism where double bonds and free radicals are formed while aliphatic hydrogen is consumed. | 50 |
| Figure 17 Phenol cross-linking reaction producing water and a diphenyl ether suggested by Niksa [59] and Solomon [63]..... | 51 |

| | |
|--|----|
| Figure 18 Bubble model schematic taken from Yu et al to show how the bubbles form and escape through bubble growth | 52 |
| Figure 19 Formation of cenospheric char structure taken from Yu et al shows how the structure differs at various extents of pyrolysis | 53 |
| Figure 20 List of the relevant free radical mechanisms for the thermal treatment of hydrocarbons credited to Savage [66] | 55 |
| Figure 21 The Fabuss-Smith-Satterfeild and Rice-Kossiakoff mechanisms as they apply to coal pyrolysis | 57 |
| Figure 22 Mechanism for representative coke growth reaction from Reyniers et al..... | 58 |
| Figure 23 Examples of pyrolytic PAH growth mechanism (a) is taken from Mulholland et al showing indene and cyclopentadiene forming larger PAH species and (b) is taken from Pope et al showing naphthalene forming perylene | 59 |
| Figure 24 Three different coke fingers (a) is a coke finger which has some gray patches and some coke hairs (b) shows a silver coke finger (c) coke hair with a large patch of coke hair | 74 |
| Figure 25 Thermogravimetric analysis of Jewell coal pyrolysis at 3 °C min ⁻¹ to 1100 °C..... | 81 |
| Figure 26 Gas evolution for Jewell coal pyrolysis at 3 °C min ⁻¹ to 1100 °C measured by GC ... | 83 |
| Figure 27 Oxygen signals from two detectors from Oak Grove coal pyrolysis | 86 |
| Figure 28 Ellingham diagram for metal and carbon oxides present in coal pyrolysis..... | 87 |
| Figure 29 Tar and gas evolution profile during Jewell coal pyrolysis at 3 °C min ⁻¹ to 1100 °C.. | 87 |
| Figure 30(a) from shortest to longest retention time (1) benzene (2) toluene (3) 2-nonanone (4) 1,1,3-trimethyl-cyclohexane (5) solvent peak (6) 2,6-diisopropyl-naphthalene (7) 5-methylethylidene-1,3-cyclopentadiene (8) 1,2,4-trimethyl-cyclohexane (9) 1-ethyl-4-methylcyclohexane (10) 9,10-dihydro-1-methyl-phenanthrene and (b) from shortest to longest | |

retention time (1) 2-methyl-naphthalene (2) o-tert-butyl cyclohexyl acetate (3) cis-4-methoxy thujane (4) 1,5-dimethyl-naphthalene(5) tetradecane (6) 3-methyl-3-phenyl-ethyl ester, trans-oxiranecarboxylic acid (7) α isomethyl ionone (8) 1,6,7-trimethyl-naphthalene (9) 1-(2,6,6-trimethyl-2-cyclohexen-1-yl)-1-penten-3-one (10) 3-(1,1-dimethylethyl)- α -methyl-benzenepropanal (11) 2,3,6-trimethyl-naphthalene (12) 1H-phenalene (13) 5-(1-hydroxyethylidene)-2-methyl-methyl ester 1,3-cyclopentadiene-1-carboxylic acid (14) 8-methyl-heptadecane, (15) benzophenone (16) 2-phenyl-2,4-octadienol (structure not shown in figure) (17) 3,3-diethyltridecane (structure not shown in figure) (18) 3-oxo-2-pentyl-methyl ester cyclopentane acetic acid (structure not shown in figure) (19) 4-methyl-9H-Fluorene (20) 3-dodecyl-2,5-furandione (structure not shown in figure) (21) 2-methyl-pentadecane (structure not shown in figure) (22) 1,1'-(3,3-dimethyl-1-butenylidene)bis-benzene (23) 2-(tetradecyloxy)-ethanol (24) 1,7-dimethyl-3-phenyltricyclo[4.1.0.0(2,7)]hept-3-ene (25) benzyl benzoate..... 90

Figure 31 LDI-TOF spectra for four coals a) Big Fork (VM-29.7%) b) ICG East Gulf (VM - 18.9%) c) Chilton (VM – 35.2%) d) Glamorgan (VM - 38.9%) 94

Figure 32 TG of eleven coals with varying volatile material content at 3 °C min⁻¹ to 1100 °C in an argon environment 96

Figure 33 (a) DTG of coals with the apparent volatile production of 23.9 wt. % or less heated at 3 °C min⁻¹ to 1100 °C in Ar (b) coals with apparent volatile production of 23.9 wt. % or more. 98

Figure 34(a) TG and DTG of low-VM heated at 3 °C min⁻¹ in pan and cup confinement (b) TG and DTG of mid-VM heated at 3 °C min⁻¹ in pan and cup confinement..... 100

Figure 35(a) Tar and gas evolution of low-VM heated at 3 °C min⁻¹ in pan and cup confinement (b) Tar and gas evolution of mid-VM heated at 3 °C min⁻¹ in pan and cup confinement..... 102

| | |
|---|-----|
| Figure 36 Hydrogen, methane, and C2 hydrocarbons (ethane and ethylene) evolution measured by gas chromatography from mid-VM heated at 3 °C min ⁻¹ in pan and cup confinement..... | 104 |
| Figure 37 TG and DTG of High-VM heated at 3 °C min ⁻¹ in pan and cup confinement | 106 |
| Figure 38 Comparison of total volatile material produced for 40 and 1000 micron coal particles in two confinements | 109 |
| Figure 39 Comparison of H/C ratio of the gas products for 40 and 1000 micron coal particles in each confinement | 110 |
| Figure 40(a) TG and (b)DTG of low-VM coal at heated at 1, 3 and 10 °C min ⁻¹ in argon | 111 |
| Figure 41 (a) TG and (b) DTG of Mid-VM heated at 1 and 10 °C min ⁻¹ in pan and cup confinement..... | 112 |
| Figure 42 LDI-TOF spectra for Jewell coal tar produced in the (a) pan and (b) cup confinement | 114 |
| Figure 43 TG of pecan shells heated at 10 °C min ⁻¹ to 500 °C in a N ₂ atmosphere | 117 |
| Figure 44 GC measurements of pecan shells pyrolysis gas products during heating at 10 °C min ⁻¹ to 500 °C in a N ₂ atmosphere..... | 119 |
| Figure 45 Empirical (points) and predicted (dash lines) rate profiles of methane, carbon monoxide, carbon dioxide, ethane, ethylene, and tar during pecan shell pyrolysis at 10 °C min ⁻¹ up to 500 °C. Thin solid lines are pseudocomponents from normal distribution fitting of volatile evolution rates for tar (a), methane (b), carbon dioxide (c), carbon monoxide (d), ethane (e), and ethylene (f). The thick solid line represents temperature..... | 121 |
| Figure 46 In situ DRIFTS monitoring of slow pyrolysis for pecan shells | 125 |
| Figure 47 Deconvoluted DRIFTS peaks between 1860 –1450 cm ⁻¹ as function of pyrolysis temperature for (a) pecan shells, (b) cottonseed hulls, (c) cotton gin waste, (d) flax shives..... | 127 |

| | |
|--|-----|
| Figure 48 Cross-validation scatter plots of measured and estimated mass loss data from TG. Lines are the fit (red) and 1:1 (green). | 131 |
| Figure 49 Cross-validation scatter plots of measured and estimated mass of CO ₂ , CO, CH ₄ , C ₂ H ₆ , and C ₂ H ₄ , and total gas (sum of CH ₄ , C ₂ H ₄ , C ₂ H ₆ , CO ₂ , and CO). Lines are the fit (red) and 1:1 (green). | 132 |
| Figure 50 Cross-validation scatter plots of measured and estimated mass of tar and deconvoluted tar psuedo-components. Lines are the fit (red) and 1:1 (green). | 134 |
| Figure 51 Temperature program for TGA of tar samples..... | 136 |
| Figure 52 (a) The TG profile of birch wood tar heated at 10 °C min ⁻¹ to 550 °C (b) The gas evolution profile from birch wood tar pyrolysis | 137 |
| Figure 53 TGA of four coal tar samples at 3 ° min ⁻¹ to 1100 °C | 138 |
| Figure 54 LDI-TOF spectrum of coal tar thermally treated at 3 °C min ⁻¹ | 139 |
| Figure 55 Annotated XRD spectrums of two powdered silver coke samples and a powdered coke hair sample | 141 |
| Figure 56 Six SEM images of coke hairs..... | 144 |
| Figure 57 EDS mapping of a single carbon filament with low to no concentration of potassium, nickel, silicon, aluminum and oxygen atoms..... | 145 |
| Figure 58 Cross-sectional SEM images of coke hairs embedded in a polymer cast | 146 |
| Figure 59 XRD of carbon filaments and various reference compounds with matching peaks... | 146 |
| Figure 60 A carbon filament among iron particles generated catalytically at 400 °C in a flow- through reactor | 147 |
| Figure 61 Carbon filament network generated at 270 °C and 40 atm of methane | 148 |
| Figure 62 Methane, ethylene, ethane and hydrogen evolution from pyrolysis of Jewell coal ... | 153 |

| | |
|--|-----|
| Figure 63 Methane, ethylene, and ethane evolution from pyrolysis of pecan shells | 154 |
| Figure 64 Predicted volatile product evolution from pecan shell pyrolysis | 156 |
| Figure 65 Predicted and measured mass loss profiles | 157 |
| Figure 66 Predicted and measured H/C and O/C ratios of pecan shell char during pyrolysis.... | 158 |
| | |
| Table 1 PAH compounds labeled as priority emissions by EPA and IARC (in gray)..... | 25 |
| Table 2 Bond dissociation energies (BDE) for several bonds relevant to coal pyrolysis..... | 50 |
| Table 3 Proximate and ultimate analysis of the pecan shell and coal samples used in this work | 63 |
| Table 5 Ultimate and proximate analysis of pecan shell and pecan shell char at various pyrolysis temperatures | 70 |
| Table 6 Average product distribution from three coking coals (samples contained nominally 1 wt. % moisture) and pecan shells..... | 81 |
| Table 7 Average product distributions in percent by mass of the low and mid-VM coals studied in two confinements heated at 3 °C min ⁻¹ | 103 |
| Table 8 Total production of gas species on a mg per mg of initial coal mass basis at 3 °C min ⁻¹ in each confinement for the low and mid-VM coal and the p-value between the different conditions | 105 |
| Table 9 Average product distributions in percent by mass of the high-VM coal per confinement heated at 3 °C min ⁻¹ | 108 |
| Table 10 Total production of gas species (mg/mg of initial coal mass) at 3 °C min ⁻¹ in each confinement for the high-VM coal and the p-value between the different conditions | 108 |
| Table 11 Difference in solid yield between cup and pan for the low, mid and high-VM coal at 1, 3, and 10 °C min ⁻¹ | 113 |

| | |
|--|-----|
| Table 12 Average MW of Jewell tar produced at three different heating rates measured by LDI-TOF | 115 |
| Table 13 Cross-validation statistics of the Partial Least Squares calibration between DRIFTS and predicted gas evolution for pecan shell pyrolysis at 10 °C min ⁻¹ | 130 |
| Table 14 Silver coke elemental composition determined by ICP-MS..... | 142 |
| | |
| Schematic 1 (a) the vertical oriented configuration of the TGA (b) schematic of the TG-GC system used for pyrolysis studies..... | 65 |
| Schematic 2 MicroGC schematic from Inficon | 66 |
| Schematic 3 Glass impinger design and gas flow path..... | 67 |
| Schematic 4 On the left, the short (pan) confinement used in TGA pyrolysis experiments is shown, and on the right, the tall (cup) confinement used in TGA pyrolysis experiments is shown | 68 |
| Schematic 5 MALDI-TOF positive-ion reflectron mode | 71 |
| Schematic 6 Schematic of the in situ DRIFTS apparatus..... | 73 |

Table of Abbreviations and Notation

| | |
|--------------|--|
| TG-GC | Thermogravimetry-Gas Chromatography |
| DRIFTs | Diffuse Reflectance Infrared Fourier Transform Spectroscopy |
| MALDI-TOF/MS | Matrix-assisted Laser Desorption/Ionization-Time-of-flight Mass Spectroscopy |
| GC-MS | Gas Chromatography-Mass Spectroscopy |
| MW | Molecular Weight, amu |
| MWD | Molecular Weight Distribution |
| PAH | Polynuclear Aromatic Hydrocarbon(s) |
| PLS | Partial Least Square regression |
| SEM | Scanning Electron Microscopy |
| EDS | Energy Dispersive Spectroscopy |
| XRD | X-Ray Diffraction |
| ICP-MS | Inductively Coupled Plasma-Mass Spectroscopy |
| EPA | Environmental Protection Agency |
| MACT | Maximu Achievable Control Technology |
| PM | Particulate Matter |
| CRI | Coke Reactivity Index |
| CSR | Coke Strength after Reaction |
| DSC | Differential Scanning Calorimetry |
| TG-FTIR | Thermogravimetry-Fouier Transform Infrared spectroscopy |
| TGA | Thermogravimetric Analyzer |
| NMR | Nuclear Magnetic Resonance spectroscopy |
| VM | Volatile Material Content |

| | |
|----------------------------|---|
| GC/ μ GC/ μ GC-TCD | Micro-gas chromatograph |
| HHV | Higher Heating Value, kJ kg^{-1} |
| EBSD | Electron Backscatter Diffraction |
| v_{Total} | Total volumetric flow rate, mL min^{-1} |
| v_{Sweep} | Volumetric flow rate of sweep gas, mL min^{-1} |
| y_{Sweep} | Mole fraction of sweep gas |
| v_i | Volumetric flow rate of i, mL min^{-1} |
| y_i | Mole fraction of i |
| r_{tar} | Rate of tar production, mg min^{-1} |
| r_{solid} | Rate of solid consumption, mg min^{-1} |
| r_{gas} | Rate of gas production, mg min^{-1} |
| α | Amplitude, mg min^{-1} |
| β | Mean temperature of the distribution, $^{\circ}\text{C}$ |
| Γ | Standard deviation of temperature range, $^{\circ}\text{C}$ |
| T | Sample Temperature, $^{\circ}\text{C}$ |
| n | Number of distributions |
| LDI-MS | Laser Desorption/Ionization-Mass Spectroscopy |
| FI-MS | Field Ionization-Mass Spectroscopy |
| H/C | Molar hydrogen to carbon ratio |
| O/C | Molar oxygen to carbon ratio |
| RMSEC | Root Mean Square Error of Calibration |
| RMSECV | Root Mean Square Error of Cross Validation |
| T_M | Melting Temperature, $^{\circ}\text{C}$ |

Chapter 1: Introduction

Historically, charcoal and coke has been produced by pyrolysis processes and used in the purification of metals. Today, pyrolysis is being adapted as a carbon negative process for recycling secondary biomass and waste to produce fuels and higher value chemicals. The work presented investigates the pyrolysis reaction mechanism for coke and charcoal production as well as alternative solid carbon products.

The description of this work begins with a discussion on the current and conceptual roles of solid carbon products in society. The processes currently used in commercial production of coke from coal and charcoal from biomass are presented. The discussion includes environmental concerns and quality margins associated with the industry. These topics introduce the need for yield investigations in slow pyrolysis.

Overall, there is a clear need for metallurgical coke and charcoal in our society at a global scale. Chemical engineers must design pyrolysis processes that are both efficient and environmentally benign. Scientific knowledge about pyrolysis reaction mechanisms is required for building more efficient, safer and more economic pyrolysis processes used to produce solid carbon materials. The three most important process components to understand about slow pyrolysis are (1) choice of feedstock, (2) the temperature sequence of pyrolysis reactions, and (3) the impact of secondary volatile reactions on yield. The novel phenomenological developments of the experiments to be provide new insights for building better pyrolysis processes.

1.1 Application for Solid Carbon Products

Pyrolysis is the thermal decomposition of a material without the presence of an oxidant. For coal, biomass, and many other cases, the products of pyrolysis are permanent gases, condensable gases, and solid products. The carbon-rich solid product generated by the pyrolysis

of biomass is referred to as char, while the residual product from coal is referred to as coke. Chemically, chars consist of functionalized highly condensed aromatic structures and inorganic mineral inclusions. Meanwhile, coke is mainly graphitized carbon with minerals and little to no functional groups or heteroatomic species. Physically, char and coke have a high surface area and large pore size distributions. In this chapter, the applications of each of these products are explained.

1.1.1 Biochar Concept

Biochar is a term created for biomass char used in various sustainability applications. Biochar applications include renewable energy production, waste recycling, soil amendment, pollution remediation, and carbon sequestration.^{1, 2} Energy applications include the utilization of volatile products from pyrolysis and the utilization of char as a solid fuel.

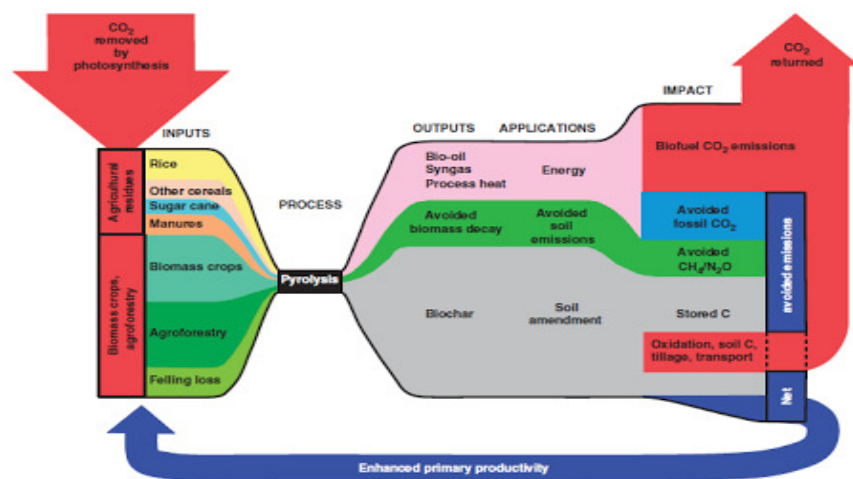


Figure 1 Flow diagram from Woolf et al. illustrating how agricultural and agroforestry secondary biomass through pyrolysis may avoid greenhouse gas emissions and produce bio-oil, syngas, heat, and biochar.

Figure 1 illustrates the biochar concept. Waste may be transformed through pyrolysis to produce bio-oil, syngas, process heat, biochar and to avoid biomass decay, which produces

greenhouse gas products. In pyrolysis, a portion of the decayable material is partitioned into the biochar product where the carbon is “locked-in” the solid phase rather than emitted into the atmosphere. Secondary biomass such as crop residue, animal manure, sewage sludge, forest debris, commercial waste, and municipal solid waste have all been used to produce biochar.¹ The energy production from biomass pyrolysis offsets fossil fuel utilization and the CO₂ produced is still within the natural carbon cycle. In this assessment, it is assumed that a yield of 35% biochar could produce 8.7 MJ of bioenergy per kg of biomass (which includes burning of methane).³ Pyrolysis of biomass waste avoids greenhouse gas, CH₄ and N₂O emissions, and environmental health effects by killing microbes in animal manure and sewage sludge.¹ Figure 1 focuses on the use of biochar in soil amendment, which serves to improve crop production while sequestering carbon.

The application of biochar in soil amendment has attracted much attention as a practical solution to agronomic and environmental problems.⁴ Biochar exists naturally in soils of the Central Amazon from wildfires and was historically used in ancient Japanese horticulture.² Biochar is proven to be a long-term soil amendment that improves physicochemical and biological properties of soil while sequestering carbon.^{1,5} Studies show the high surface area and hydrophobicity of biochar enable it to increase water retention capacity of sandy soils.^{1,5} The hydraulic characteristics of soil improve within months after the addition of biochar.⁵ The mineral content of biochar supplies macro- and micro-nutrients for the plants and increases crop yield.⁶ Figure 1 illustrates that increased production of biochar results in increased production of biomass feedstock.

The biochar concept has greater climate change mitigation potential than first-generation bioenergy (i.e., enzymatic ethanol production or gasification) because biochar retains half of the

carbon fixed in biomass during photosynthesis.³ As a result, biochar has been estimated to be capable of offsetting 12% of current anthropogenic CO₂ equivalent emissions. However, the stability of biochar in soil is of importance to consider in carbon sequestration.^{1,7} The highly condensed aromatic structure of biochar is resistant to microbial oxidation, which eliminates greenhouse gas emissions.⁴ However when biochar is incubated in soil, an early flush of CO₂ is emitted which is attributed to both abiotic and biotic processes, i.e., microorganisms seem to be able to degrade highly aromatic structures.⁷ However, biochar is still considered to be largely refractory and this emission of CO₂ is factored into the concept shown in Figure 1. Other research shows that biochar can reduce N₂O and CH₄ emissions from soil by both biotic and abiotic mechanisms.¹

Another viable application of biochar is activated carbon. Activated carbon is an expensive universal adsorbent typically made from nonrenewable fossil fuels.² Biochar has similar adsorbent properties due to the large surface area, pore size distribution and ion-exchange capacity.¹ Production of biochar for adsorption application from waste biomass is more sustainable and cheaper than current activated carbon processes while adding the carbon negative advantage.² Biochar could replace the currently used activated carbons as a low-cost sorbent for contaminants and pathogens in groundwater, drinking water, and wastewater.² Studies show that biochars have been able to remove Cu²⁺, Zn²⁺, Cd²⁺, and Pb²⁺ and cationic organic compounds from aqueous systems.^{1, 2} The organic contaminants include pesticides, herbicides, polynuclear aromatic hydrocarbons (PAHs), dyes, and antibiotics.¹

1.1.2 Carbothermic Reduction

Biochar has the potential for many applications, however, the largest current use of the solid carbon products is as a reductant in metal production. Prehistorically, charcoal was used to

smelt tin for bronze making. Modern day technology still relies on charcoal to smelt metal ores in the metal industry.^{8,9,10} Charcoal and coke are used in the U.S. silicon industry to reduce quartz to pure silicon in arc furnaces ($\text{SiO}_2(\text{s}) + 2\text{C}(\text{s}) \rightarrow \text{Si}(\text{s}) + 2\text{CO}(\text{g})$).^{9,11} Titania is another metal reduced by carbothermal techniques to produce titanium carbide, which is used in automotive, electrical and refractory industries.¹² Charcoal can also be used in the refining of copper, nickel, aluminum, and electro-manganese.¹³ Unfortunately, secondary-use biomass is not routinely used for metallurgical charcoal production. This would help to mitigate mass deforestation. However, charcoal utilization in the metallurgical process is meager compared to the use metallurgical coke from coal.

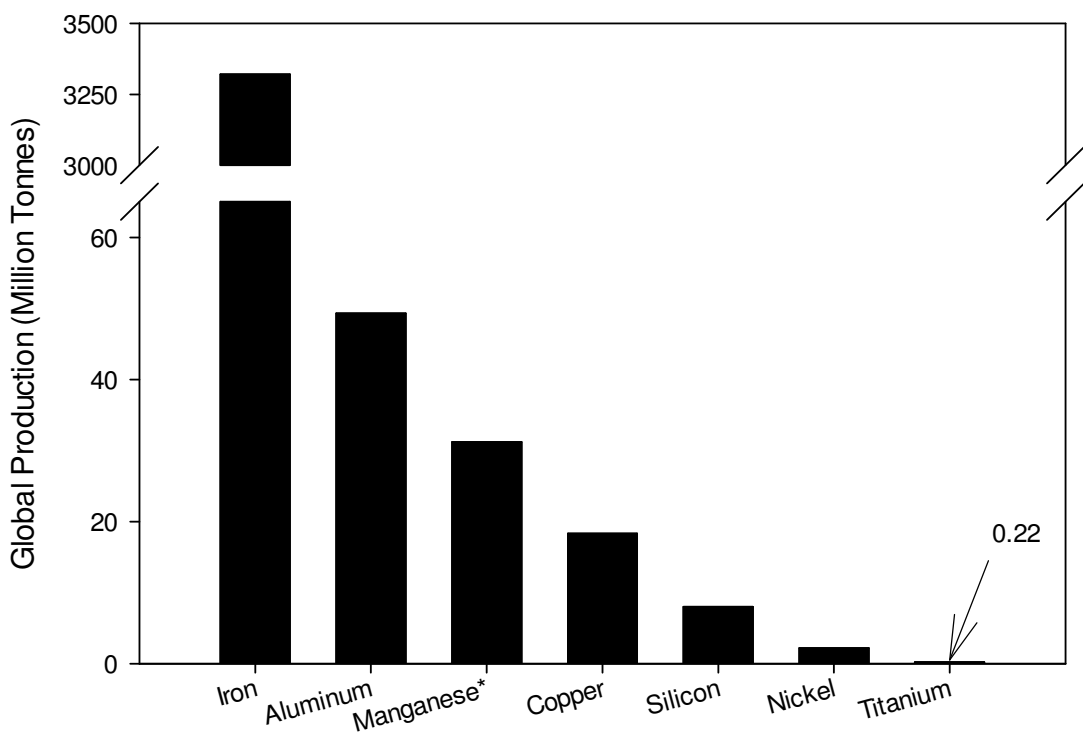


Figure 2 Global productions of various metals from United States Geological Survey (USGS) and British Geological Survey (BGS).

Figure 2 shows the scale of iron production compared to copper, silicon and other metals refined by metallurgical charcoal. Iron production is majorly reliant on metallurgical coke rather than charcoal. Metallurgical coke is used in blast furnaces for iron production. The role of metallurgical coke is threefold; (1) it is a fuel that provides heat for the melting of slag and metal, (2) it is a chemical reducing agent in the reduction of iron oxides and (3) it is a permeable support in the furnace that supports the iron and provides a permeable matrix necessary for slag and metal to pass down into the hearth and for hot gases to pass upwards into the stack.¹⁴ There is currently no other material available that can fully or partially replace metallurgical coke in blast furnaces.¹⁴ Blast furnaces are the only practiced method for producing steel at commercial scale.

1.2 Commercial Production

For many years, charcoal production took place in large kilns.⁹ For example, pyrolysis of logs at 400 °C is carried out in a kiln for 90-150 minutes to produce charcoal.¹⁵ The kilns were sealed causing elevated pressures during pyrolysis.^{8, 9, 10, 15, 16} Continuous pyrolysis systems are in development and some have reached scales of 93 tons per day (tpd) of dry feedstock.¹⁷

Commercial metallurgical coke production resembles the common batch production of charcoal in kilns. Vertical by-product ovens are the conventional coke ovens used in many blast iron furnace facilities. Vertical by-product coke ovens are more than 8 m in height and less 1 m in width where the coal is sandwiched between two refractory walls.^{14, 18} The oven operates between 950 and 1100 °C in a non-oxidizing atmosphere.¹⁸ The extent of carbonization is determined by the amount of volatiles produced.¹⁸ Pressure is built in the reactor throughout pyrolysis causing pollutants to be emitted through cracks in the oven refractory or doors.¹⁹ The volatiles produced are recovered and refined into chemicals.¹⁸

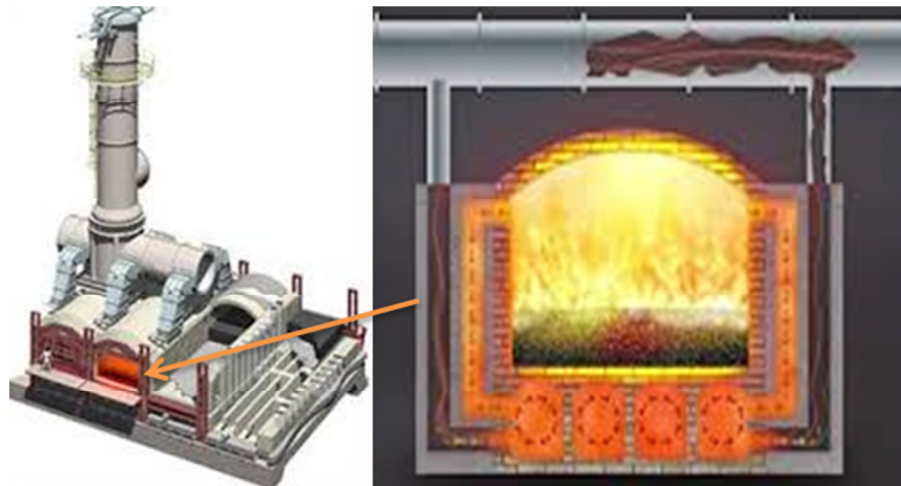


Figure 3 Suncoke horizontal heat recovery oven design

Over the past two decades, the coke-making industry has seen substantial technological modernization.¹⁸ The horizontal heat recovery ovens are considered to be a major technical feat in coke making. The horizontal heat recovery oven is shown in Figure 3. It is about 13.5 m long, 4.6 m wide and 2.4 m high and is charged with 36 to 41.5 tons of coal (about 1 meter in thickness), which takes 48 hours to carbonize.¹⁴ During pyrolysis, the volatiles are burnt directly above the coal and throughout ducts inside the oven walls and floor to generate the heat for pyrolysis, shown in Figure 3.¹⁴ The process continuously draws in air by a vacuum in order to contain pollutants and to achieve complete combustion.^{14, 19} The combustion gases are led to a boiler to create steam, which can be fed into a steam grid or used for generating electricity. About 75– 95 MW of electric power can be generated for every megaton of coke produced.¹⁴

Environmental Considerations of Commercial Production

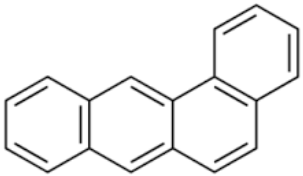
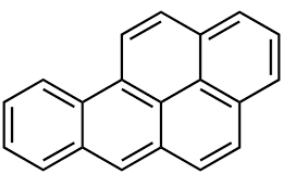
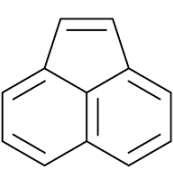
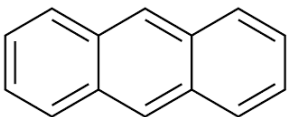
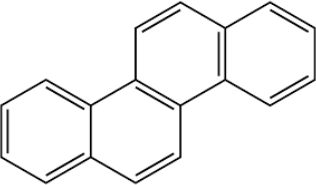
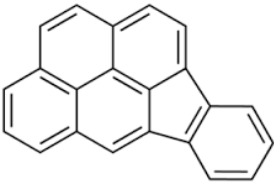
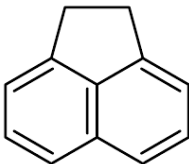
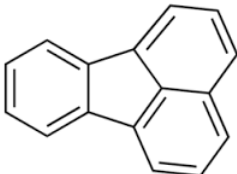
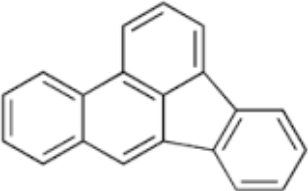
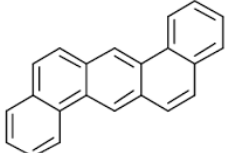
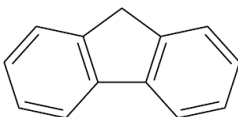
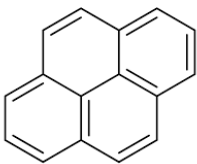
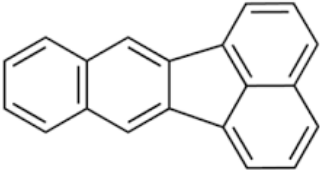
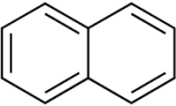
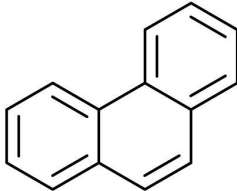
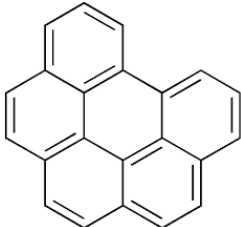
As in many chemical and energy processes, the focal point of environmental impact is on process emissions. Coke ovens have been recognized by the U.S. Environmental Protection Agency (EPA) as one of the main sources of PAHs and particulate matter emissions.²⁰⁻²²

Therefore, in the Clean Air Act Amendments of 1990, EPA established the Maximum

Achievable Control Technology (MACT) standards for coke facilities. The horizontal heat recovery oven process achieves EPA's MACT emission standards.¹⁹

Table 1 shows the 16 PAHs listed by the U.S. EPA as priority pollutants and indicates seven PAHs, which are also classified as carcinogenic PAHs by the International Agency for Research on Cancer (IARC).²⁰

Table 1 PAH compounds labeled as priority emissions by EPA and IARC (in gray)

| | | | |
|---|---|--|---|
|  |  |  |  |
| benzo[a]anthracene | benzo[a]pyrene | acenaphthylene | anthracene |
|  |  |  |  |
| Chrysene | indeno[1,2,3-cd]pyrene | Acenaphthene | fluoranthene |
|  |  |  |  |
| benzo[b]fluoranthene | dibenzo[a,h]anthracene | Fluorine | Pyrene |
|  |  |  |  |

| | | | |
|----------------------|-------------|--------------|----------------------|
| benzo[k]fluoranthene | naphthalene | Phenanthrene | benzo[g,h,i]perylene |
|----------------------|-------------|--------------|----------------------|

Coke oven mostly emit PAHs consisting of three or four rings.²¹ Primary concerns for biomass pyrolysis are benzene, naphthalene, and particulate matter (PM). The soot from biomass pyrolysis is typically in the 2.5-10 micron size range, which poses respiratory hazards.¹⁷ It should be mentioned that concentrations of PAH emission are dependent on process design and operation.²¹

Another emission considered as toxic by the EPA is hydrochloric acid (HCl). British and American coals have relatively high chlorine content.²³ During carbonization, chlorine in coal is released as HCl with increased temperature and time of carbonization.²³ The amount of chlorine in metallurgical coke is a critical concern for blast furnace prolongation because HCl may cause high-temperature corrosion problems in boilers and downstream processes.^{23, 24, 25} However, HCl should not be emitted from the process.

In addition to air emissions, contamination of water effluent from the process must be considered. Wastewater from coal and biomass pyrolysis processes alike may have detrimental environmental and ecological effects if emitted into any surface water, rivers, lakes, streams, or agricultural land.^{17, 26} Water is used in coke production for quenching of hot coke. Coke oven wastewater contains a high concentration of ammonium, cyanide, phenolic compounds, heterocyclic nitrogenous compounds, PAHs, and fullerenes.^{26, 27} Water-stable fullerenes are intrinsically reactive as both an oxidative chemical and a nanoparticle.²⁷ In summary, wastewater from pyrolysis must receive proper treatment before discharge.²⁶

Besides emissions, the use of natural resources for charcoal and coke production is environmental and sustainability concern in and of itself. While coal is a known nonrenewable resource, charcoal resources compete with the environmental barrier of deforestation. Food and

Agriculture Organization reported global charcoal production exceeded 55 million tons per year in 2012. Charcoal is on an upward trend which is expected to continue growing. However, the increased production of char must be handled responsibly. The low efficiency of charcoal kilns is a principal cause of the deforestation in many tropical countries and a net contributor to global warming. Based on thermochemical equilibrium calculations for wood pyrolysis, traditional kilns have efficiencies as low as 8% and as high as only 36%.¹⁶ Deforestation could be mitigated by using secondary biomass waste as feedstock for charcoal, biochar and activated carbon production. These aspects all emphasize the importance of yield in commercial pyrolysis processes and utilization of waste biomass sources.

Product Quality Margins of Commercial Production

Quality assurance is a common task for chemical engineers. With all materials, there exist a universal relationship between structure, processing, and performance. The production of metallurgical coke and charcoal are no exceptions. This section describes quality standard in coke and outlines how they are achieved through feedstock selection and pyrolysis conditions. Lastly, the desirable properties of metallurgical charcoal, activated carbon, and biochar for soil amendment are discussed. The assurance of products to meet the current quality standard is paramount if the sustainable production of the material is to be commercially viable.

High mechanical strength is a unique physical property of metallurgical coke among carbon products. Coke must support the weight of iron at high temperatures in order to give a permeable matrix for gas products and molten material to percolate.¹⁴ The particle size distribution of a coke bed must be narrow, usually between 50 –55 mm.¹⁴ The mechanical and thermal stability is a function of the order of stacked polynuclear aromatic carbon layers in coherent units, the size of the carbon layer and minimal in-plane defects.²⁸ In practice, coke

strength has been correlated with coal rank (i.e., inert content), rheological properties, total dilatation, and petrographic compositions of the parent coal.¹⁴ Therefore, a special category of “coking coals” were identified that are needed to produce a metallurgical coke of sufficient quality.¹⁴ These coals are typically bituminous coals.

To ensure good blast furnace performance, coke must retain high mechanical strength throughout high-temperature reactions with carbon dioxide (CO₂) and alkali metals.¹⁴ Reactive coke will weaken and degrade into smaller particles leading to a reduction in permeability and, hence, lower efficiency.¹⁴ High coke reactivity also causes burn losses when hot coke is exposed to oxidative environments. It was found that for most coals, reactivity decreases with increasing extent of carbonization and pyrolysis temperature.^{29, 30} This decrease in reactivity could be explained by the material becoming more isotropic therefore losing active sites.^{29, 30} Furthermore, the reactivity of coke decreases with increasing parent coal rank.²⁹ This is because coal rank is related to the weight percent of aromatic carbon in coal which decreases active sites on the carbon structure. Investigations of particle size, specific surface area, anisotropy, and crystallite stacking height showed that oxidation activity of condensed aromatic materials is linked to structural properties.³¹ The structural properties generally depict the number of exposed edge atoms of the lamellae that act as active sites.²⁹ The nature of active sites on the edge were shown by X-ray diffraction (XRD), Raman spectroscopy, and transmission electron microscopy.³¹ Raman spectroscopy measures D1- and G- bands which are correlated to stacking order while XRD is used to measure crystallite stacking height. Aromatic structure either have “armchair” or “zigzag” edge structures as illustrated in Figure 4. For the armchair-edge structure, electron densities are rather evenly distributed over the structure making a stable structure, while for the zigzag edge-structure, densities are concentrated at the edges making them more

reactive.³² In other words, the loss of reactivity is related to the loss of free electrons in stable carbon ring structures. Meanwhile, the quantities of active sites are affected by temperature³⁰ due to the increase in unit size.

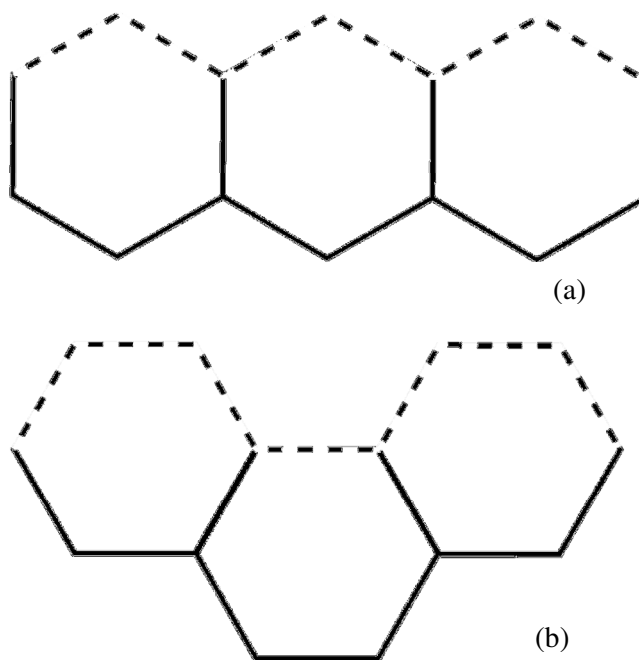


Figure 4 Two edge-structures of aromatic carbon (a) zigzag and (b) armchair edge-structures of coke

In general, samples with low oxidation reactivity are associated with the low surface area, large particle diameter, and large crystallite stacking height. Samples with high reactivity can be summarized as samples with the high surface area, small particle diameter, and small crystallite stacking height.³¹ Fundamental research on how carbon isotropy, porosity, and ash chemistry affects coke strength and reactivity led to development of a standardized test for measuring the coke reactivity and post-reaction strength.¹⁴ The test is based on the extent of reaction between coke and CO_2 at $1100\text{ }^\circ\text{C}$ for 2 hours under standardized gas flow rate conditions.¹⁴ The results of the experiment determine the Coke Reactivity Index (CRI). The coke mechanical strength is then

measured after reacting with CO₂, which results in a specific Coke Strength after Reaction (CSR) index.¹⁴ For a good quality coke, the CRI should be low and the CSR index should be high.¹⁴ The correlation between CSR and CRI indices are linear, such that lower reactivity means higher coke strength.¹⁴ The CRI and CSR of coke can be correlated to vitrinite reflectance and fluidity of parent coals where vitrinite reflectance is determined by non-destructive petrographic analysis.¹⁴ The indices allow for an operating window of specific coking coals to be developed for high-quality commercial coke production.¹⁴

Char properties and yields are mainly dependent on the biomass type and pyrolysis temperature.¹ Slow pyrolysis of these feedstocks were investigated temperatures from 100 to 900 °C. Up to pyrolysis temperature of 640 °C, char yield tends to decrease due to the loss of volatile matter and non-condensable gas products (CO₂, CO, H₂, and CH₄).¹ Char properties as a function of pyrolysis temperature have also been studied.¹ Chars produced at temperatures less than 500 °C are suitable for adsorption of polar organic or inorganic contaminants due to the presence of oxygenated functional groups that facilitate electrostatic attraction and precipitation.¹ At pyrolysis temperatures greater than 500 °C, char become less polar, more aromatic, and exhibits increases in surface area and microporosity.¹ High-temperature char is preferred for the adsorption of organic contaminants and soil amendment due to their refractory nature.¹ At extremely high temperature like 950 °C, charcoal resembles graphite.¹⁶ Metallurgical grade charcoal generally must contain high fixed carbon content of 85-90% with low ash and volatile matter contents.^{8, 33} In the following chapter, the exact mechanism of the transformations for biomass and coal during pyrolysis will be discussed in more detail.

Chapter 2: Fundamentals of Pyrolysis

In this chapter, the fundamental pyrolysis mechanisms of coal and biomass are described. This description is based on the literature for each respective field. The two feedstocks are discussed in separate sections, 2.1 and 2.2. Before discussing the mechanisms, the chemical constitution and origin of each feedstock are discussed in a general sense. The mechanistic description includes temperature-dependent chemical, energetic, and physical transformations of the raw materials. Secondary tar reactions in regard to solid carbon production are given special attention in the discussion of each feedstock. These reactions are again highlighted in a review of experimental investigations involving reaction confinement, pressure, and heating rate dependence of the pyrolysis mechanism. Lastly, the known heterogeneous reactions with ash in feedstock are listed. Throughout the chapter, gaps in the literature addressed in this thesis are identified.

2.1 Biomass

2.1.1 Biomass Constitution

Biomass is a term that encompasses all plant life and by-products of biology. The chemical composition of biomass depends on various factors such as plant species, the plant component, growth processes, growing conditions, the age of the plant, and blending of plants.³⁴ Growing conditions are the largest variable, which includes access to sunlight, geographic location, climate, seasons, soil types, use of fertilizer, pesticide doses, water, pH level, nutrients, proximity to a forest, proximity to a sea, and proximity to a polluted area.³⁴ All of these factors make biomass an inherently heterogeneous sample in the chemical perspective. Fortunately, all biomass is composed of only C, O, H, N, Ca, K, Si, Mg, Al, S, Fe, P, Cl, Na, Mn, and Ti (in

order of decreasing concentration).³⁴ The organic elements (C, O, H, N, and S) compose the carbohydrates, lignins, proteins, lipids, wax, and resin substances in biomass.³⁵ Furthermore, these organic constituents make up biomolecules like cellulose, hemicellulose, and lignin content³⁶ shown in Figure 5. Amino acids, terpenes, fatty acids and other water-soluble compounds combined comprise less than 10% of the biomass.³⁶ Cellulose, hemicellulose, and lignin are not individual units in the cell wall of plants but rather, are intimately interconnected.³⁷ Cellulose is a semi-crystalline linear polymer comprised of β -linked glucose, which is bound together via hydrogen bonding networks to form semi-crystalline rods called microfibrils.³⁸ The structural characteristics of cellulose vary in crystallinity, degree of polymerization, and surface structure.³⁷ Hemicellulose is a more amorphous co-polymer than cellulose made up mainly of 5-carbon sugar monomers.³⁸ Lignin is a 3-dimensional structural molecule produced by the polymerization of p-coumaryl alcohol, coniferyl alcohol, and sinapyl alcohol shown in Figure 5c.³⁹ The structure and composition of lignin binds cellulosic fibers together similar to a composite structure.³⁷ The composite of biochemical macromolecules in biomass can be characterized by the functional groups which are sufficient for determining the reactivity of the material which is a major point of this thesis. Overall, biomass functional groups are mostly of alkenes, esters, aromatics, ketones, and alcohols.⁴⁰

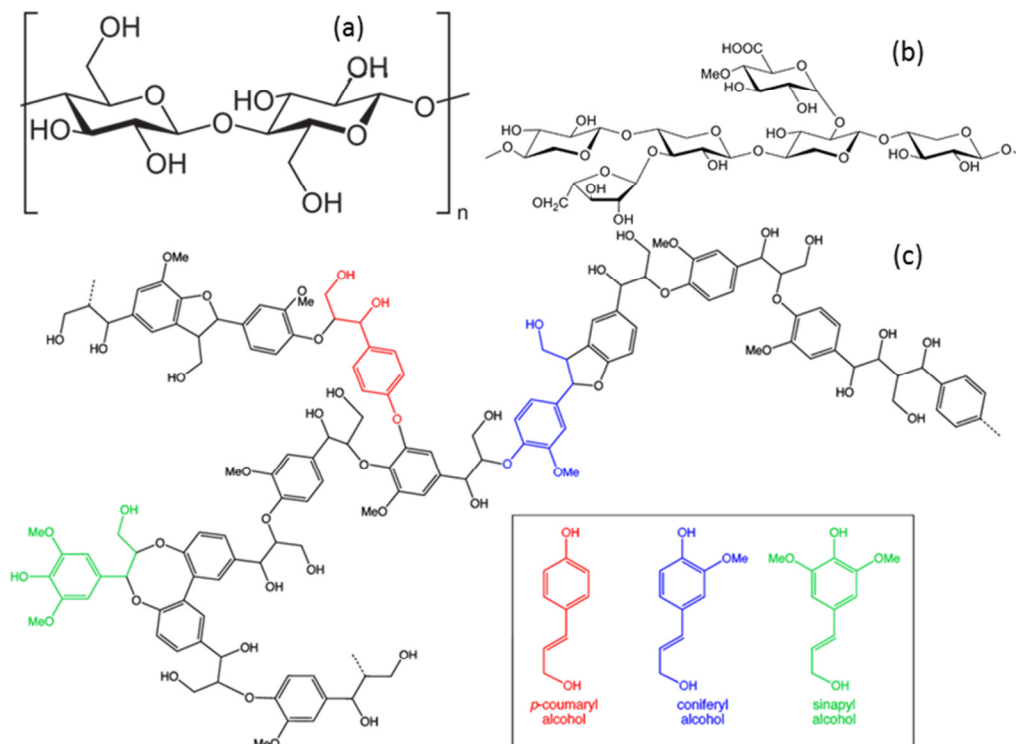


Figure 5 Representative molecules of (a) cellulose (b) hemicellulose and (c) lignin, which are the main components of biomass

The inorganic component of biomass (Ca, K, Si, Mg, Al, Fe, P, Cl, Na, Mn, and Ti) exists as entrapped ions and/or minerals.³⁶ Different plant types tend to vary in mineral composition. For instance, high Ca and Mn content are characteristic of woods (i.e., tree branches, stems, and trunks), barks, foliage, and chicken litter. High K₂O concentration is characteristic of herbaceous and agricultural biomass, particularly shells and husks. High P₂O₅ content is characteristic of animal manures, herbs, and agricultural biomass. Many shells, husks, and some woody biomasses contain MgO. High Na₂O content is characteristic of olive husks and pits. SiO₂ and Fe₂O₃ are rarely found in biomass. SiO₂ is found in reed canary grass, sorghastrum grass, rice straw, and rice husks.³⁴ Fe₂O₃ content is characteristic of pistachio shells, groundnut

shells, and sugar cane baggase.³⁴ Examples of how inorganic components affect the pyrolysis reaction mechanism are shown in the thesis work presented.

2.1.2 Biomass Pyrolysis Mechanism

In this section, the events during generic “wood” pyrolysis will be described in segments of temperature as a sample is heated. Overall, the pyrolysis reaction mechanism will consist of dehydration, depolymerization, re-polymerization, fragmentation, isomerization, and condensation reactions.⁴¹ All of these reactions arise from the decomposition of the biomass macromolecules. It is known from isolated studies that hemicellulose decomposes between 220 and 315 °C, cellulose will decompose between 315 and 400 °C and lignin will decompose over a wide temperature range from 160 to 900 °C.^{36, 40} However, the interconnection of these three macromolecules and coincidence of their decomposition creates a more complex reaction system than the three systems analyzed separately. The mechanism is more accurately explained in terms of reactions involving functional groups as will be illustrated in work presented in Chapter 8. The discussion will feature the effects of particle size, pressure, and heating rate on pyrolysis, which are heavily dependent on mass transfer limited secondary reactions demonstrated in this work.

Initial heating to 280 °C

Before 280 °C, pyrolysis reactions are predominantly solid state reactions that produce CO, CO₂ or H₂O. Water is the first volatile product observed. Water evolution from wood occurs both physically through desorption and chemically by the elimination of hydrolyzable functional groups.⁴² The weight loss of wood between 100-220 °C appears to be mainly due to loss of physically absorbed and entrapped water.^{16, 42} An example of chemical production of water is cellulose converting into anhydrocellulose as shown in Figure 6. The differential scanning

calorimetry (DSC) of cellulose thermal decomposition shown in Figure 7 illustrates an exotherm at 220 °C attributed to the formation of the anhydrocellulose.⁴³ This is the first example of many exothermic reactions divulged in this work which produce solid and gaseous products. Spectroscopic techniques are required to measure solid-state reactions like this however, macroscopic observation suggests their occurrence. Wood “retification”, shown in Figure 8, is known to occur between 230 and 250 °C where the wood color becomes reddish brown or chocolate. Retification can be attributed to degradation reactions of anhydrocellulose and hemicellulose up to 250 °C, which forms CO, CO₂, and H₂O and char products.^{16, 43, 44} Wood thermally treated at these temperatures is known to become resistant to biological attack due to the loss of acid hydrolysable groups.^{2, 16}

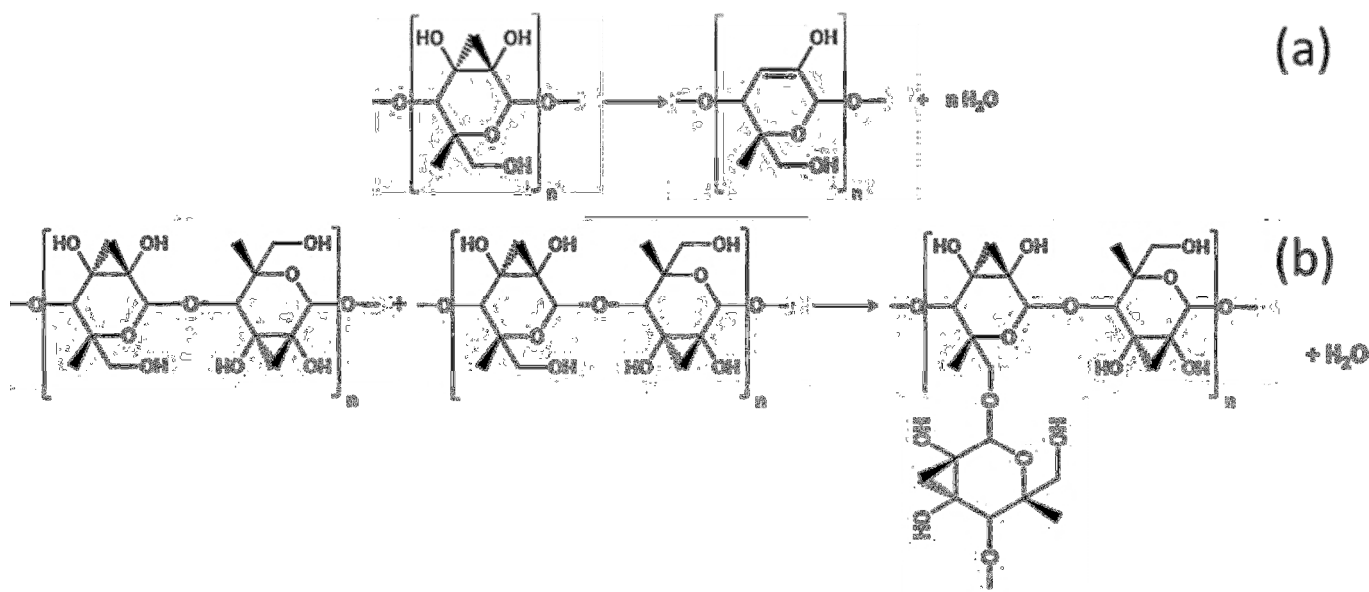


Figure 6 Two dehydration reactions in biomass pyrolysis (a) an intramolecular formation of anhydrocellulose and (b) an intermolecular formation of a glucose cross-link

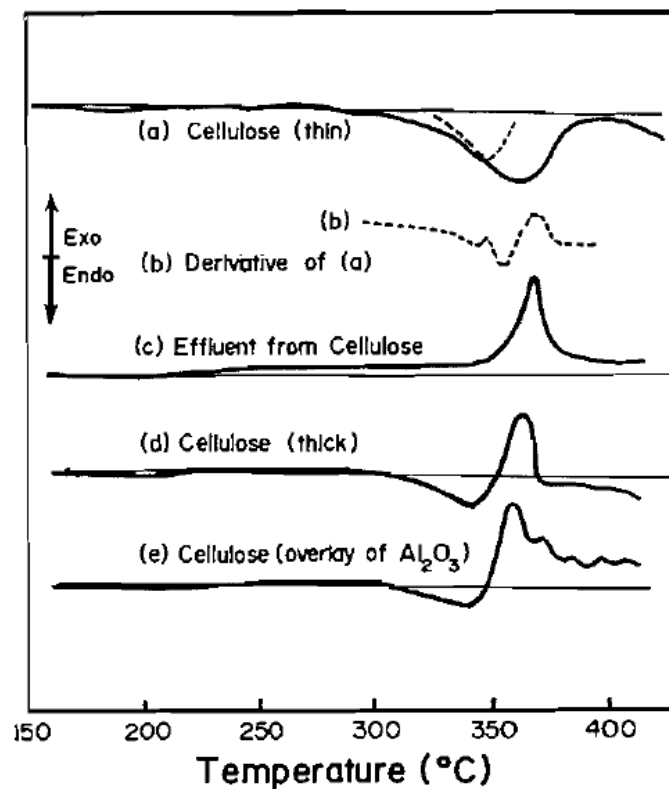


Figure 7 Differential Scanning Calorimetry (DSC) from Areneau [43] of cellulose between 150 and 400 °C in three conditions (a-b) thin sample (c) reprocessed tar from cellulose (d) thick sample and (e) capped.

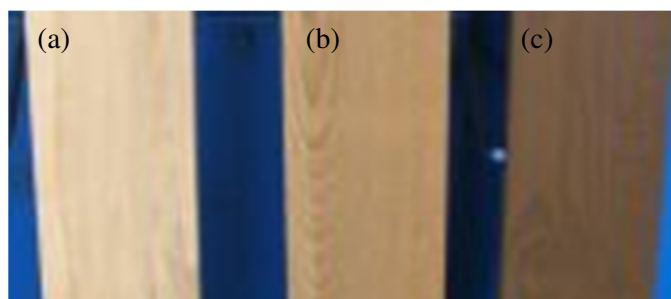


Figure 8 Wood color change during retification; (a) untreated beechwood, (b) beechwood treated at 190 °C, and (c) beechwood treated at 200 °C (image public domain)

Between 220 and 550 °C, water is produced by dehydration reactions.⁴² Peak production of water from cellulose pyrolysis is reached at 300 °C.⁴² Up to 240 °C, cellulose hydroxyl groups

were shown to form ketone groups,⁴² which degrade further to produce CO starting at 170 °C⁴⁵ however, this must also produce H₂. Hydrogen is transferred continuously between condensed phase donor and acceptor molecules. The hydroxyl elimination reactions yield unsaturated compounds and ultimately char.⁴² The onset of CO₂ evolution occurs at 255 °C from decarboxylation reactions shown in a most generic form in Figure 9.⁴⁵ Intraparticle gas sampling from biomass depicted a maximum CO₂ and CO production at 325 °C.⁴⁶

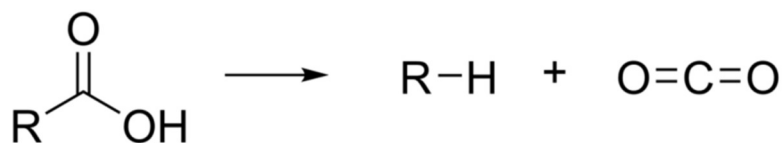


Figure 9 Decarboxylation reaction

For slow heating rates, wood goes through “torrefaction” between 250 and 280 °C.^{2, 16} The wood color becomes brown or black as shown in Figure 10.^{2, 16} To recap, only water, CO, CO₂, and char have been produced at this point. Between 220 and 270 °C, the acid hydrolyzable content of the char declines from 90 to 35%.^{2, 16} During torrefaction, the wood increases in hydrophobicity, energy density, and reduces in strength.² For example, the torrefaction of pecan shell increased the energy density of the solid product by 61.8%. It is very important to realize the significant transformation of the solid material at temperatures lower than 280 °C.



Figure 10 Torrefied wood samples. Image from Heyl & Patterson.

Tar Formation and Secondary Char Forming Reactions

Above 280 °C, thermal degradation of anhydrocellulose and lignin begins to produce tar.⁴³ Tar is a large mixture of organic compounds including sugars, anhydrosugars, oligomers, fragments of sugars, and lignin moieties that are highly unstable at elevated temperatures and are liquid or solid at room temperature.¹⁶ Tar formation is primarily an evaporation process which involves some degree of secondary reactions. Therefore, the production of tar is a strongly endothermic process but, some of the ongoing char formation reactions between the products are exothermic.⁴⁶ In 1892, Chorley and Ramsay reported that wood pyrolysis is net exothermic above 280 °C.¹⁶ In addition, it is known that the viability of commercial charcoal production relies on exothermic pyrolytic reactions.⁹ Results from DSC and Thermogravimetry-Fourier Transform Infrared Spectroscopy (TG-FTIR) analysis indicate secondary reactions between evolving tars and primary char causes strongly exothermic secondary reactions resulting in the formation of secondary char, CO₂, CH₄, H₂, CO, and water.^{16, 43, 47} Importantly, the exothermic secondary reactions had a strong correlation with char yield. Lignin decomposition, for instance, is exothermic and generates up to a 40 wt. % char.⁴⁰ Other researchers claim the contributions of

secondary tar reactions and lignin decomposition to exothermicity of pyrolysis are small and the decomposition of an intermediate solid is the primary source.⁴⁸ The overall illustration of biomass pyrolysis energetics is still debated even though it has been shown from numerous experiments that the events are dependent on the pyrolysis conditions.

Klason et al established 100 years ago that secondary vapor-phase pyrolytic reactions contribute to the formation of char, i.e., char is not solely a product of primary solid-phase pyrolysis reactions, rather it results from “primary” and “secondary” pyrolysis reactions.¹⁶ Secondary char formation reactions have been claimed to be as important as primary char formation reactions.³³ Thermodynamic calculations indicate that tar products are not stable at elevated temperature and favor solid carbon and light gas products.³³ It was shown by the TGA of various sample sizes of cellulose in open or closed pans that the char yield varied by 4 to 20%.³³ The carbonization of small particles in open crucibles gave the lowest fixed-carbon yields.³³ The use of both higher sample masses and covered pans resulted in increased char, CO₂, and CO production.^{33, 47} It was concluded that the prolonged reactions involved secondary tar cracking and char formation reactions.⁴⁷ The entrapment of volatile products increased fixed-carbon yield in addition to char yield meaning the tar graphitized along with the char product.³³ This work provides quantitative supportive data on a detailed mechanism that explains this phenomenon.

These insights explained the well-known fact that larger particles favor the formation of char.^{9, 33} Furthermore, under slow pyrolysis conditions, small particles of wood show a net endothermic behavior and large particles exhibit exothermic behaviors.⁴⁷ This difference involves an exothermic secondary reaction that leads to the formation of CO₂ and char.⁴⁷ Any condition that prolongs the contact of the vapor phase species with the solid phase carbon such as

increasing pressure, increasing particle size, and decreasing heating rate will augment the char and fixed carbon yield.³³ This phenomenon is proven experimentally in this work giving deeper insight into the reaction mechanism.

High-Temperature Biomass Pyrolysis Reactions (300-500 °C)

The tar production between 280 and 400 °C is the greatest loss of material throughout pyrolysis. In atmospheric conditions, the extent of secondary reactions with tar is relatively small. Gas production in this temperature regime is depicted in Figure 11(a-c) for cellulose, hemicellulose, and lignin. The production of permanent gas products assists in transporting the larger tar species into the gas phase. It has been shown as the temperature exceeds 300 °C, the amount of hydroxyl and aliphatic C–H groups decreases significantly due to direct cleavage or shuttling away amongst the tar.⁴⁴ Lignin undergoes chain fragmentation primarily between 300–480 °C releasing monomeric phenol units into the vapor phase and simultaneously condensing into a graphitic structure.^{45, 49} Nuclear Magnetic Resonance spectroscopy (NMR) shown in Figure 12 indicates a great reduction in O- and N-alkyl functionality with an increase in the aromaticity between 300 and 500 °C.⁴⁵ DRIFTS indicates an increase in aromaticity up to 500 °C, which will be shown in more detail in Chapter 8.⁵⁰ The increase in aromaticity indicates the simultaneous occurrence of char formation reactions with tar production. At 415 °C, ethane (C₂H₆) and ethylene (C₂H₄) evolution is shown in Figure 11 (a-c) is likely resultant from gas phase reactions.^{36, 45} However, ethane and ethylene evolution are insufficiently described in the literature for reasons divulged in Chapter 11. Hydrogen is produced at 500 °C due to carbonization of aromatic clusters in char.^{45, 51} However, intraparticle gas sampling indicates that H₂ is produced as low as 300 °C followed by a significant reduction coincident with the increase of CH₄ and other hydrocarbons.^{41, 46} This suggests that hydrocarbon production occurs after

hydrolyzable compounds are greatly diminished. Above 500 °C, methyl groups are cleaved during secondary degradation of lignin.^{44, 45, 49, 52}

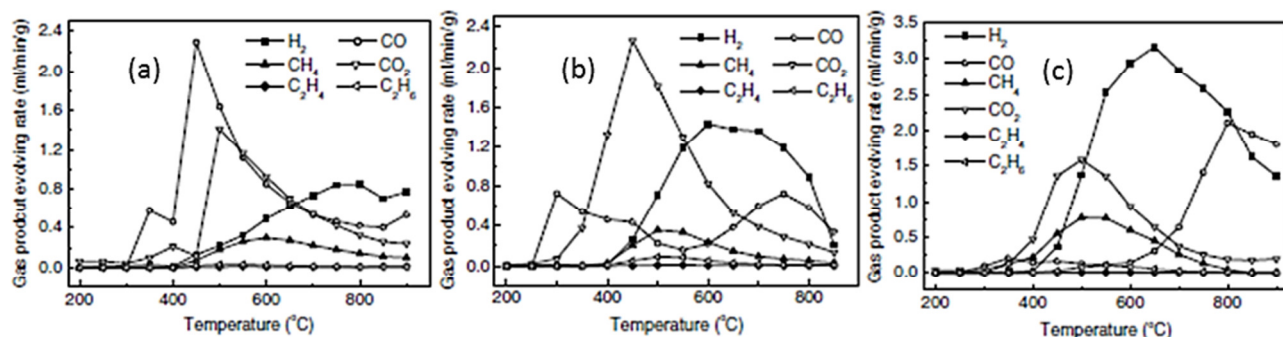


Figure 11 Gas evolution plots from (a) cellulose (b) hemicellulose and (c) lignin heated at 10 °C min⁻¹ accredited to Yang et al.

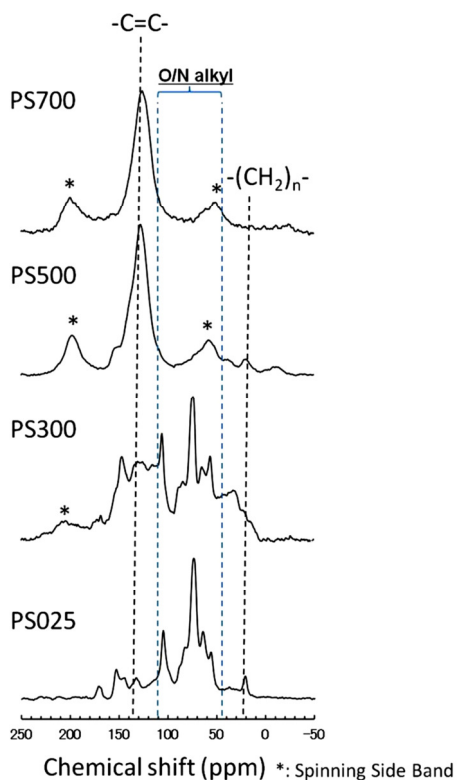


Figure 12 Solid-state ¹³C NMR spectra of pecan shells showing spectra from slow pyrolysis biochars at final temperatures of 300, 500, and 700 °C⁴⁵

Effect of Pressure

Pressure dependence has a profound effect on the yield of char. At elevated pressure, fixed carbon yields for flash carbonization are optimal.³³ There are three mechanisms by which pressure increases char yield. First, the flow of gas through the particle or particle bed is decreased at elevated pressure. This is because the pressure outside of the particle is greater than atmospheric pressure (i.e., decreasing the pressure difference across gas passageways in the particle). The decrease in flow rate increases the residence time of all volatile products inside the particle. Second, elevated pressure raises the saturation temperature and pressure of tar thereby delaying transition into the vapor phase and favoring liquid phase coking reactions. Third, elevated pressure increases the partial pressure of the tar in the pores of the reacting solid, thereby enhancing the rate of vapor-phase secondary reactions.^{16, 33}

Effect of Heating Rate

Since 2001, it has been well accepted that high temperatures, high heating rates, and small samples favor production of volatile species over char formation.⁴² This can be regarded as the main distinction between “slow” and “fast” pyrolysis. A change from “slow” to “fast” pyrolysis can decrease char yields by 2 to 10 wt % depending on the feedstock.¹⁶ Similarly to particle size and pressure effects, sufficient contact time between volatile pyrolysis products and the intermediate solid give rise to secondary reactions creating the effect of heating rate.² Ranzi et al. noted that volatile product residence time of 2 seconds or less at 425 °C limits the extent of secondary reactions.³⁶ Another effect of heating rate is that the extent of dehydration reactions increases at slow heating rates.⁴² This affects both the char and water yields. It was found that rapid pyrolysis of cellulose preconditioned at 200-250 °C has a lower char yield than for rapid pyrolysis of unconditioned cellulose.⁴² The thermal conditioning of exothermic reactions convert

cellulose into anhydrocellulose which is less reactive than cellulose. At higher heating rates, the endothermic tar formation and exothermic secondary reactions overlap, however, the two reaction sets of opposing energetics are more distinguishable at lower heating rates.⁵³ This arises directly from the heating rate dependence of dehydration reactions which form anhydrocellulose. In summary, heating rate affects (1) the transport rate of volatile products and (2) the low-temperature reaction sequence prior to tar formation.

Inorganic Mineral Reactions

Some investigations in literature focus on the role of inorganic minerals in pyrolysis. Some inorganic minerals in ash are known to increase char yield.⁴⁷ Ash affects both yields and product release rates in biomass pyrolysis.⁵⁴ When all metal ions are removed by acid-washing the rate of weight loss and yields of volatile products, like CO₂ and formic acid are reduced.⁵⁵ It is well-known that dehydration reactions are favored by the presence of acid catalyst, especially sulfate. Sulfate increases water, acid, carbonyl compounds, gas yields and char links which suppress tar production.^{42, 54} Meanwhile, depolymerization reactions are favored by alkaline catalyst present in biomass ash.⁴² It is generally accepted that catalytic effects of ash need to be considered in biomass pyrolysis.

2.2 Coal

2.2.1 Coal Constitution

Coal is a well-known fossilized plant material.³⁵ Much of the coals unearthed to today are derived from plants in the Carboniferous and Cretaceous periods. The most abundant of the plants in the swamps of the Carboniferous age were cryptogams. In the Cretaceous and Cenozoic periods, conifers and floral plants became the most popular plants.³⁵ However, no

macroscopically recognizable plant residues are found in coal.³⁵ This is due to the extreme extent and complexity of the coalification reaction mechanism. Coalification reactions are very similar to the mechanism of pyrolysis. Coalification, in fact, is the largest and slowest pyrolysis process in the history of the Earth!

Coalification is the decomposition of organic materials from swamps that were buried and exposed to the geological forces of sinking, geothermal energy, and tectonic shear.³⁵ In the “swamp-stage”, the plants were converted into peat by microbes.³⁵ Peat is a substance that is more than 90% water and strongly hydrophilic.³⁵ The Carboniferous swamps and peat deposits were buried under layers and layers of younger Carboniferous sediment to a depth of several thousand meters through phenomena called “geosynclines”.³⁵ The decomposing peat bed was covered by impervious sediment where a condition of elevated temperature and pressure emerged. The conversion of peat into lignite or brown coal and subsequent metamorphosis is outlined in Figure 13. There was a gradual elimination of polar hydroxyl and carboxylic groups³⁵ producing H₂O and CO₂, respectively. The cellulose from decayed plants underwent hydrolytic decomposition into sugars followed by condensation.³⁵ Lignin from plants were transformed into xylite.³⁵ Nitrogen in coal is the only evidence of proteins and chlorophyll from plants, which were transformed by condensation to pyridinic derivatives.³⁵ This process continued from lignite into sub-bituminous coal and into bituminous coal where the carbon content increases with every step. After bituminous coal is formed the carbon content is up to 70 wt. %, the moisture content is low, and the substance is hydrophobic.³⁵ The final form of coal is anthracite with a fixed carbon content of 87 wt. % and would require temperatures of approximately 200 °C.³⁵ At the point of extreme temperature condition, graphite may form. The extent of coalification affects the volatile material content, which in turn affects pyrolysis behavior as illustrated in Chapter 5.

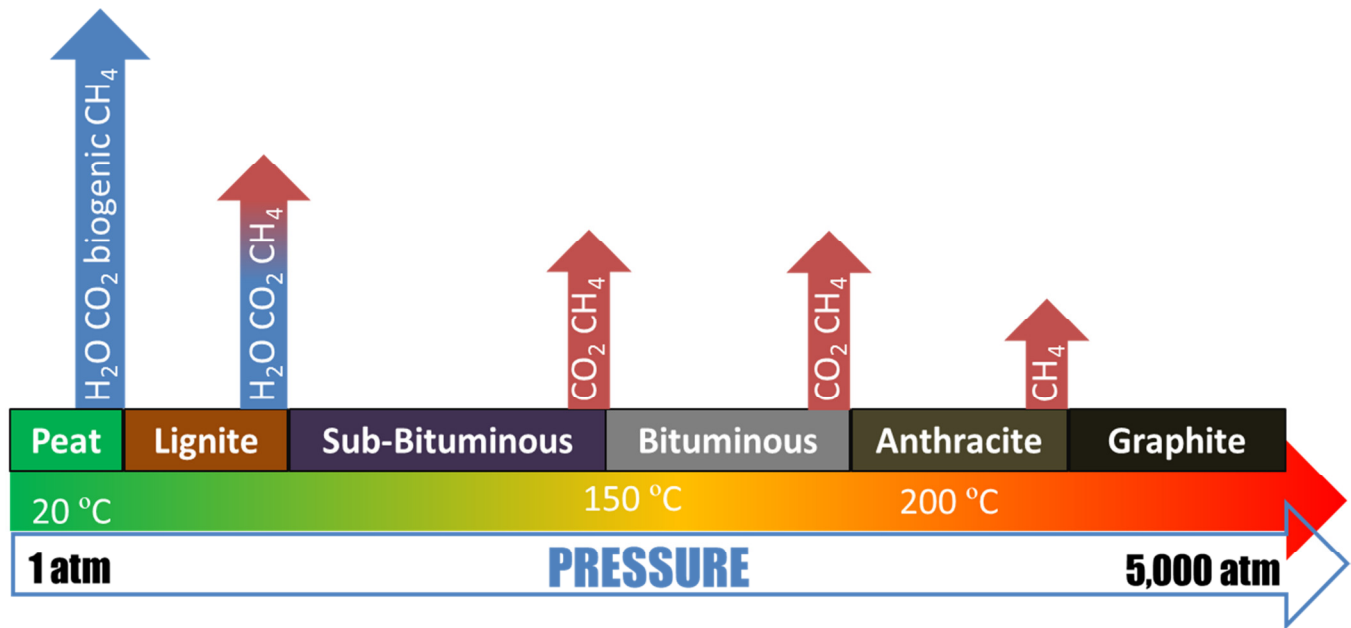


Figure 13 The coalification sequence along with geological pressure, temperature and evolution of gaseous products

The final coal product is not a homogeneous substance rather it is a solid colloid of various constituents called macerals. In coalification, all vegetable tissues have been converted into one or several macerals.³⁵ The kind of maceral formed depends primarily on the ecological conditions during coalification.³⁵ The three main maceral groups are vitrinite, liptinite, and inertinite, shown in Figure 14. Vitrinite is considered the standard coalification product of woody tissues.³⁵ Vitrinite macerals are formed from leaves, bark, branches, roots, and humic gels. Materials with much higher hydrogen content than vitrinite are called liptinite.³⁵ Liptinite macerals are derived from spores, pollen, cuticles, resins, waxes, algae, and bark tissue. A number of macerals have much lower hydrogen content than vitrinite and are grouped under the name inertinite.³⁵ Inertinite macerals are made from woody tissue, gelified plant material, and fungus.³⁵

| Lignite | Sub-Bituminous | Bituminous | Anthracite |
|--|----------------|--|------------|
| <u>Huminite</u> <ul style="list-style-type: none"> • Woody tissue • Humic debris • Humic gels • Tannins | | <u>Vitrinite</u> <ul style="list-style-type: none"> • Woody tissue • Humic gels • Aged vitrinite | |
| <u>Liptinite</u> <i>Spores, pollen, cuticles, resins, waxes, algae, bark, aged liptinite</i> <i>High hydrogen content</i> | | | |
| <u>Inertinite</u> <i>Woody tissue, oxidized gel, fungus, aged inertinite</i> <i>Low hydrogen content</i> | | | |

Figure 14 Coal macerals categorized and defined. Low-rank coals have huminite macerals and higher rank coals have vitrinite macerals. Liptinite and inertinite are present in all types of coal.

Fortunately, coals belonging to a broad range of rank and maceral content can be characterized by a common set of functional groups and mainly differ in the concentrations of these functional groups.^{56, 57} The main functional groups of coals are aromatic nuclei, hydroaromatic structures, alkyl chains, alkyl bridges, and oxygen groups.⁵⁷ Though the functional groups are known, the precise molecular representation of coals is still evasive. Modular units in the coal macromolecule consist of an aromatic nucleus, for instance, naphthalene, with hydroxyl and/or carboxylic acid substituents, which are linked by methylene, ethylene, and ether bridges.⁵⁷ For example, a representative bituminous coal molecule is shown in Figure 15, which is in the range of 1,000-4,000 g mol⁻¹ although many smaller molecules are present.^{56, 57} Matrix-assisted laser desorption/ionisation-mass spectrometry (MALDI-MS) and Size Exclusion Chromatography (SEC) suggests the pyridine extracts of coal has a bimodal molecular weight distribution (MWD) between 130 - 600 and 1300 and 3500 amu.⁵⁸ Assuming a MW of the monomer unit to be between 200-250 g mol⁻¹, the coal molecule should contain 5 to

20 monomer units (the calculation result is 10-27 modular units using the MALDI-MS data).⁵⁷ NMR spectroscopy of coals has established that 40-75% of carbon in sub-bituminous and bituminous coals are aromatic and that aromaticity increases with rank.⁵⁷ The consensus from both NMR and X-Ray diffraction is that lignite and sub-bituminous coals contain nuclei with one to three condensed rings, while bituminous coals contain nuclei of two to four condensed rings with a small but appreciable amount of single and double rings.⁵⁷ Some of the aromatic rings contain oxygen, sulfur, or nitrogen.⁵⁶ The aliphatic segments of coal include methyl and ethyl aliphatic chains, methylene bridges, ethylene bridges, and hydroaromatic clusters.⁵⁷ The largely aromatic structure of coal is important when developing a pyrolysis reaction mechanism.

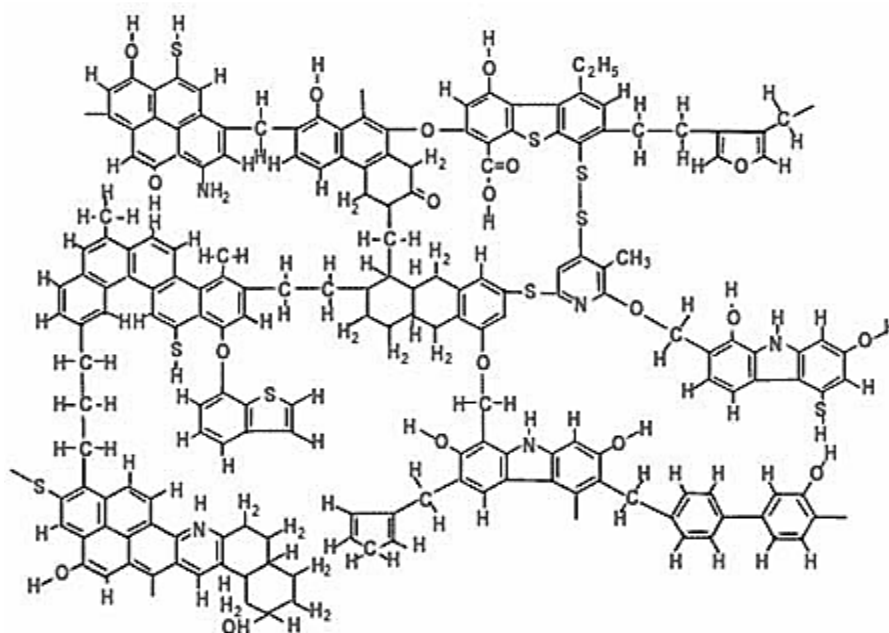


Figure 15 Representative bituminous coal molecule

The spectrum of oxygen functional groups in coal is well known, but not the quantitative distribution.⁵⁹ Oxygen is present as phenolic hydroxyl groups, carboxylic acid groups, ether bridges, and heterocyclic structures.⁵⁷ The gap in knowledge of oxygen in coal is partially due to the fact that it has become standard that oxygen content is determined by difference from the C,

H, N, and S determination. This technique, therefore, accumulates all the errors made in the determination of the other elements and of the mineral matter.³⁵ It is evident by infrared spectroscopy that phenolic hydroxyls constitute one to two-thirds of the oxygen in coal.⁵⁷ The percent of oxygenated groups, which are phenolic groups, increases with rank from 40 wt. % in lignites to 60 wt. % in high-volatile bituminous coal and higher ranks.^{59, 60} Carboxylic groups are found in considerable concentration in sub-bituminous coals and lignites^{57, 60} but decrease significantly for bituminous coals.⁵⁹ Methoxyl groups are only found in lignites and in small concentrations.^{35, 59} Detailed surveillance of gaseous products during coal pyrolysis presented in this thesis has revealed production of oxygen from coal, which has not been reported in scientific literature. Nitrogen has been better quantified and is present in fewer than a third of all aromatic nuclei and in only about 1 in 10 ring structures.⁶¹

Coal ash contains minerals derived from SiO_2 , Al_2O_3 , Fe_2O_3 , Na_2O , CaO , MgO , K_2O and TiO_2 . The minerals in coal form clays. Hydroxyl groups exist in clays such as kaolinite and montmorillonite,⁵⁹ which could have reactive significance. Metallurgical coal contains 8-12 wt. % ash.¹⁴ It is generally accepted that the effect of ash in the coal pyrolysis mechanism is small. However, Chapter 4 presents new roles of metal oxides in the coal pyrolysis reaction mechanism.

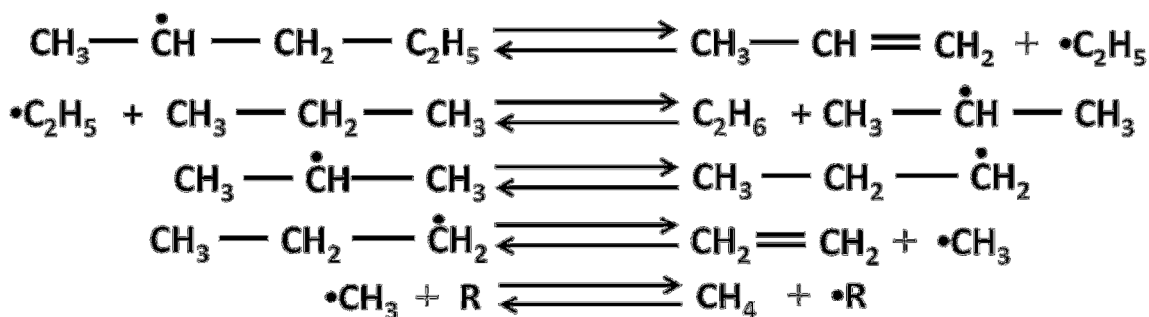
2.2.2 Coal Pyrolysis Mechanism

In many regards, coal pyrolysis is similar to biomass pyrolysis. The process involves a mix of bond breakage and bond formations with complex internal hydrogen transfer and mass transport mechanisms.^{57, 62} Below 300 °C, there is less activity in coal pyrolysis than in biomass due to a lower concentration of oxygenated functional groups. At 350-400 °C, depolymerization of weaker C-C bridges will produce smaller organic fragments.^{63, 64} The fragments will form a “metaplast”, which is a key difference from biomass pyrolysis.⁶³ The fragments produced will

either (1) transport through the metaplast and vaporize or (2) cross-link with other metaplast fragments to form a solid.^{63, 64} The cross-linked fragments of the metaplast eventually graphitize into coke by 1000 °C.^{63, 64} In this section, each step of this mechanism will be described in detail beginning with the breakage of bonds and ending with secondary reactions of released volatile species. The effects of pressure and heating rate as they pertain to secondary reactions will also be discussed.

Bond Cleavage

Coal has a variety of bond types therefore bond cleavage is complex. Bond cleavage involves homolytic cleavage, ipso substitution, or hydrogen-transfer-induced bond-scission; all of which generate radicals.⁶³ Each dissociated bond is accompanied by the consumption of donatable hydrogen and a formation of carbon-carbon double bond to stabilize a radical, as shown as in Figure 16. Hydrogen is abstracted from ethylene bridges, hydroaromatic, or aliphatics throughout pyrolysis until donatable hydrogen is depleted and the coal becomes increasingly aromatic.^{63, 64} Generation of transferable hydrogen begins at 350 °C and increases with increasing temperature up to 425 °C.⁶⁵ The coincidental decrease of hydrogen content and increase of double bonds in coal is a critical realization for the pyrolysis mechanism. Table 2 lists bond dissociation energy from which the sequence of bond rupture in pyrolysis may be inferred.



*Then the $\cdot\text{R}$ goes on to abstract another $\cdot\text{H}$ from a saturated compound which then goes through isomerization (if necessary) and β -scission forming another **double bond** and **free radical** and this repeats*

Figure 16 Representative bond breaking and formation sequences illustrating the free radical mechanism where double bonds and free radicals are formed while aliphatic hydrogen is consumed.

Table 2 Bond dissociation energies (BDE) for several bonds relevant to coal pyrolysis

| Bond | Average BDE (kJ) | Bond (-) | Specific BDE (kJ) |
|------|------------------|--|-------------------|
| N-O | 200 | H ₅ C ₂ -C ₂ H ₅ | 365 ± 4* |
| C-S | 260 | H ₅ C ₂ -CH(CH ₃) ₂ | 363 ± 4* |
| C-N | 300 | H ₅ C ₂ -C(CH ₃) ₃ | 353 ± 4* |
| C-Cl | 330 | CH ₃ - | 301 ± 3* |
| H-S | 340 | CH ₃ -CH ₂ CH=CHCH ₃ | 305 ± 3* |
| C-O | 350 | CH ₃ - | 285 ± 6* |
| C-C | 350 | H-CH ₂ C ₂ H ₅ | 420 ± 2* |
| C-H | 410 | H-CH(CH ₃) ₂ | 413 ± 2* |
| C=C | 611 | H-C(CH ₃) ₂ CH ₂ CH ₃ | 404 ± 6* |
| C=O | 732 | H-CH ₂ CH=CH ₂ | 361 ± 6* |

*Values are taken from Savage [66]

Low-Temperature Crosslinking Reactions

During hydrogen redistribution, functional groups are homolytically cleaved releasing CO₂, CH₄ and H₂O.⁶³ The evolution of H₂O, CO₂ and CH₄ correlate with cross-linking within the coal molecule.^{59, 62, 63} For instance, condensation of two phenolic hydroxyl groups form water and an ether linkage as shown in Figure 17.^{59, 63} At slightly higher temperature, substitution

reactions between larger aromatic molecules and methyl groups releases methane while increasing the aromatic cluster size.⁶³ These reactions produce gas products and a more conjugated char structure. The cross-linking reactions exemplify the importance of oxygen reactivity in pyrolysis because these groups are the active sites. Some oxygen in coal is released as an element in tar molecules but, it was calculated that 80% of oxygen in coal is released as CO₂, H₂O, and CO mostly as a result of cross-linking reactions.⁵⁹ The low temperature cross-linking from carboxyl groups has been correlated with FTIR measurements to the formation of carbonyl groups or ether linkages in char which are released as CO at higher temperatures.^{59, 62, 63}

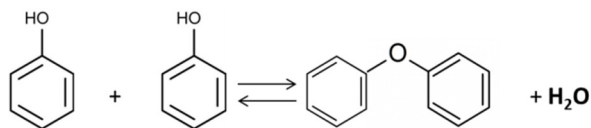


Figure 17 Phenol cross-linking reaction producing water and a diphenyl ether suggested by Niksa [59] and Solomon [63]

Metaplastic State

Following the low-temperature cross-linking reactions, a portion of the metallurgical coal decomposes into a fluid-like viscous matter at ~400 °C referred to as the metaplast.⁶⁸ The metaplastic regime is most critical in the mechanistic understanding of coking coal pyrolysis. Gas products and metaplast fragments are transported through the melt in bubbles.^{63, 68} Bubbles originate from macropores in solid coal or are nucleated within the molten coal, as shown in Figure 18.⁶⁸ The bubbles are stationary due to the high viscosity of the melt.⁶⁸ Heavy hydrocarbons which diffuse into the bubbles undergo secondary reactions to form both lighter and heavier products causing the bubble to grow.⁶⁸ The increase in total bubble volume inside the metalplast causes the entire coal particle to grow. The bubbles eventually expand to the particle surface and rupture to release the volatiles from the coal into the vapor phase, as shown

in Figure 18.⁶⁸ However production of volatile species is not the only reaction set occurring in the metaplast regime. Crosslinking reactions between larger non-volatile metaplast fragments occur in the metaplast forming more char product. It should be noted that the mechanism of tar formation is different for woods and other coals where an appreciable metaplast does not form.

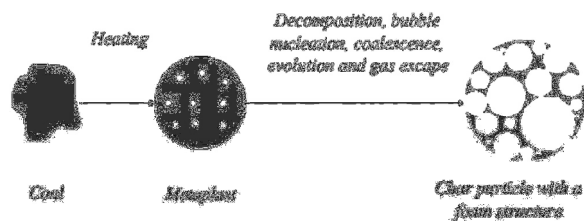


Figure 18 Bubble model schematic taken from Yu et al to show how the bubbles form and escape through bubble growth

Resolidification and Char Structure

Metaplast eventually resolidifies forming gas products and a solid char.⁶⁸ Resolidification occurs when the donatable hydrogen from a hydroaromatic or aliphatic portion of the coal is depleted.⁶³ Resolidification marks the end of tar production through the bubble mechanism. Figure 19 illustrates the radical physical changes in coal structure during the metaplast regime.⁶⁸ The resultant char structure obtains a structure of a hollow inverse mold of a sphere from the bubbles which existed in the metaplast.⁶⁹ This was the primary evidence that bubble mechanism existed.

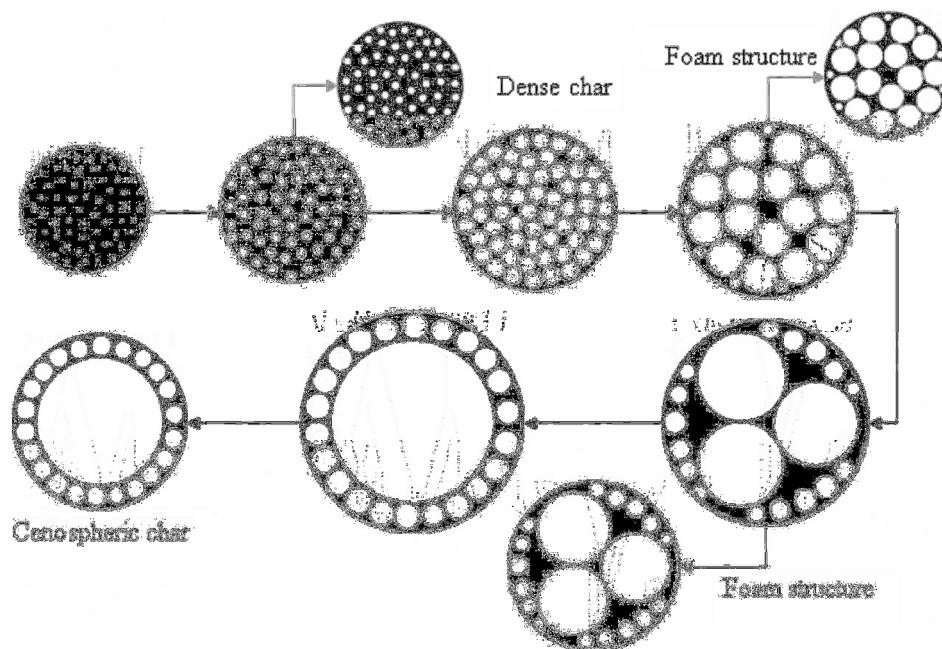


Figure 19 Formation of cenospheric char structure taken from Yu et al shows how the structure differs at various extents of pyrolysis

Tar Shuttling

The metaplastic regime is the period in which a great amount of material is lost from the reacting media. Tar shuttling and gas production are the two competing mechanisms for removal of functional groups.^{59, 63} This competition partitions the elements among gas, tar, and char products. Crosslinking is the primary route for char and gas production. Tar shuttling from the metaplast has been shown to obey Raoult's law in a flash distillation analogy where tar production rates and tar MWD are related to metaplast concentrations.^{59, 70} However, prediction and quantification of tar species is a hard problem in coal pyrolysis which is discussed in more detail in Chapter 4. For simplicity, coal tar can be lumped into three categories of reactivity. The reactivity goes from decomposition at low severities to being totally unreactive.⁷¹ Tar reactivity can be inferred from ^1H NMR measurements and is directly proportional to the fraction of aromatic hydrogen or aromatic carbon in the tar.⁷¹ Chen and Niksa claim that tar aromaticity

increases throughout pyrolysis.⁷² The basis is that aliphatic peripheral groups and bridge remnants are progressively eliminated from aromatic nuclei before being released from the coal as a tar species.

Evolution of Heteroatomic Species

It is found that coal tars contain substantially less oxygen than the parent coal due to oxygen's participation in low-temperature cross-linking reactions which evolve oxygen as CO₂ or H₂O.⁵⁹ Nitrogen release during pyrolysis involves the shuttling of nitrogen in tar molecules and the conversion of nitrogen from char into HCN.^{61, 63} Under conditions of rapid heating, tar shuttling is the only mechanism for nitrogen release.⁶¹ Nitrogen in coal tar exists as pyridines, quinolines, carbazoles, and indoles.⁷³ Volatiles in hot gas have been shown to undergo secondary reactions that convert the nitrogen in tar into hydrogen cyanide (HCN).⁶¹ Nitrogen decomposition chemistry does not play any discernible role in the coal pyrolysis mechanism.⁶¹ High sulfur content (~5 wt. %) increases the propensity for cross-linking and has a positive correlation with coal fluidity.^{74, 75} This is attributed to the property of elemental sulfur to act as a hydrogen acceptor.⁷⁵ Organic sulfur produces H₂S or is shuttled by tar between 200 and 350 °C as thiophene species.⁷⁵ FeS₂ in coal also decomposes to H₂S and FeS above 350 °C.⁷⁵

Cracking Reaction: Free Radical Mechanisms

After tar production ends at nominally 500 °C, cracking reactions occur producing small permanent gas hydrocarbons and large aromatic clusters. These reactions are properly described in the context of free radical mechanisms. To date, free radical mechanisms are not mechanistically or empirically grounded for predicting product yields or distributions from pyrolysis.⁷⁶ Meanwhile, the considerations of cross-linking, depolymerization and flash distillation have been sufficient for modeling purposes. In general, the thermal cracking of all

hydrocarbons proceeds through free radical mechanisms.^{77, 78} As shown in Figure 20, free radical thermal cracking mechanisms involve a small set of reversible reactions.^{66, 77} This type of mechanism for the thermal cracking of light hydrocarbons (such as CH₄) results in 500 reactions.⁷⁷

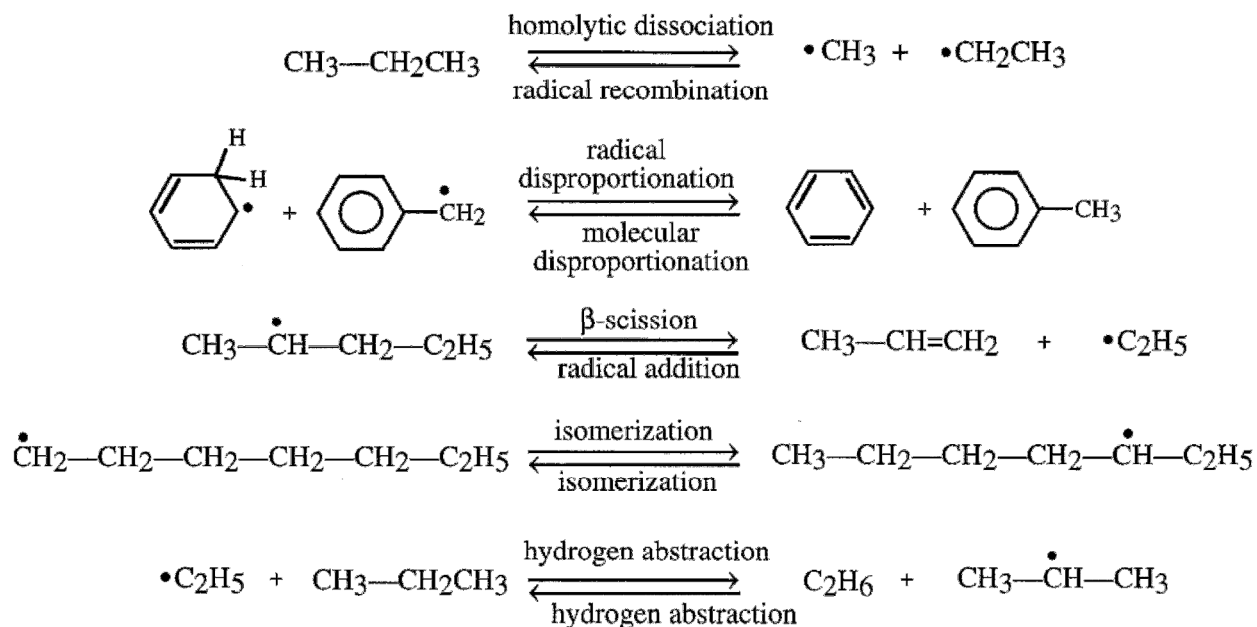


Figure 20 List of the relevant free radical mechanisms for the thermal treatment of hydrocarbons credited to Savage [66]

In this sequence, the initiation step is mainly the rupture of a C-C bond (most probable for coal pyrolysis) or a C-H bond.⁷⁷ The relative strength of C-H and C-C bonds depend on bond order (primary, secondary, or tertiary) and the presence of a double bond or an aromatic ring.⁶⁶ Bond breakage may occur in one of two ways; (1) by homolysis of a covalent bond to produce two radicals or (2) by β -scission of a radical to produce an unsaturated molecule and one radical.⁶⁴ As bond breaking continues, a pool of H \bullet , CH₃ \bullet , and C₂H₅ \bullet radicals develop and most commonly react by addition or hydrogen abstraction^{56, 64, 70, 79} but may also experience radical decomposition or isomerization.⁷⁷ Most radicals will form small permanent gas molecules

such as H₂, CH₄, CO, and H₂O by abstracting hydrogen from an available donor molecule.^{56, 64} Therefore globally in coal pyrolysis, the formation of small permanent gas molecules is accompanied by the formation of two other free radicals or a double bond within the condensed phase.^{57, 78} Recombination occurs if a hydrogen donor molecule is not immediately available and in such case two large aromatic radicals form stable char-like molecules and H₂.⁶⁴ When a pair of free radicals is produced from the dissociation of bridges, a large probability exists that they will recombine before diffusing apart.⁵⁷ It is generally accepted that the activation energy for radical recombination reactions is equal to zero.⁷⁷

The free radical mechanisms described in the metaplastic regime of coal pyrolysis can be categorized into two regimes. At moderate temperatures, high pressure and high substrate concentrations (e.g., liquid/metaplast phase), the radical formed by β -scission of a substrate radical will undergo hydrogen abstraction by the Fabuss–Smith–Satterfield mechanism.^{64, 66} The substrate, in this case, are hydrogen-donor species. Each molecule, through this mechanism, produces one alkene and one alkane shown in Figure 21.⁶⁴ The characteristic alkane cracking reaction at ~400 °C produces mixtures of smaller alkenes and alkanes.⁶⁴ Direct homolytic cleavage of methylene cross-links in coal are not expected in this regime.⁶⁴ At high temperature, low pressure, and low substrate concentration (e.g., gas phase), radicals tend to break down all the way to CH₃• or H• by the Rice–Kossiakoff mechanism.^{64, 66} For example, a larger linear alkane will decompose to a smaller alkene, several molecules of C₂H₄, and one molecule of CH₄ or H₂⁶⁶ as shown in Figure 21. These free radical mechanisms are considered in the evaluation of the experimental work presented in this thesis.

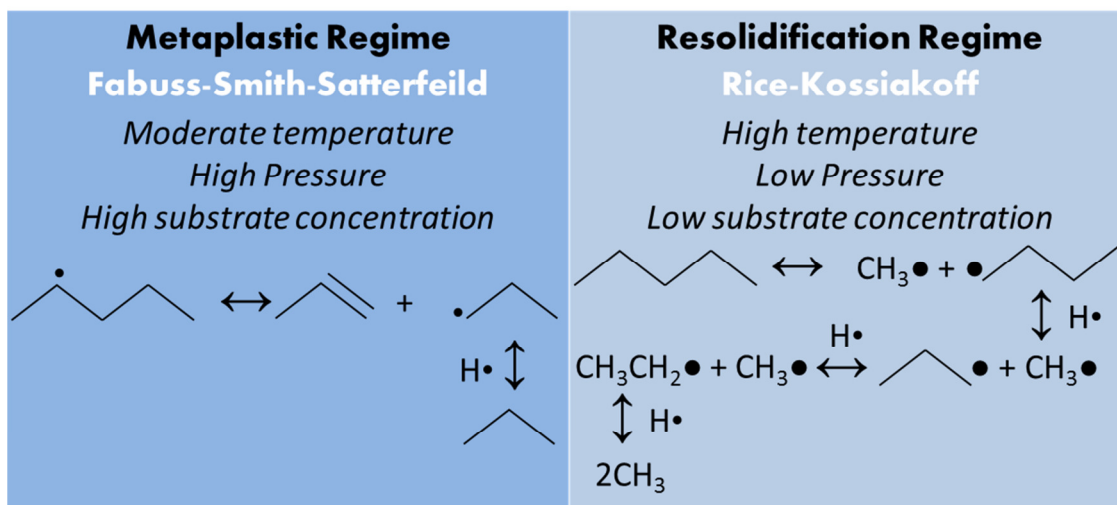


Figure 21 The Fabuss-Smith-Satterfeild and Rice-Kossiakoff mechanisms as they apply to coal pyrolysis

Metaplast Resolidification

The resolidification, or graphitization, mechanisms at high temperature is a separate regime to consider. In this regime, large species are recombined and rearranged, preserving a macroradical state of solid species. At the gas-coke interface, the polyaromatic layer is not yet completely dehydrogenated, therefore hydrogen abstraction reactions by free radicals in the gas phase can occur at this interface.⁷⁹ This contributes to coke product. Every molecule from the gas phase, especially unsaturated molecules, is a potential coke precursor by the mechanism shown in Figure 22.⁷⁹ Methane and ethane have relatively low coking rates⁸⁰ however ethane is much more reactive than CH₄.⁸¹ Methane can form coke which is later shown by experiment in Chapter 10. Paraffin species beyond pentane do not increase coking propensity.⁸¹ The benzene coke rate is about 50% higher than that of paraffin species.⁸¹ The coking potential of aromatic molecules strongly increases with increasing number of aromatic rings.^{79, 81} As coke precursors are added, a sequence of dehydrogenation and cyclization reactions incorporate carbon atoms of the once gas-phase coke precursor into the coke layer.⁷⁹ The addition of coke precursors regenerates free

radical sites by further hydrogen abstraction so that the total number of active sites on the coke macroradical is constant.⁷⁹

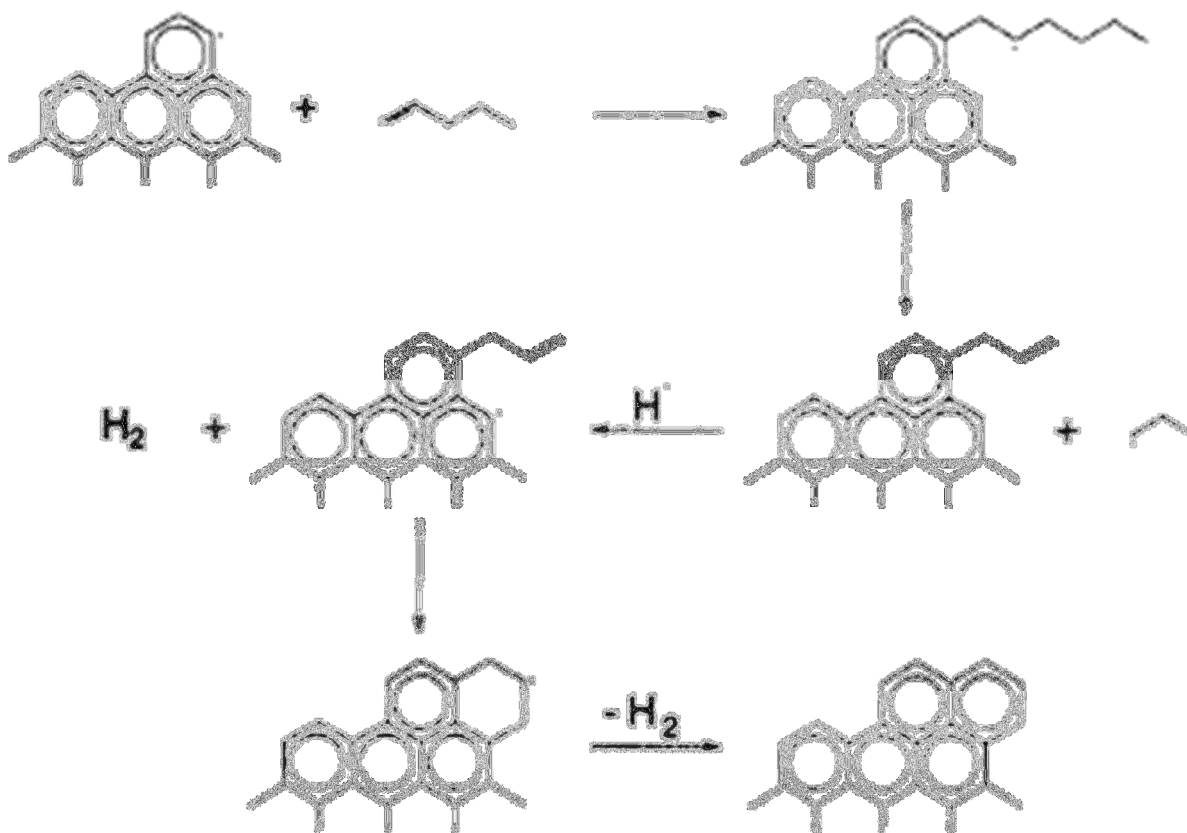


Figure 22 Mechanism for representative coke growth reaction from Reyniers et al.

The last free radical mechanism to be discussed in coal pyrolysis is PAH growth in the gas phase. These large volatile molecules grow into tar droplets or even solids (soot) by a mechanism similar to those shown in Figure 23.⁷⁹ Tars in hot gas have a propensity for soot formation.⁸² During the later stages of primary devolatilization, additional C₁-C₂ compounds and substantial amounts of the CO come from PAH growth.^{72, 82} Light hydrocarbons from CH₄ to propane participate in soot formation as well.⁸² The characteristic reaction of unsubstituted arenes at ~1000 °C is condensation that produces biaryls plus H₂ or a partially hydrogenated

arene.⁶⁴ Characterization of coal pyrolysis tar in the experimental portion of this work suggests PAH growth occurs in the gas phase and at solid-gas interphases above 550 °C in this manner.

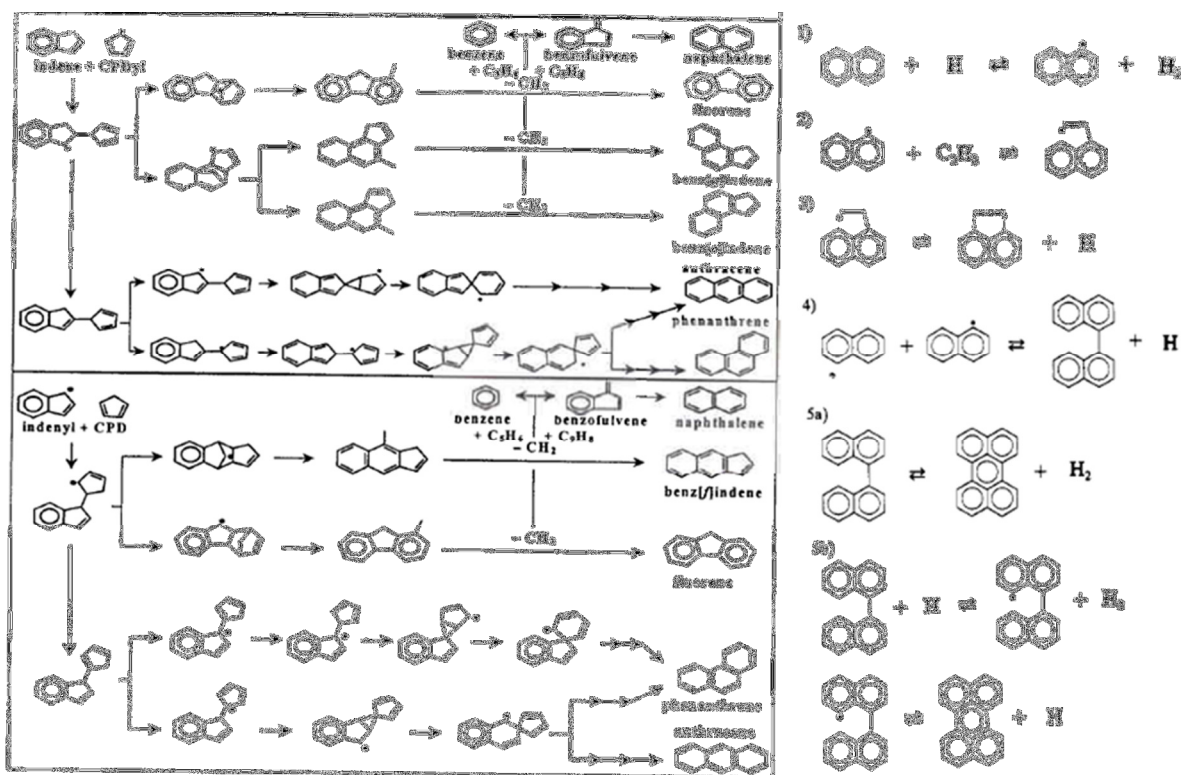


Figure 23 Examples of pyrolytic PAH growth mechanism (a) is taken from Mulholland et al showing indene and cyclopentadiene forming larger PAH species and (b) is taken from Pope et al showing naphthalene forming perylene

Secondary Reactions

Secondary reactions of volatiles in the gas phase and solid-gas interfaces can significantly influence the distribution and yield of pyrolysis products.⁶⁸ In any macroscale application, the primary products of coal are radically transformed by secondary reactions when transferred into the gas phase.⁸² Similar to the point made in biomass pyrolysis, extended residence times of volatile product in the reacting media will increase the degree of secondary reactions thus changing the product distribution. Experiments on the effect of bed depths between 25-250 mm

in isothermal coal pyrolysis show the influence of secondary reaction on volatile yields and speciation.⁸³ Methane and hydrogen production increases as a result of tar cracking or repolymerization reactions with bed depth up to 1000 °C.⁸³ The kinetics of gas phase secondary reactions of prompt coal tars were studied at temperatures and residence times of 500-900 °C and 0.03-3.9 seconds, respectively.⁷¹ Gas phase tar cracking is unfavorable at residence times between 0.03-0.14 seconds at temperatures above 550 °C.⁷¹ Between 0.6 and 1.1 seconds, tar conversion was insignificant below 600 °C but, extensive (30-50%) at 700-800 °C, with light gas species as the major products. For residence time of 0.6 seconds, conversion modestly increased between 750 and 800 °C. For residence time of 1.1 seconds, conversion increased with increasing temperature up to 60% at 900 °C.⁷¹ In summary, extending the residence of volatile species at temperatures over 750 °C has been previously shown to cause significant cracking. Experimental evidence presented in Chapter 6 will modify this finding on secondary reactions.

Effect of Pressure

The effect of pressure is analogous to that for biomass pyrolysis. At elevated pressures, an improvement in solid yield, reduction of tar and increase of gas has been observed using various types of reactors.⁶⁹ It has been clear that high pressure suppresses the formation and release of tar and promotes secondary reactions, hence increases the total yield of light gas products.⁶⁹ Tars prepared at higher pressure have lower average MW due to reduced or seized transport of heavier molecules.^{63, 84}

Effect of Heating Rate

As observed for biomass pyrolysis, heating rate effects the transport rate of volatile products and reaction sequence prior to formation. Peters and Bertling in 1964 were first to report on the effect of heating rate on coal pyrolysis. It is now well-known that rapid heating will

increase the amount of volatiles produced, independent of the reactor type.^{63, 85, 86} The rate of devolatilization increases in almost direct proportion to increases in heating rate.⁷⁴ For increases in heating rate from 1 to 10^3 °C s⁻¹, the volatile yield increases by 11-12 wt. %.^{69, 84} This effect is attributed to depolymerization reactions prevailing over cross-linking reactions.^{63, 84} Rapid heating rates substantially reduces pre-metaplast and metaplast cross-linking leading to a tar product with higher oxygen content.^{62, 63} Due to the effects on low temperature cross-linking, CO yields are also affected by heating rate.⁵⁹ However, the rapid volatile transport rates serve to increase the average MW of the tar as the heating rate increases due to fewer secondary cracking reactions.^{63, 84, 85} For example, average MW increases by 40% as the heating rate was increased from 1 to 10^3 °C s⁻¹.⁸⁵ Rapidly heating coal reduced secondary cracking which produced a tar with a higher fraction of light oils.⁸⁵ This work is focused on slow pyrolysis, therefore the effects of heating rates across a narrow range of slow heating rates are assessed, including analysis of the tar product. The work provides a more detailed perspective on changes in the pyrolysis reaction mechanism with respect to heating rate.

Inorganic Mineral Reactions

The ash in coal is largely inert when compared to biomass pyrolysis. By petrography, most common mineral inclusions are calcite, kaolinite, pyrite, illite, and montmorillonite.³⁵ The phenolic hydroxyl groups in clays such as kaolin, montmorillonite, and illite decompose and form H₂O. Carbonates, siderite, and calcite decompose to form CO₂ and minor amounts of CO.⁵⁹ Similarly to biomass, cations lead to a suppression of tar production however, they do not to affect the overall weight loss.⁵⁷ Calcium is capable of absorbing HCl produced during pyrolysis. Specific studies of iron oxide reduction, reduced iron can by 447 °C in 5% H₂ which also

generates H₂O.⁸⁷ In Chapter 10, the role of iron in coal pyrolysis is explored in more detail and it appears to reactive component in large-scale systems.

2.3 Pyrolysis Models

Models found in the literature have been constructive towards the current understanding of the pyrolysis mechanism. Existing pyrolysis models can be divided into four categories. The first and simplest model type is “weight loss models” employing a single rate, multiple parallel rates, or distributed rate to predict the mass loss profile of a sample. These models do not account for the variations in tar yield with reaction conditions. Second, “Tar formation models” incorporate char-forming reactions (i.e., cross-linking) and mass transport and are able to account for variation of tar with reaction conditions. These models have been largely sufficient in modeling combustion and gasification systems. The third type of models is “species evolution/functional group models” that employ parallel first-order reactions to predict the evolution of gas species. In these models, decomposition and repolymerization of the macromolecular network may be modeled by using statistical methods but require knowledge of functional groups present. The fourth type and most sophisticated models are the “mechanistic models”, which describe the composition of the tar and char as a function of pyrolysis. The “species evolution/functional group models” or “mechanistic models” may be required in predicting the energy released from combustion of the volatiles or the physical structure and composition of char. “Mechanistic models” are needed in order to predict product composition from solvolysis or liquefaction processes for alternative fuel production.⁶³ For a pyrolysis model to be useful in practical application, it should be based only on the proximate and ultimate analysis of the feed and the pertinent conditions of pyrolysis. The functional group and mechanistic models require functional group concentrations or NMR data inputs, which are

impractical input parameters.^{57, 63, 88} Existing coal pyrolysis models consider heating rate ranges between 0.05 - 20,000 °C s⁻¹.

The work in this thesis considers pyrolysis between heating rates of 0.01 – 0.1 °C s⁻¹. The experimental data offer the enormous modeling simplification of having the mass balance closed at each temperature during pyrolysis by measurement. Therefore, the observed rates of production of each component are the kinetic rates of reaction. In addition, the prediction accuracy of each species can be properly assessed on account of the high degree of mass closure and known statistical error. The models developed can predict the evolution profiles of each volatile product, an estimated number of reactions per species, mass loss profile, the rate of mass loss profile, O/C and H/C ratio of the char product. Thermodynamic equilibrium models were used to confirm the observed trends for secondary reactions.

Chapter 3: Experimental Procedure and Methods

This chapter introduces the samples analyzed, techniques used, and calculations performed in this work.

3.1 Samples and Sample Preparation

Table 3 Proximate and ultimate analysis of the pecan shell and coal samples used in this work

| | C | H | N | S | O | Ash | Fixed C | Moisture | VM |
|----------------------|-----|-----|-----|-----|-----|-----|---------|----------|-----|
| | wt% | wt% | wt% |
| Pecan Shells | 52 | 6.0 | 0.4 | 0.6 | 42 | 1.8 | 29 | 8.6 | 56 |
| Jewell | 82 | 4.7 | 1.5 | - | 3.9 | 6.8 | 59 | 8.0 | 26 |
| ICG East Gulf | 84 | 4.4 | 1.5 | 0.6 | 2.4 | 6.6 | 66 | 10 | 17 |
| Glamorgan | 80 | 5.3 | 1.9 | - | 5.5 | 6.6 | 50 | 6.9 | 36 |

The coking coals in this study were obtained by Suncoke Energy and are used in the commercial production of coke in the United States. The proximate and ultimate analyses of three coals are shown in Table 3. The coals vary between 17 and 36 wt. % volatile material (VM)

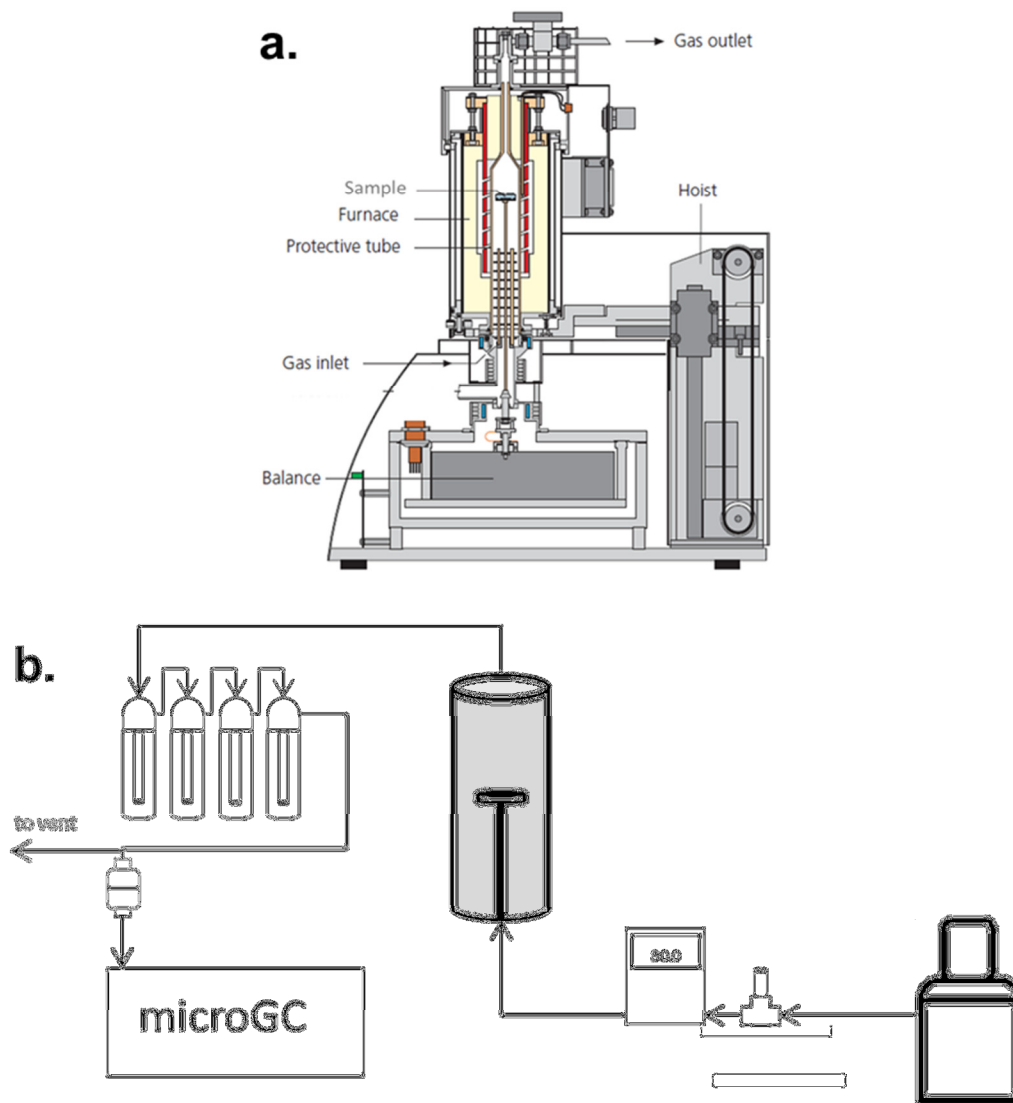
composition and between 80 and 84 % carbon. This is a wide variation in VM over a narrow range of coal rank. For thermal analysis, the samples were crushed via a mortar and pestle and sieved to a uniform particle size of $48 \pm 5 \mu\text{m}$ (mesh 270/325).

Pecan shells obtained from sheller, were ground (SM 2000 cutting mill, Retsch GmbH, Haan, Germany), and sieved to $<2 \text{ mm}$. Moisture, ash, VM, and fixed carbon contents of the pecan shell were determined by following American Society for Testing and Materials (ASTM, method D7582) using a LECO thermogravimetric analyzer. The proximate and ultimate analysis results for pecan shells are reported in Table 3.

3.2 Experiments

3.2.1 Thermogravimetric-Gas Chromatography (TG-GC)

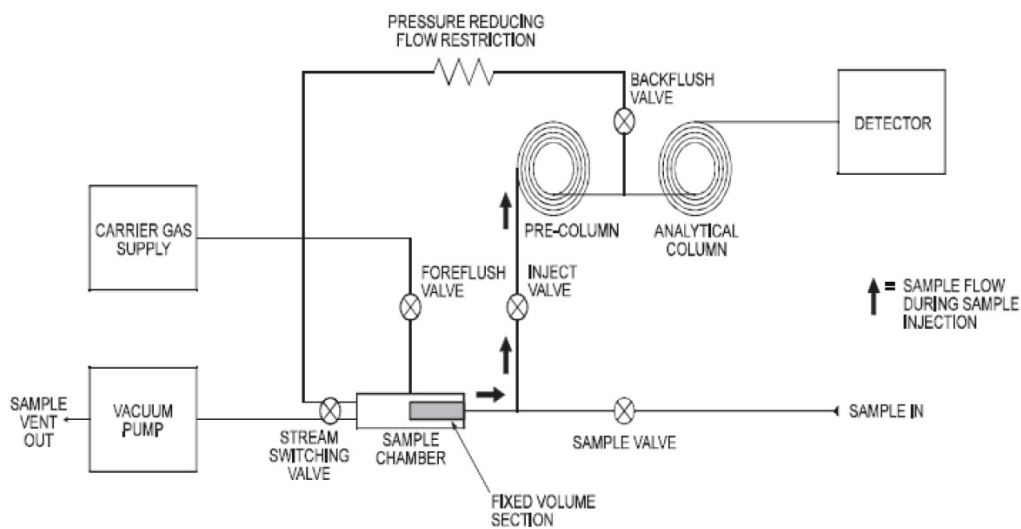
The experimental set-up used for investigation was a Netzsch Luxx simultaneous thermal analyzer 409PC close coupled to an Inficon 3000 μGC , equipped with a thermal conductivity detector (TCD). This system is shown in Schematic 1. Schematic 1a shows the internal configuration of the TGA alone. The coal sample size was 40 mg and analyzed as a 6.5 mm x 1 mm pellet. A vertically oriented sweep gas of research grade argon (Airgas AR R300) was maintained constant at 30 mL min^{-1} . Pecan shell pyrolysis tests were performed using a 100 mg sample and ultra-high purity nitrogen (Praxair 5.0) sweep gas maintain at 40 mL min^{-1} .



Schematic 1 (a) the vertical oriented configuration of the TGA (b) schematic of the TG-GC system used for pyrolysis studies

The effluent of the TGA was connected to a quarter-inch passivated (Silcotek SilcoNert2000) stainless steel tube constituting an inert transfer line in order to have no impact on the sample. The transfer line was heated and routed the TGA gaseous effluents to a series of four impingers (SKC Midget Impinger, 225-35-1). For the coking coal experiments, the transfer line was heated to 275 °C and the series of impingers were kept in an ice bath at 0 °C and 1.0

bar. For the pecan shell experiments, the transfer line was maintained at 315 °C and routed to a series of impingers in a methanol-dry ice slurry providing a temperature of at -80 °C. The transfer line has been operated at 270 °C which is proved by vapor-equilibrium calculations to be sufficient for retaining species up to two-ring membered PAHs in a saturated vapor stream. The tar capture system is discussed in greater detail in Section 3.2.1.1. Any uncondensed gaseous effluent that exited the train was analyzed by the μ GC-TCD. The flow diagram of the μ GC-TCD is shown in Schematic 2. Gas sampling from the TGA effluent stream was performed at a frequency of 3 minutes providing very good temperature resolution of the evolved chemical species. The gaseous species that were identified and quantified were H₂, O₂, CH₄, CO, CO₂, C₂H₄, and C₂H₆. The 14 m OV-1 column of the Inficon 3000 micro-GC is capable of measuring C₃ and C₄ order hydrocarbons but, these species either are not present in the gas product or below detection limits of 100 ppm.

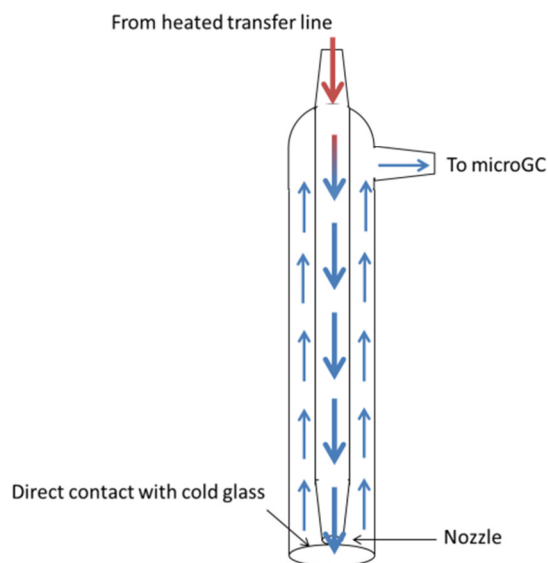


Schematic 2 MicroGC schematic from Inficon

The coal samples were subjected to a constant heat rate of 1, 3, and 10 °C min⁻¹ up to 1100 °C in the TGA. The commercial coke making operating temperature is 1100-1200 °C. For

each test, the temperature was held isothermally at 1100 °C until the differential thermogravimetry (DTG) reached and remained at zero. The pecan shells were treated to a constant heat rate of 10 °C min⁻¹ up to 500 °C. For the pecan shells, the temperature was held isothermally at 500 °C for 4 hours.

3.2.1.1 Tar Capture

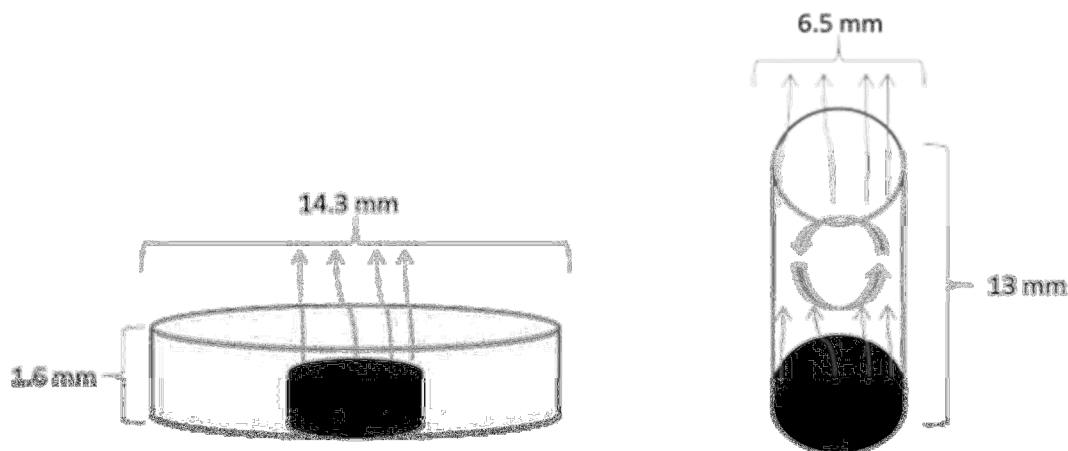


Schematic 3 Glass impinger design and gas flow path

Tar and water produced from pyrolysis were collected in the condensation unit and measured gravimetrically. Reviews of efficient on-stream tar capture demonstrated the use of a condenser train system.^{17, 89, 90} The cooling rate immediately downstream of the heated and insulated transfer line was 150 and 287 °C s⁻¹ for the coal and pecan shell tests, respectively. It was determined by iterations that these cooling rates were sufficient for condensation of all tar products. Other studies have employed extreme quench rates of 3,000-9,000 °C s⁻¹ under vacuum.⁷² The impinger design in this work was such that the internal tube ended in a nozzle so that the tar products impact the chilled inner wall of the glass tube container, as shown in

Schematic 3. A solvent was not used for tar capture in this work. The use of solvents to capture tar is recommended to suppress polymerization and oxidation reactions amongst captured tar species⁸⁹ yet this was determined to be unnecessary in our system due to negligible reaction extent at 0 °C. The main disadvantage of using a solvent in this work is the step of solvent removal which adds uncertainty to the measured yields and composition.

3.2.1.2 Confinement



Schematic 4 On the left, the short (pan) confinement used in TGA pyrolysis experiments is shown, and on the right, the tall (cup) confinement used in TGA pyrolysis experiments is shown

Two different confinements, shown in Schematic 4, were utilized to observe how volatile species interact as a function of increased residence time above the reacting solid residual. Experiments with these configurations provide insight into the secondary pyrolysis reactions during devolatilization. The impact of the bed geometry (i.e., confinement) on tar yield has been speculated yet never quantified or linked to a commensurate difference in solid and/or gas product.⁶³ The confinement with a smaller aspect ratio of 0.11:1.0 (14.3 mm in diameter and 1.6 mm in height), designated as the “pan,” was designed to favor rapid removal of devolatilization products leading to minimal secondary reactions. The confinement with a larger

aspect ratio of 2.0:1.0 (6.5 mm in diameter and 13 mm in height), designated as the “cup,” creates a zone above the sample where the volatile species evolving are not immediately swept away by the inert gas. The region above the sample therefore provides the opportunity for secondary reactions to affect the product distribution. The use of a pellet ensures that interparticle and intraparticle pyrolysis reaction extents are uniform between the two confinements. The Biot numbers (the ratio of the conductive heat resistance and convective heat transfer at the surface of an object) of each confinement are between 0.04 and 0.11 indicating a uniform temperature distribution. This means the solid-gas interface reaction monitored are occurring at the sample temperature. Therefore, the variable between the two confinements is the extended volatile residence time in the cup confinement. The residence time of volatile products is estimated using the ratio of the height of the confinement divided by the rate of mass loss in the confinement. The space above the sample in the cup confinement was 10 mm and the approximated residence time is 0.35 seconds. The tests were repeated in triplicate for each coal, heating rate, and confinement to obtain representative statistical values. The averages and p-values for gaseous products reported are based on nine repetitions. The p-value is the resultant value from a statistical t-test between the pan and cup confinement in order to determine if the effects of confinement are statistically significant.

3.2.2 Carbon, Hydrogen, Nitrogen, Sulfur, Oxygen (CHNSO) analyzer

Elemental composition (CHNSO) was determined for chars by controlled combustion using a Perkin-Elmer 2400 Series II CHNS/O analyzer (Perkin-Elmer, Shelton, CT). The chars analyzed were produced from pecan shells by pyrolysis at 300, 350, 400, 500, 600, and 700 °C under 1,600 mL min⁻¹ N₂ flow rate for 4 hours using a laboratory scale box furnace (22 L void

volume) with a retort (Lindberg, Type 51662-HR, Watertown, WI). Table 4 displays ultimate and proximate analysis of char between 300 and 700 °C.

Table 4 Ultimate and proximate analysis of pecan shell and pecan shell char at various pyrolysis temperatures

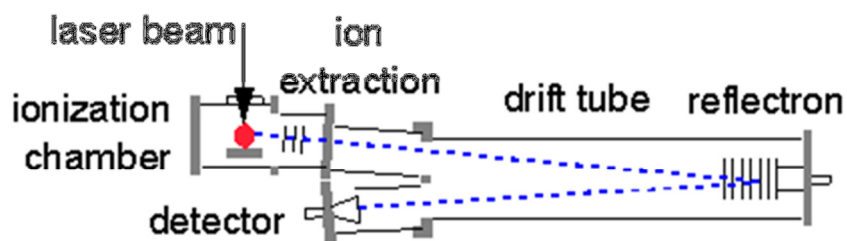
| | C | H | N | S | O | Ash | Fixed C | Moisture | VM |
|---------------|-------|-------|-------|-------|-------|-------|---------|----------|-------|
| | wt. % | wt. % | wt. % |
| 300 °C | 68 | 6.6 | 0.57 | 1.4 | 24 | 1.94 | 41.9 | 2.1 | 56.2 |
| 350 °C | 75 | 5.3 | 0.64 | 0.75 | 19 | 2.78 | 59.9 | 2.69 | 37.3 |
| 400 °C | 79 | 5.1 | 0.65 | 0.5 | 15 | 3.13 | 65.6 | 2.9 | 31.3 |
| 500 °C | 89 | 3.8 | 0.7 | 0.46 | 6 | 3.8 | 76.7 | 2.4 | 19.5 |
| 600 °C | 92.8 | 3.2 | 0.81 | 0.5 | 2.7 | 4.1 | 83.7 | 2.33 | 12.2 |
| 700 °C | 95.1 | 1.7 | 0.7 | 0.1 | 2 | 4.47 | 86.9 | 2.45 | 8.7 |

3.2.3 Gas Chromatography-Mass Spectroscopy (GC-MS)

Quantitative analysis by GC-MS can be used to characterize compounds in the tar sample. The gas chromatographic analysis techniques were designed for the detection of aromatic hydrocarbons. The addition of an internal standard is used to estimate semi-quantitatively the composition of the tar.⁸⁹ The collected tar from the series of impingers were measured gravimetrically and dissolved in 20 mL of acetone. A 2 µL aliquot of the solution was injected into an Agilent 7890B Gas Chromatography Instrument (GC), equipped with an Agilent 5977A Mass Selective Detector (MSD). An Agilent HP-5MS, (30 m x 250 µm ID x 0.25 µm film thickness) column was used as an inert non-polar column capable of measuring active compounds such as PAHs. The GC oven was held at 30 °C for 18 min then heated at 2 °C min⁻¹ ramp to 270 °C with three 10 minute isotherms at 100, 130, and 170 °C, a isotherm at 220 °C for 30 minutes and an isotherm at 270 °C for 10 minutes. The MS ion source temperature was maintained at 230 °C and the transfer line was 270 °C and scanned between m/z of 5 and 550. A separate inert polar column optimized for measuring water-soluble compounds (ZB-WAXplus, 30 m x 250 µm x 0.25 µm)

was used as a cross reference for pecan shell tar. For this test, the sample (dissolved in acetone) was analyzed by the GC (Shimadzu GC-2010 Plus with a MS-QP2010 Ultra) injection port temperature of 250 °C, and the following temperature program: initial column temperature of 30 °C held for 3 min, and then heated at 2 °C min⁻¹ to 180 °C and held for 1 min. The MS ion source temperature was maintained at 200 °C for scanning between the mass to charge ratios (m/z) of 34 and 150. Agilent Chemstation equipped with National Institute of Standards and Technology (NIST) library was used to analyze the chromatograms and electron ionization mass spectra. Not all of the tar constituents are amenable to GC analysis, because of the presence of high MW material. GC analysis has the potential to determine more than 80% of the tar, the remainder being high MW material of >350 g/mol.⁸⁹

3.2.4 MALDI-Time of Flight (TOF)



Schematic 5 MALDI-TOF positive-ion reflectron mode

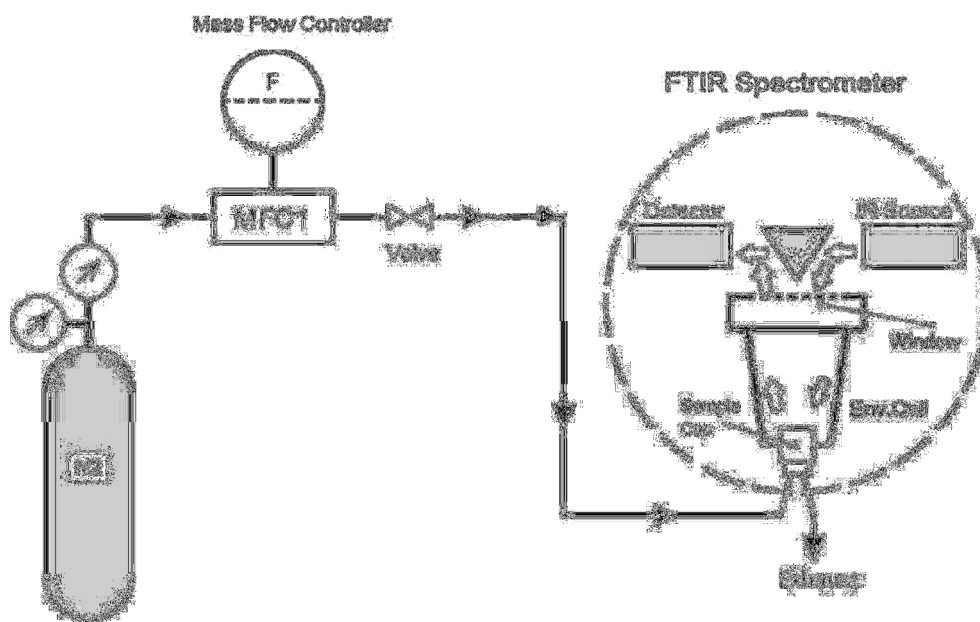
A Bruker autoflex MALDI-TOF was used for the analysis of coal tar. This data was used to 1) characterize the MWD of the tar samples and 2) compare the effect of pyrolysis conditions on the MWD. A diagram of the MALDI-TOF system is shown in Schematic 1. The tar samples were dissolved in acetone and applied to target in 0.5 µL drops. Each sample was applied at three different concentrations (1 drop, 2 drops, and 3 drops). The acetone was allowed to evaporate from the sample. The coal tar samples were analyzed three times at the various analyte

concentrations. No discernible differences or detector overload in the spectrum arose from a single drop or multiple drop samples. In the analysis, the sample targets were shot 500 times each. The shots were taken from random multiple points on the target and from samples duplicated on multiple targets. A set of repeated scans of samples on separate targets are shown in the Appendix. The standard deviation of a tar sample's average MW determined from six repeated scans, of samples on separate targets is ± 7 amu or 2.6%. The laser power was varied between 20 and 50% of the maximum power. The laser power governs the ability to desorb larger and more complex molecules but also has the ability to fragment the molecule if set too high. This causes a limitation on the structural information provided by this technique. The coal tar sample was analyzed three times at various laser powers. Increasing the laser power did not affect the mass spectrum of the coal tar other than increasing the signal intensity. The signal-to-noise ratio for each sample at 40-50% laser power was 100 or more. It has been shown that noise and standard deviations of the mass spectra decreased with increasing numbers from 10 to 100 scans therefore, the use of 500 shots produced a clean spectrum as expected. Scans of coal using different laser powers are shown in the Appendix. The TOF detector was operated in reflectron positive-ion mode in the MW range of 100 to 3,000 amu. In reflectron mode, the detection of smaller ions is favored due to the larger ions not being able to be reflected due to a lack of kinetic energy. The pulsed ion extraction was set to a 120 nanosecond delay. Matrix suppression was turned off.

The samples were analyzed either without a matrix or in a 1:1 matrix to analyte volume ratio with 2,5-dihydroxybenzoic acid (DHB), dithranol, or sinapinic acid. The results of the matrix-assisted tests on coal tar are shown the Appendix. In addition, the coal tar may be

analyzed by LDI-TOF with the sample acting as its own matrix. The results from LDI-TOF were found to be most satisfactory those with a matrix.

3.2.5 Diffuse Reflectance Infrared Fourier Transform Spectroscopy (DRIFTs)



Schematic 6 Schematic of the in situ DRIFTs apparatus

Finely ground pecan shells (2 mg) were pyrolyzed in a time-resolved (1 min^{-1}) DRIFTs environmental chamber (Nicolet 6700; Thermo Scientific, Waltham, MA) with a SMART Collector accessory under $30 \text{ cm}^3 \text{ min}^{-1}$ N_2 flow rate. Schematic 6 shows a schematic of the in situ DRIFTs technique employed in this study. As the name suggests, the technique uses infrared beam to radiate the surface of a solid sample in an environmental chamber. The Fourier transform infrared collects spectral resolution data over a wide spectral range. The temperature of the environmental chamber was increased at $10 \text{ }^\circ\text{C min}^{-1}$ until $550 \text{ }^\circ\text{C}$ and was then held at $550 \text{ }^\circ\text{C}$ for 1 hour. The temperature, time, and spectral data were automatically recorded by a pulse-width modulation controller connected to a thermocouple feedback loop. The spectral data depicts the surface chemical changes of the sample during pyrolysis.

3.2.6 Scanning Electron Microscopy (SEM)/Energy Dispersive Spectroscopy (EDS)

Silver coated and fibrous coke samples were harvested from the commercial coke samples obtained from Suncoke Energy. These samples are pictured in Figure 24(a-c). Each sample was analyzed separately by SEM and EDS on a Zeiss Supra 55 field emission SEM/EDS with a maximum resolution of 1 nm. The instrument was operated using backscattered electron imaging in variable pressure mode and electron backscatter diffraction (EBSD).

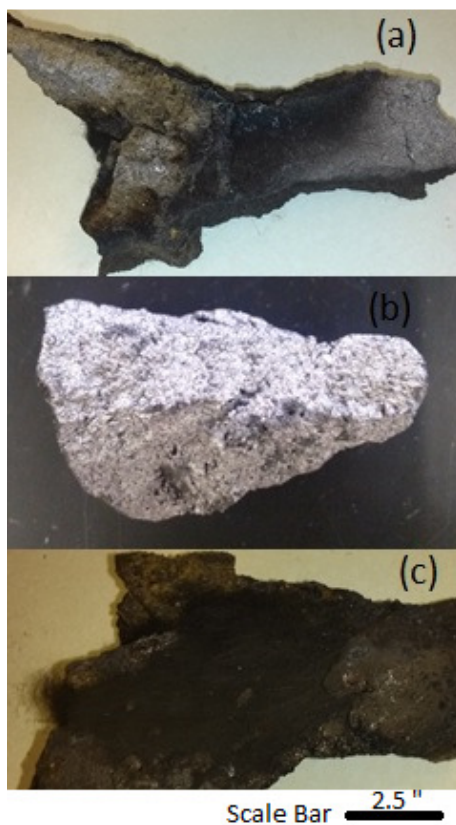


Figure 24 Three different coke fingers (a) is a coke finger which has some gray patches and some coke hairs (b) shows a silver coke finger (c) coke hair with a large patch of coke hair

3.2.7 X-Ray Diffraction (XRD)

Commercial samples of metallurgical coke obtained from Suncoke Energy were finely ground and analyzed by PANalytical X'Pert Pro Powder Diffraction XRD instrument. A

PANalyticalx'pert pro was used for XRD in order to detect crystalline compounds in coke samples. The step size was 0.026° with a step time of 27.54 seconds.

3.2.8 Inductively Coupled Plasma (ICP)-Mass Spectroscopy

A finely ground silver coke sample (Figure 24b) of 0.1 grams was dissolved in 6 mL of 20% HCl and 2 mL of HNO₃ and heating the solution by closed autoclaves resistant against high pressure to 220 °C for 35 minutes. After cooling, deionized water is added to the system so that the final volume is 25 mL. The sample was analyzed by ICP-MS (Center RAPSODEE Energetique, Albi, France).

3.3 Calculations

3.3.1 Mass balance

In this work, the mass of solid, condensable (tar and water) and gaseous products were measured in a TG-GC system with an impinger condenser unit. The mass closure was 99.2% or better for three coking coal samples and one pecan shell sample. The solid product was directly measured as function of time in the TGA (i.e., the solid residual is known). The volumetric rate of inert gas was measured via a flow meter (Alicat M-100). The volumetric rate of the gas produced during the pyrolysis reactions was calculated using the μ GC measurements and argon or nitrogen as an internal standard.

$$v_{Total} = \frac{v_{sweep}}{y_{sweep}} \quad \text{Equation 1}$$

$$v_i = y_i v_{Total} \quad \text{Equation 2}$$

In Equations 1 and 2, v_{Total} is the total gas volumetric rate, v_{sweep} is the volumetric rate of the sweep gas, v_i is the volumetric rate of species i, y_{sweep} is gas mole fraction of sweep gas, and y_i is the gas mole fraction of species i. The density at normal temperature and pressure was used to

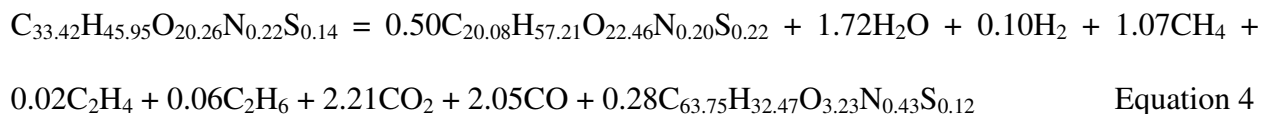
calculate the total mass. Tar, tar aerosols, and water were collected in the condensation unit and measured gravimetrically. By subsequently measuring the mass balances the aggregate may be divided to reflect its time-dependent evolution. This was done using the gas and solid residual measurements to determine the amount of tar released at the corresponding times.

$$r_{tar} = r_{solid} - r_{gas} \quad \text{Equation 3}$$

where r_{solid} is the rate of solid consumption (measured by DTG), r_{gas} is the rate of gas production (measured by μ GC) and r_{tar} is the rate of tar production (by-difference) which are all known as a function of temperature. The critical aspect is that the total amount of tar that is projected over time matches the measured amount in the experiment, thus fixing the total mass evolved during the test. Condensable observed below 200 °C in is attributed to water.

3.3.2 Stoichiometric Equations

The empirical stoichiometric equation for the slow pyrolysis of pecan shell (10 °C min⁻¹ up to 500 °C) was determined based on the mass balance of 99.7% and elemental composition for solid, liquid, and gas-phase products. All elemental compositions are empirical (by ultimate analysis for solid, and by TG-GC for gas products), except tar. The tar elemental composition therefore must be calculated by difference based on the mass balance and elemental composition of the reactant and other products. The stoichiometric equation for pecan shells pyrolysis at 10 °C min⁻¹ is shown in Equation 4.



The left-hand side of the equation is the chemical formula for pecan shells. The right-hand side of the equation contains all of the measured products from pecan shell pyrolysis at 500 °C when heated at a constant heating rate of 10 °C min⁻¹. The reaction stoichiometry pertains to organic

species composed of C, H, O, N and S because the ultimate analysis results for the feedstock and char product are on a dry, ash-free basis. However, the gaseous products could originate from the ash components of the feedstock, such as calcium oxalate. The lack of elemental characterization on the solid product from coal pyrolysis inhibited stoichiometric equations to be developed. The pecan shell calculation demonstrates how the analysis is performed.

3.3.3 Energy Balance

Eleven empirical correlations were evaluated to calculate the higher heating value (HHV) of pecan shell feedstock and char produced at 500 °C based on the ultimate analysis results, and assuming negligible contribution of the ash components. The ultimate correlations in literature claim an absolute error as low as 1.45% and are valid for gas, liquid, and solid.⁹² The empirical correlations were based on the ultimate and proximate analysis. These correlations were used to evaluate the higher heating value (HHV) of the pecan shell feedstock, tar, and char. It was determined that the Gumz correlation most accurately predicted the HHV of pecan shells reported in literature. The energy contents of the pecan shell, tar, and char products were determined by the Gumz correlation using the measured ultimate analysis of the tar and char. The complete product distribution between tar, char, H₂, CO, CO₂, CH₄, C₂H₆, and C₂H₄ had been determined from experiment. The HHV of gas-phase products were determined based on the μ GC measurements and standard HHV of each gaseous species.⁹³ Pyrolysis at 10 °C min⁻¹ up to 500 °C produces a solid product with a calorific value 61.8% higher than the pecan shell. The energy content of the feedstock and the calculated total energy of the pyrolysis products are compared. The total energy from the pyrolysis products was found to be 18.8 MJ/kg which is 87.3% of the energy in the pecan shell (21.5 MJ/kg). From this, it is inferred that 2.73 MJ are required to decompose 1 kg of pecan shells.

3.3.4 Gaussian Fits

In the 1980's, researchers in biomass and coal pyrolysis used the Gaussian distribution of the overall rate of weight loss profile in reaction models. The method was not computationally cumbersome and had even been extended to individual species evolution.⁹⁴ In this work, TG-GC-based volatile product evolution rate profiles were matched via normal distributions:

$$f(T) = \alpha e^{-\frac{(T-\beta)^2}{2\gamma^2}} \quad \text{Equation 5}$$

where α is the amplitude of the gas rate curve, β is the mean temperature of the distribution, γ is the standard deviation of temperature from measured gas rate curves, and T is the sample temperature during pyrolysis. Most gas species rate profiles in pyrolysis cannot be described by a single normal distribution, therefore a sum is used. In such cases, summations of multiple numbers (n) of normal distributions are fitted by varying adjustable parameters α , β , γ , and n to match the measured rate profile. The individually measured rates at specific temperatures were matched by minimizing the percent errors between the prediction and measurement. Equation 5 is not suggesting that any of product profiles are only a function of temperature. The Gaussian fits are necessary for develop a continuous function for product/conversion profiles. The time-dependent tar rate profile was calculated as the difference between the DTG and gas product evolution rate determined by μ GC as shown in Equation 3.

3.3.5 DRIFTS-GC Partial Least Squares (PLS) Calibration

Observable links between the evolved gas profile and char surface functional groups motivated the correlation between the gas and solid phase during pyrolysis. In-situ DRIFTS monitoring of pecan shells gave the time courses of characteristic surface functional groups as it transforms into char and gas upon heating. If the infrared spectrometry results are to be regarded as an absolute change in functional group concentration then a calibration to absolute

measurements is needed.⁹⁵ A PLS calibration is useful for doing so because PLS correlate a 2D data set, like spectroscopy data, to an assay value. Furthermore, establishing a PLS calibration reduces the number of tests for further determination on the surface functional groups. Therefore, this technique demonstrates how interfaces between chemometric tools and infrared spectroscopic data offer new possibilities for the quantification and qualification of char products.

The PLS analysis was employed to obtain predictive correlations between (i) the surface functional groups on the solid phase monitored by DRIFTS at 900-4000 cm^{-1} in the unit absorbance and (ii) modeled gas- and liquid-phase product mass based on TGA-GC. The number of points was determined by the frequency of gas phase measurements. Because of the limited number (46) of matching temperature data points between the gas and liquid evolution rates and DRIFTS, cross-validation was performed, instead of an independent prediction using a new data set. The PLS was performed using MATLAB version 8.5.0.197613 (R2015a) (Mathworks, Natick, MA) with PLS toolbox version 8.0.1 (Eigenvector Research, Manson, WA). The raw DRIFTS spectra were pre-processed by (1) removing the regions affected by moisture (2000-2500 cm^{-1}) and scattering at <1000 and >3600 cm^{-1} , (2) multiplicative signal correction for weighted normalization and baseline removal, (3) first derivative with Savitzky-Golay smoothing and then (4) mean centering to remove the mean offset from each variable. The y-variables were the percent of initial mass from the TG profile or Gaussian fits of gas-phase products (CH_4 , C_2H_4 , C_2H_6 , CO_2 , CO , and the sum of all species in mg) and tar (in mg), and were mean centered. Other pretreatments including the conversion to log-scale and second derivative did not improve the fits. Cross-validation statistics were evaluated by the root mean

square error of cross validation (RMSECV) and calibration (RMSEC), calibration/cross-validation bias, R^2 of calibration and cross-validation, and the number of latent variables.

Chapter 4: Investigation of Coal Pyrolysis

Chapter 4 focuses on the experimental findings on coal primary pyrolysis reactions. The mass balance and measured product distributions from coal is first presented. The high mass closure and in-situ techniques developed for monitoring pyrolysis reactions are the major contributions of this work. The results of TG-GC on Jewell coal pyrolysis are used to demonstrate the time-resolved reaction information extracted from a pyrolysis system. Ex-situ Methods of characterizing tar products are then discussed and demonstrated. The combined analyses reveal a comprehensive picture for primary coal pyrolysis reactions.

4.1 Mass Balance

Excellent work on coal pyrolysis from the literature has reached a 95% mass closure on pyrolysis products in an encapsulated pyrolysis unit.⁹⁶ Similar balances were obtained in an entrained flow reactor for more rapid heating conditions.⁷² However, in many other reports on coal pyrolysis, the tar and water yields were determined by difference (i.e., not measured) and more often the mass balance was not reported. In the present work, the masses of solid, condensable (tar and water) and gaseous products were measured and closed to 99.2% or better for three coking coals and for pecan shells. The solid product was directly measured as the residual mass in the TGA. The gas products were measured from the GC measurements and the volumetric rate of inert gas. Tar, tar aerosols, and water were collected in the condensation unit and measured gravimetrically. The measurement of condensable yield fluctuated by 30-50% between repeated tests depending on coal with the high-VM coal (Glamorgan) resulting in the

greatest variability. The average product distributions for three coking coals and pecan shells are given in Table 5. The coal product distributions are in good agreement with other researchers with high mass closure. The cumulative tar yields were between 20 and 32% for bituminous/subbituminous coals and 18.3-23.7% for lignite.⁹⁶ No complete pyrolysis product distributions for pecan shells have been found in the literature. However, the char yield is in agreement with values in the literature.⁹

Table 5 Average product distribution from three coking coals (samples contained nominally 1 wt. % moisture) and pecan shells

| | Solid (%) | Tar and Water (%) | Gas (%) |
|-------------------------------|------------|-------------------|------------|
| ICG East Gulf (Low-VM) | 78.6 ± 2.3 | 11.8 ± 2.9 | 9.4 ± 1.6 |
| Jewell (Mid-VM) | 77.4 ± 1.7 | 15.2 ± 3.8 | 7.3 ± 0.79 |
| Glamorgan (High-VM) | 68.3 ± 1.5 | 25.5 ± 7.4 | 5.5 ± 0.68 |
| Pecan Shells | 31.8 | 45.8 | 22.1 |

4.2 Thermogravimetry of Jewel Coal Pyrolysis

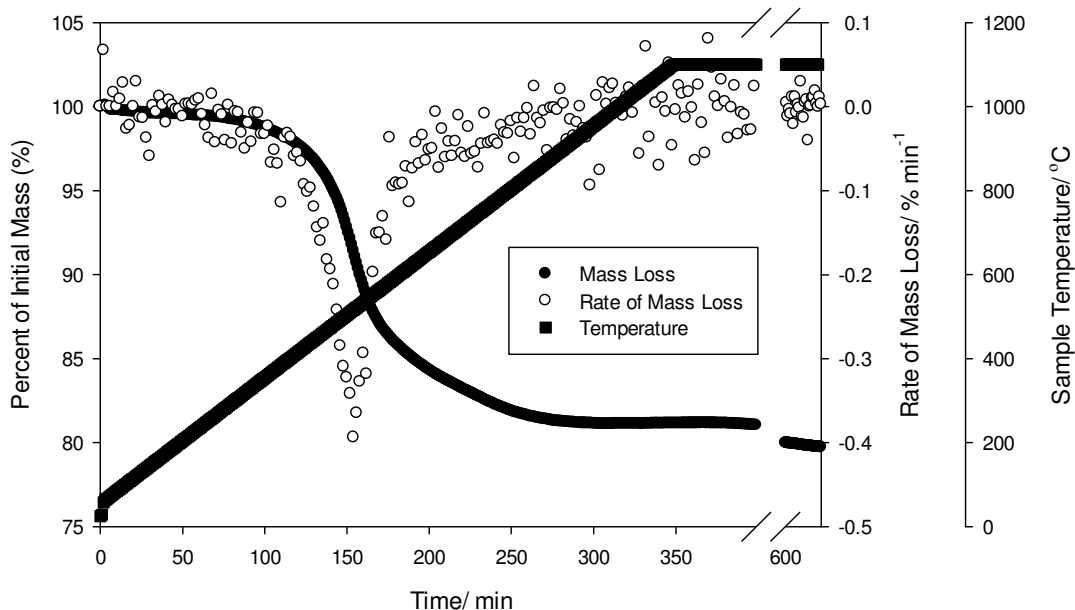


Figure 25 Thermogravimetric analysis of Jewel coal pyrolysis at 3 °C min⁻¹ to 1100 °C

Figure 25 gives an example of data produced from TGA for coal pyrolysis. Figure 25 specifically shows Jewell coal pyrolysis at $3\text{ }^{\circ}\text{C min}^{-1}$ up to $1100\text{ }^{\circ}\text{C}$. The final temperature of $1100\text{ }^{\circ}\text{C}$ was held constant for 5 hours. The coal particles were 40 microns in diameter and contained in a pan confinement. The sample temperature is measured by a thermocouple in direct contact with the base of the sample confinement. Both the mass loss (left vertical axis) and rate of mass loss (right vertical axis) are presented along with sample temperature (offset right axis) against time. In TGA, mass loss is solely due to the evolution of volatile products due to the temperature effect on the sample. The mass of sample residual is traced as a function of either time or temperature. The final value on the mass loss curve is the percent mass of residual solid product. The difference between the final and initial mass percent is the total volatile product evolved. The mass loss profile observed for Jewell coal during a constant heating rate is a classic profile observed for many solid fuels. Repeated experiments with controlled conditions have shown variations of $\pm 1.7\text{ wt. }%$ in the mass loss profile. The rate of mass loss curve depicts very clearly the stages of constant pyrolysis with respect to temperature. The pre-metaplast regime spans the first 100 minutes of the test or between $25\text{ }^{\circ}\text{C}$ to $400\text{ }^{\circ}\text{C}$. The mass loss in this regime is only $2\text{ wt. }%$ which is attributed to the loss of loosely bound C-O bonds and loss of occluded water. At $400\text{ }^{\circ}\text{C}$, Jewell coal transitions to a metaplastic state. The onset of the metaplast can be observed in the rate of mass loss profile by the large valley. The large value corresponds to the production of tar species, i.e., a great loss of material. This process of sudden rapid volatile production is called primary devolatilization. The initiation of the metaplastic state determined by TGA agrees with the softening point determined for Jewell coal by the Gieselier test. The maximum rate of primary devolatilization occurs at $516\text{ }^{\circ}\text{C}$ or at 154 minutes. Following the maximum, a shoulder-valley exists between 600 and $950\text{ }^{\circ}\text{C}$, which then decays to a rate of zero.

The regime between 600 and 950 °C is called secondary devolatilization. Secondary devolatilization includes resolidification of the metaplast which produces cracking products like CH₄, H₂, C₂H₆, C₂H₄, and CO as will be shown in the following section. The cracking sequence occurs via the free radical mechanism described in Chapter 2. It can be seen from 1000 °C until the end of the 5 hour isotherm at 1100 °C, that the average rate of mass loss is zero. The mass loss during the 5 hour isotherm is only 1.4 wt. %. The main product during this period is hydrogen from graphitization of the coke.

4.3 Gas Chromatography of Jewell Coal Pyrolysis

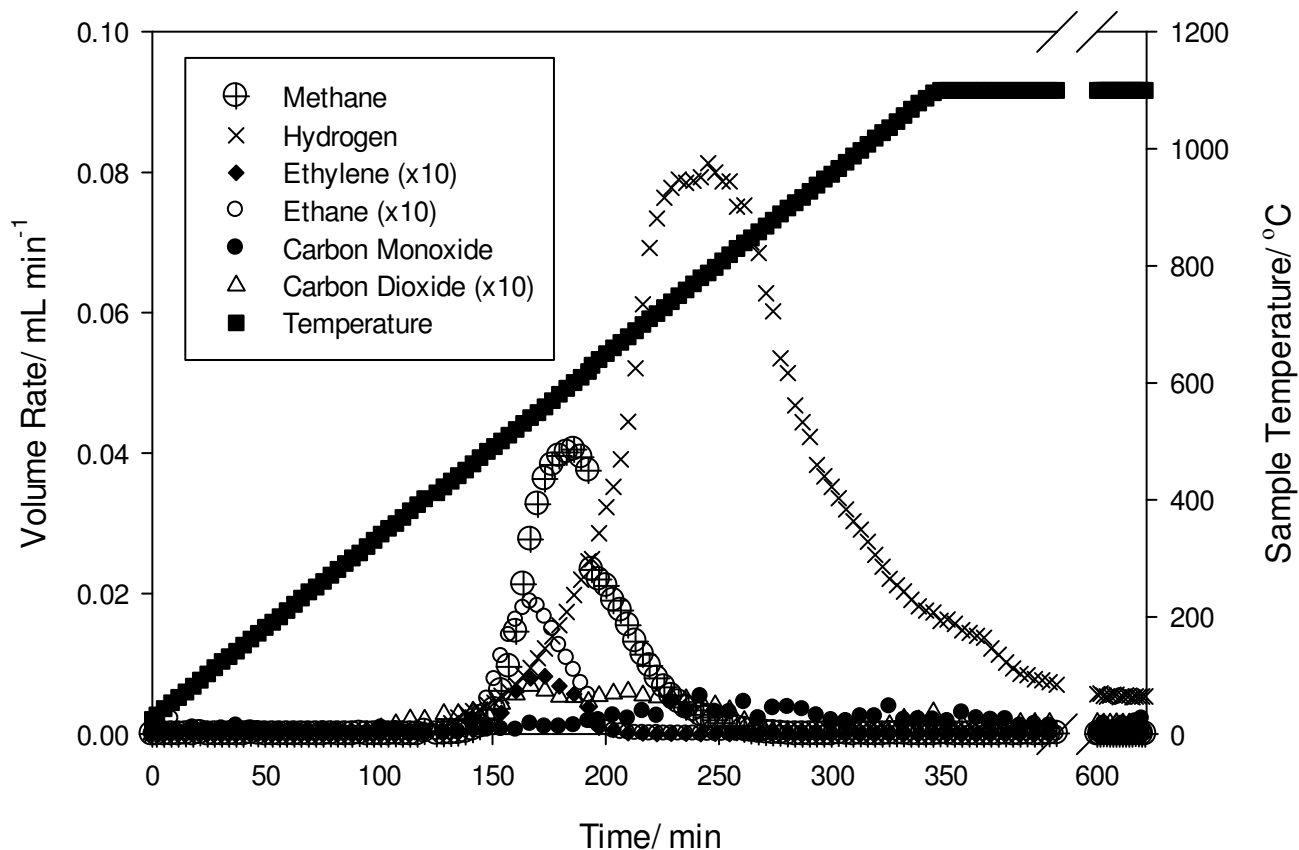


Figure 26 Gas evolution for Jewell coal pyrolysis at 3 °C min⁻¹ to 1100 °C measured by GC

Figure 26 shows the complimentary GC data for the Jewell coal pyrolysis experiments. In Figure 26, the volumetric rates (left axis) of CO₂, CH₄, H₂, C₂H₆, C₂H₄, and CO produced during coal pyrolysis are plotted with sample temperature (right axis) against time. The permanent gas products can be correlated to the mass loss events determined by TGA. The carbon dioxide, ethane and ethylene evolution profile are exaggerated by a factor of 10 on the plot for visibility. At 100 minutes, carbon dioxide begins to evolve corresponding to the disassociation of C-O bonds in the pre-metaplast regime. This event coincides with metaplast onset and initiation of primary devolatilization. Tar species from primary devolatilization are not measured by the GC, however, it should be recalled that maximum devolatilization occurs at 516 °C/154 minutes. The evolution of methane, hydrogen, and light hydrocarbons initiate at 435 °C. These products evolve following the point of maximum devolatilization from cracking of larger hydrocarbons in the metaplast condensed phase. The cracking of metaplast species eventually bring out resolidification, i.e., transferrable hydrogen is depleted. Ethane and ethylene are minor products. Both species reach a maximum at 545 °C and subside by 650 °C. Methane reaches a maximum at 600 °C and ceases by 800 °C. Carbon dioxide evolves throughout primary devolatilization until 850 °C from moderate temperature crosslinking reactions. Carbon monoxide does not initiate until secondary devolatilization at 600 °C. The reaction source of carbon monoxide is most likely dissociation of phenolic species within the solid intermediate produced during the metaplastic regime because is the only bond in biomass char capable of withstanding temperatures above 500 °C. Hydrogen, methane, and carbon monoxide are the main gas products during secondary devolatilization. Carbon dioxide is present at a low concentration as a result of carbon-metal oxide interaction. Hydrogen production is primarily due to the coke graphitization. Graphitization is a solid-state reaction between aromatic clusters reorganizing and combining to

form large 3-dimensional continuous graphite sheets. As graphitization proceeds, the H/C ratio of the solid product attenuates to a low constant value. The one remaining permanent gas species to be discussed is molecular oxygen.

The lack of oxygen quantification in coal has been discussed in the review presented in Chapter 2. Determination of oxygen content by difference has been an accepted practice for many years, therefore the literature has been largely oblivious to this deficiency in oxygen characterization. Moreover, the atomic balance on the product distribution from coal pyrolysis has not been realized although the quantification of heteroatom species in tar has made a great improvement.^{61, 63, 73, 74, 75} For the first time, we have detected the evolution of molecular O₂ as a product from coal pyrolysis. The scientific importance of this finding is (1) it may reveal a missing realization in the closure of the oxygen balance from coal pyrolysis and (2) will divulge specific reaction mechanisms never before considered in the coal pyrolysis mechanism. More applicable importance will be in the consideration of burn losses in coke production or polymerization of unsaturated tars creating a viscous black residual. The evolution of O₂ does not occur for all coals but, it was mentioned in U.S. Patent 7008459B1. The inventors of a pretreatment for removing oxygen coal suggest loosely bound organic oxygen evolves as O₂ at 177 °C.⁹⁷

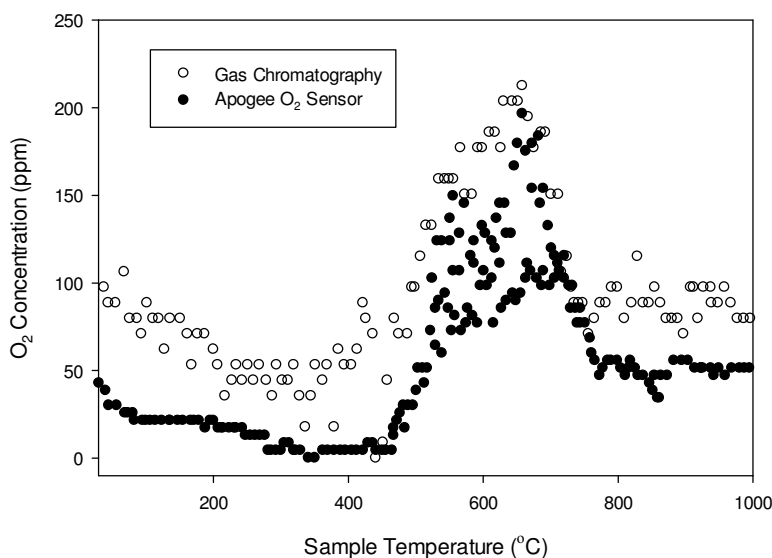


Figure 27 Oxygen signals from two detectors from Oak Grove coal pyrolysis

Using the TG-GC system, a commercial coal from the coke-making industry (Oak Grove) was observed to evolve O_2 during pyrolysis between 450 and 970 °C. The evolution was confirmed by both μ GC measures and an electrochemical O_2 sensor (Apogee). Figure 27 shows the measured O_2 signal from the two sensors as a function of pyrolysis temperature. The maximum concentration of O_2 in the effluent is nominally 200 ppm. The evolution of O_2 occurs during the middle to later stages of the metaplastic regime along with other gaseous species production. The evolution coincides with the reduction temperature of iron oxide (Fe_2O_3 to Fe_3O_4 , Fe_3O_4 , and FeO) which is nominally 500 °C.¹² Based on Ellingham diagrams shown in Figure 28, the only other feasible oxide reduction to produce O_2 would be CO. The peculiarity of metal oxide reduction being the source is that the presence of gaseous O_2 in coal above 450 °C should produce combustion products through secondary oxidation reactions. The only way around this contradiction is to assume that the metal oxide inclusions are present on the surface of the material. Nevertheless, the O_2 evolution phenomenon deserves more attention in pyrolysis research.

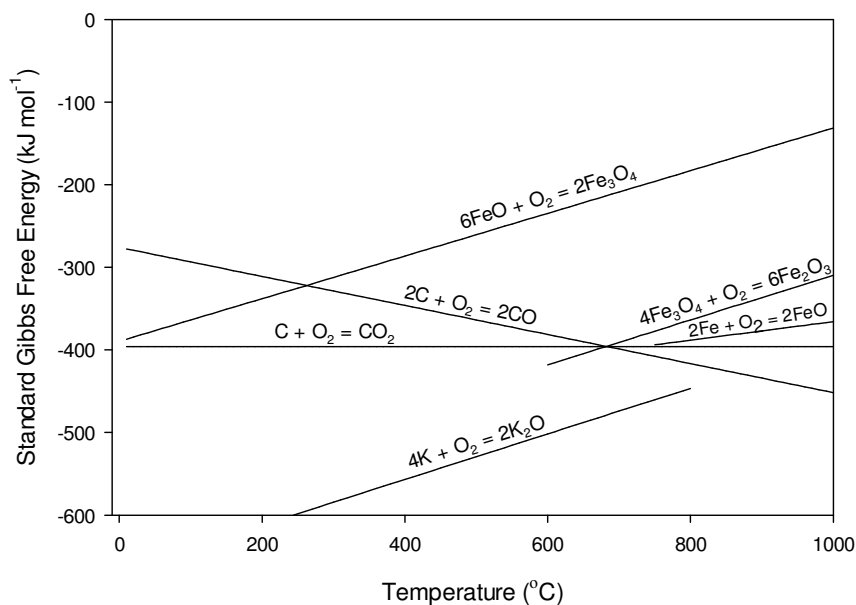


Figure 28 Ellingham diagram for metal and carbon oxides present in coal pyrolysis

4.4 Tar Analysis of Jewell Coal Pyrolysis

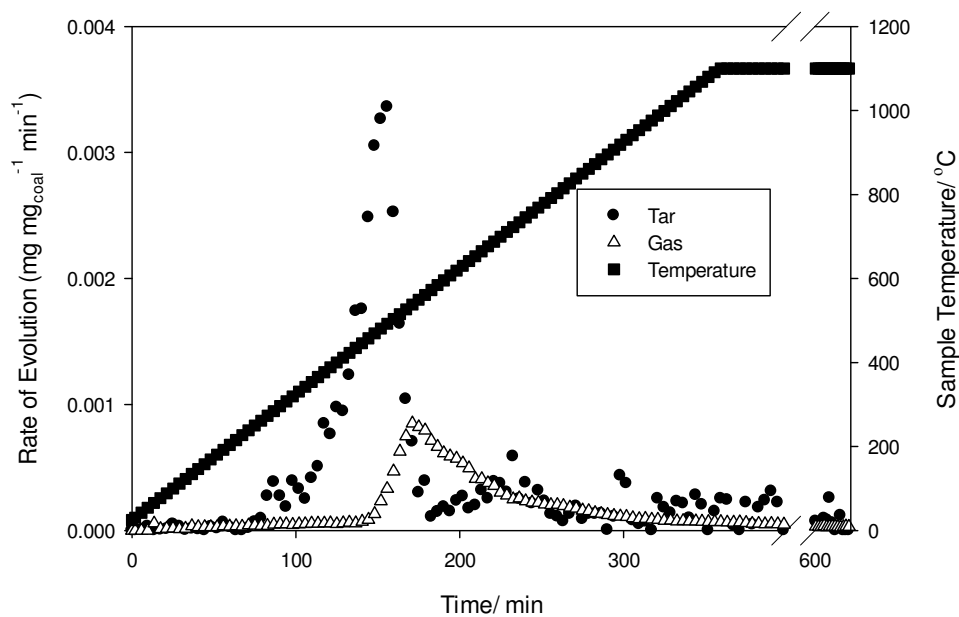


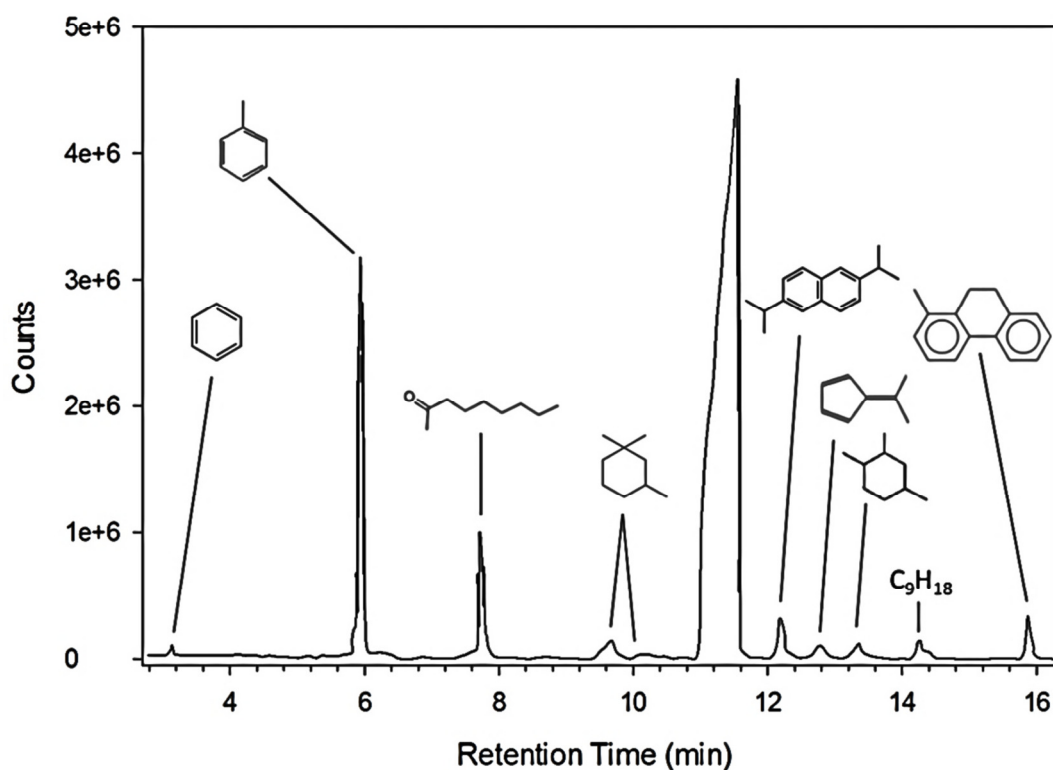
Figure 29 Tar and gas evolution profile during Jewell coal pyrolysis at $3\text{ }^{\circ}\text{C min}^{-1}$ to $1100\text{ }^{\circ}\text{C}$

Figure 29 shows the total tar and gas evolution profiles for Jewell coal pyrolysis. The tar evolution profile is calculated from the corresponding TGA and GC real-time data as described

in section 3.3.1. The plot shows the production rates (left axis) in mg of product per mg of coal per minute along with sample temperature (right axis) against time. The tar evolution profile indicates volatile production begins at 273 °C. This evolution is attributed to the emission of occluded water in the coal. After 350 °C, there is a sharp increase in tar production. This analysis of the data enables the maximum rate of tar production to be located at 492 °C which is slightly lower than the maximum primary devolatilization rate at 516 °C. The analysis also shows the clear separation between dominant tar production in primary devolatilization and dominant gas production in secondary devolatilization. This plot illustrates the event of metaplast formation that gives rise to tar products followed by metaplast resolidification giving rise to gases. The events have a brief 50-60 °C overlap. The gas product individual profiles have already been presented. Due to the complex mixture of species in tar, an ex-situ technique must be resorted to for chemical characterization.

Characterization of tar is the single largest experimental obstacle in the field of pyrolysis. Coal tar is a mixture of thousands of compounds with a high concentration of aromatics, PAHs, and nitrogen/sulfur-containing aromatics. Work-to-date has reported complete mass and carbon closures, however the comprehensive characterization of the products from a single coal does not exist in the literature. As one could imagine, this fact has implications for both applied and scientific interests. Gas chromatography-mass spectrometry is a suitable technique for analyzing volatile, thermally stable, low polarity molecules up to 400-500 amu and the best option for detecting low molecular weight (MW) saturated hydrocarbon.⁹⁸⁻¹⁰¹ Therefore, GC-MS has been a widely used technique in the characterization of pyrolysis tar. However, GC-MS is not sufficient for the analysis of less volatile, high MW, or strongly polar species.^{89, 98} Additional complications involve the presence of PAH impairing the detection of heteroatom species by co-

elution and/or high spectral similarity.¹⁰² However, there is still a considerable fraction of tar molecules detectable by GC-MS. Gas chromatography-mass spectrometry of coal tar in this work identified 120 distinct compounds. A representative chromatogram is shown in Figure 30. Despite efforts to optimize the GC oven temperature program, a portion of each tar sample co-eluted from the column as bis(2-ethylhexyl) phthalate at a column retention time of 109 minutes or formyl salicylic acid at 108.845 minutes.



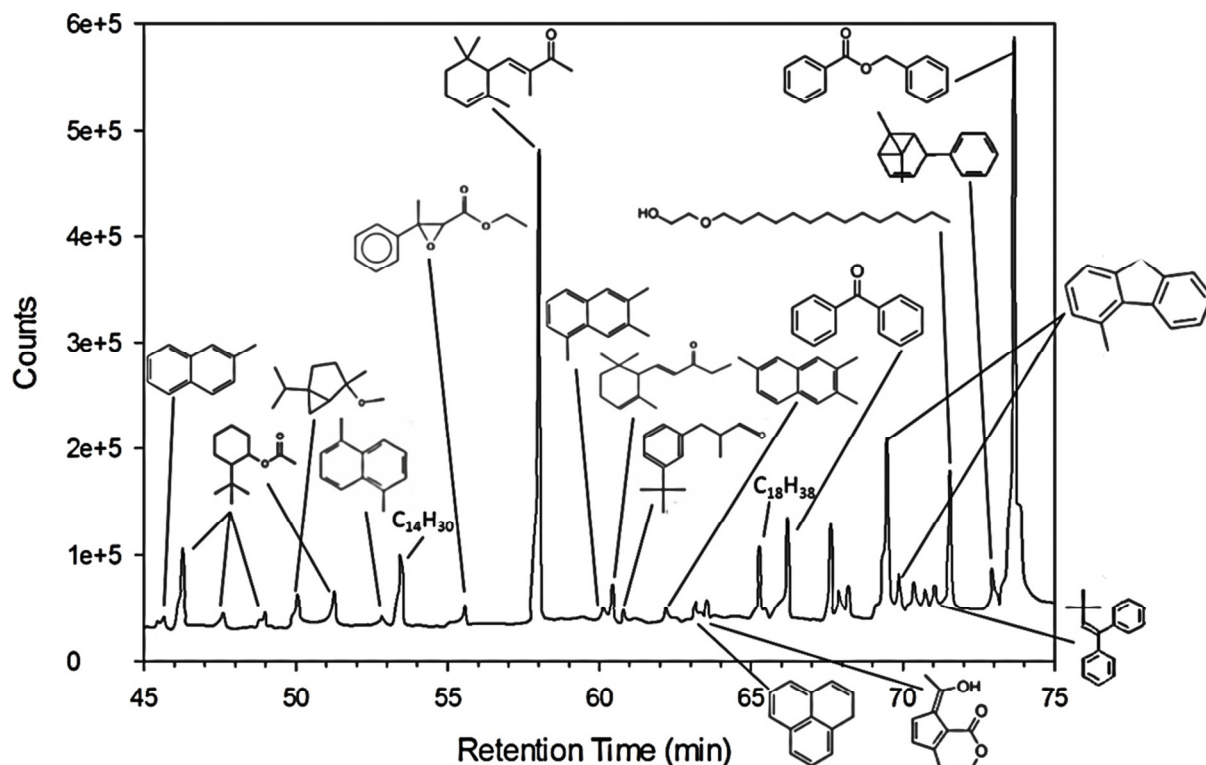


Figure 30(a) from shortest to longest retention time (1) benzene (2) toluene (3) 2-nonanone (4) 1,1,3-trimethyl-cyclohexane (5) solvent peak (6) 2,6-diisopropyl-naphthalene (7) 5-methylethylidene-1,3-cyclopentadiene (8) 1,2,4-trimethyl-cyclohexane (9) 1-ethyl-4-methylcyclohexane (10) 9,10-dihydro-1-methyl-phenanthrene and (b) from shortest to longest retention time (1) 2-methyl-naphthalene (2) o-tert-butyl cyclohexyl acetate (3) cis-4-methoxy thujane (4) 1,5-dimethyl-naphthalene(5) tetradecane (6) 3-methyl-3-phenyl-ethyl ester, trans-oxiranecarboxylic acid (7) α isomethyl ionone (8) 1,6,7-trimethyl-naphthalene (9) 1-(2,6,6-trimethyl-2-cyclohexen-1-yl)-1-penten-3-one (10) 3-(1,1-dimethylethyl)- α -methyl-benzenepropanal (11) 2,3,6-trimethyl-naphthalene (12) 1H-phenalene (13) 5-(1-hydroxyethylidene)-2-methyl-methyl ester 1,3-cyclopentadiene-1-carboxylic acid (14) 8-methyl-heptadecane, (15) benzophenone (16) 2-phenyl-2,4-octadienol (structure not shown in figure)

(17) 3,3-diethyltridecane (structure not shown in figure) (18) 3-oxo-2-pentyl-methyl ester cyclopentane acetic acid (structure not shown in figure) (19) 4-methyl-9H-Fluorene (20) 3-dodecyl-2,5-furandione (structure not shown in figure) (21) 2-methyl-pentadecane (structure not shown in figure) (22) 1,1'-(3,3-dimethyl-1-butenylidene)bis-benzene (23) 2-(tetradecyloxy)-ethanol (24) 1,7-dimethyl-3-phenyltricyclo[4.1.0.0(2,7)]hept-3-ene (25) benzyl benzoate

Figure 30(a-b) show representative ion chromatograms for coal tar and depicts commonly identified structures. Figure 30a shows benzene (78.110 amu) eluting at 3.174 minutes, toluene (91.140 amu) at 5.938 minutes and benzophenone (182.217 amu), shown in Figure 30b, at 66.208 minutes. Other common low MW molecules include 5-(1-methylethylidene)-1,3-cyclopentadiene (106.15 amu), 1-methyl-2-cyclohexen-1-ol (112.153 amu), 1,1,2-trimethyl-cyclohexane (126.216 amu), 4-(2-propenyl)-phenol (134.159 amu), 2-methyl-naphthalene (142.18 amu), 6-methyl-4-indanol (148.183 amu), 1,4-dimethyl-naphthalene (156.204 amu), 1-phenyl-1,2-butanediol (166.196 amu), 1H-phenalene, 1,6,7-trimethyl-naphthalene (170.228 amu), and 4-methyl-9H-Fluorene (180.224 amu). It can be observed between Figure 30(a-b) that number of carbons, oxygen, rings and MW per molecule generally increase with retention time. Ring structures dominate the mixture and evidence of aromatic clusters of three or fewer rings were observed. Oxygen appears in many probable structures in the form of ketone group. After oxygen, nitrogen was the next most common heteroatom detected. Nitrogen was not only observed in amine or amide functional groups, but also in ring structures. Most nitrogen species eluted from the column between 72 and 102 minutes with a few nitrogen structures eluting at earlier times. Sulfur heteroatomic structures were found to elute from the column between 50 and 77 minutes. For example, detected sulfur-species include thioxanthene, sulfamide, naphthalene sulfonic acid, benzothiophenes, thiols and alkyl thiophenes. Chlorinated/fluorinated

species were detected and within the same molecules such as 3-trifluoromethylbenzhydryl chloride or 1-chloro-4-(trifluoromethyl)-benzene.

In the last 20 years, MS coupled with various sample inlet techniques have greatly improved the analysis of complex organic samples.¹⁰⁰ MS techniques used in the analysis of coal derived liquids include GC-MS, heated-probe MS¹⁰³, laser desorption ionization (LDI-MS)¹⁰³, matrix-assisted laser desorption/ionization (MALDI-MS)^{58, 103-107}, field desorption (FD-MS)¹⁰³, fast atom bombardment (FAB-MS)¹⁰³, field ionization (FI-MS)^{63, 103, 108}, electrospray ionization (ESI)^{103, 109}, ESI-Fourier transform ion cyclotron resonance mass spectrometer (ESI-FT-ICR-MS)^{89, 98, 101}, atmospheric pressure photoionization (APPI-MS)¹⁰⁹, and ESI-Orbitrap MS.¹⁰⁰ Each MS and sample inlet technique has advantages and disadvantages. ESI is a soft ionization technique suitable for analyzing volatile, thermally stable, polar molecules^{98, 107, 109} and therefore is useful for the light fraction of coal tar.¹⁰⁰ ESI poorly ionizes less polar molecules.¹⁰⁹ Meanwhile, ESI-FT-ICR-MS is advantageous for characterizing complex molecules such heteroatomic organic species.^{89, 100} ESI-FT-ICR-MS has been used to successfully resolve ~4000 distinct molecules in a single coal liquid sample at 500 ppb concentration.¹⁰¹ ESI-Orbitrap MS has been effective for analysis of nonvolatile polar molecules with low thermal stability in coal tar.¹⁰⁰ Meanwhile, APPI has been used for the analysis of less polar molecules.¹⁰⁹ Heated-probe MS is a classic technique in coal science. It only requires the sample to be volatile therefore does not depend on the polarity of the compounds like in GC-MS, ESI, and APPI.¹⁰³ However, the mass limit for aromatics seems to be below m/z 600 for heated-probe MS, depending, to some extent, on the geometry of the ion source.¹¹⁰ Among these techniques, the largest MW in coal-derived materials has been observed by FI-MS at 1200-1500 amu.¹¹⁰ FI-MS was first used in coal pyrolysis and the analysis coal pyridine-extract in 1984.¹¹¹ FI-MS was later used to analyze

coal tar of the eight Argonne coals produced by pyrolysis at $3\text{ }^{\circ}\text{C min}^{-1}$ to $450\text{ }^{\circ}\text{C}$.¹⁰⁸ The average MW of the lowest (Beulah-Zap lignite) and highest rank (Pocahontas) coals were within a narrow range, 277 amu, and 299 amu, respectively.¹⁰⁸ Pocahontas (low volatile bituminous) and Upper Freeport (medium volatile bituminous) coal tars show low intensities at MW between 100-200 amu and high intensity in the 200-600 amu range.¹⁰⁸ The intermediate-rank coals, Pittsburgh, Lewiston-Stockton, Utah, and Illinois have MWD with substantial intensities in the 100-200 amu and 200-600 amu regions.¹⁰⁸ The functional group/depolymerization-vaporization-crosslinking (FG-DVC) model was able to predict the average tar MWD from FI-MS data.⁶³

Herod and co-workers have successfully developed LDI-MS and MALDI-MS methods for the characterization of heavy hydrocarbons mixtures from coal. MALDI-MS alleviates issues of polarity and volatility by ionizing the entire sample into the drift tube by laser excitation and detecting the species in an ionized state by an MS detector such as time-of-flight (TOF). Therefore, MALDI-MS is a viable method for measuring the comprehensive MWD of coal-derived liquid. The MWD from MALDI-MS was found to match those of SEC.¹¹²⁻¹¹⁴ Many analyses indicate upper mass limits of $\sim 1000\text{-}1500$ amu for coal tars, pitches, and petroleum asphaltene.^{110, 115, 103-106} However, a significant amount of substance in coal extracts fall within the 100–500 amu range with low intensity depreciating towards higher masses being found by MALDI-TOF in agreement with FI-MS.⁵⁸ In this work, LDI-TOF was performed on the tar products of five different coals, four of which are shown in Figure 31.

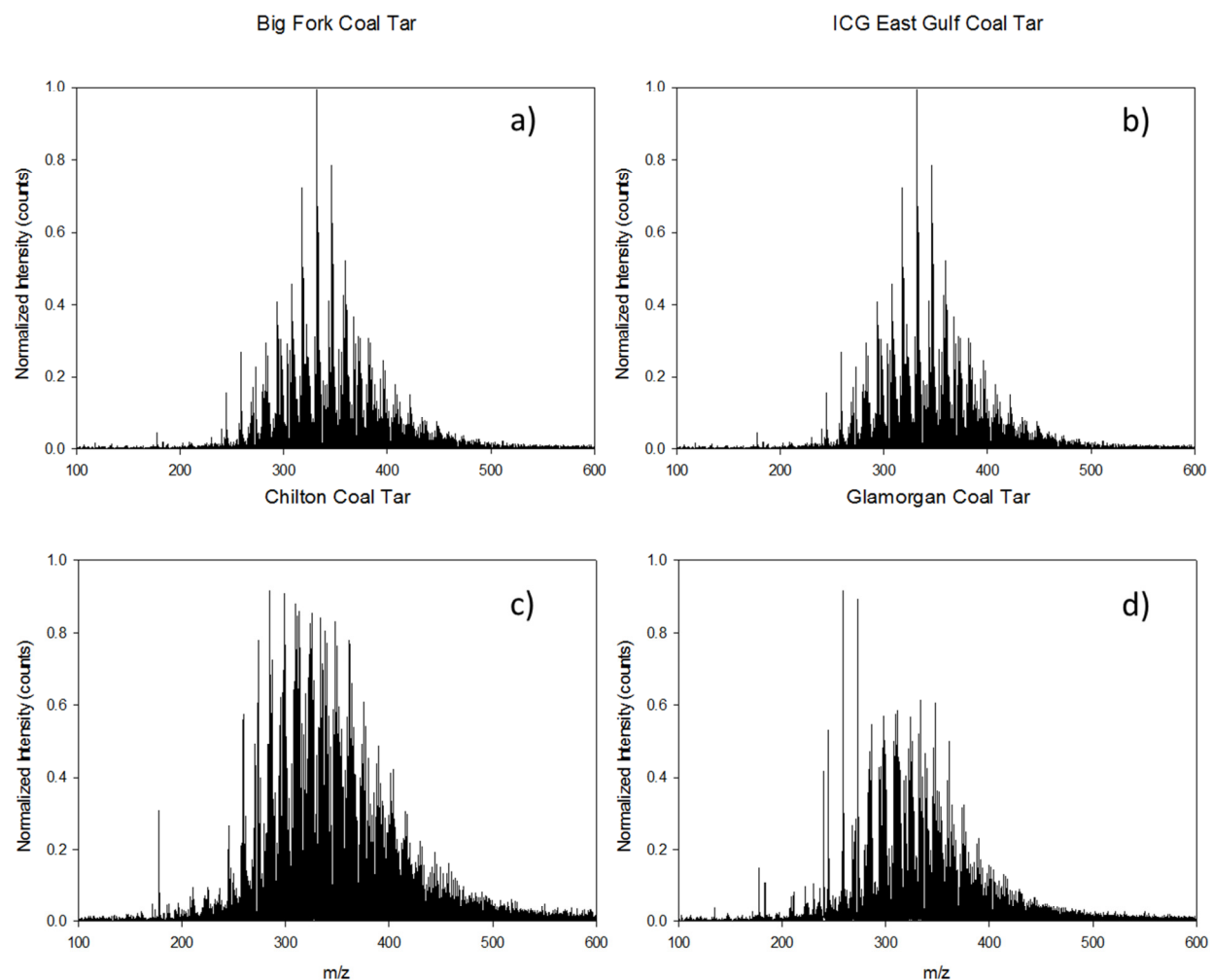


Figure 31 LDI-TOF spectra for four coals a) Big Fork (VM-29.7%) b) ICG East Gulf (VM - 18.9%) c) Chilton (VM – 35.2%) d) Glamorgan (VM - 38.9%)

Figure 31 (a-d) shows the spectra of four tar samples. Each tar sample was generated at $3\text{ }^{\circ}\text{C min}^{-1}$ in the cup confinement. The intensities on the y-axis were normalized by the maximum intensity of each test. The samples were analyzed three times and the averages of the three tests are presented in Figure 31(a-c). It has been shown that noise and standard deviations of the mass spectra decreased with increasing numbers from 10 to 100 scans¹⁰⁶ therefore, the use 500 shots produced a clean spectrum as expected. No discernible differences in the spectrum arose from a

single drop and multiple drop samples. Increasing laser power did not affect the mass spectrum of the coal tar other than increasing the signal intensity.

The MWD of each coal tar sample ranges between 200 and 450 amu in Figure 31(a-c). This is in good agreement with the Argonne premium coal tar MW data determined by FI-MS (produced at the same heating rate) and predicted in the FG-DVC model.^{63, 108} The average MW were 258.4, 284.6, 347.6, and 331.6 amu for the Glamorgan, Chilton, Big Fork and ICG East Gulf coal, respectively. The polydispersity of each tar sample was between 7.5 and 13. LDI-TOF analysis of high MW molecules has been shown to be dependent on polydispersity, especially in the presence of compounds <2,000 amu.¹¹⁶ Therefore, the underestimation of the high MW fractions in coal tar by LDI-MS was a major concern.^{105, 106} It was found necessary to reduce the polydispersity of coal derived liquids by separating large and small molecules by SEC, solvent separation, planar chromatography, or column chromatography before MS analysis to determine the limitations of the technique due to polydispersity.^{103, 110} However, this issue was shown to be absent for samples <3,000 amu.¹¹⁶ Overall, the present LDI-MS results suggest the major components in the coal tar produced in TG-GC pyrolysis experiments does not exceed m/z of 600. These results are found to corroborate the FI-MS analysis of tar produced by Argonne premium coals heated at 3 °C min⁻¹.¹⁰⁸ As stated previously, FI-MS has an upper MW detection limit of 1,200 amu. This analysis provides confidence that the MWD of coal tar determined by LDI-TOF of is comprehensive.

In summary, coal pyrolysis has been studied via TG-GC along with tar characterization via GC-MS and LDI-TOF to develop a comprehensive perspective of the reaction sequence and product distribution. The following two chapters present systematic investigations on the effects of feedstocks and pyrolysis conditions

Chapter 5: Effect of Volatile Material Content

Now that a set of TG-GC data set has been related to the pyrolysis reaction mechanism for a single coal, investigations of multiple coals will be presented to illustrate the effect of VM content of on the pyrolysis behavior. Volatile material content is the fraction of reactive material that varies for all coal samples. During coalification, volatile material decreases with depth and age due to condensation reactions (i.e. decrease in H/C and O/C). In pyrolysis, the difference in VM affects the product distribution between gas, tar, and char. In this work, eleven different coking coals were analyzed by TG. The data from these analyses will be discussed in regards to VM trends.

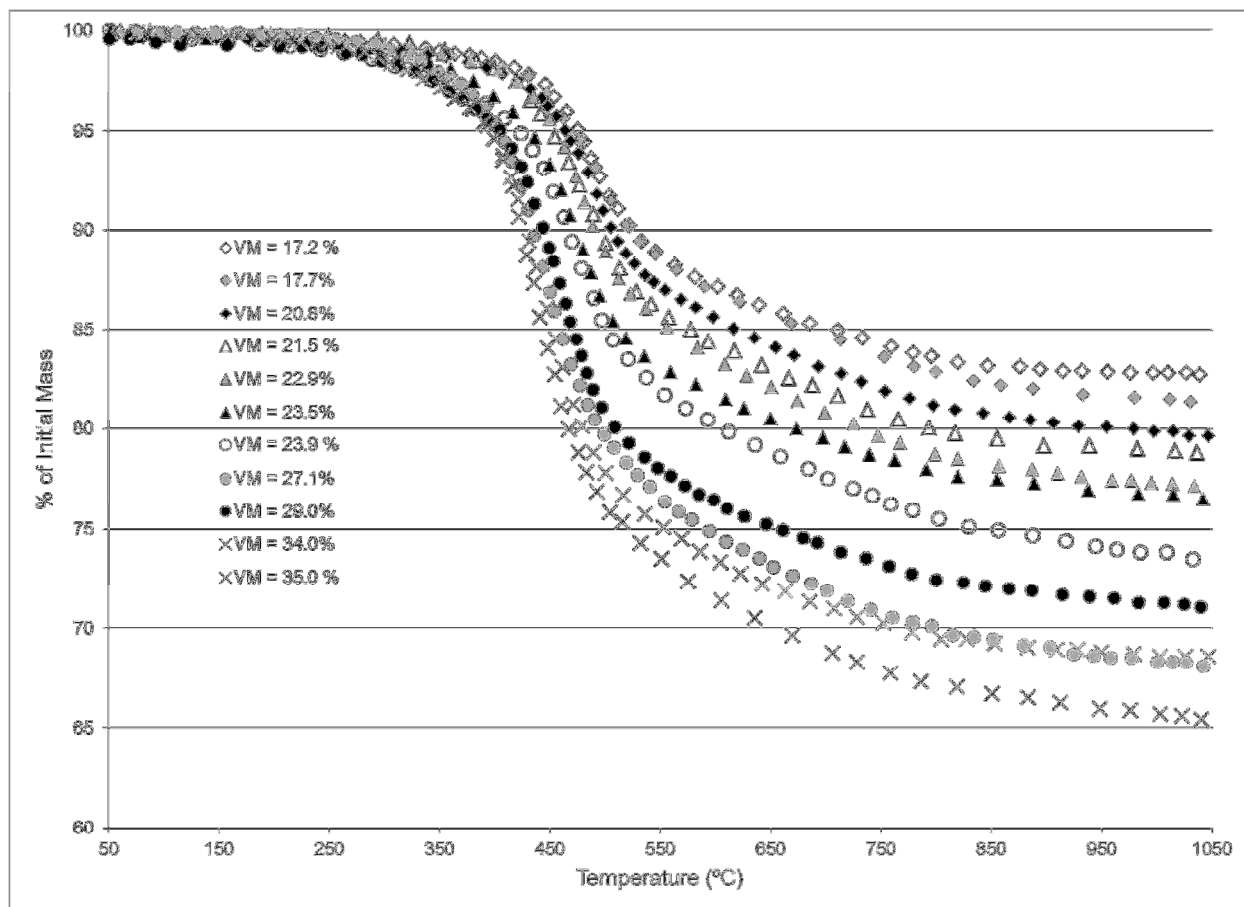


Figure 32 TG of eleven coals with varying volatile material content at $3\text{ }^{\circ}\text{C min}^{-1}$ to $1100\text{ }^{\circ}\text{C}$ in an argon environment

Figure 32 shows the TG profiles of eleven coals versus sample temperature. The eleven coals presented are actually similar in rank (79.6-84.4 wt. % C) but, vary widely in VM (17.2-35 wt. %). The TG profiles shown in Figure 32 are produced at constant pyrolysis conditions. The operating conditions are coal particles of 48 microns in diameter in a pan confinement packed to a bed density of 0.75 grams per cm³ and heated at a rate of 3 °C per minute to 1100 °C under 30 mL min⁻¹ flow of argon. Thus, the final residual mass percent (at 1050 °C) in Figure 32 is indicative of the VM content, i.e., the primary difference between the coals.

In each individual profile in Figure 32, the mass of the sample is unchanged up to 250 °C. After 250 °C, each coal sample begins to lose mass. The samples with higher VM content (> 23 wt. %) lose mass at a higher rate than the samples with lower VM content (< 23 wt. %). The mass loss is linear from 250 °C up to 360 or 380 °C (depending on coal). The mass loss between 380 °C until 510 or 530 °C (depending on the coal) is designated as primary devolatilization. Primary devolatilization is the period where tar is emitted from the metaplastic state of the coal. The coals of increasing VM (1) have a greater mass loss and (2) a higher mass loss rate during primary devolatilization. Beyond 550 °C, the metaplast begins to resolidify and produce gaseous products. The greater mass losses from increases in VM are manifested in greater tar and gas production.

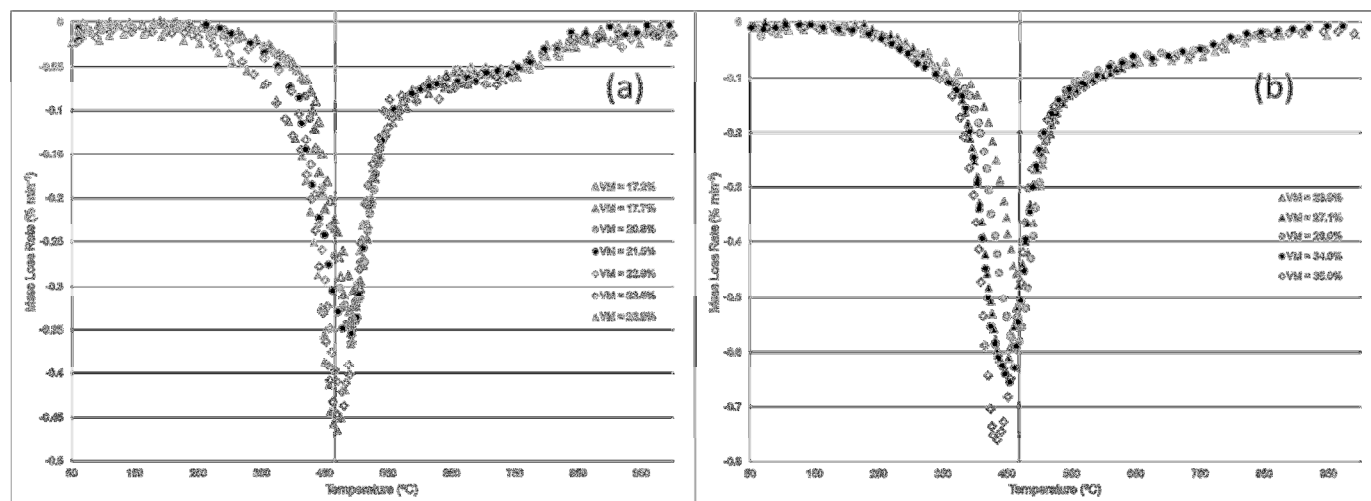


Figure 33 (a) DTG of coals with the apparent volatile production of 23.9 wt. % or less heated at $3\text{ }^{\circ}\text{C min}^{-1}$ to $1100\text{ }^{\circ}\text{C}$ in Ar (b) coals with apparent volatile production of 23.9 wt. % or more

Figure 33 (a-b) shows the rate of mass loss, or differential thermogravimetry (DTG), of the eleven tested coals. The coal samples have been split into (a) samples below 23.9% VM (low VM coals) and (b) samples above 23.9% VM (high VM coals). The sample with 23.9 wt. % VM appears on both Figure 33 (a) and (b) with a line indicating the temperature of the maximum rate of devolatilization for this coal. The effects of VM can be observed between these two plots. It can be seen that as VM increases, the maximum rate of devolatilization (peak) shifts to lower temperatures, i.e., all of the coals with $<23.9\%$ VM (Figure 33a) are to the right of the tie-line and coals with $>23.9\%$ VM (Figure 33b) are to the left of the tie-line. The trend corresponds to the increase in reactivity of the coal with increasing VM content. Furthermore, the maximum rate of devolatilization increases with increasing VM content. This observation is attributed to coals of high VM coals, which produce more tar and gas products than low VM coals. As shown for Jewell coal, tar is the dominant volatile product until the point of maximum devolatilization. Tar devolatilization is a process that is dominated by evaporation of the metaplast, therefore, is related to the MW and concentration of the metaplast. The MW of the tar is a function the

molecular structure of the parent material, which was demonstrated previously in the LDI-TOF analysis shown in Figure 31a-d. These two observations are evidence for (1) a lower decomposition temperature for higher VM and (2) a greater degree of fragmentation for higher VM (i.e., smaller fragments). At the point of maximum devolatilization, gas products like CO₂, H₂, CH₄, C₂H₆, and C₂H₄ will sharply increase due to both crosslinking and cracking reactions. From 600 to 1000 °C, a subsequent shoulder-valley is produced in DTG profile for each coal. This is the regime of cracking and coke forming reactions, which produces gaseous products. Finally, the DTG profile approaches a rate of zero.

In summary, VM effects the product distribution between solid and volatile products as well as the rates of volatile product and temperature of process events. In the following chapter, it will be shown that the VM content of the coal is important to consider in the evaluation secondary pyrolysis reactions.

Chapter 6: Investigation of Secondary Pyrolysis Reactions

Until this point, the experimental results presented have only considered the pyrolysis reaction mechanism observed in a single reaction condition. As presented in the literature review, pyrolysis condition such as heating rate, particle size, bed depth, and pressure affects the reaction mechanism and product distribution. The influences of these conditions are important for understanding large-scale pyrolysis applications. The influences of reaction confinement, heating rate, and particle size are described in separate sections of this chapter. The governing variables between these pyrolysis conditions are the transport rate or diffusion length of the volatile products formed. Each of these variables can be summed as a difference in the residence times of volatile products in the pyrolysis environment. The effect of confinement on coal pyrolysis is a unique contribution of this work, which isolates the residence time effect. The

effects of confinement on ICG East Gulf coal (VM = 18.93 wt. %) and Jewell coal (VM = 26.02 wt. %) are discussed first. In this section, ICG East Gulf coal will be referred to as low-VM coal and Jewell coal will be referred to as mid-VM coal.

6.1 Effect of Confinement

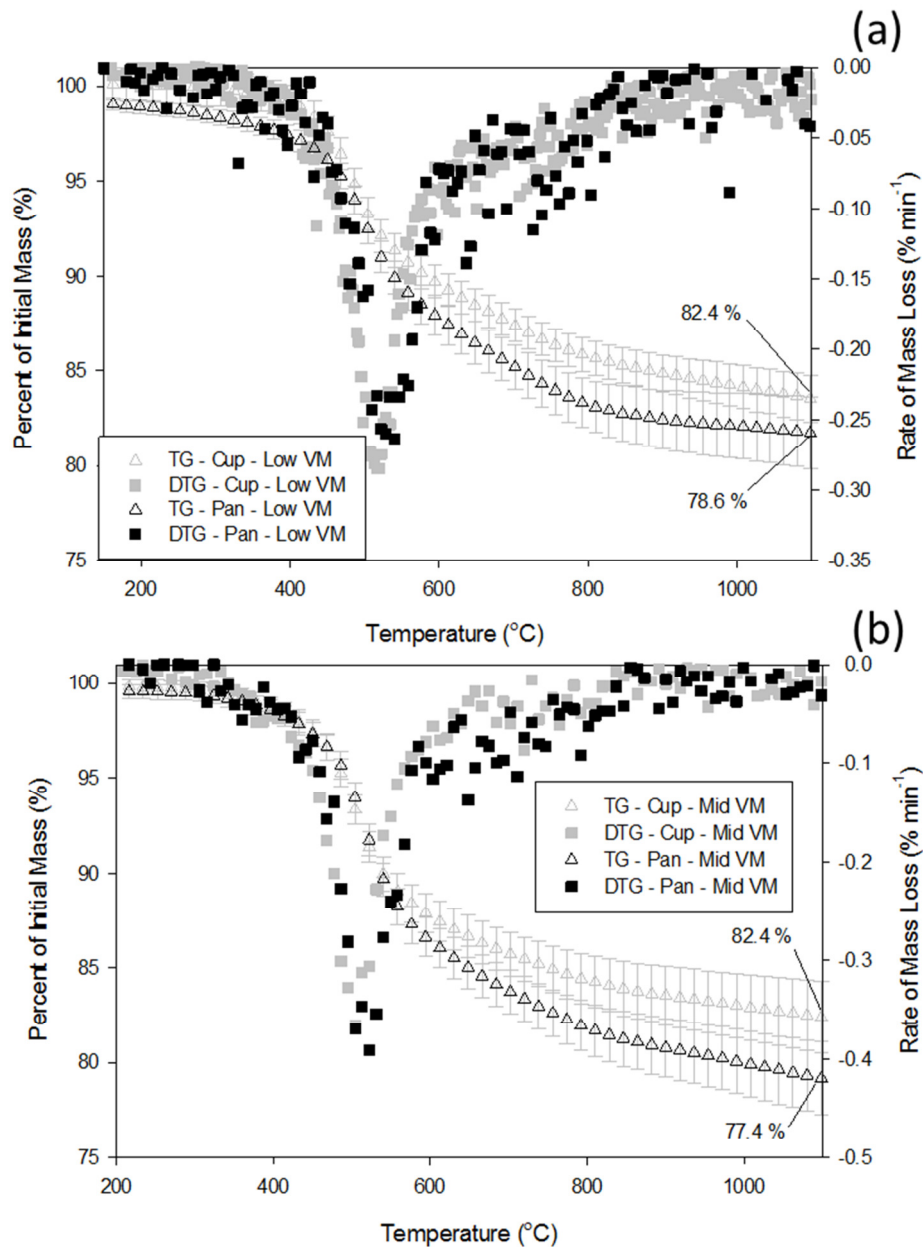


Figure 34(a) TG and DTG of low-VM heated at 3 °C min⁻¹ in pan and cup confinement (b) TG and DTG of mid-VM heated at 3 °C min⁻¹ in pan and cup confinement

Figure 34 (a-b) shows the TG and DTG profile of two coals heated in the pan and cup confinement at $3\text{ }^{\circ}\text{C min}^{-1}$. The two coals are designated as low-VM (ICG East Gulf, Figure 34a) and mid-VM (Jewell, Figure 34b) coals. The errors shown are the standard deviations based on repeated tests as discussed in the experimental section. The error arises from a combination of sample heterogeneity and experimental procedure. For each coal, the solid product yield is greater in the cup confinement than in the pan confinement demonstrating an effect of increased residence time of volatile products. Note that the TG profiles for each coal and condition resemble the well-known result for coal pyrolysis shown Figure 32, and previous works.¹¹⁷ The major peak observed between 370 and 625 $^{\circ}\text{C}$ in the DTG plot in Figure 34 (a-b) represents the primary devolatilization. The maximum rate of mass loss increases with increasing VM as expected. The maximum rate of mass loss shifts to lower temperatures as VM increases as shown previously by experiments using TGA^{118, 119} and the Gieseler test.³⁵ Metaplast resolidification occurs between 550 and 800 $^{\circ}\text{C}$ and yields gaseous products. For all coals, the DTG asymptotically approaches zero during resolidification signifying that reactions are depleting as coke is produced.

A statistical t-test using a 95% confidence interval in Figure 34 (a-b) shows that the residual mass difference between confinements for the low and mid-VM coals is significant. The effect of confinement on solid yield was observed to be greater for the mid-VM coal than the low-VM coal. In Figure 34 (a-b), the separation of the TG curves in the different confinements occurs between 520 and 550 $^{\circ}\text{C}$ for each coal. In Figure 34 (a-b), the magnitude of the DTG (rate) measurement between 550 and 800 $^{\circ}\text{C}$ is higher in the pan as compared to the cup. These effects on solid yield are due to tar species being retained for extended residence times at the solid-gas interface by the confinement, therefore reacting with each other and solid product.

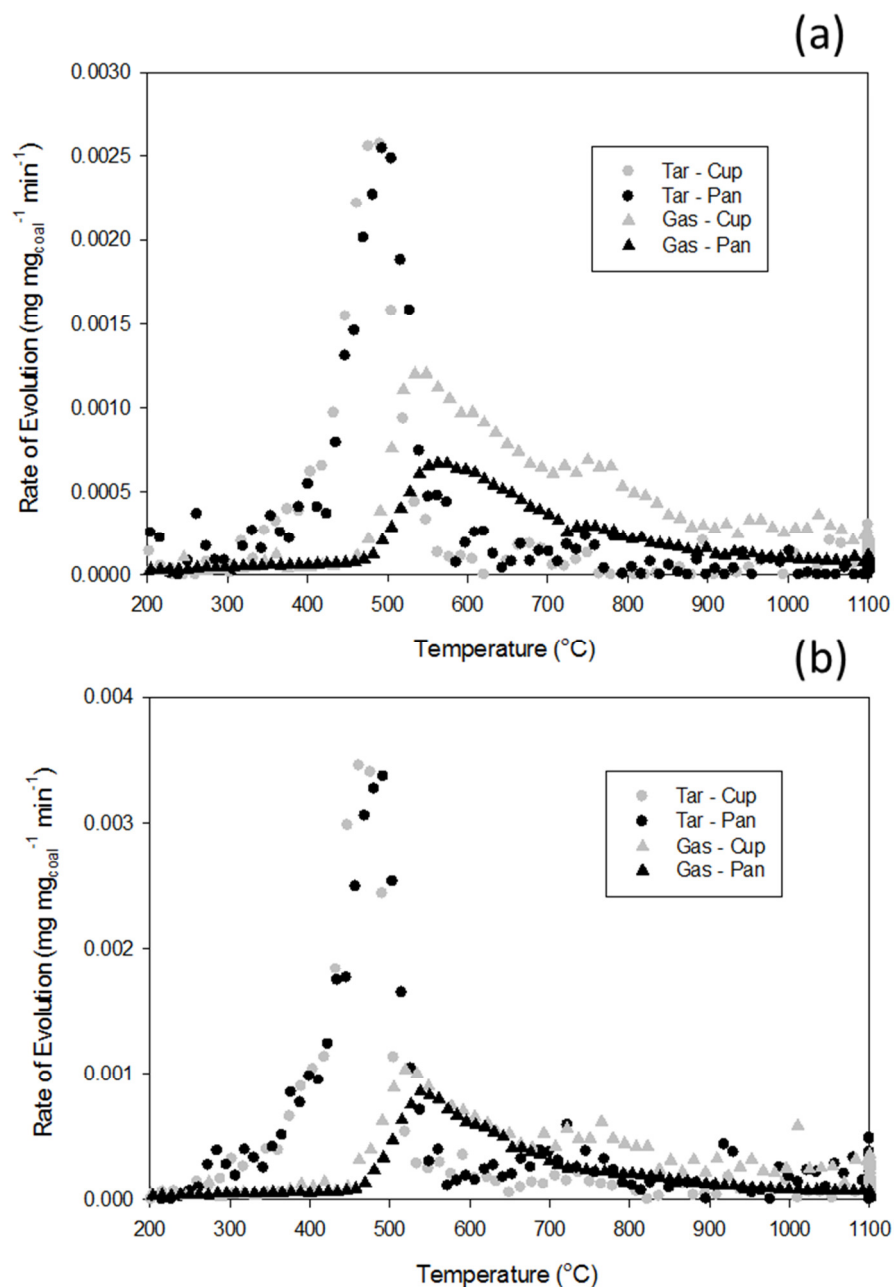


Figure 35(a) Tar and gas evolution of low-VM heated at $3\text{ }^{\circ}\text{C min}^{-1}$ in pan and cup confinement
 (b) Tar and gas evolution of mid-VM heated at $3\text{ }^{\circ}\text{C min}^{-1}$ in pan and cup confinement

Figure 35 (a-b) shows the calculated time-dependent tar and gas production profiles for low- and mid-VM coals at $3\text{ }^{\circ}\text{C min}^{-1}$ in each confinement. Tar production initiates at $225\text{ }^{\circ}\text{C}$. Tar is the only volatile product until $475\text{ }^{\circ}\text{C}$ and continues to evolve until $625\text{ }^{\circ}\text{C}$. Gas

production begins at 475 °C for both coals and confinements. The gas production rate is observed to be higher in the cup compared to the pan for both coals. It should be recalled from the TG results in multiple confinements (Figure 34) that solid yield from the two confinements begin to diverge between 520 and 550 °C. The increased gas production in the same temperature range indicates secondary reactions occurring in the cup confinement form solid and gas products. There is a 2.1 % and 2.3 % decrease in tar production in the cup as compared to the pan for the low and mid-VM coals, respectively. Table 6 shows the average product distributions in percent mass for the low-VM coal and mid-VM coal heated at 3 °C min⁻¹ per confinement.

Table 6 Average product distributions in percent by mass of the low and mid-VM coals studied in two confinements heated at 3 °C min⁻¹

| | Solid (%) | Tar and Water (%) | Gas (%) |
|--------------------------|------------------|--------------------------|----------------|
| Low-VM Coal – Pan | 78.2 ± 3.14 | 12.8 ± 4.29 | 9.0 ± 2.2 |
| Low-VM Coal – Cup | 82.3 ± 3.84 | 10.7 ± 4.37 | 7.0 ± 0.83 |
| Mid-VM Coal – Pan | 77.2 ± 3.60 | 15.9 ± 3.28 | 6.9 ± 1.1 |
| Mid-VM Coal – Cup | 82.2 ± 5.38 | 13.8 ± 4.04 | 4.0 ± 1.7 |

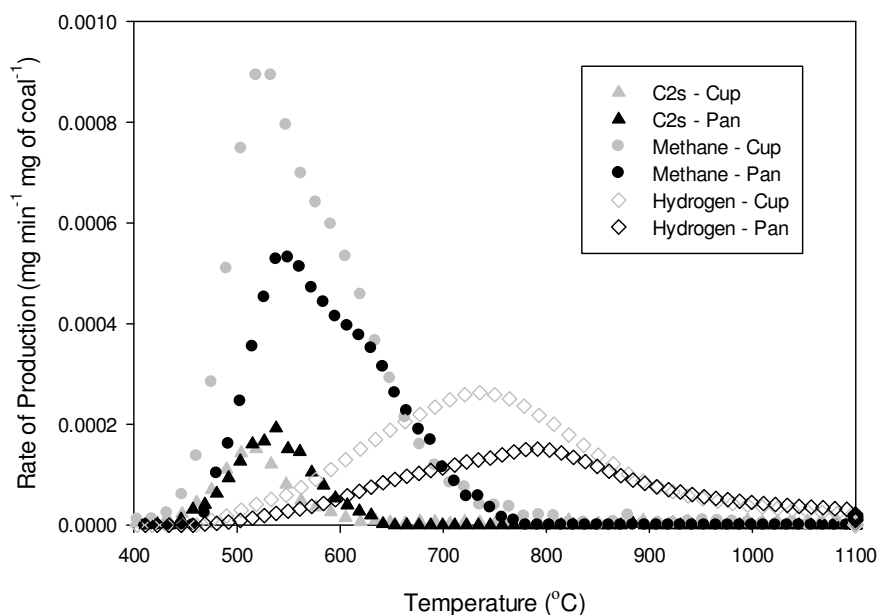


Figure 36 Hydrogen, methane, and C2 hydrocarbons (ethane and ethylene) evolution measured by gas chromatography from mid-VM heated at $3\text{ }^{\circ}\text{C min}^{-1}$ in pan and cup confinement

Figure 36 shows the evolution profiles of CH_4 , C_2 hydrocarbons, and H_2 during pyrolysis at $3\text{ }^{\circ}\text{C min}^{-1}$ for the mid-VM coal in both confinements. The total H_2 production is 30% higher in the cup compared to the pan. Increased rate of H_2 production is observed between 475 to 840 $^{\circ}\text{C}$ in Figure 36. Hydrogen gas is produced from recombination reactions during PAH growth near the solid-gas interface and integration of tar into the coke product.³² The total production of CH_4 is 40% higher from the cup than from the pan. The increased rate of CH_4 production occurs between 475 and 640 $^{\circ}\text{C}$. Throughout the tar evolution sequence, the concentration of hydrogen donor species in the metaplast decreases. As discussed in the review, the coal molecule loses saturated functional groups and becomes more aromatic, which has been measured by NMR.^{45, 63} The two main CH_4 forming reactions are thermal cracking of paraffinic groups and demethylation which is associated with moderate temperature crosslinking.⁶³ Thermal cracking

will be favored in the gas as shown in the Rice-Kossiakoff mechanism, where radicals tend to break down all the way to $\text{CH}_3\bullet$ or $\text{H}\bullet$ due to high temperature and lack of hydrogen-donor species. Therefore, suspending tar products in the gas phase within the pyrolysis environment is expected to lead to more CH_4 production.

Table 7 Total production of gas species on a mg per mg of initial coal mass basis at $3\text{ }^\circ\text{C min}^{-1}$ in each confinement for the low and mid-VM coal and the p-value between the different conditions

| | Low-VM –Pan | Low-VM –Cup | Mid-VM – Pan | Mid-VM – Cup |
|-----------------|---------------------|---------------------|---------------------|---------------------|
| Hydrogen | 5.6×10^{-3} | 7.3×10^{-3} | 4.7×10^{-3} | 5.2×10^{-3} |
| p-value | | 1.2×10^{-2} | | 0.55 |
| Methane | 6.6×10^{-3} | 9.4×10^{-3} | 6.9×10^{-3} | 9.6×10^{-3} |
| p-value | | 0.10 | | 0.26 |
| Ethane | 0.9×10^{-3} | 0.6×10^{-3} | 1.2×10^{-3} | 0.7×10^{-3} |
| p-value | | 2.9×10^{-2} | | 9.0×10^{-4} |
| Ethylene | 2.0×10^{-4} | 2.0×10^{-4} | 2.0×10^{-4} | 2.0×10^{-4} |
| p-value | | 0.84 | | 0.78 |

Table 7 shows the average total production of gaseous products from the pan and cup confinements for low- and mid-VM coals. The C_2 hydrocarbon production is greater in the pan than in the cup and occurs at a slightly higher temperature (shown in Figure 36). Due to the high coking propensity of C_2 hydrocarbons, it is possible for C_2 hydrocarbon to be involved in coke forming reactions above $490\text{ }^\circ\text{C}$ and thereby decrease the overall C_2 production in the cup.⁷⁹ The mechanism of how paraffin species are incorporated into PAH and coke species are discussed in previous works.^{79, 120} However, C_2H_6 consumption will be discussed more in future sections. The greatest difference is the yield of C_2H_6 and CH_4 between confinements for both coals. The pan

confinement produces more C_2H_6 and less CH_4 than the cup. The reduction of C_2H_6 production in the cup only accounts for 10 and 20% of the increased CH_4 production for low- and mid-VM coal, respectively. Therefore, approximately 80-90% of the increase in CH_4 must come from gas-phase cracking or demethylation of tar species. Ethylene production between 425 and 625 °C appears unaffected by increased residence time for both coals. This indicates that C_2H_4 is not impacted by the secondary reactions.

In summary, increases in coke, CH_4 , and H_2 production and decreases in tar and C_2H_6 production are a result of the secondary reactions of suspended tar in the cup confinement. This is in agreement with what was observed for increased coal bed thickness.⁸³ These reactions are likely a combination of gas phase thermal cracking of tar species followed by integration into solid products. Now the same investigation will be presented for a high-VM coal, which gives a very different result.

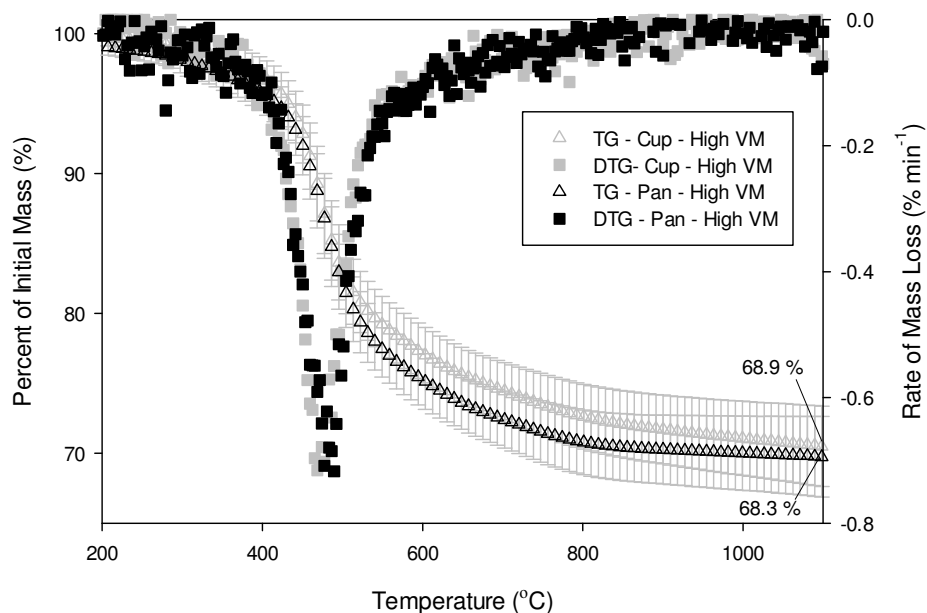


Figure 37 TG and DTG of High-VM heated at $3\text{ }^{\circ}\text{C min}^{-1}$ in pan and cup confinement

Figure 37 shows the TG and DTG profile for the high-VM coal (Glamorgan, VM - 38.94 wt. %) heated in the pan and cup confinement at $3\text{ }^{\circ}\text{C min}^{-1}$. The effect of confinement on solid yield for the high-VM coal is statistically insignificant. The ineffectiveness of the confinement on the high-VM coal is attributed to the increased release rates resulting in a residence time too short for the extent secondary reactions to be observed. The rate constants for secondary tar cracking reactions between 500 and 600 $^{\circ}\text{C}$ are on the order of 10^3 s^{-1} .⁷¹ The residence times in the cup for the mid and low-VM coals are approximately 0.35 seconds, which is sufficient to observe impacts of secondary reactions. The secondary reactions occur to a minimal or insignificant extent for the high-VM coal where the residence time is only 0.22 seconds. The minimum residence time required to observe a significant effect on the solid carbon yield is 0.27 seconds (the residence time for the low-VM coal in the cup confinement at $3\text{ }^{\circ}\text{C min}^{-1}$). Therefore, the phenomena observed in the low and mid-VM are not observed for the high-VM coal.

Table 8 shows the average product distributions in percent by mass for the high-VM coal heated at $3\text{ }^{\circ}\text{C min}^{-1}$ per confinement. Gas production is slightly higher in the pan than in the cup confinement. Table 9 shows the average total production of gaseous products in the pan and cup confinements for the high-VM coal. The pan confinement results in 35% higher H_2 production than the cup. Methane yield from the pan and cup are the same. All of these observations oppose what has been observed for the low- and mid-VM coal in regards to the effect of confinement.

Table 8 Average product distributions in percent by mass of the high-VM coal per confinement heated at 3 °C min⁻¹

| | Solid (%) | Tar and Water (%) | Gas (%) |
|---------------------------|------------------|--------------------------|----------------|
| High-VM Coal – Pan | 68.4 ± 1.5 | 26.2 ± 7.4 | 5.4 ± 0.68 |
| High-VM Coal – Cup | 69.0 ± 1.3 | 25.1 ± 7.9 | 5.9 ± 0.98 |

Table 9 Total production of gas species (mg/mg of initial coal mass) at 3 °C min⁻¹ in each confinement for the high-VM coal and the p-value between the different conditions

| | High-VM Pan | High-VM Cup |
|-----------------|------------------------|------------------------|
| Hydrogen | 7.0×10 ⁻³ | 5.2×10 ⁻³ |
| p-value | | 5.6×10 ⁻⁵ |
| Methane | 1.3×10 ⁻² | 1.3×10 ⁻² |
| p-value | | 0.66 |
| Ethane | 0.9×10 ⁻³ | 1.0×10 ⁻³ |
| p-value | | 0.3277 |
| Ethylene | 2.0×10 ⁻⁴ | 3.0×10 ⁻⁴ |
| p-value | | 1.4×10 ⁻³ |

In summary, the confinement has been used to extend volatile residence time in the pyrolysis environment. Extended residence time has been shown to cause tar cracking reactions above 550 °C which produces CH₄, H₂, and secondary coke. However, the effect of confinement is contingent on the devolatilization rate, which is inherent to coal VM content. Overall, this shows that residence time of the volatile products in the pyrolysis environment is the governing

parameter for secondary reaction extent, i.e., long tar diffusion lengths and slow transport rates will favor secondary reactions. The following sections provide further evidence for this statement using other variation in pyrolysis reaction conditions.

6.2 Effect of Particle Size

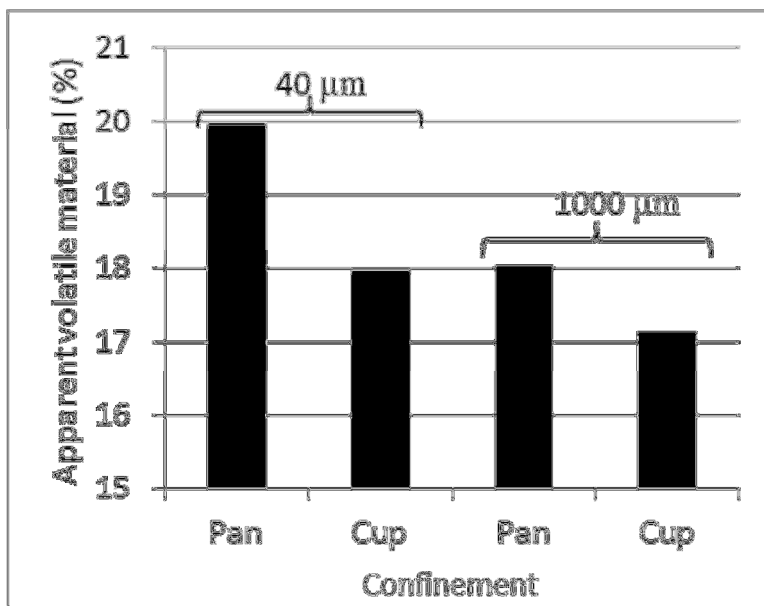


Figure 38 Comparison of total volatile material produced for 40 and 1000 micron coal particles in two confinements

The effect of particle size on coal pyrolysis has been a topic studied in much earlier works on coal.¹²¹ Particle size governs heat transfer, which correlates to the reaction profile on the radius of the particle. The Biot number for particles less than 300 microns in diameter is less than 0.1 therefore, the temperature difference across the particle is negligible. In addition, smaller particles are in a kinetically-controlled regime, which results in a higher yield of volatile products because devolatilization is not inhibited by intraparticle transport limitation. A low-VM coal (VM-18.8 wt. %) was analyzed via the TG-GC system for 40 and 1000 micron coal particles in the pan and cup confinements. The increase in mass loss due to the volatile production of

smaller particles is demonstrated in Figure 38. For each reaction confinement smaller particles yielded a 9 – 14 wt. % increase in volatile material produced. Therefore, longer intraparticle diffusion lengths of 1000 microns are responsible for the increase of solid carbon yield from coal pyrolysis.

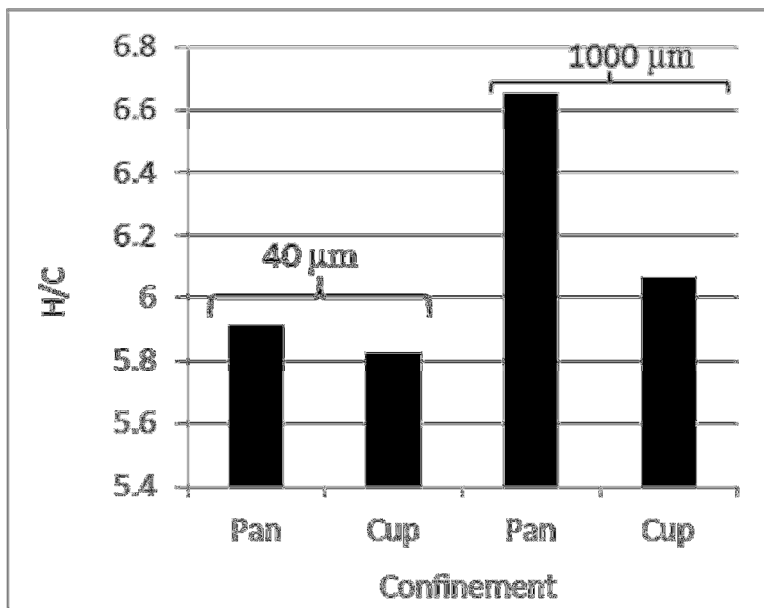


Figure 39 Comparison of H/C ratio of the gas products for 40 and 1000 micron coal particles in each confinement

In Figure 39, the cumulative H/C ratios of gaseous products for two particle sizes in two reaction confinements determined by GC analysis are shown. An increase in the cumulative H/C ratio of gaseous products is observed to be higher for larger particles in either reaction confinement. This is further evidence of the increased intraparticle residence time in large particles increasing the extent of secondary tar cracking reactions. The results of particle size investigation agree with that of confinement. It is concluded that increases of intraparticle or interfacial residence times of volatile products will (1) increase solid yield and (2) increase the H/C of the gaseous product.

6.3 Effect of Heating Rate

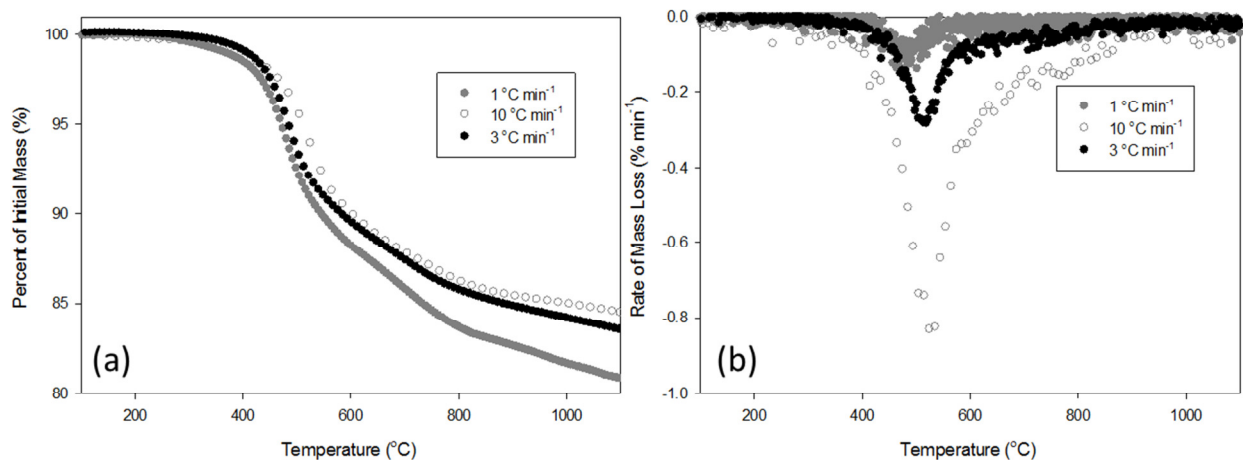


Figure 40(a) TG and (b)DTG of low-VM coal at heated at 1, 3 and 10 °C min⁻¹ in argon

Figure 40 (a-b) shows TG and DTG results from pyrolysis of a low-VM coal at 1, 3 and 10 °C min⁻¹ in a single confinement. There is no universal correlation between residual mass with heating rate observed in this work even though Figure 40a shows an increase in residual mass with increasing heating rate. The initiation of primary devolatilization shifts to lower temperatures with increased heating rate. Figure 40b shows that the maximum rate of devolatilization shifts to a higher temperature by 40 °C as heating rate increases by a factor of 10. This shift to a higher temperature with increasing heating rate agrees with accounts in the literature using TGA^{118, 119} and other apparatuses such as wire-mesh reactors, electrical strip furnaces⁸⁶ and predictions in FLASHCHAIN⁸⁴. The shift of peak devolatilization to a higher temperature is attributed to a delay in the onset of the metaplast caused by a negative relationship of heating rate and low-temperature crosslinking reactions.^{63, 84} The DTG increases by a factor of 10 as the heating rate increases from 1 to 10 °C min⁻¹. The higher rate of mass loss has been attributed to an increase of tar and CH₄ production during primary devolatilization.³⁵

6.4 Effect of Heating Rate and Confinement

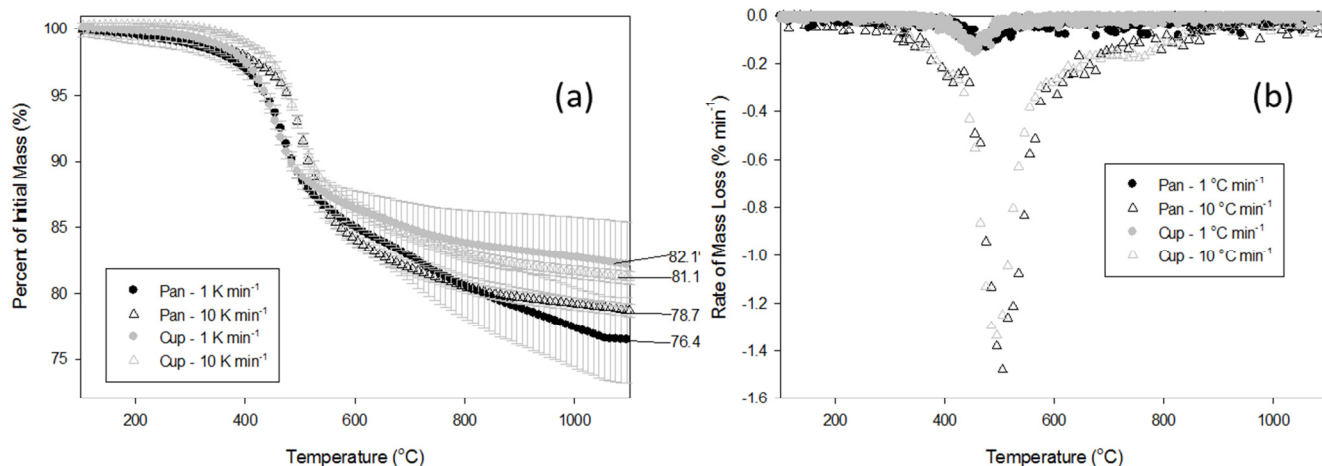


Figure 41 (a) TG and (b) DTG of Mid-VM heated at 1 and 10 °C min⁻¹ in pan and cup confinement

Figure 41 shows the TG of the mid-VM coal heated at 1 and 10 °C min⁻¹ in both confinements. The effect of confinement on the solid residual persists at heating rates of 1 to 10 °C min⁻¹ (not statistically significant at 10 °C min⁻¹). Figure 41 shows the DTG of the mid-VM coal heated at 1 and 10 °C min⁻¹ in both confinements. The residence time in the cup confinement ranges from 0.11 and 1.0 seconds for the 1 and 10 °C min⁻¹ cases, respectively. Table 10 shows the solid yield differences between the cup and pan confinements for the low and mid-VM coals at 1, 3, and 10 °C min⁻¹. The difference in solid yield in the cup is inversely proportional to heating rate (i.e., it increases as the heating rate decreases). The extents of secondary reactions decrease due to increased transport rates. In the case of secondary tar reactions, a faster tar evolution rate would decrease the residence time of chemical species above the sample. The separation of the TG curves of each confinement shown in Figure 41 occurs between 520 and 550 °C for the mid-VM coal heated at 1 and 10 °C min⁻¹. This shows that at vastly different release transport rates (from 1, 3, and 10 °C min⁻¹) the temperature of separation due to reaction at the gas-solid interface in the cup confinement consistently occurs within a 30

°C temperature span for the mid-VM and low-VM coal, respectively. This confirms that the temperature range of secondary reactions in the cup confinement is between 520 and 550 °C.

Table 10 Difference in solid yield between cup and pan for the low, mid and high-VM coal at 1, 3, and 10 °C min⁻¹

| Heating Rate, °C min ⁻¹ | Mid-VM (%) | Low-VM (%) | High-VM (%) |
|------------------------------------|------------|------------|-------------|
| 1 | 5.7 | 5.4 | 3.7 |
| 3 | 3.2 | 1.8 | 0.7 |
| 10 | 2.4 | 0.6 | 0.6 |

Chapter 7: Investigation of Secondary Tar Products

To review, the TG-GC experimental set-up has been demonstrated to have the ability to measure time-resolved pyrolysis products to a high degree of mass closure. Coals of three different VM compositions were analyzed by TG-GC to evaluate secondary pyrolysis reactions. The variation of confinement, heating rate, and particle size for coal pyrolysis establishes a means of comparing similar systems with variation only in the tar residence time. These perspectives ultimately offered the ability to discern between primary and secondary pyrolysis reactions. The pyrolysis product distributions of low- and mid-VM coals were affected by conditions of extended secondary reactions. The high-VM experienced an insignificant extent of secondary reaction due to rapid transport rates of volatile species. However, to this point, only solid and gas yield have been evaluated with regard to the extent of secondary tar reactions. The secondary reactions will undoubtedly alter the distribution of escaped tar products as well, for instance through cracking and PAH growth reactions discussed in Chapter 2. The tar products produced from secondary reactions are called “secondary tar products”. This chapter provides a detailed characterization of secondary tar products from systems of various tar residence times.

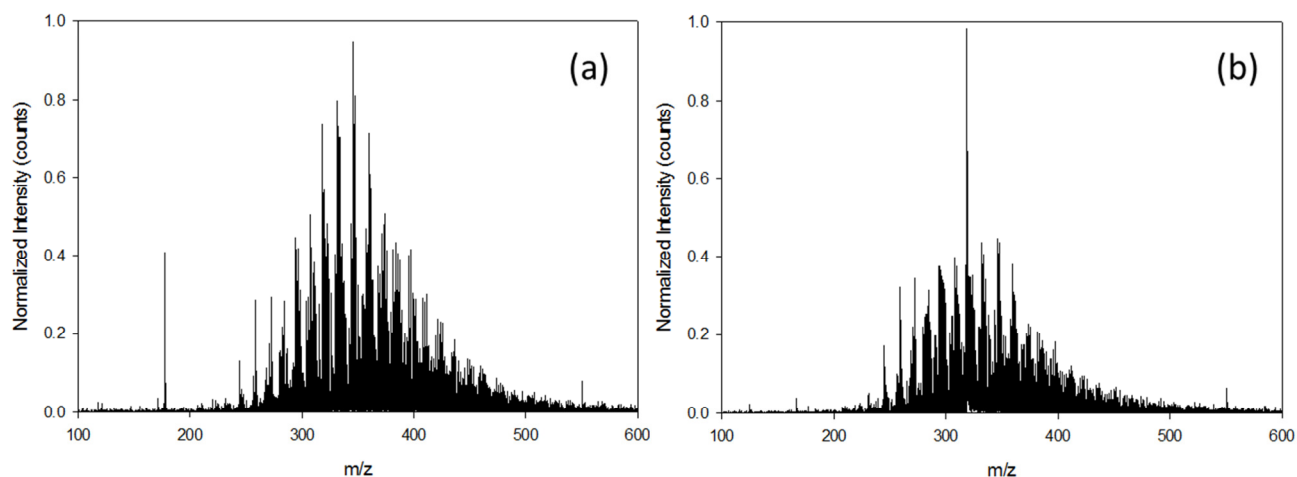


Figure 42 LDI-TOF spectra for Jewell coal tar produced in the (a) pan and (b) cup confinement

The coal tar produced from Jewell coal pyrolysis in two reaction confinements were analyzed by LDI-TOF. Figure 42 (a-b) shows two spectra of tar produced from the Jewell coal in the pan and cup confinements at $3\text{ }^{\circ}\text{C min}^{-1}$. The spectra of the Jewell coal tars are similar to the previous coal tars shown in Section 4.4. However, it is observed that the MWD of tar produced in the cup shifted to slightly lower MW as compared to the tar produced in the pan. The average MW from the cup and pan were 318.6 and 345.6 amu, respectively. It is found that the tar produced in the pan had a higher polydispersity index. The polydispersity of tar was 7.6 and 8.5 from the cup and pan, respectively. The shift to a lower MW and lower polydispersity for the tar from the cup is attributed to enhanced cracking and incorporation of high MW tar species into the coke product during pyrolysis. Meanwhile, the pan confinement favors devolatilization and disfavors secondary reactions when compared to the cup confinement. Therefore a more expansive range of decomposition products are released including heavy MW molecules which have experienced less cracking in the vapor phase. The largest species detected in coal tar is 550 amu (shown in Figure 42a-b).

Table 11 Average MW of Jewell tar produced at three different heating rates measured by LDI-TOF

| Avg. MW (amu) | |
|-------------------------|---------|
| 1 °C min ⁻¹ | 267.558 |
| 3 °C min ⁻¹ | 318.581 |
| 10 °C min ⁻¹ | 345.671 |

Tars produced at heating rates of 1 and 10 °C min⁻¹ in the cup confinement were also analyzed by LDI-TOF. The average MW for tar produced at 1, 3, and 10 °C min⁻¹ are shown in Table 11. The MWD were similar between the three heating rates. However, it was found that the average MW varies by 15-32 amu between the three heating rates which is a greater variation than the standard deviation determined for the measurement technique. It was found that the average MW of the tar increases with increasing heating rate in agreement with literature, even at a much shorter range of heating rates.^{63, 84, 85} The decrease in MW as heating rate decreases attributed to longer tar residence time leading to more extensive gas phase cracking reactions. This corroborates the observed effect of confinement on secondary tar cracking reactions. However, the comparison to confinement is not direct because changing the heating rate can also affect the pyrolysis reaction mechanism as well as intraparticle residence time.

Differences were detected by GC-MS in speciation between coal tars generated from the cup and pan confinements (list of identified compounds are given in the Appendix). A qualitative comparison between samples was performed. In the TG-GC effect of confinement study, it was shown that the increase of volatile residence time at the solid-gas interface increased solid carbon, H₂, and CH₄ production. From GC-MS analysis, the tar produced from the cup confinement was found to have a lower molar H/C ratio (1.50) than tar from the pan (1.55) for

low and mid-VM coals. Specifically, the cup yields more pyrene, indene, indanol, and naphthalene derivatives indicating tar cracking at the solid-gas interface during the increased residence time. For high-VM coals, the tar produced in the pan (1.55) was found to have a lower molar H/C ratio than the cup (1.57) which is the opposite finding with the lower VM coals. It was noted that difference in the molar ratios is smaller than in the previous comparison. This observation in the tar products of high-VM coal is attributed to the ineffectiveness of confinement on high-VM coal pyrolysis.

Another confinement trend from the tar analysis involves nitrogen and sulfur species. It was found that the tar produced in the cup confinement contained 26 distinct nitrogen species and 5 distinct sulfur species. The tar produced in the pan confinement was found to contain 10 distinct nitrogen species and 2 sulfur species. However, the total concentrations of nitrogen and sulfur species between the two confinements were nominally the same. The decrease in nitrogen species in tar at extended residence times is an interesting observation because it suggests that the nitrogen and sulfur species are prone to experiencing secondary decomposition in the extended residence time in the solid-gas interface. This is attributed to C-S and C-N bonds being more labile than C-O and C-C bonds, as shown in Table 2. Nitrogen molecules coal tar have been shown to undergo secondary reactions in the gas phase to produce hydrogen cyanide (HCN, not detected by μ GC).⁶¹ Collectively the tar characterization between the two confinements is evidence that tar experienced further thermal cracking in extended residence times of nominally 0.35 seconds in the solid-gas interface.

Chapter 8: Investigation of Biomass Pyrolysis

To review, in-situ techniques were able to highlight the pyrolysis behavior of different coals and effect of secondary pyrolysis reactions in the solid-gas interface. Ex-situ

characterizations must be used for determining tar composition. Laser ionization and chromatographic MS techniques suggest that coal tar experienced further thermal cracking at extended residence times of nominally 0.35 seconds in the solid-gas interface. This was inferred by the fact that decreases in the average MWD of the tar, decreases the H/C ratio of the tar, and results in a broader distribution of nitrogen and sulfur species for pyrolysis tars of extended residence time in the solid-gas interface. This concluded our insights in secondary coal pyrolysis reactions. In this chapter, the focus will be shifted to biomass pyrolysis analyzed by the TG-GC technique along with an additional in-situ technique used to monitor changes in surface functional groups during pyrolysis.

8.1 Thermogravimetry on Pecan Shell Pyrolysis

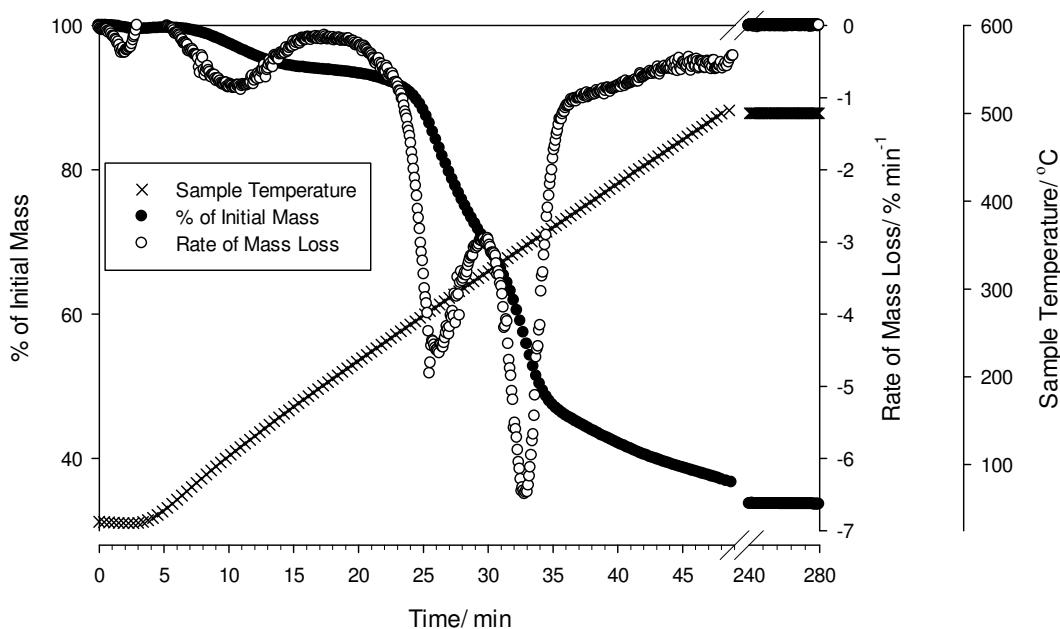


Figure 43 TG of pecan shells heated at $10\text{ }^{\circ}\text{C min}^{-1}$ to $500\text{ }^{\circ}\text{C}$ in a N_2 atmosphere

Figure 43 shows TG results for pecan shell pyrolysis at $10\text{ }^{\circ}\text{C min}^{-1}$ and held at $500\text{ }^{\circ}\text{C}$ for 4 hours. The percent mass loss with respect to the initial feedstock weight (99.6 mg), the rate

of mass loss ($\% \text{ min}^{-1}$), and the sample temperature as a function of time is shown. The majority of the mass loss occurred before reaching the peak temperature of 500 °C. The slight weight loss during the initial 10 minutes ($<100 \text{ }^\circ\text{C}$) results from the evaporation of water. The xylan of hemicellulose degrades at 150-300 °C contributing to the mass loss between 20 and 30 minutes.⁴⁹ Subsequently, cellulose decomposes at 280-350 °C into volatile tar products producing the mass loss between 30 and 35 minutes.⁴⁹ Hemicellulose and cellulose decompose by 350 °C.¹²² Lignin undergoes chain fragmentation primarily between 300-480 °C to release monomeric phenol units into the vapor phase.⁴⁹ Lignin is thermally more stable and affords higher char yield than cellulose or hemicellulose.⁴⁰

The major mass loss at 210-370 °C is accompanied by two sharp peaks at 278 °C and 345 °C shown as the mass loss rate (see open circles in Figure 43). The mass loss rate reaches a maximum in this temperature range because of tar evaporation, which contains heavy hydrocarbons and oxygenated hydrocarbons.⁵² The remaining weight of the solid stabilized at 400-500 °C, and the mass loss rate plateaued approximately 10 minutes after reaching the peak temperature of 500 °C. Over a 4 hour period at 500 °C, only 3.5 % of the initial mass is lost, indicating that 96.5 % of all reactions have completed within 60 minutes of pyrolysis. These observations are in agreement with other reported TGA and DTG analyses of pecan shell decomposition.¹²²

8.2 Gas Chromatography on Pecan Shell Pyrolysis

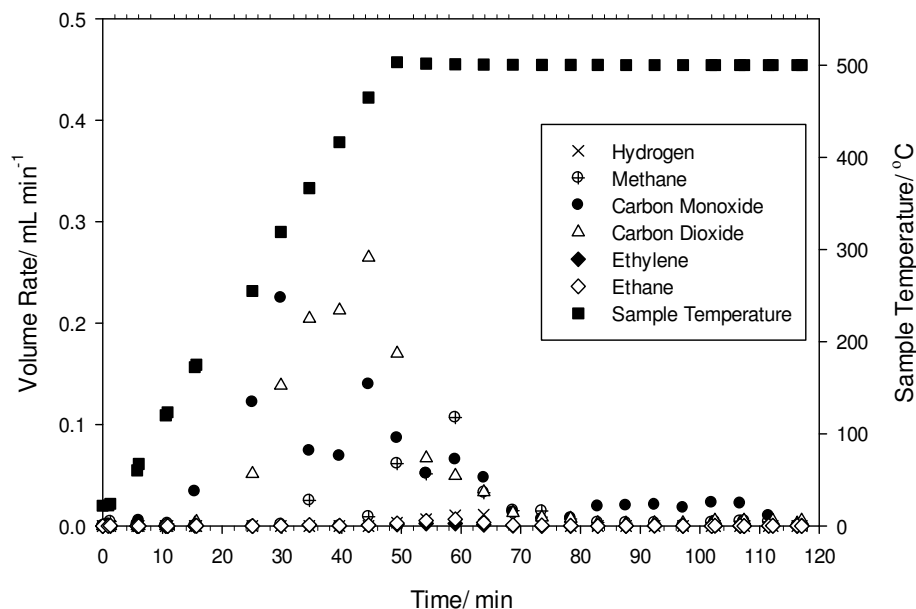


Figure 44 GC measurements of pecan shells pyrolysis gas products during heating at $10\text{ }^{\circ}\text{C min}^{-1}$ to $500\text{ }^{\circ}\text{C}$ in a N_2 atmosphere

Figure 44 presents the gas product evolution rate (in mL min^{-1}) and temperature as a function of time from pecan shell pyrolysis. Figure 44 shows the onsets of evolution for CO at $170\text{ }^{\circ}\text{C}$ and CO_2 at $255\text{ }^{\circ}\text{C}$. Within this temperature range, cellulose and hemicellulose decompose into monomers that undergo decarbonylation and decarboxylation reactions to yield CO and CO_2 .⁵² Carbon dioxide increased with temperature and reached a maximum at $460\text{ }^{\circ}\text{C}$. Carbon monoxide had three peaks: one at $320\text{ }^{\circ}\text{C}$, a second at $460\text{ }^{\circ}\text{C}$ coinciding with the peak of CO_2 , and the third at $500\text{ }^{\circ}\text{C}$ coinciding with the peak of CH_4 . In Figure 44, CO evolution at $320\text{ }^{\circ}\text{C}$ is attributed to hemicellulose and cellulose, while CO evolution at $460\text{ }^{\circ}\text{C}$ originates from cellulose.⁴⁰ The CO_2 evolution at $460\text{ }^{\circ}\text{C}$ is attributable to cellulose and lignin.⁴⁰ Char formation from lignin and the cellulose/hemicellulose decomposition products contribute to the CH_4 peak at $500\text{ }^{\circ}\text{C}$ in Figure 44. Evolution of CH_4 initiated at $360\text{ }^{\circ}\text{C}$, coinciding with the peak rate of

mass loss (shown by DTG in Figure 43). Therefore, CH₄ likely originated from cleaving of methyl groups or the secondary cracking of heavy tars as cleaving from the char surface, i.e., breaking a C-C bridge.^{44, 52} At 415 °C, C₂H₆ and C₂H₄ are observed in Figure 44. Hydrogen production begins at 500 °C, causing the H/C ratio of char product to progressively decrease. Lignin is the largest contributor to char and H₂ products⁴⁰; however, hemicellulose derivatives could produce H₂ near 500 °C.⁴⁴

8.3 Tar and Gas Evolution Fits from Pecan Shell Pyrolysis

As seen for pyrolysis of Jewell coal, the combination of TG and GC with mass closure can lead to accurate tar evolution profiles. In this analysis, the resolution of the evolution profiles is limited by the frequency of the GC measurements. It was desired to fit the time-resolved evolution data to known functions of temperature described in the Experimental Procedure and Methods. Gaussian fits of DTG curves has been employed to estimate the contributions of cellulose, hemicellulose, and lignin components for biomass pyrolysis kinetics.¹²³ However, the only available report on the deconvolution of specific gas species is on pine sawdust.¹²⁴ Implementation of this technique to time-resolved tar evolution is a unique contribution from this work. The contribution of the cellulose, hemicellulose, and lignin were deduced from the multiple distributions of a specific gaseous or tar species profile. The existing knowledge of temperature-dependent behavior of functional groups and condensation of char product will allow the connection between gas, tar, and char compositions.⁴⁵

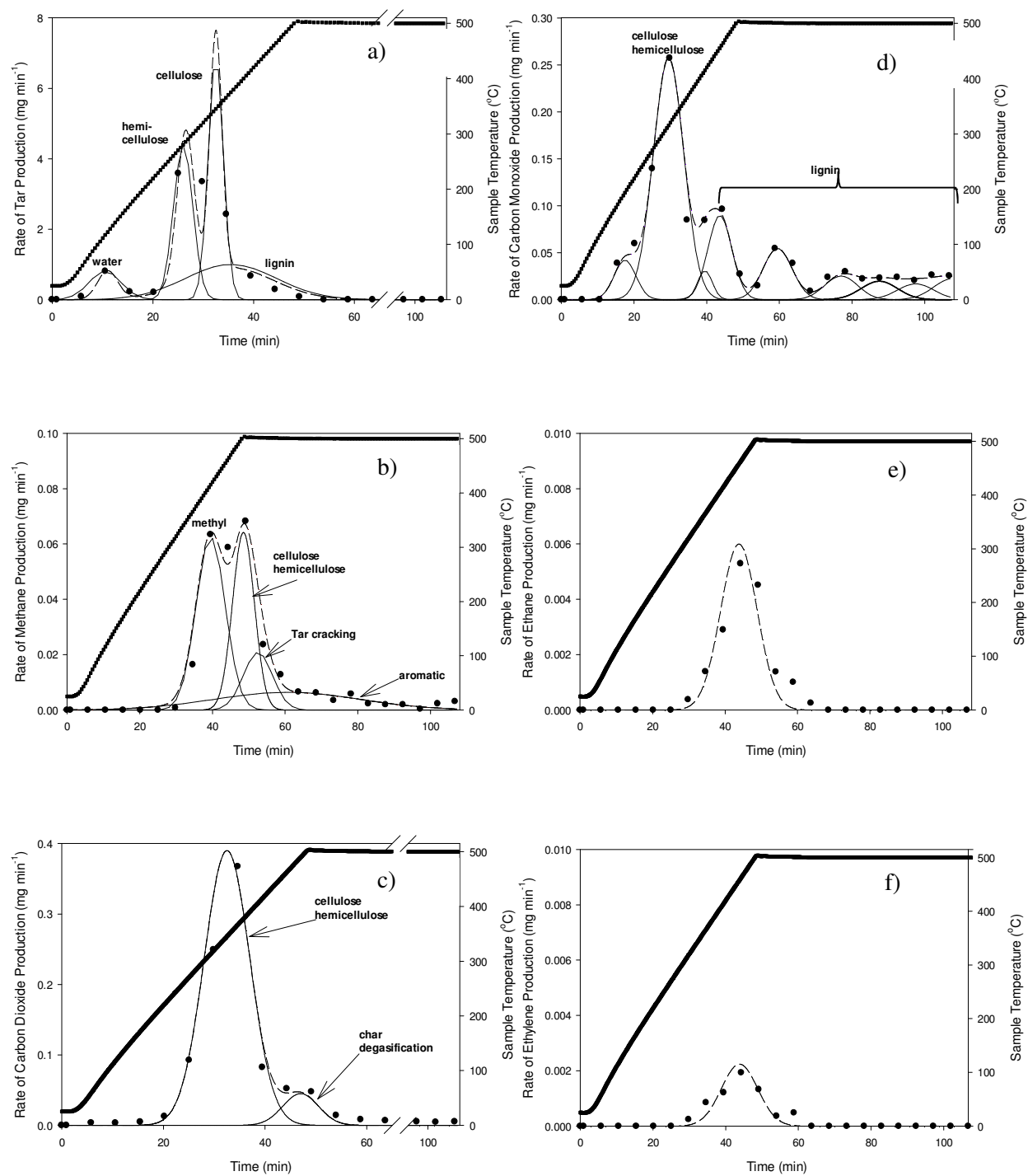


Figure 45 Empirical (points) and predicted (dash lines) rate profiles of methane, carbon monoxide, carbon dioxide, ethane, ethylene, and tar during pecan shell pyrolysis at $10\text{ }^{\circ}\text{C min}^{-1}$ up to $500\text{ }^{\circ}\text{C}$. Thin solid lines are pseudocomponents from normal distribution fitting of volatile

evolution rates for tar (a), methane (b), carbon dioxide (c), carbon monoxide (d), ethane (e), and ethylene (f). The thick solid line represents temperature.

Figure 45 shows the measured (points) and predicted (dash lines) rate profiles of (a) tar, (b) CH₄, (c) CO₂, (d) CO, (e) C₂H₆, and (f) C₂H₄ during the pecan shell pyrolysis at 10 °C min⁻¹ up to 500 °C. Ethane and ethylene had the lowest concentrations and were sufficiently described by a single normal distribution equation (Figure 45e-f). Methane, carbon dioxide, carbon monoxide, and tar were composed of multiple distributions (thin solid lines in Figure 45a-d). From the deconvoluted rate profiles, the underlying reactions producing each species can be assigned to specific possible pyrolysis reactions.

In Figure 45a, the evolution peak between 25 and 160 °C is attributed to water. The remainder of the tar is separated into three peaks, which correlate with three MW groups of tar and biomolecular sources (cellulose, hemicellulose, and lignin). The second peak (labeled “hemicellulose” in Figure 45a) at 278 °C corresponds to the reported hemicellulose decomposition temperature range. The third “cellulose” peak is produced within a narrow range of 290-390 °C and is attributed to cellulose decomposition into levoglucosan, other anhydroglucoses, oligosaccharides, and derivatives of glucose.⁴⁹ The fourth peak (labeled “lignin” in Figure 45a) is attributed to lignin decomposition over a broad temperature range. Lignin releases monomeric phenol units into the vapor phase at 300-480 °C.⁴⁹

Figure 45b shows four individual normal distributions within the rate profile of CH₄ attributable to different CH₄-forming reactions.¹²⁵ The first CH₄ evolution (labeled “methyl” in Figure 45b) initiating at 280 °C is generated by the cracking of labile bonds, e.g., C-O and C-S, having lower bond dissociation energies than the C-C bonds.¹²⁵ The initiation of this peak is coincident with the maximum rate of tar production. The cellulose/hemicellulose distribution in

Figure 45b is associated with the cracking of C-C bonds to produce light aromatics. All C-S, C-C, and C-O bonds have bond energies less than 350 kJ mol^{-1} ¹²⁶, which are cleaved by $400 \text{ }^\circ\text{C}$ leading to the onset of primary devolatilization. Therefore, the char at this point will be mostly aromatic. The third peak (labeled “tar cracking” in Figure 45b) originates from the scission of alkyl groups of the char.^{16, 38} The final CH_4 forming reaction (labeled “aromatic” in Figure 45b) is the decomposition of ring structures and subsequent char formation over a broad temperature range. For instance, methyl groups decompose to form CH_4 and allow for the combination of aromatic clusters to form larger char molecules.^{63, 127} Temperature dependence of the “aromatic” methane evolution profile is consistent with the increase in the aromaticity of char products at $300\text{-}500 \text{ }^\circ\text{C}$ observed by the solid state ^{13}C NMR⁴⁵ and with the increase in fixed carbon content.¹²⁸ The aromaticity of char is reflected in the decreasing H/C ratio in the char as function of pyrolysis temperature.⁵¹

Figure 45c shows two distributions that comprise the rate profile of CO_2 . Carbon dioxide evolution begins at approximately $250 \text{ }^\circ\text{C}$. Carbon dioxide evolution is attributed to cellulose and hemicellulose forming monomers that undergo decarboxylation reactions.⁵² The measurement of decarboxylation in solid-phase will be presented in the following section. The small secondary CO_2 peak at $460 \text{ }^\circ\text{C}$ had been attributed to cellulose and lignin decomposition in the literature.⁴⁰ However, the temperature range (near $400 \text{ }^\circ\text{C}$) coincides with the formation and removal of carboxyl functionality on char.⁴⁵ Therefore, decarboxylation of the char could contribute to the second peak in Figure 45c.

Carbon monoxide exhibited the most complicated rate profile consisting of nine different reaction steps (Figure 45d). The first CO forming reaction initiates at $100 \text{ }^\circ\text{C}$ likely as a result of reactions involving inorganic species or water production. The second CO peak labeled

“cellulose/hemicellulose” in Figure 45d is the major CO peak. The peak initiates at 170 °C and is attributed assigned to decarbonylation of cellulose and hemicellulose monomers yielding CO.⁵² The measurement of decarbonylation in solid-phase will be presented in the following section. Carbon monoxide evolution near 320 °C had been attributed to hemicellulose and cellulose.⁴⁰ The small CO peak between 300 and 400 °C is attributed to secondary tar cracking. The final six of the CO peaks likely resulted from successive phenolic decomposition within lignin. The majority of lignin component in Figure 45d appeared at the isothermal (500 °C) region. This evolution is not directly comparable to the non-isothermal kinetics for all other components in Figure 45. The following section introduces another in-situ technique able to probe primary pyrolysis reactions in a most comprehensive manner when combined with TG-GC.

8.4 Biomass Surface Functional Groups

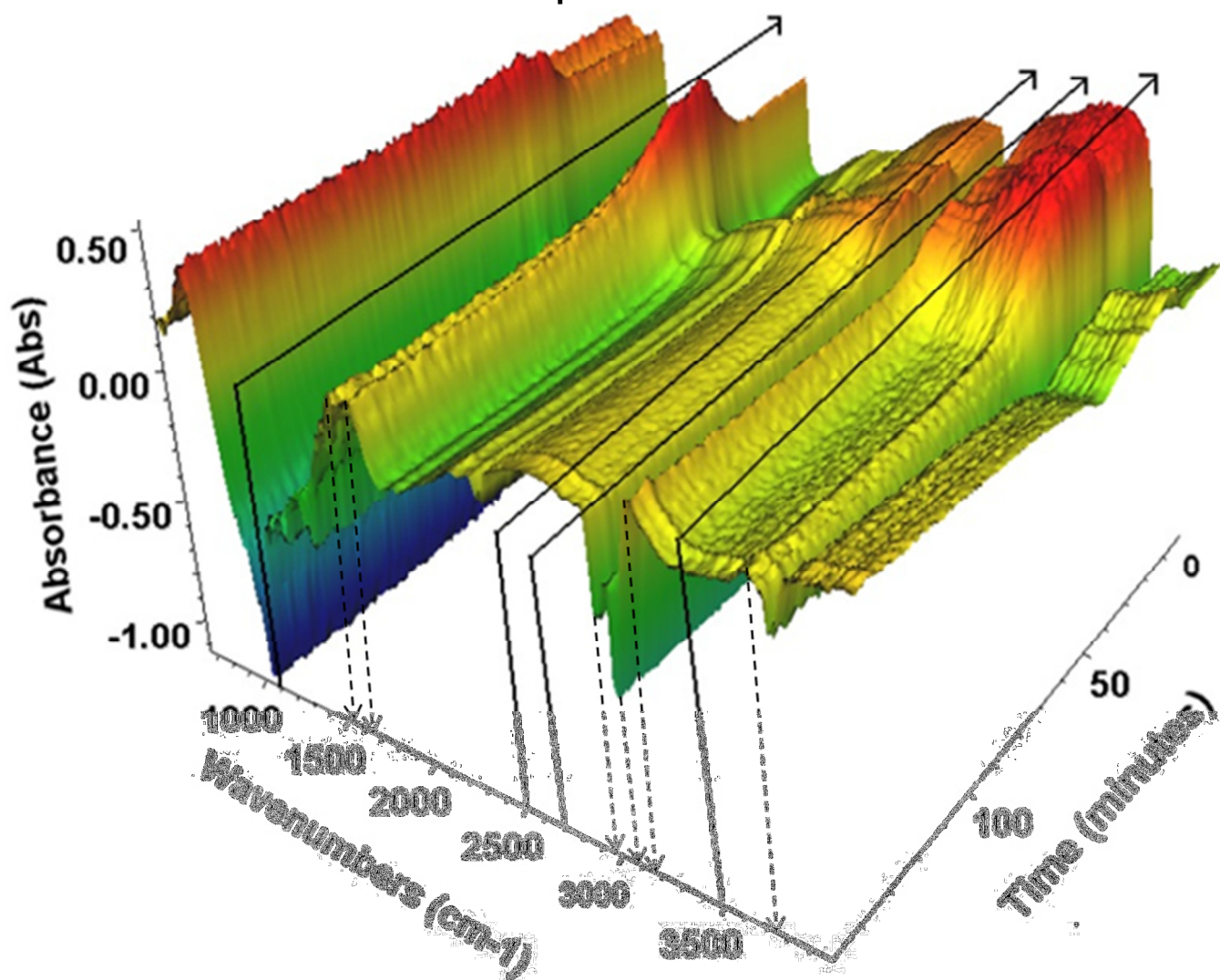


Figure 46 In situ DRIFTs monitoring of slow pyrolysis for pecan shells

Figure 46 shows DRIFTs results for pecan shell pyrolysis at $10\text{ }^{\circ}\text{C min}^{-1}$ and held at $500\text{ }^{\circ}\text{C}$ for 4 hours. The infrared Fourier transform spectra are in the wavelength range of $900\text{-}4000\text{ cm}^{-1}$. Only three peak sets are pertinent to biomass pyrolysis. The peak at $3750\text{-}3200\text{ cm}^{-1}$ is attributed to three bonds; hydroxyl groups associated with hydrogen, stretching of N-H bonds, and C-H stretching in polynuclear aromatic hydrocarbons.¹²⁹ The resultant band is a broad isolated peak. The area of this peak decreases throughout pyrolysis. The largest decrease in peak

area during pecan shell pyrolysis occurs before 205 °C. The decrease is largely attributed to the loss of bound water in the biomass. The next set of peaks is between 3100-2750 cm^{-1} is attributed to aliphatic groups. The two convoluted peaks are asymmetric (2935 cm^{-1}) and symmetric (2885 cm^{-1}) C-H bonds. Note that these are negative peaks in Figure 46. Both peaks decrease in magnitude throughout pecan shell pyrolysis. The final peak set considered is between 1860-1450 cm^{-1} . This peak should be separated into an aromatic peak at 1600-1490 cm^{-1} and one oxygenated group peak at 1740-1650 cm^{-1} . The aromatic peak at 1600-1490 cm^{-1} is expected to increase throughout pyrolysis as shown for date pits.¹²⁹ The oxygenated group peak at 1740-1650 cm^{-1} is expected to generally decrease throughout pyrolysis. Each of these peaks will be discussed in more detail. The region between 2700 and 1900 cm^{-1} has not been attributed to any functional groups in this work.

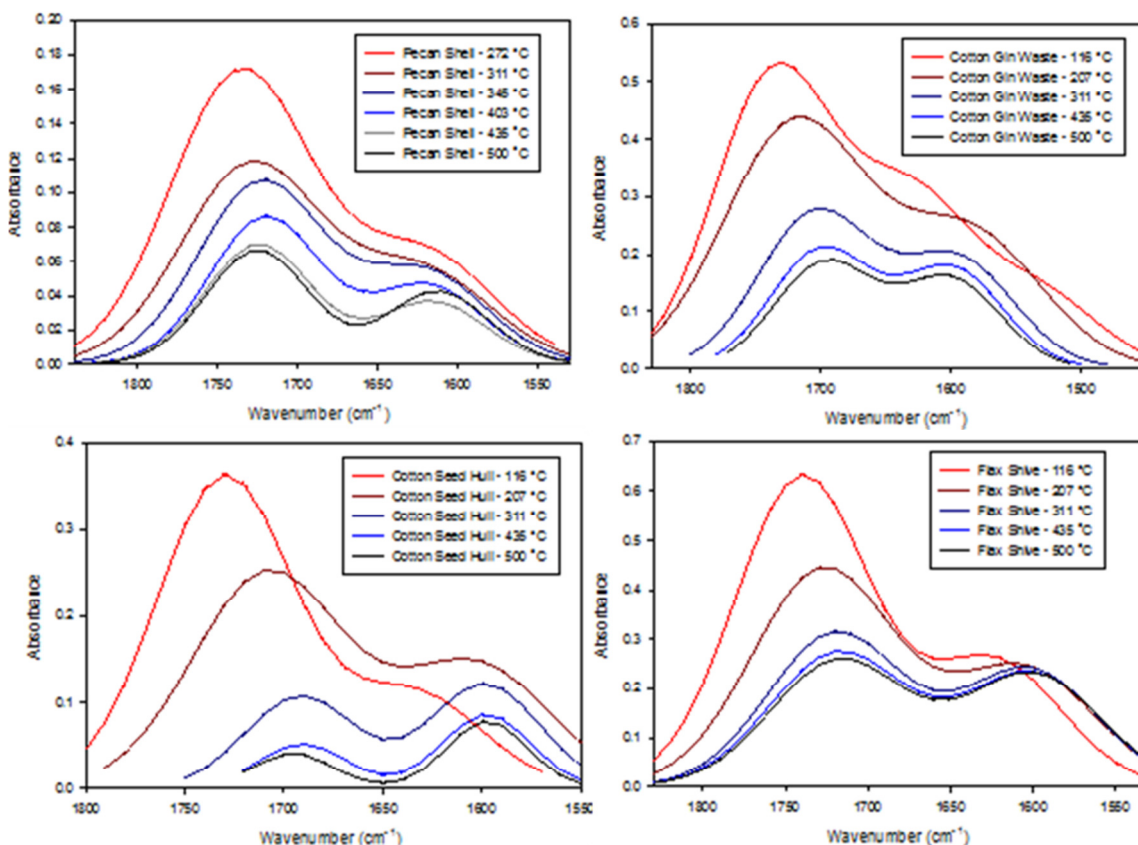


Figure 47 Deconvoluted DRIFTs peaks between 1860 –1450 cm⁻¹ as function of pyrolysis temperature for (a) pecan shells, (b) cottonseed hulls, (c) cotton gin waste, (d) flax shives

Figure 47 above shows the set of convoluted peaks between 1860 –1450 cm⁻¹ for the four types of biomass at various temperatures. For each biomass type, the original large skewed peak transforms into a smaller two-headed peak as temperature increases. More specifically, the large peak at higher wavenumbers (1740-1650 cm⁻¹) decreases in size throughout pyrolysis while the peak at lower wavenumbers (1600-1490 cm⁻¹) becomes more pronounced. The two-headed peak is discernible for scans above 405 °C for each biomass type. The transformations of these peaks are (1) the decrease in C-O bonds and (2) the increase of aromatic bonds in the biomass char. It should also be noted that the amplitude of the C-O bond peak (1740-1650 cm⁻¹) shifts to lower wavenumbers during pyrolysis. First, we will focus on the amplitude decrease and shift of the peak between 1860 and 1650 cm⁻¹.

The decrease in amplitude was previously reported to be the loss of carboxylic acid and lactone groups resulting in the production of CO₂.¹³⁰ The shift of the carbonyl absorption band is evidence that the nature of the remaining carbonyl groups is changing during pyrolysis. There are various types of carbonyl groups detected in distinct wavenumber ranges. Stretching of anhydride groups absorbs in the range of 1850-1786 cm⁻¹. Lactone stretching produces bands from 1740-1724 cm⁻¹. Carboxylic groups produce a band in the 1710-1680 cm⁻¹ range. Quinones are the most stable carbonyl subgroup and result in a band between 1670 and 1660 cm⁻¹. Each carbonyl group except anhydrides was reported to be present in poplar char at significant proportions.¹³⁰ For each type of biomass in Figure 47, the wavenumber of carbonyl bond absorption band decreases from 1735 or 1745 cm⁻¹ throughout pyrolysis. The shift in wavenumber is attributed to conjugation in the char molecule and loss of the less stable (higher wavenumber) carbonyl groups. These results suggest that C-O group reactivity in biomass pyrolysis begins as low as 97 °C. This is consistent with the reactivity reported for poplar wood char.¹³⁰

The second important feature is the growing of the aromatic absorbance peak during pyrolysis of four biomass samples between 272 to 500 °C. The evolution profiles of aromatic bonds between the four biomasses are remarkably consistent. In addition, previous research using ¹³C NMR spectroscopy has detected increases in aromaticity in pecan shells⁴⁵ and cotton seed hulls¹³¹ between 300 and 500 °C. These results are novel in-situ measurements on solid-state reactions during pyrolysis. The next section correlates these DRIFTS measurements with TG-GC measurements taken at identical conditions.

8.5 DRIFTS-TG-GC PLS Calibration

The utility of TG-GC has been thoroughly illustrated. In the previous section, DRIFTS has proven to provide complimentary novel insights into the pyrolysis reaction mechanism. In this section, the combination of in-situ TG-GC and DRIFTS links gas, liquid, and solid phase nonisothermal pyrolysis reactions. The observable link between the evolved gas species profile and char surface functional groups motivated a predictive PLS calibration between gas and solid phase pyrolysis reactions. Gaussian fit-based deconvolution of gas product formation rate suggested relationships between (1) evolved CH_4 and increased aromaticity of the char product at 300-500 °C, and (2) evolved CO_2 and decarboxylation of the char product up to 400 °C. Such a correlation will allow one to predict the gas product based on the char surface functional group measurement, and vice versa.

In-situ DRIFTS monitoring of the solid phase residual observes the time-dependent characteristics of the surface functional groups. Observations include the removal of O-H, C-H, and C-O bonds.¹²⁸ The DRIFTS monitoring of the condensed¹³² and gas phase^{40, 133} have been widely employed for slow and fast pyrolysis. No prior study employed PLS to calibrate the multiphase pyrolysis reactions. The establishment of a calibration between (1) DRIFTS on the solid phase and (2) the mass loss and volatile formation profile allows prediction of the volatile evolution rate based on the surface chemistry of solid-phase reaction products. The PLS calibration validations are presented in this section.

Table 12 Cross-validation statistics of the Partial Least Squares calibration between DRIFTS and predicted gas evolution for pecan shell pyrolysis at 10 °C min⁻¹

| compound (unit) | n | mean | s.d. | min | max | latent | RMSEC | R ² | RMSECV | R ² |
|------------------------------------|-----------------|-------|-------|-------|--------|----------|-------|----------------|--------|----------------|
| | | | | | | variable | | calibration | | validation |
| <i>gas phase</i> | | | | | | | | | | |
| CO (mg) | 49 | 1.25 | 1.36 | 0.00 | 3.67 | 8 | 0.06 | 1.00 | 0.17 | 0.98 |
| CO ₂ (mg) | 49 | 1.27 | 1.69 | 0.00 | 4.48 | 7 | 0.13 | 0.99 | 0.29 | 0.97 |
| CH ₄ (mg) | 48 ^c | 0.11 | 0.20 | 0.00 | 0.91 | 7 | 0.02 | 0.98 | 0.04 | 0.93 |
| methyl ^b (mg) | 48 ^c | 0.08 | 0.16 | 0.00 | 0.49 | 7 | 0.02 | 0.98 | 0.04 | 0.92 |
| aromatic ^b (mg) | 48 ^c | 0.02 | 0.02 | 0.00 | 0.09 | 7 | 0.00 | 0.99 | 0.00 | 0.97 |
| C ₂ H ₄ (mg) | 48 ^c | 0.00 | 0.01 | 0.00 | 0.05 | 7 | 0.00 | 0.97 | 0.00 | 0.89 |
| C ₂ H ₆ (mg) | 48 ^c | 0.00 | 0.00 | 0.00 | 0.02 | 7 | 0.00 | 0.97 | 0.00 | 0.89 |
| total gas ^a (mg) | 49 | 2.64 | 3.21 | 0.00 | 9.13 | 7 | 0.21 | 1.00 | 0.49 | 0.98 |
| <i>liquid phase</i> | | | | | | | | | | |
| tar (mg) | 49 | 21.52 | 23.21 | 0.00 | 59.45 | 8 | 1.51 | 1.00 | 3.62 | 0.98 |
| water ^b (mg) | 49 | 3.04 | 1.62 | 0.00 | 4.01 | 6 | 0.20 | 0.99 | 0.30 | 0.97 |
| hemicellulose ^b (mg) | 49 | 7.93 | 8.83 | 0.00 | 18.38 | 7 | 0.64 | 1.00 | 1.40 | 0.97 |
| lignin ^b (mg) | 49 | 4.61 | 5.60 | 0.00 | 16.96 | 7 | 0.40 | 1.00 | 0.91 | 0.97 |
| <i>solid phase</i> | | | | | | | | | | |
| solid (mass%) | 49 | 76.50 | 23.53 | 36.69 | 100.00 | 8 | 1.0 | 1.0 | 3.3 | 0.98 |

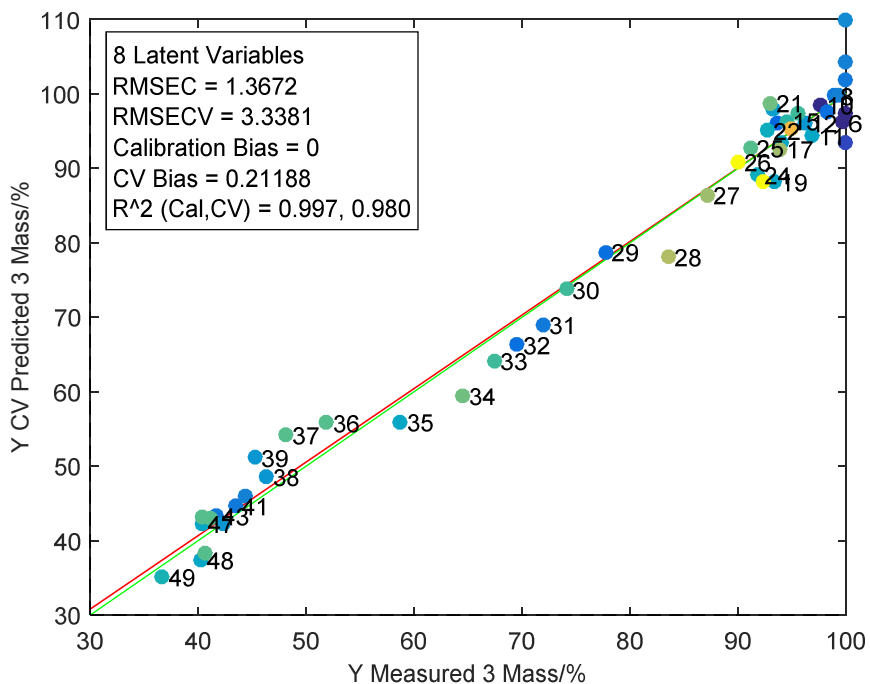


Figure 48 Cross-validation scatter plots of measured and estimated mass loss data from TG. Lines are the fit (red) and 1:1 (green).

The PLS was first performed between the percent mass loss profiles determined by TGA and the DRIFTs spectrum to investigate the correlation between the condensed phase observed in two experimental methods. Cross-validation statistics in Table 12 indicates the ability of DRIFTs to predict the weight loss profile determined by TGA (in mass %). Figure 48 shows the cross-validation scatter plots of measured and predicted mass percent, also known as the calibration curve. The close correlation between the predicted and measured values represents the ability to infer the material loss and condensation of material in TG or DRIFTs measurements. The color is indicative of the q-residuals, which grade how well a value conforms to the calibration model. Shades of blue indicate small q-residuals. Points 22, 24, and 26 have high q-residual which means there is a large difference between the measured value and the model projection.

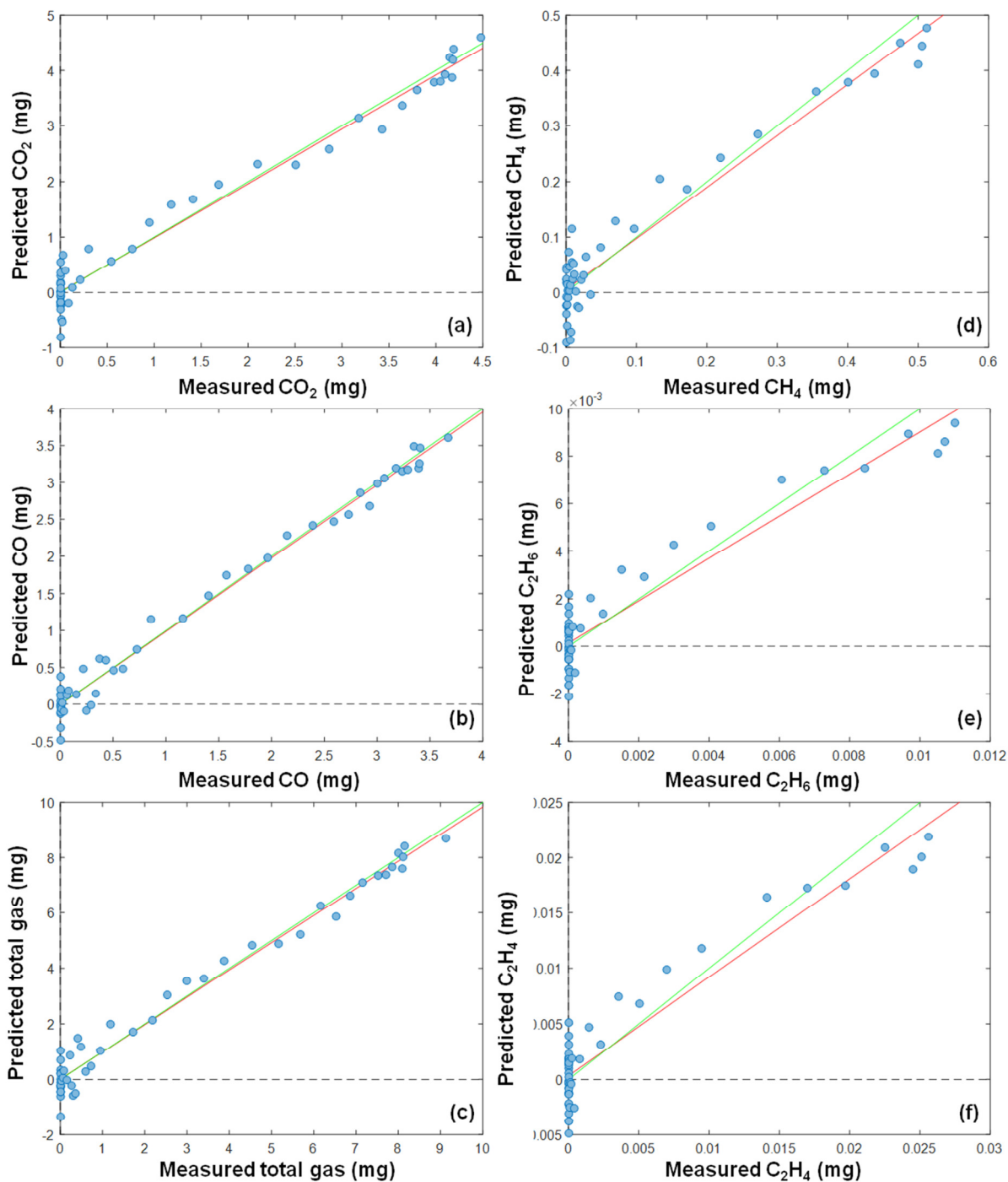


Figure 49 Cross-validation scatter plots of measured and estimated mass of CO_2 , CO, CH_4 , C_2H_6 , and C_2H_4 , and total gas (sum of CH_4 , C_2H_4 , C_2H_6 , CO_2 , and CO). Lines are the fit (red) and 1:1 (green).

Table 12 also shows the cross-validation statistics on CO, CO₂, CH₄, C₂H₄, C₂H₆, and total gas production rates profiles with respect to temperature. Cross-validation scatter plots of measured and predicted CO, CO₂, CH₄, C₂H₄, C₂H₆, and total gas production rates are provided in Figure 49. The RMSECV R² value for C, CO₂, and total gas production were 0.97 or better. This indicates a strong correlation between the loss of functional groups on the surface and production of these products. For CH₄, the overall RMSECV R² value was 0.93 so the correlation is not strong. However, after separating the CH₄ evolution into pseudo-components, it was found that the “aromatic CH₄” had a much higher RMSECV R² value because this pseudocomponent involved a solid-state reaction. In addition, C₂H₄ and C₂H₆ have very weak correlations to the solid-state chemical change because their production results from tar cracking following the Fabuss-Smith-Satterfield reaction sequence.

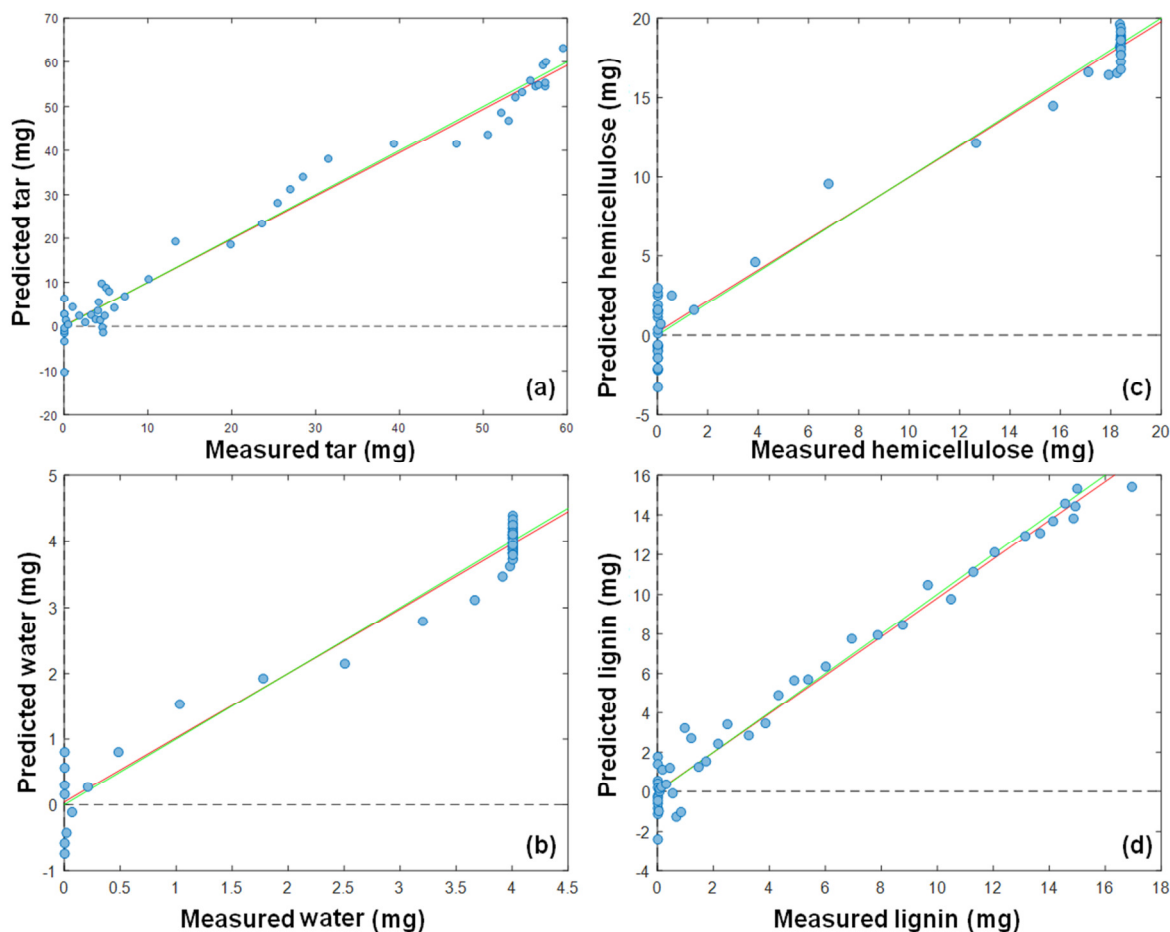


Figure 50 Cross-validation scatter plots of measured and estimated mass of tar and deconvoluted tar psuedo-components. Lines are the fit (red) and 1:1 (green).

Figure 50 shows cross-validation scatter plots of measured and predicted tar production rates. Figure 50b-d are generated using the deconvoluted Gaussian psuedo-component fits for tar evolution. The tar evolution profile and all of the pseudo-components have strong correlation the solid-state chemical changes as indicated by strong RMSECV R^2 values in the TG-GC-DRIFTS calibration.

Scatter plots of CO_2 (Figure 49a), tar, hemicellulose, and water (Figure 50a-c) exhibit an overall linear response with some non-linearity, which is different from an overall non-linearity

that will have a single U-shaped curvature. Figure 48 also shows non-linearity in mass loss scatter plot. There are several possible sources of non-linearity in the PLS calibration. There can be a time lapse between the sample collection and the analysis that could cause a systematic error; however both the DRIFTS and TG-GC analyses were performed in-situ with constant time intervals. Alternatively, evolution and condensation of volatile species during the peak production (300-500 °C in Figure 50) could contribute to the nonlinearity of tar calibration. Non-constant error variance, an outlier, and other sources of non-linearity have been observed in the PLS scatter plots of complex samples including biochar.¹³⁴

In summary, replicated conditions of pecan shell pyrolysis in a TG-GC and DRIFTS analysis were used to correlate gas and tar production to loss of surface functional group and increase in char aromaticity through a PLS calibration. This technique has realized and quantified the inherent connection between char surface functionality and volatile products. All previous pyrolysis works relied on product measurements in one phase and the composition of counter phase(s) was inferred. Therefore, this analysis is a breakthrough in the pyrolysis field. Next chapter shift the focus back to secondary pyrolysis reactions of tar.

Chapter 9: Tar Thermal Treatment

To this point, the primary pyrolysis mechanisms of coal and biomass have been investigated. For coal, we have also provided an extensive investigation of secondary pyrolysis reactions. The tar was found to be primary reactant in secondary pyrolysis reactions. It was of interest to investigate the reactions during thermal treatment of tar from biomass and coal pyrolysis, separately, in the TG-GC system. This study allows a comparison of the differences in reactivity of the two materials. The tar samples collected from coal or biomass pyrolysis were kept at 0 °C dissolved in acetone. Prior to TGA, the samples were evaporated at 25 °C under

argon flow and concentrated to a volume of 0.4 mL, which was the maximum sample volume able to be analyzed in the cup crucible. Trial TGA runs with acetone were performed to determine the time sufficient for evaporating 200 mg of acetone at 35 °C under 30 mL min⁻¹ of argon. Figure 51 shows the temperature program for analyzing the coal tar samples.

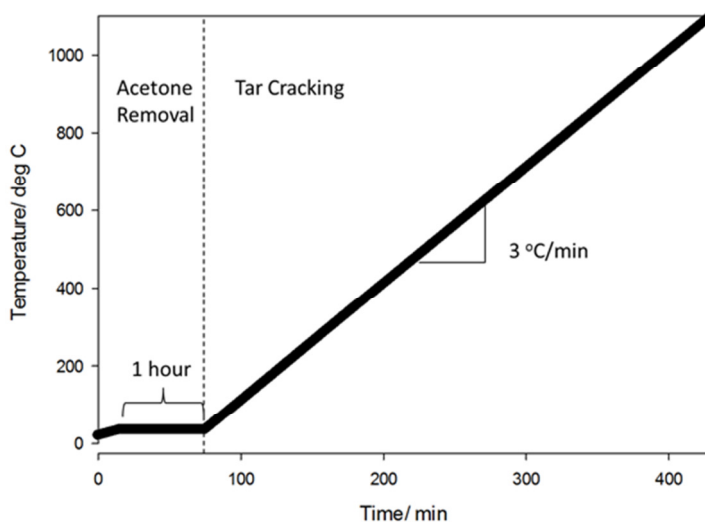


Figure 51 Temperature program for TGA of tar samples

The temperature program was designed to simulate the pyrolysis conditions at which the tars were generated. The acetone was removed immediately before secondary heating of tar. The mass of the sample and acetone before the test is known to ± 2.5 mg due to continuous evaporation of the sample at room conditions. Therefore, the sample mass after each test was measured using a separate balance in order to correct the sample mass, if necessary. For this, the virgin mass of the crucible was weighed and recorded before each test.

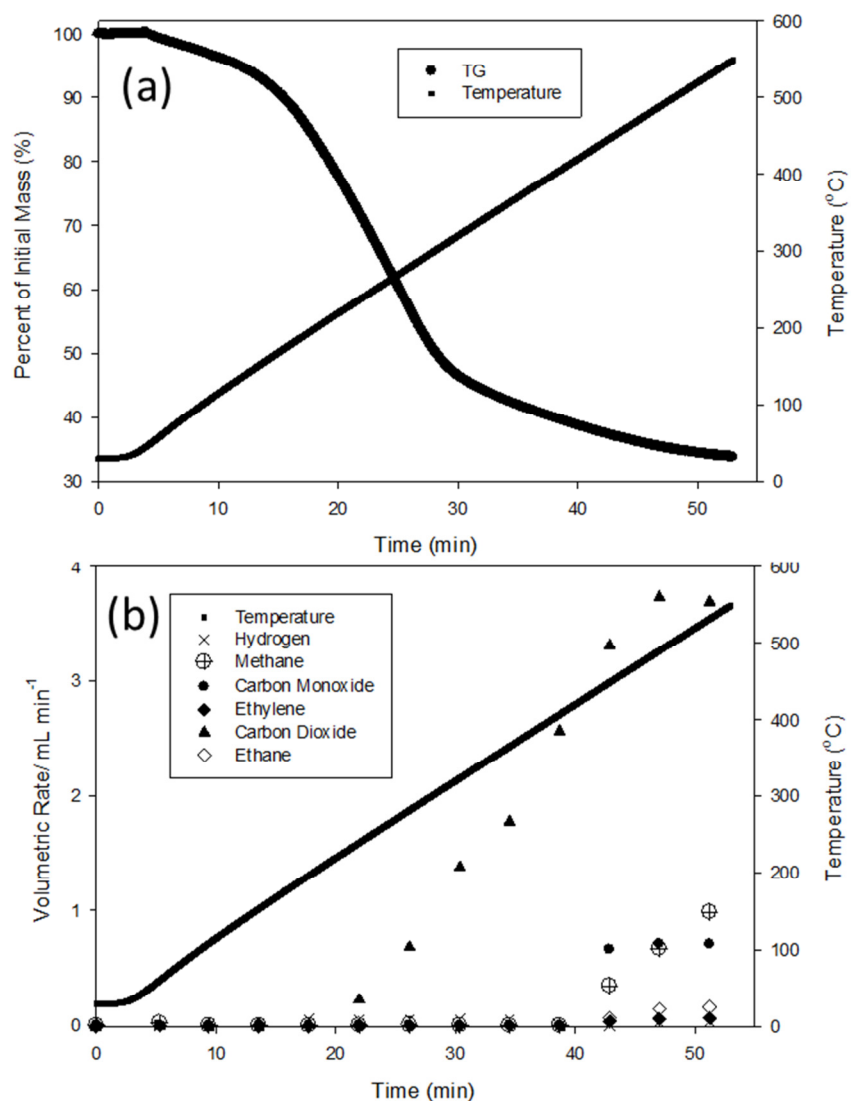


Figure 52 (a) The TG profile of birch wood tar heated at $10\text{ }^{\circ}\text{C min}^{-1}$ to $550\text{ }^{\circ}\text{C}$ (b) The gas evolution profile from birch wood tar pyrolysis

Figure 52a shows TGA of birch wood tar from flash pyrolysis ($\sim 86\text{ }^{\circ}\text{C min}^{-1}$). The birch wood tar retains 33.8 wt. % char residual after thermal treatment at $10\text{ }^{\circ}\text{C min}^{-1}$ up to $550\text{ }^{\circ}\text{C}$. The complex and oxygenated nature of biomass tar causes polymerization leading to water production and production of char from tar.¹⁷ A major portion of the weight loss happens before $310\text{ }^{\circ}\text{C}$. Figure 52b shows gas evolution from the pyrolysis of birch wood tar at $10\text{ }^{\circ}\text{C min}^{-1}$ to

550 °C. At 239 °C and throughout the major mass, CO₂ is evolved from the reacting tar species. Evolution of CH₄, CO, C₂H₄, and C₂H₆ occur after 448 °C. There is a small amount of H₂ production at 490 °C. The production of all these gases is a result of char formation reactions between the birch wood tar species. This analysis suggests that secondary tar reactions in biomass pyrolysis are potentially more extensive than that of coal!

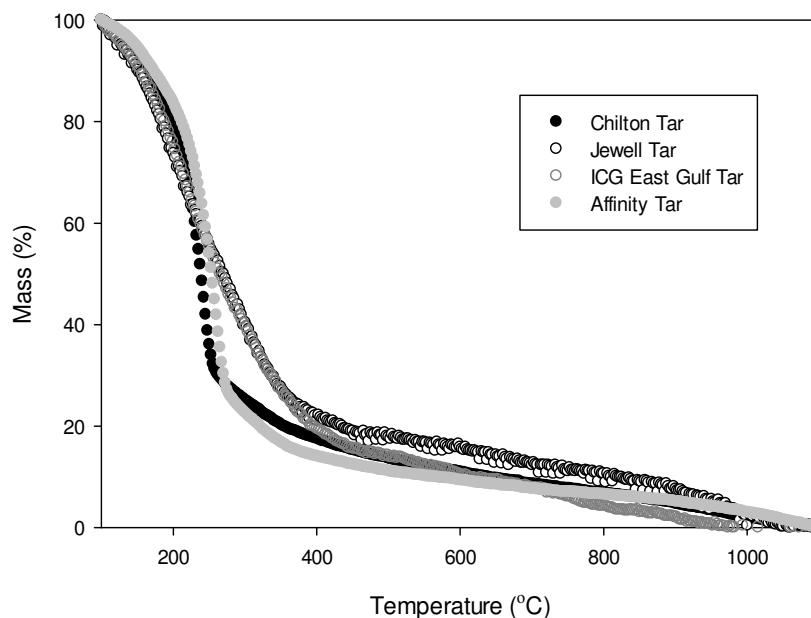


Figure 53 TGA of four coal tar samples at 3 ° min⁻¹ to 1100 °C

Four different coal tar samples were analyzed in the TGA. The tar concentrate is 6.8 – 15.8 wt. % of the liquid sample introduced to the TGA. Figure 53 shows the TG of coal tar heated from 100 °C to 1100 °C at 3 °C. It was observed that 88 to 97 % of the sample is lost in 35 °C isotherm under argon flow (not shown in Figure 53). It can be seen that 75-90% of the remaining tar products vaporize before 400 °C. It should be noted that this is near the temperature of the onset of the metaplastic state. This is evidence that a large portion of coal tar is compounds with high vapor pressure. This supports the flash distillation analogy in which tar devolatilization is an evaporation process explained by Raoult's law.^{57, 70} It also suggests that the

maximum GC column operating temperatures, for instance, 270°C, are not sufficient for volatilizing many of the molecules in coal tar. The remaining 10-25% of the tar vaporizes by 1000 °C. The GC was installed downstream of the TGA during tar thermal treatment and no gas products were observed. Therefore, the coal tar products have vaporized without producing gas or solid phase products. The condenser impinger train was coupled to the system in order to recollect the tar. The secondary tar products were collected from the impinger train to be analyzed by LDI-TOF.

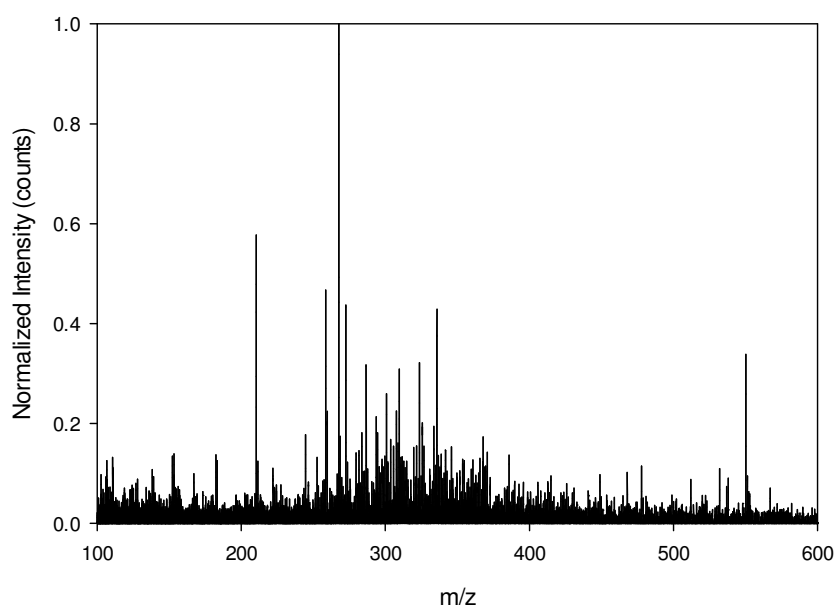


Figure 54 LDI-TOF spectrum of coal tar thermally treated at 3 °C min⁻¹

The tar collected via the impinger train from thermal treatment of Jewell coal tar was analyzed by LDI-TOF in order to investigate the thermal reactions within the tar product. Figure 54 shows the spectra of tar thermally treated at 3 °C min⁻¹. The spectra of thermally treated tar are different than the spectra of the original tar products (Figure 42). The spectra had spread to lower and higher MW. However, the average MW of 267.6 amu is much lower than the primary coal tars. It is inferred that the molecules detected in the primary tar with m/z of 250 or larger

amu crack to form molecules with an amu less than 220. Molecules between 467 and 567 amu may form by recombination or cracking of even larger mass species (species not detected by LDI-MS of the primary coal tar). Some molecules between 250 and 450 amu completely vanished from the spectra while others depreciated in intensity. In TGA, the majority of the tar product evaporated before 400 °C. It is expected that upon thermal treatment the tar molecules begin to form stabilomers through radical pathways. There are ten molecules with great increases in intensity compared to the original coal tar sample. These molecules are of the MW 152.2, 182.2, 210.4, 221.9, 267.6, 336.7, 351.7, 448.9, 538.1, and 550.3 amu. At temperatures greater than 400 °C, a relatively small portion of the tar sample reacted in the condensed phase until it completely decomposed into volatile species. The final stable tar species are not reactive even at long residence times and high temperatures. These tar compounds are stable aromatic species, known as stabilomers.

In summary, the tar products of biomass and coal pyrolysis were analyzed separately by the TG-GC technique. The temperature program for the thermal treatment of tar was identical to that at which the tars were generated from the respective material parent material. It was found that the biomass tar was more reactive, generating both gaseous and solid product during thermal treatment. The coal tar completely decomposed during heating however no gaseous products were observed. The analysis of secondary tar by LDI-MS showed the coal tar composition had greatly changed. Overall, these analyses suggest that biomass tar has a higher potential for secondary reactions than coal tar.

Chapter 10: Coke Hairs and Silver Coke

The importance and distinction of quality in the solid carbon product has been emphasized in Chapter 1. The feedstocks in this work are known to produce high quality and

high fixed carbon yield of solid carbon product through slow pyrolysis. Section 2.2.2 included a discussion on the bubble transport model able to describe the formation of char structure during coal pyrolysis. This section discusses the anomalous silver coated and fibrous coke samples introduced in Section 3.2.6. Each of these coke specimens were produced in commercial coke ovens. The characterization and mechanism of formation are discussed in this section.

10.1 Silver Coke

The silver coke samples collected from commercial coke sample (Figure 24b) were characterized using XRD and ICP-MS. The results of the analysis are presented below. The characterization of the material is used to postulate the formation mechanism during coal pyrolysis.

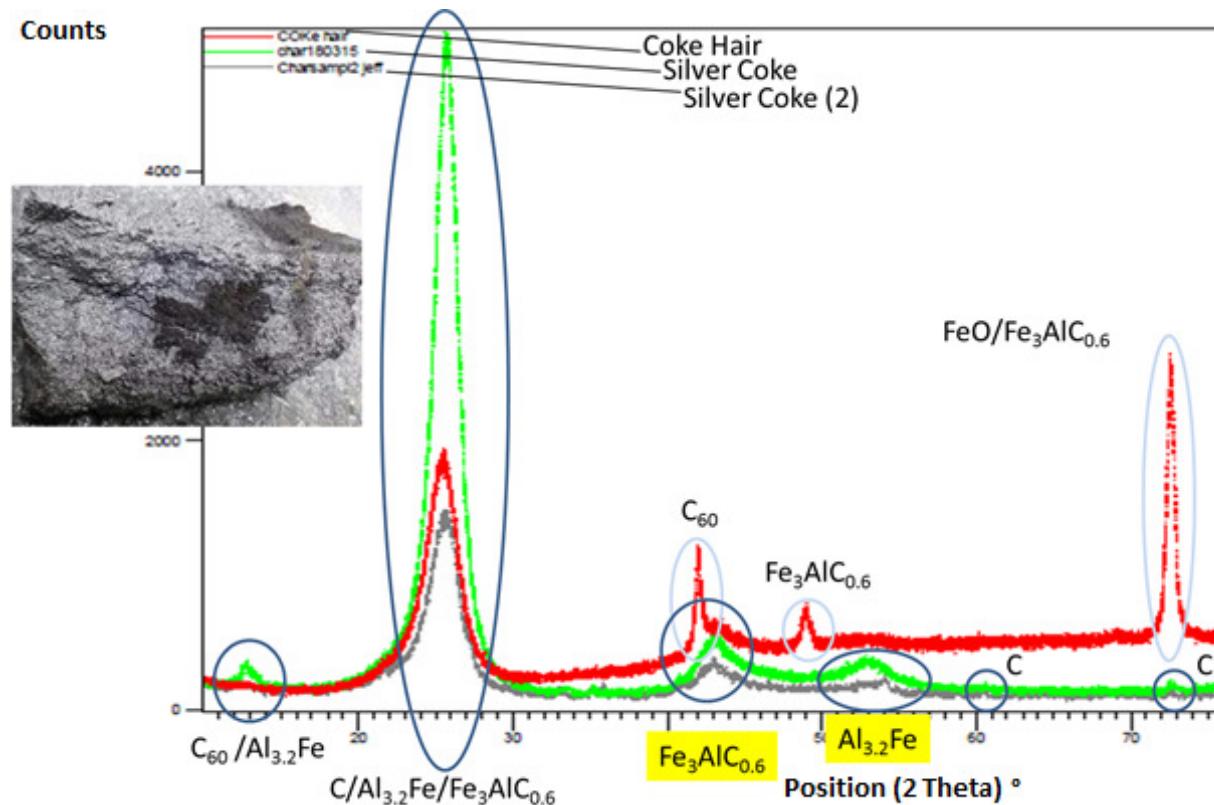


Figure 55 Annotated XRD spectrums of two powdered silver coke samples and a powdered coke hair sample

The silver coke layer of a parent coke specimen was mechanically shaved off using a sharp hard object resulting in a silver coke powder. In Figure 55, the XRD spectrum of the silver coke powder (green and grey) sample is shown along with the coke hair spectrum (red). Duplicate samples of silver coke were analyzed. Both silver coke samples share matching peaks with $\text{Al}_{3.2}\text{Fe}$ and $\text{Fe}_3\text{AlC}_{0.6}$. Detection of mineral inclusions by XRD indicates that the crystallite size is > 4 nm in size.¹³⁵

Table 13 Silver coke elemental composition determined by ICP-MS

| Element | Concentration ($\mu\text{g}/\text{mg}_{\text{coal}}$) |
|-----------------|---|
| Sulfur | 1.26 |
| Silicon | 0.75 |
| Aluminum | 0.12 |
| Iron | 0.09 |
| Calcium | 0.03 |
| Cobalt | 0.03 |

The silver coke powder was dissolved in acid solution as described in the Experimental Procedures and Methods (Section 3.2.8). The resulting solution was analyzed by ICP-MS. Table 13 shows the mineral content of silver coke determined by ICP-MS. The presence of iron and aluminum agrees with the XRD result. The molar ratio of aluminum to iron from ICP-MS is ~ 2.8 . This molar ratio is due to the mix of $\text{Al}_{3.2}\text{Fe}$ and $\text{Fe}_3\text{AlC}_{0.6}$ compounds. However, the high presence of sulfur suggests a significant presence on sulfides.

The nature of silver coke formation is postulated to involve the diffusive properties of minerals at high temperature. A study of particle mobility on graphite surfaces observed that particle motion took place at the Tammann temperature, which is defined as $0.51 T_M$, where T_M is the melting temperature of the metal.¹³⁶ For instance, CaO becomes mobile at $\sim 1200^\circ\text{C}$ while iron is mobile at temperatures as low as 700°C . At these temperatures, these minerals tend to agglomerate.¹³⁶ Aluminum in coal primarily exists in kaolinite, which has a Tammann

temperature of ~890°C. The change of metal dispersion in coke at elevated temperatures is an important realization. X-ray photoelectron spectroscopy measurements of char heated up to 1000 °C showed migration of metals minerals to the surface of the char to eventually form a nearly continuous layer on the surface.¹³⁷ It is inferred that a similar mechanism is occurring in the formation of silver coke. The concentrations of metals increase on the surface and thereby reduce the number of accessible sites on the carbon structure. This results in a decrease of coke reactivity.

10.2 Coke hairs

The coke hair samples collected from commercial coke sample (Figure 24c) were analyzed by SEM, EDS and XRD analysis. Images from SEM and EDS are presented below. The coke hairs were isolated from the parent coke specimen using forceps. The coke hairs were imaged (1) directly on the SEM stage and (2) embedded in a resin to analyze the radial cross section. Carbon tape was not used instead the sample was analyzed on a silver paste (Ted Pella, Product number: 16059-10) in order to perform elemental analysis of carbon. The characterization of the material is used to postulate the formation mechanism during coal pyrolysis.

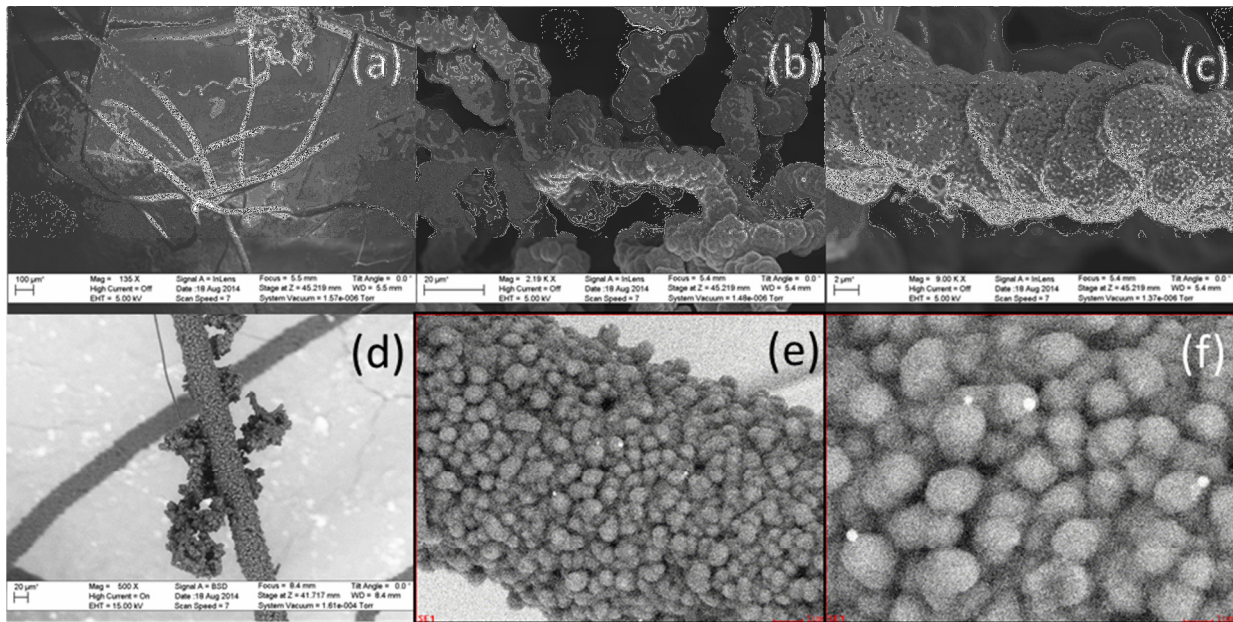


Figure 56 Six SEM images of coke hairs

The SEM images of coke hairs are shown in Figure 56a-f. Figure 56a-b shows a network of carbon filaments at various magnifications. The coke hairs were nominally 10-50 μm in diameter and up to 5 cm in length. Figure 56c shows a magnified image of the carbon filament surface. The surface resembles a rough topology of agglomerated carbonaceous material. Figure 56d-f shows images of the surface at varying magnification with the EBSD. With the EBSD, small spherical inclusions constitute the surface of the filament.

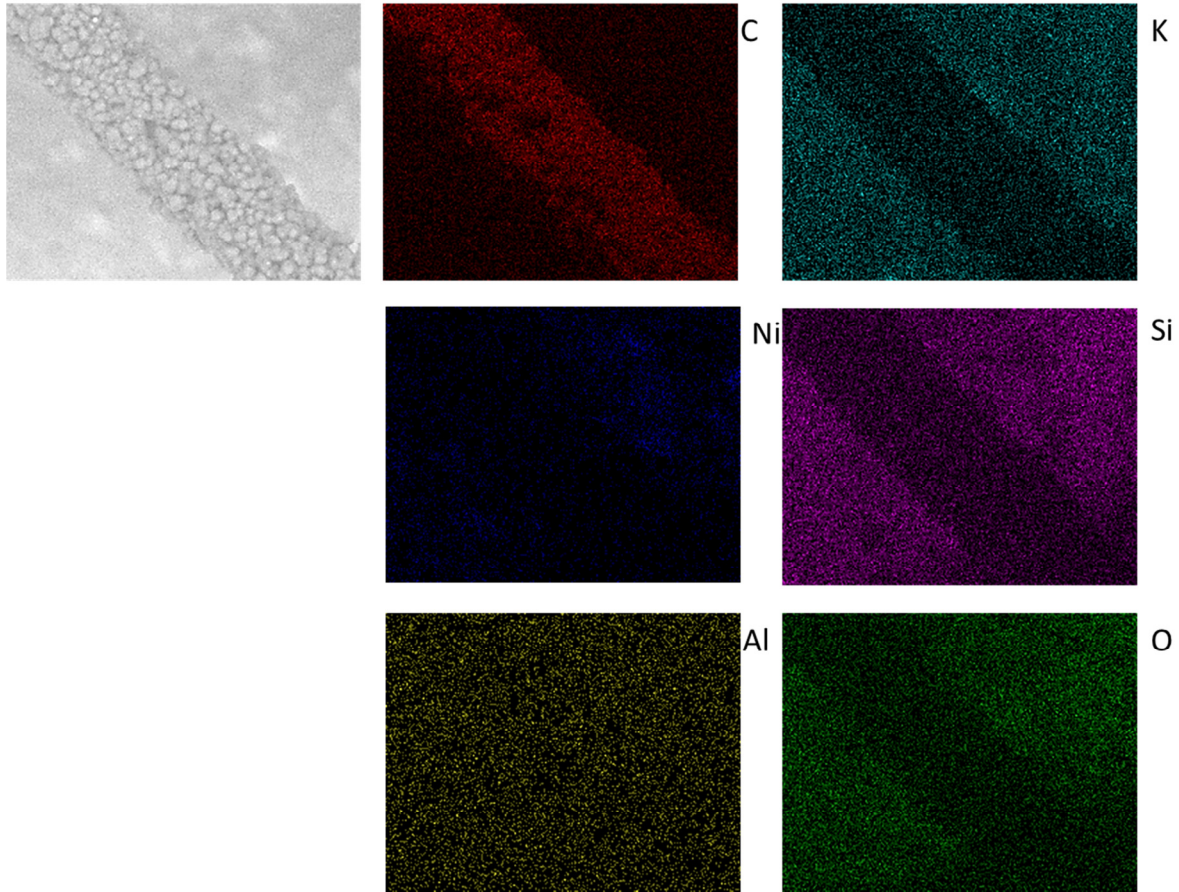


Figure 57 EDS mapping of a single carbon filament with low to no concentration of potassium, nickel, silicon, aluminum and oxygen atoms

Figure 57 shows the result of EDS mapping on coke hair. The EDS map for carbon produced a red outline of the coke hair from the SEM image. The EDS maps for potassium, silicon, and oxygen produced a black outline of the coke hair from the SEM image. The EDS map of nickel and aluminum produced noise. It was concluded from the analysis that the coke hair was entirely carbon.

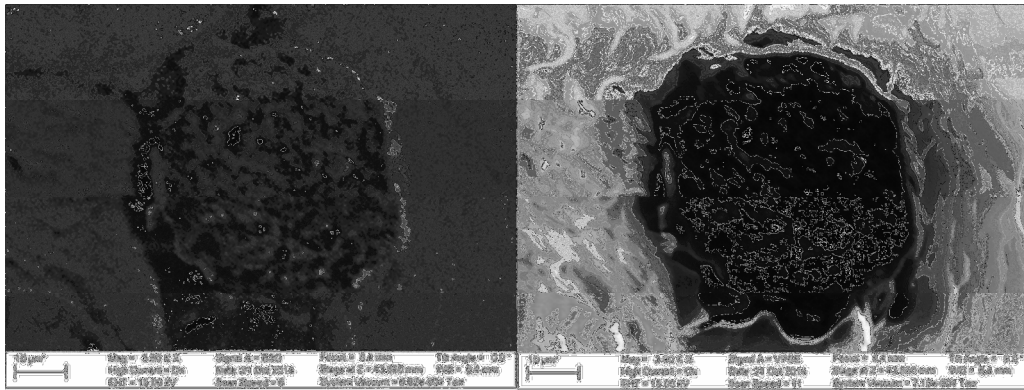


Figure 58 Cross-sectional SEM images of coke hairs embedded in a polymer cast

The SEM of the cross-section analysis of the coke hair was executed by embedding a coke hair in a polyester resin (Pace Technologies) and slicing the resin. Figure 58 shows the SEM of the coke hair cross-section. It can be seen that the core of the coke hair is solid carbon.

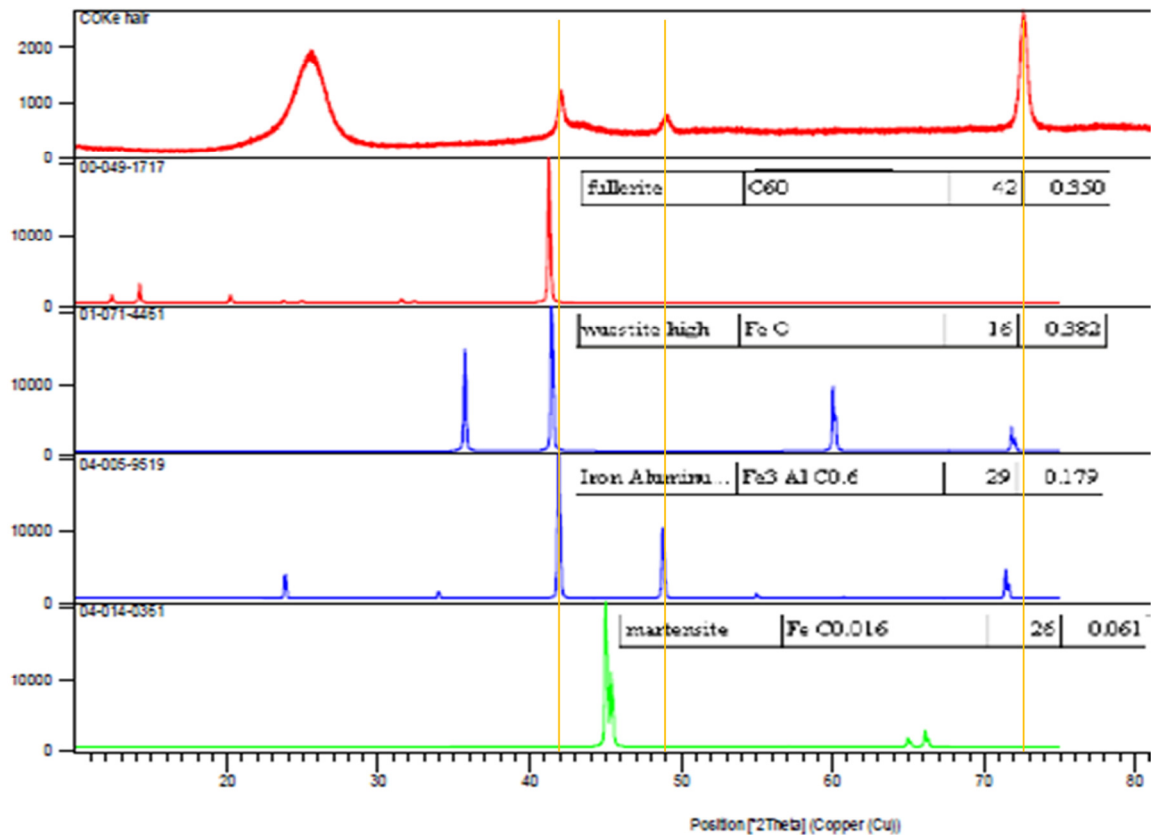


Figure 59 XRD of carbon filaments and various reference compounds with matching peaks

The isolated coke hairs were also ground to a powder and analyzed by XRD. Figure 59 shows the XRD spectrum of the coke hair and several matched compounds. First of all, the XRD detected amorphous carbon (not shown, 00-054-0501) which corroborated the EDS result. Carbon is also detected in the form of fullerenes (00-049-1717). The match of peaks at $2\theta=42^\circ$ is a primary match with carbon compounds. X-ray diffraction also detected several iron compounds present in the sample including $\text{Al}_{3.2}\text{Fe}$ (00-038-1147, not shown), $\text{FeC}_{0.016}$ (04-014-0361), $\text{Fe}_3\text{AlC}_{0.6}$ (04-005-9519) and FeO (01-017-4461). The match with $\text{FeC}_{0.016}$ and $\text{Fe}_3\text{AlC}_{0.6}$ at $2\theta=42^\circ$ and 49° suggest the initiation of coke hairs are by catalytic interactions with iron.

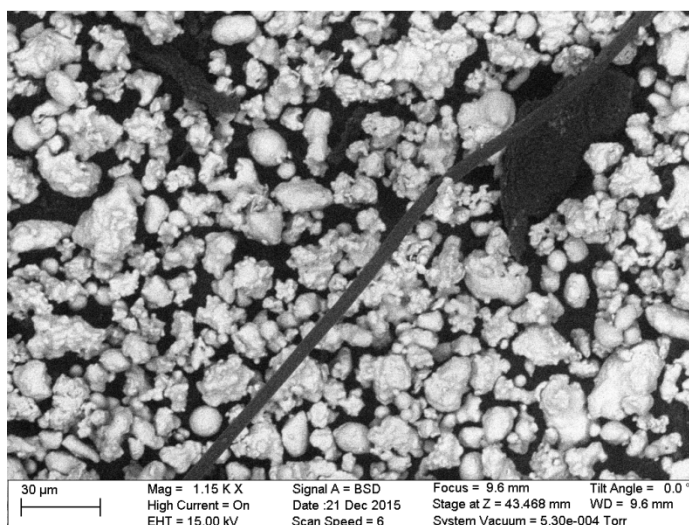


Figure 60 A carbon filament among iron particles generated catalytically at 400 °C in a flow-through reactor

Coke hairs or filamentous carbon formation was investigated in individual direct experiments. Methane decarbonization on iron powder was investigated in a flow-through reactor at 400 °C. The resultant coke product formed on the iron powder was analyzed by SEM. Figure 60 shows carbon filaments produced on the iron powder. Aluminum and pyrite were also tested in this set-up and were found to not form carbon filaments.

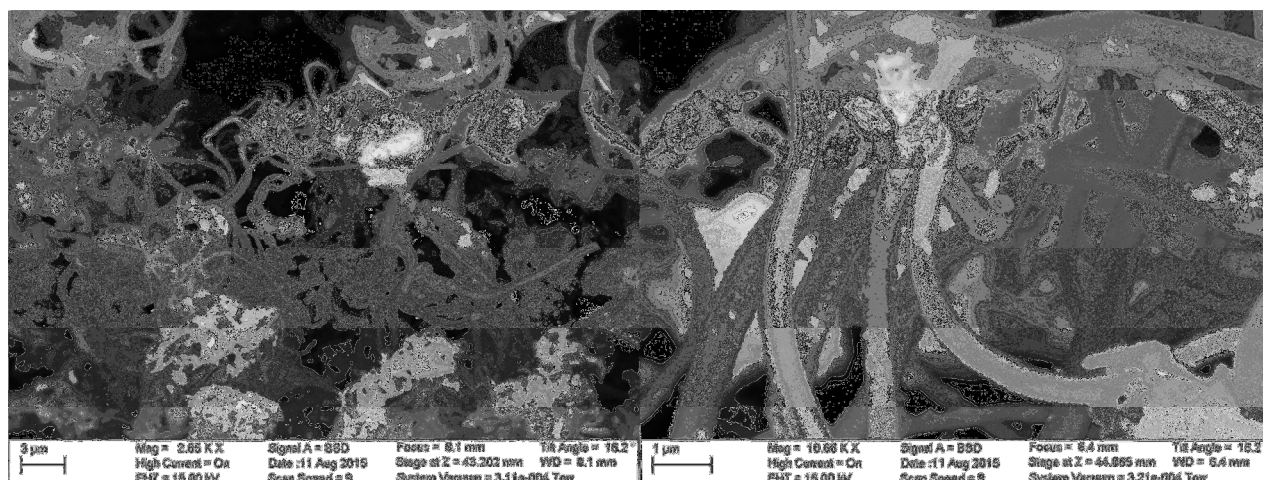


Figure 61 Carbon filament network generated at 270 °C and 40 atm of methane

A separate experiment designed to investigate methane-hydrate formation and dissociation was found to produce carbon filaments through methane decarbonization. In this experiment, CH₄ decomposition at 270 °C and 40 atm created carbon filament deposits on a stainless steel 321 heater during methane-hydrate dissociation. The carbon deposits formed on the heater were analyzed by SEM. Figure 61 shows a network of carbon filaments formed. Iron and nickel catalysts are both present in stainless steel 321, at 70 and 10 wt. %, respectively. The propensity of coke formation on nickel and iron has been previously observed as well as the promotion of coke formation by high pressures.¹³⁸⁻¹⁴⁰ Related work in industrial naphtha cracking reactors at 620 °C and 1.43 atm showed the formation of a dense network of filaments with a diameter between 2 and 5 µm and a length between 20 µm and 1 mm on Incoloy 800H.⁷⁹

The growth of filamentous carbon during catalytic decarbonization of hydrocarbon on 3d metals has been investigated by several researchers. Nickel is most extensively investigated metal substrate.¹³⁸⁻¹⁴³ Helveg et al capture the mechanism of carbon filament growth on Nickel substrate by in-situ tunneling electron microscopy (TEM). The mechanism proceeds by chemisorption where a metal-hydrocarbon complex is formed on the nickel crystallite then

decarbonizes.⁷⁹ The carbonaceous product diffuses and precipitates at the grain boundary.⁷⁹ The carbon precipitate removes the nickel crystallite from the metal structure.⁷⁹ As more carbon is deposited, a carbon filament with a metal tip is grown longitudinally.⁷⁹ Researchers have used scanning tunneling microscopy (STM) and extended x-ray absorption fine structure (EXAFS), as well as XRD and SEM, to characterize such carbon filaments. The carbon filaments produced on iron or nickel is found to be both filamentous and turbostratic.

Laboratory produced carbon filaments are 5-1000 nm in diameter and 5-100 mm in length. The carbon filaments produced in the naphtha cracker have a diameter between 2 and 5 μm and lengths between 20 and 1000 μm . The carbon filaments produced in the flow-through reactor on iron powder were 5.4 μm in diameter and >240 μm in length. The carbon filaments extracted from the methane-hydrate reactor were a dense network of filaments of 0.7 μm in diameter. The carbon filament network was much denser from the methane-hydrate reactor than from the flow-through reactor. This is most likely due to high pressure. It is clear that the coke hairs found in commercial coke samples were much larger in size than carbon filaments from any other sources. This is most likely a function of the high concentration and contact time of coke precursor in the coke oven.

The postulated mechanism for coke hair formation is as follows. During commercial coke production, fissures are formed throughout the coke bed. The fissures are channels by which pyrolysis gas escapes the reacting bed. The iron minerals diffuse to the surface of the coke finger during pyrolysis. Therefore, along a given channel the gas-solid interfaces where iron mineral inclusions exist becomes the site of coke hair formation. The carbon filament initiates by the heterogeneous reactions and precipitate through the mechanism illustrated in the mentioned isolated studies. However, as the carbon filament grows in the longitudinal direction,

noncatalytic heterogeneous reactions involving gas-phase coke precursor assist in the radial growth of the filament. This forms the agglomerated carbonaceous surface topology observed in Figure 56c.

To review, extended residence times of pyrolysis tars promote secondary reactions which increase char, H₂, and CH₄ production while decreasing tar and C₂H₆ production, average tar MW, molar H/C ratio of the tar and results in a broader distribution of nitrogen and sulfur species. In commercial production with large bed diffusion lengths, secondary reactions of volatiles are inevitable. This chapter provides evidential insight that minerals in coal can participate in secondary pyrolysis reactions. It has been shown that minerals in coal diffuse to the surface and participate in catalytic reactions with volatiles. The diffusion and agglomeration of minerals during pyrolysis have been seen in the formation of “silver coke” while the formation of coke hairs have been shown to be due to catalytic reactions between hydrocarbons and iron minerals. Therefore, knowledge of secondary reactions has been successfully applied to explain anomalous coke formation in commercial pyrolysis systems.

Chapter 11: Analysis of Experimental Data

The experiments presented in the previous seven chapters illustrate the complexity of the competing phenomena in coal and biomass pyrolysis. In such a case, fundamental chemical engineering principles must be applied in order to simplify the process. For this, the TG-GC technique is an excellent tool for providing the conversion and production profiles as a function of pyrolysis extent with measured mass closure capability. The proceeding analysis and discussions in this chapter reveals the difficulty in obtaining a kinetically-controlled pyrolysis regime in TG-GC system. For instance, the cup confinement by design has mass transfer limitation. Meanwhile, the pan confinement was known to be more kinetically-controlled than

the cup but, not absolutely kinetically-controlled. The variations in confinement also affect the reaction sequence. For example, the number of Gaussian distributions required for matching the H₂, CO₂, CO, and tar production profiles vary with coal, confinement, and heating rate. This chapter presents (1) a thermodynamic analysis related to secondary tar reaction and (2) data fits enabling the development of “species evolution model” (See Section 2.3).

11.1 Thermodynamics Analysis of Secondary Reactions

The thermodynamic limits of pyrolysis have been previously considered in the literature by experiments and calculations.^{9, 10, 16} Thermochemical equilibrium calculations for biomass pyrolysis predict that solid carbon, CO₂, H₂O, CH₄, and trace amounts of carbon monoxide are preferred products at moderate temperature.^{9, 10} This is perfectly aligned with the natural coalification process.³⁵ The distribution of products at equilibrium are found to be not strongly dependent upon pyrolysis temperature or pressure.¹⁰ Therefore, long exposures of organic matter at elevated temperatures generally approach this bound of solid carbon and stable gaseous products.³³ This indicates at infinitesimally small heating rates, pyrolysis will not produce volatile tar. In the work presented, it was determined by experiment that solid carbon and gases are produced through secondary tar reactions at residence times of ≥ 0.27 seconds and temperatures above 510 °C. Model tar compounds in GasEq were used to investigate the thermodynamics of these reactions.

Benzene and toluene were used as model tar compounds for thermodynamic calculations in GasEq to understand the thermodynamic limitations of tar species at extended residence times. Thermal reaction of benzene and toluene between 300 and 1100 °C have ΔH and ΔS less than zero. This means these reactions are theoretically reactant-favored. Benzene has no coking propensity of reactivity up to 700 °C and very low propensity even at 1000 °C. Toluene was

found to be more reactive. Toluene produces solid carbon above 500 °C, which is a similar result to the TG-GC confinement experiments with coal tar. The same behavior was observed for equimolar mixtures of toluene and benzene. The GasEq analysis confirms that CH₄, C₂H₆, C₂H₄, C₂H₂, H₂ and solid carbon are thermal decomposition products of aromatic species. However as temperature increased from 500 °C, it was found that CH₄ decreased and solid carbon increased. In the TG-GC coal pyrolysis experiments at 3 °C min⁻¹, methane production above 500 °C increased while the solid product being consumed. In the thermodynamic predictions, ethylene, acetylene and hydrogen production increased as coke production increased. Therefore, these species can be considered as products of PAH growth or graphitization. Meanwhile, C₂H₆ production increased until 600 or 700 °C then decreased at higher temperature. The decrease of C₂H₆ production observed in pyrolysis experiments at ~800 °C is therefore attributed to an equilibration of these tar decomposition reactions at the solid-gas interface. We will now take a closer look at C₂H₆ and C₂H₄ formation in coal and biomass pyrolysis.

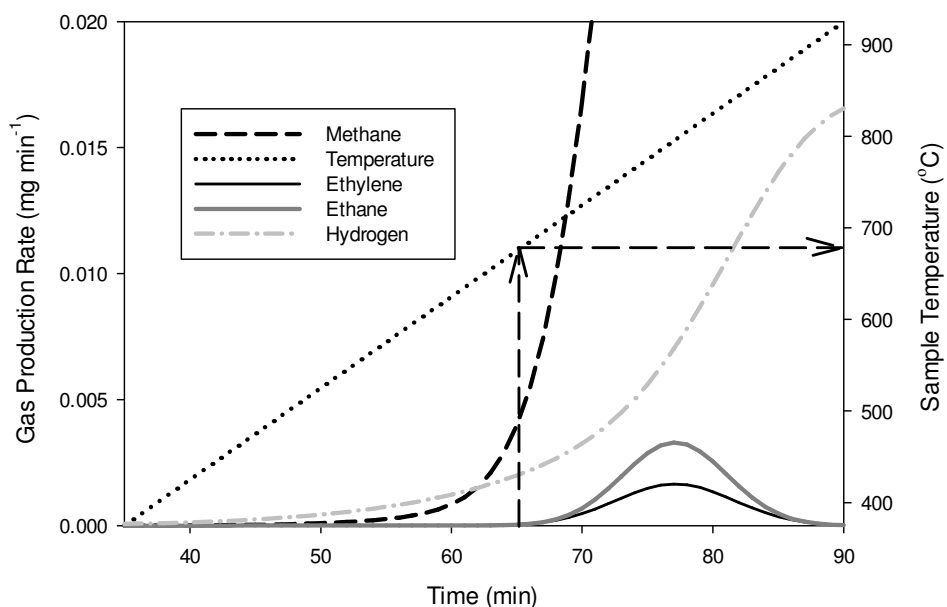


Figure 62 Methane, ethylene, ethane and hydrogen evolution from pyrolysis of Jewell coal

The evolution sequence of gases in pyrolysis is always H_2 , CH_4 , C_2H_6 , and C_2H_4 , all of which occurs after the point of the maximum rate of tar devolatilization. Figure 62 shows this evolution sequence for pyrolysis of Jewell coal. The gaseous hydrocarbon sequence occurs over a temperature range between 375 to 685 °C. Hydrogen at low temperatures is attributed to H_2 from hydrogen-transfer reactions in the metaplast.^{63, 64, 65} Methane evolution begins 100 °C after H_2 initiation and precedes C_2H_6 production by 200 °C. Methane has an exponential increase at 640 °C which is indicated by a crosshair on Figure 62. Ethane and ethylene production begins just 45 °C after the rapid increase in CH_4 production at ~685 °C. We will now look at C_2H_6 and C_2H_4 for pecan shell pyrolysis.

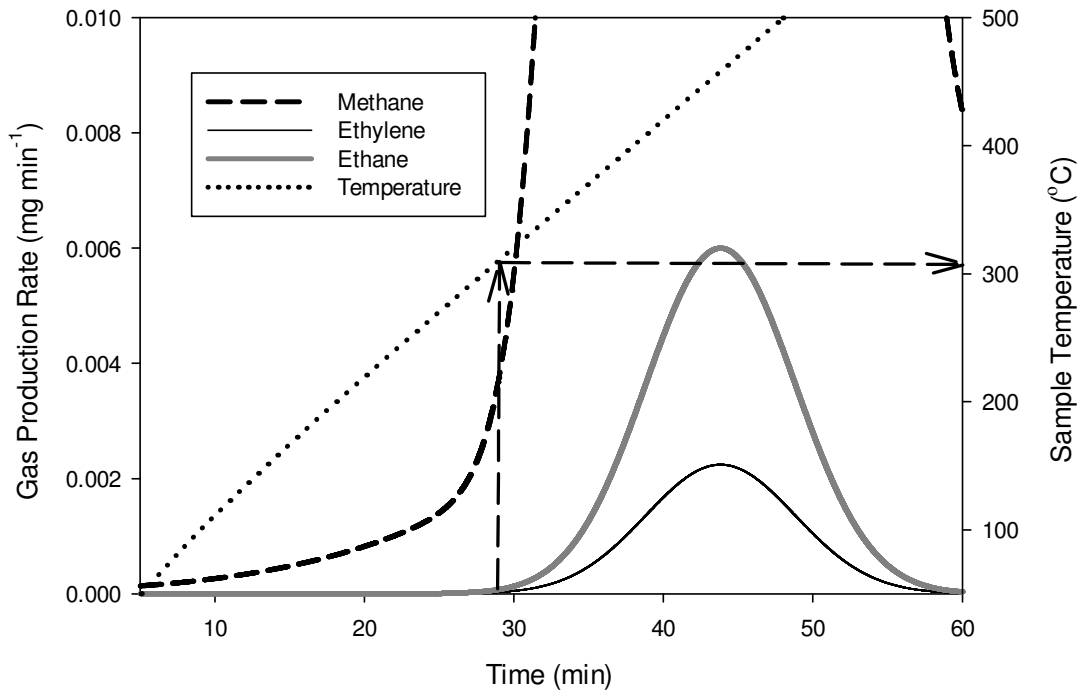


Figure 63 Methane, ethylene, and ethane evolution from pyrolysis of pecan shells

Figure 63 shows the evolution sequence of CH_4 , C_2H_6 , and C_2H_4 for pyrolysis of pecan shells. Hydrogen is not detected by the GC because an appreciable metaplastic state in biomass does not form contrary to suggestions in literature.¹⁴⁴ Intraparticle gas sampling has succeeded in detecting H_2 at 3000 ppm at 300 °C.^{41, 46} The CH_4 profile is similar to that of Jewell coal. Again, C_2H_6 and C_2H_4 are nearly coincident with the exponential rise in CH_4 production. However, for pecan shells pyrolysis, this occurs at 305 °C, which is 380 °C lower than C_2 production from Jewell coal and the productions are comparable. This suggests that C_2H_6 and C_2H_4 production is not a function temperature. The mechanism of C_2H_6 has previously been treated as a primary decomposition product of C-C bonds in the parent structure. This postulation would mean the reaction is temperature dependent. However, this data suggests that CH_4 or hydrogen-donor concentration causes an equilibrium shift in the cracking mechanism between the Fabuss–Smith–

Satterfield and Rice–Kossiakoff mechanism (shown in Figure 21). A shift between these two would explain C_2H_6 and C_2H_4 production as well as the trade-off between CH_4 and H_2 in Figure 26, Figure 36, Figure 44, Figure 45, and Figure 52 from the TG-GC experiments. In Figure 52 for birch wood tar, it should also be noted that ethane and ethylene initiates at 449 °C just after an increase in methane product. This suggests the activation temperature may be dependent on the concentration of substrate. This is an observation in pyrolysis which is uncharted in literature.

This analysis illustrates one of the main points of this work because the analysis is a testament to how difficult it is to observe the intrinsic decomposition kinetics of macromolecules or complex mixtures of molecules. Several accounts in literature target kinetically-controlled regimes. Experimentally, one typically achieves this by decreasing sample length, increasing heating rate, using high inert flow rates or sampling volatile products very near or inside the sample. All of these aim to minimize heat and mass transfer limitations in the system. Another option is performing experiments at multiple heating rates or even in degrees of convective transport and processing the data in a way that normalizes the heat mass transfer limitations.¹⁴⁵ However, it is difficult to ascertain if the system is absolutely intrinsic reaction dominated. This work is directed toward resolving this paradox by (1) analyzing systems on the opposing ends of the spectrum, (2) measuring the nature and extent of secondary reactions in systems, and (3) quantifying the relative residence time of volatile products between the two systems therefore, providing the ability to back calculate the degree at which the system is removed from an ideal system for determining intrinsic kinetics. Of course, the inability to obtain intrinsic kinetics for a reaction inhibits the development of an absolute mechanistic model.

11.2 Exercising the Measured Mass Closure

This section presents an example “species evolution model”. The premise of the model is to simplify the analysis of the competing phenomena in coal and biomass pyrolysis by following fundamental chemical engineering calculations (i.e., material balance). The model relies on fitted product evolution curves from experiments with reported mass closure ($\geq 99.2\%$). The volatile product evolution profiles and the volatile speciation are used to predict the mass loss profile and the C, H, and O composition of the char, respectively. This section demonstrates utility and accuracy of the model giving continuous mathematical functions of reaction profiles. A complete example of the calculations in this section is provided in the Appendix.

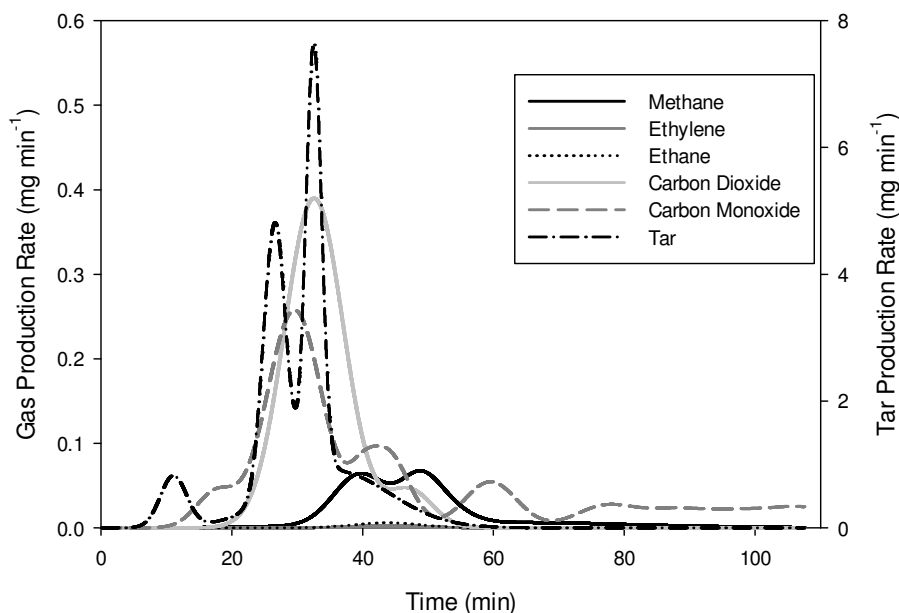


Figure 64 Predicted volatile product evolution from pecan shell pyrolysis

Pecan shell pyrolysis is used to demonstrate the nature of the model, however, similar models were produced for ICG East Gulf, Jewell, and Glamorgan coals. The tar and gas evolution from pecan shell pyrolysis at $10\text{ }^{\circ}\text{C min}^{-1}$ to a temperature of $500\text{ }^{\circ}\text{C}$ have been modeled. Figure 64 shows the predicted CH_4 , C_2H_4 , C_2H_6 , CO_2 , CO , and tar evolution during

pecan shell pyrolysis from summation of Gaussian distributions. The predicted total production of a given species is within 10% error of the measured value where the measured value for the tar is amount measured from the condenser unit. Therefore, the mass closure from experiment is inherent to the model.

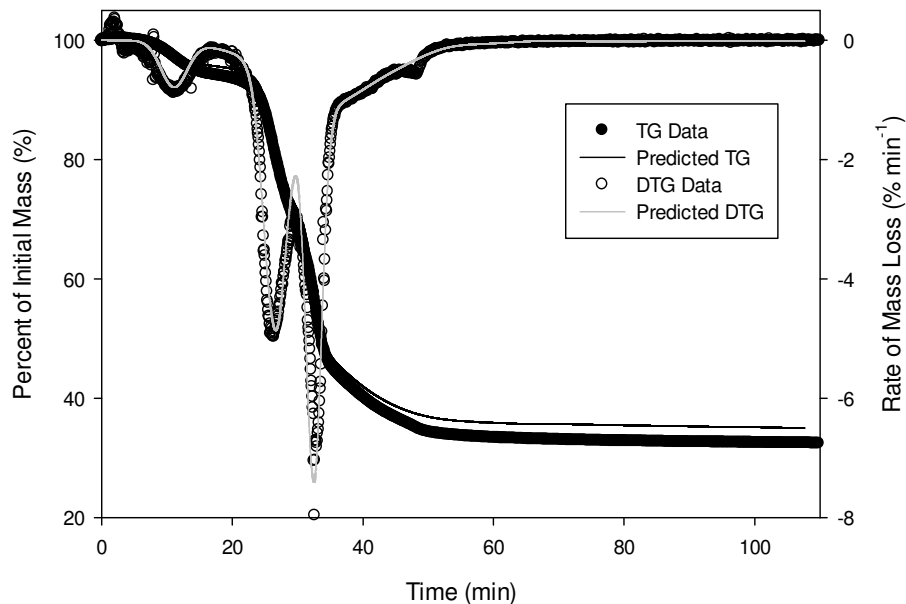


Figure 65 Predicted and measured mass loss profiles

From the summation of the volatile production rates in Figure 65 the total volatile production during pyrolysis may be calculated. The inverse of the volatile production is the rate of conversion of VM with the pecan shell during pyrolysis at $10\text{ }^{\circ}\text{C min}^{-1}$. With the known initial ash composition (by weight), the concentration of ash in the char product throughout pyrolysis can be determined based on the conversion of volatile material. The ash component is considered inert in regards to mass change. Using the volatile conversion and ash composition function, the total sample mass loss can be predicted. The DTG is predicted by taking the first derivative of the mass loss curve as a function of time. Figure 65 shows the predicted mass loss compared to

experimental results. This comparison demonstrates the accuracy of the measured mass closure. The residual mass prediction was overestimated by only 2.5 wt. %. It can be seen that the mass loss and derivative of mass loss curves fits are fair. In the derivative of mass loss, the rate between the first (25 minutes) and second (32 minutes) mass loss peaks are under-predicted. Also, the maximum of the second mass loss peak devolatilization at 32 minutes is under-predicted. The water loss was predicted.

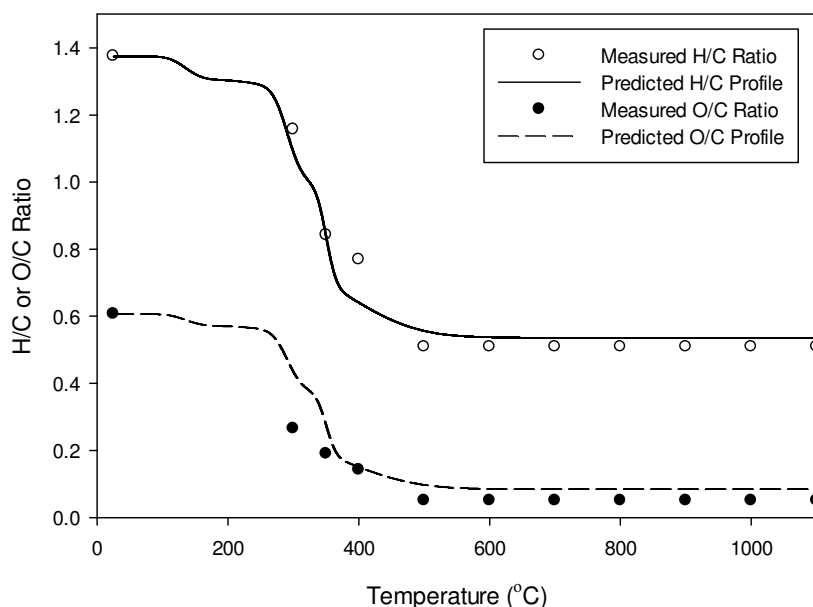


Figure 66 Predicted and measured H/C and O/C ratios of pecan shell char during pyrolysis

The volatile species evolution may be used to predict the carbon, hydrogen and oxygen composition of char as a function of pyrolysis by difference from the known elemental composition of the feedstock. The tar was assumed to have an average elemental composition. Figure 66 shows the molar H/C ratio and molar O/C ratio of the char product as a function of temperature during pyrolysis at $10\text{ }^{\circ}\text{C min}^{-1}$ to $500\text{ }^{\circ}\text{C}$. The ultimate analysis (C, H, and O) of the pecan shells and char at several temperatures were known. The measured values of biomass and

char H/C and O/C ratios are plotted using circles. The model does a good job of predicting the H/C ratio of the char. The only H/C point that diverges from the prediction is at 400 °C. This likely emerges from using a lump tar molecular formula for the entire tar evolution, while in reality the tar molecular composition changes through the process. The final predicted and measured H/C values agree. The O/C ratio of the final char product is predicted fairly well but, also seems unable to predict devolatilization (300-350°C). This is also attributed to the lumped tar approximation. For an accurate prediction of the elemental composition of char, the elemental composition of tar must be accurate. It was shown previously for pecan shells in Figure 45a, that tar is partitioned into four distributions of water, cellulose, hemicellulose and lignin. Through modeling, the elemental composition of the three tar distributions may be adjusted to fit the char elemental composition. Water was separated from the tar evolution. However, tar characterization must be used to confirm this parameter. The tar speciation for pecan shells by GC-MS or LDI-TOF was not sufficient for confirming the biomass tar composition parameter.

Chapter 12: Conclusions and Future Work

In the introduction of this work, the role of solid carbon production in society and nature were explained. In Chapter 2, the scientific literature on biomass and coal pyrolysis was recapitulated. Studying the two pyrolysis systems in parallel helped to analyze the similarities and differences in the reaction mechanisms. The overlying reaction sequence in each system is (1) drying, (2) reaction of hydrolysable functional groups to form crosslinks in the char, (3) tar formation, and (4) thermal cracking reactions resulting in a gas and solid product. The tar formation step is the ultimate difference between the two systems. Secondary reactions are known to occur during the thermal cracking regime for both systems however in this work

secondary reactions in coal pyrolysis were the main focus. The extent of secondary reactions is dependent on pyrolysis conditions.

The presented work expanded the understanding of both primary and secondary pyrolysis reactions. Primary pyrolysis reactions were observed through a novel TG-GC and DRIFTS investigation. First, the mass loss during pyrolysis was correlated to gas species and tar production. Second, the gas and tar production were then correlated to the loss of surface functional group (i.e., hydroxyl, carboxyl, or carbonyl) and increase in char aromaticity. Coal tar products were characterized by LDI-TOF and GC/MC. LDI-TOF revealed a MWD between 220-550 amu in coal tar and GC/MS identified 130 distinct tar species. Secondary tar pyrolysis reactions were extensively studied using the effect of confinement study to show that extended residence time of tars in the solid-gas interface increased char, H₂ and CH₄ production, while production of tar and C₂H₆ decreased. It was also shown that increases in heating rate decreased the effect of confinement by increasing tar transport rates. Similarly, an increase in particle size increased the intraparticle distance through which tars diffused and corresponded to increase solid yield and molar H/C ratios of the gaseous products from secondary cracking reactions. This indicated that cracking reactions within the particle are equally as important to consider as cracking reactions outside the particle. Via ex-situ tar characterization, it was found that extended residence time of pyrolysis tars in the solid-gas interface decreases the average MWD of the tar, decreases the H/C ratio of the tar, and result in a broader distribution of nitrogen and sulfur species. Thermal treatment of tar species revealed that biomass tar has a high propensity for secondary char reactions while coal tar species react to form more stable volatile species.

An investigation was performed to characterize anomalous forms of coke made during commercial pyrolysis. Coke hairs with diameters between 10-50 μm in diameter and lengths up

to 5 cm were found to have formed by catalytic reactions between escaping hydrocarbon species and iron minerals. Silver coke was a result of iron/aluminum minerals diffusing to the coke surface at temperatures above 890 °C. These mechanisms were excellent examples of secondary reactions occurring in commercial systems.

A “species evolution model” that relies on fitted product evolution curves from the summation of Gaussian distributions was developed. The model can predict the mass loss profile, the estimated number of unique pyrolysis reactions and C, H and O composition of the char by-difference. Mass loss, the rate of mass loss and char composition prediction illustrate the measured mass and atomic balances. The TG-GC system was shown to provide sufficient data for measuring complete product distribution and dynamic profiles however, the system is not recommended for consideration of intrinsic kinetics. Thermodynamic predictions confirm the production of char and cracking products from tar above 500 °C observed in experiments. Ethane and ethylene production are considered to be a function of CH₄ or tar concentration at temperatures above 300 °C.

Future work should include the effect of confinement experiments on biomass pyrolysis especially provided the result from biomass tar thermal treatment. The DRIFTS-TG-GC PLS calibration can be expanded as a technique for obtaining pyrolysis kinetic rates and engineering char functionality. This technique is recommended for kinetic estimation because it is non-intrusive in-situ measurement of functional groups reacting on the sample surface. Future work on the DRIFTS-TG-GC technique could also include a non-linear regression calibration. Future DRIFTS analysis on coal pyrolysis would be a unique and valuable contribution to the pyrolysis field. The coke hair product could be investigated in multiwalled carbon nanotube which is a value added solid carbon product.

Appendix

Lists of identified compounds from GC-MS analysis of tar

The lists of identified compounds from GC-MS analysis of tars produced from three coals in two reaction confinements are provided. Each coal was close 99.2 % or greater. The lists are separated by VM content and reaction confinement. The high VM coal is Glamorgan coal, mid VM is Jewell coal, and low VM is ICG East Gulf coal. The retention time, relative percent (area basis), formula, MW and chemical names are provided. From the list, the effect of confinement and VM were inferred.

High VM Coal - Pan

| Ret Time | Relative % | Formula | MW | Name |
|----------|------------|----------|-------|--|
| 56.1 | 0.028 | C10H12O | 148.2 | 6-Methyl-4-indanol |
| 93.4 | 0.106 | C17H12 | 216.3 | 7H-Benzanthrene |
| 66.2 | 0.163 | C13H10O | 182.2 | Benzophenone |
| 17.4 | 0.056 | C11H20 | 152.3 | Bicyclo[4.1.0]heptane, 7-butyl- |
| 13.3 | 0.139 | C9H18 | 126.2 | Cyclopentane, 2-ethyl-1,1-dimethyl- |
| 53.9 | 0.020 | C12H12 | 156.2 | Naphthalene, 1,5-dimethyl- |
| 72.5 | 0.031 | C14H12O | 196.2 | Naphtho[2,1-b]furan, 1,2-dimethyl- |
| 46.3 | 0.097 | C12H22O2 | 198.3 | o-tert-Butyl cyclohexyl acetate 2 |
| 18.3 | 0.018 | C10H16 | 136.2 | (1R)-2,6,6-Trimethylbicyclo[3.1.1]hept-2-ene |
| 36.4 | 0.136 | C8H10O | 122.1 | 1,3,5-Cycloheptatriene, 1-methoxy- |
| 8.7 | 0.018 | C8H16O3 | 160.2 | 1,3-Dioxane-2-propanol, 2-methyl- |
| 23.5 | 0.022 | C13H18O | 190.3 | 1-Hexanone, 5-methyl-1-phenyl- |
| 5.3 | 0.035 | C7H10O3 | 142.1 | 2,2,6-Trimethyl-4H-1,3-dioxin-4-one |
| 71.4 | 0.023 | C14H14 | 182.2 | 2,2'-Dimethylbiphenyl |
| 5.6 | 0.161 | C6H10O2 | 114.1 | 2,3-Dioxabicyclo[2.2.1]heptane, 1-methyl- |
| 98.4 | 0.323 | C36H46O8 | 606.7 | Tetradecapentaenoic acid Derivative |
| 12.0 | 0.239 | C9H18O | 142.2 | 2-Nonanone |
| 67.6 | 0.100 | C14H18O | 202.3 | 2-Phenyl-2,4-octadienol |
| 77.7 | 0.087 | C16H18 | 210.3 | 3,5,3',5'-Tetramethylbiphenyl |
| 36.0 | 0.293 | C9H16O2 | 156.2 | 3-Hexen-1-ol, 2,5-dimethyl-, formate,(Z)- |
| 17.8 | 0.043 | C7H10O2 | 126.1 | 4-Ethyl-2-hydroxycyclopent-2-en-1-one |
| 76.8 | 0.052 | C28H24O2 | 392.4 | 5,12-Di-(2-hydroxyphenyl)paracyclophane |
| 12.4 | 0.051 | C9H18O | 142.2 | 5-Methyl-5-octen-1-ol |
| 65.5 | 0.027 | C13H10O | 182.2 | 6H-Dibenzo[b,d]-pyran |

| | | | | |
|-------|--------|-----------|-------|--|
| 106.6 | 1.635 | C30H44O11 | 580.6 | Cyclopenta[a]cyclopropa[f]cycloundecene Derivative |
| 7.1 | 0.069 | C7H12O | 112.2 | 7-Oxabicyclo[4.1.0]heptane, 1-methyl- |
| 75.6 | 0.079 | C15H14 | 194.2 | 9H-Fluorene, 2,3-dimethyl- |
| 69.6 | 0.088 | C14H12 | 180.2 | 9H-Fluorene, 4-methyl- |
| 69.9 | 0.075 | C14H12 | 180.2 | 9H-Fluorene, 9-methyl- |
| 73.5 | 0.067 | C14H10 | 178.2 | 9H-Fluorene, 9-methylene- |
| 73.5 | 0.063 | C14H10 | 178.2 | Anthracene |
| 79.3 | 0.791 | C15H12 | 192.2 | Anthracene, 2-methyl- |
| 20.9 | 0.015 | C11H14O | 162.2 | Benzene, 1-methyl-4-[(2-propenyloxy)methyl]- |
| 73.0 | 0.037 | C15H16 | 196.3 | Benzene, 3,5-dimethyl-1-(phenylmethyl)- |
| 66.2 | 0.171 | C13H10O | 182.2 | Benzophenone |
| 73.6 | 0.354 | C14H12O2 | 212.2 | Benzyl Benzoate |
| 14.8 | 0.044 | C8H12O | 124.2 | Bicyclo[2.1.1]hexan-2-ol, 2-ethenyl- |
| 108.7 | 68.508 | C24H38O4 | 390.5 | Bis(2-ethylhexyl) phthalate |
| 13.1 | 0.296 | C9H18 | 126.2 | Cyclohexane, 1,1,2-trimethyl- |
| 10.0 | 0.574 | C9H18 | 109.1 | Cyclohexane, 1,1,3-trimethyl- |
| 14.1 | 0.031 | C27H54 | 378.6 | Cyclohexane, 1,3,5-trimethyl-2-octadecyl- |
| 6.4 | 0.078 | C8H16 | 112.2 | Cyclohexane, 1,3-dimethyl-, cis- |
| 10.5 | 1.040 | C9H18 | 126.2 | Cyclohexane, 1-ethyl-2-methyl-, cis- |
| 16.2 | 0.054 | C9H18 | 126.2 | Cyclohexane, 1-ethyl-4-methyl-, cis- |
| 17.0 | 0.169 | C16H32 | 224.4 | Cyclohexane, decyl- |
| 18.0 | 0.114 | C8H14O | 126.2 | Cyclohexanone, 2,3-dimethyl- |
| 83.7 | 0.026 | C18H22 | 238.3 | Cyclopent[a]indene Derivative |
| 13.3 | 0.100 | C9H18 | 126.2 | Cyclopentane, 2-ethyl-1,1-dimethyl- |
| 6.9 | 0.044 | C8H16 | 112.2 | Cyclopropane, pentyl- |
| 83.9 | 0.043 | C26H50O2 | 394.6 | Cyclopropanetetradecanoic acid |
| 5.8 | 0.152 | C13H28 | 184.3 | Decane, 2,5,6-trimethyl- |
| 24.6 | 0.085 | C13H28 | 184.3 | Decane, 2,5,9-trimethyl- |
| 10.3 | 0.057 | C13H28 | 184.3 | Decane, 2,6,6-trimethyl- |
| 18.8 | 0.085 | C13H28 | 184.3 | Decane, 2,6,7-trimethyl- |
| 21.6 | 0.172 | C13H28 | 184.3 | Decane, 6-ethyl-2-methyl- |
| 18.5 | 0.114 | C14H26O | 210.3 | E-11,13-Tetradecadien-1-ol |

| | | | | |
|-------|--------|----------|-------|---|
| 73.9 | 0.067 | C17H26O | 246.4 | Ethanone Derivative |
| 47.0 | 0.021 | C10H22O | 158.3 | Ether, tert-butyl 3,3-dimethylbutyl |
| 58.1 | 0.063 | C11H22O2 | 186.3 | Formic acid, decyl ester |
| 114.5 | 0.468 | C20H26O6 | 362.4 | Gibbane-1,10-dicarboxylic acid |
| 18.9 | 0.069 | C19H40 | 268.5 | Heptadecane, 2,6-dimethyl- |
| 83.1 | 0.048 | C16H12 | 204.2 | Indeno[2,1-a]indene, 5,10-dihydro- |
| 83.1 | 0.046 | C16H16O | 224.3 | Isobenzofuran, 1,3-dihydro-1,1-dimethyl-3-phenyl- |
| 69.4 | 0.138 | C13H16O2 | 204.2 | Methanone, (1-hydroxycyclohexyl)phenyl- |
| 62.3 | 0.041 | C13H14 | 170.2 | Naphthalene, 1,4,6-trimethyl- |
| 52.8 | 0.221 | C12H12 | 156.2 | Naphthalene, 1,5-dimethyl- |
| 58.9 | 0.383 | C13H14 | 170.2 | Naphthalene, 1,6,7-trimethyl- |
| 45.6 | 0.125 | C11H10 | 142.2 | Naphthalene, 2-methyl- |
| 71.8 | 0.141 | C14H12O | 196.2 | Naphtho[2,1-b]furan, 1,2-dimethyl- |
| 83.9 | 0.120 | C16H32O2 | 256.4 | n-Hexadecanoic acid |
| 15.9 | 1.432 | C9H20 | 128.2 | Nonane |
| 102.7 | 0.100 | C26H54 | 366.6 | Octadecane, 3-ethyl-5-(2-ethylbutyl)- |
| 9.8 | 0.789 | C14H28 | 196.3 | Octane, 2-cyclohexyl- |
| 12.8 | 0.207 | C9H20 | 128.2 | Octane, 4-methyl- |
| 4.3 | 0.019 | C8H14O3 | 158.2 | Octanoic acid, 7-oxo- |
| 51.2 | 0.161 | C12H22O2 | 198.3 | o-tert-Butyl cyclohexyl acetate 1 |
| 55.6 | 0.029 | C12H14O3 | 206.2 | Oxiranecarboxylic acid Derivative |
| 85.0 | 0.376 | C16H14 | 206.3 | Phenanthrene, 2,7-dimethyl- |
| 80.7 | 0.096 | C15H12 | 192.2 | Phenanthrene, 4-methyl- |
| 76.2 | 0.136 | C15H14 | 194.2 | Phenanthrene, 9,10-dihydro-1-methyl- |
| 44.4 | 0.022 | C11H14O2 | 178.2 | Phenol, 3-(1-methylethyl)-, acetate |
| 32.7 | 0.115 | C10H12O2 | 164.2 | Phenol, 3,4-dimethyl-, acetate |
| 16.8 | 0.115 | C9H16 | 124.2 | Propylidencyclohexane |
| 69.3 | 0.076 | C16H20 | 212.3 | Pyrene, 1,2,3,3a,4,5,9,10,10a,10b-decahydro- |
| 86.8 | 0.013 | C16H14 | 206.3 | Pyrene, 4,5,9,10-tetrahydro- |
| 6.0 | 16.528 | C7H8 | 92.1 | Toluene |
| 14.4 | 0.195 | C16H32 | 224.4 | Trans-1-methyl-2-nonyl-cyclohexane |
| 58.0 | 0.148 | C14H22O | 206.3 | α Isomethyl ionone |

High VM Coal - Cup

| Ret Time | Relative % | Formula | MW | Name |
|----------|------------|----------|-------|---|
| 74.6 | 0.029 | C10H8O | 144.2 | 1-Naphthalenol |
| 82.3 | 0.014 | C19H24O2 | 284.4 | 5,7,9(11)-Androstatriene, 3-hydroxy-17-oxo- |
| 70.3 | 0.023 | C20H24O2 | 296.4 | 5,8,11,14-Eicosatetraynoic acid |
| 138.2 | 0.173 | C28H40O2 | 112.3 | Anthiaergostan-5,7,9,22-tetraen-14-ol-15-one |
| 108.6 | 0.505 | C24H38O4 | 390.5 | Bis(2-ethylhexyl) phthalate |
| 74.0 | 0.055 | C16H14 | 206.3 | ,4-Dihydro-1,4-ethanoanthracene |
| 76.2 | 0.952 | C16H18 | 210.3 | 1,1'-Biphenyl, 3,4-diethyl- |
| 53.3 | 0.002 | C7H14O2 | 130.2 | 1,2-Cyclohexanediol, 1-methyl-, trans- |
| 73.5 | 0.006 | C12H18 | 162.2 | 1,3,5,6,7-Pentamethylbicyclo[3.2.0]hepta-2,6-diene |
| 12.2 | 0.100 | C8H10 | 106.2 | 1,3-Cyclopentadiene, 5-(1-methylethylidene)- |
| 63.7 | 0.002 | C10H12O3 | 180.2 | 1,3-Cyclopentadiene-1-carboxylic acid Derivative |
| 52.2 | 0.006 | C8H10O2 | 138.1 | 1,4-Benzenediol, 2,5-dimethyl- |
| 76.4 | 0.009 | C10H12O3 | 180.2 | 1,6,7-Naphthalenetriol, 5,6,7,8-tetrahydro-, cis- |
| 71.5 | 0.083 | C15H16 | 197.2 | 1,7-Dimethyl-3-phenyltricyclo[4.1.0.0(2,7)]hept-3-ene |
| 79.3 | 1.501 | C15H12 | 192.2 | 1H-Cyclopropa[l]phenanthrene,1a,9b-dihydro- |
| 60.1 | 0.155 | C10H8O | 144.2 | 1-Naphthalenol |
| 65.4 | 0.195 | C11H10O | 158.2 | 1-Naphthalenol, 2-methyl- |
| 68.3 | 0.036 | C16H18O | 226.3 | Naphthalenone Derivative |
| 67.6 | 0.003 | C15H18O2 | 230.3 | 2,4,6-Cycloheptatrien-1-one Derivative |
| 148.0 | 0.395 | C30H48 | 408.6 | 2,6,10,14,18,22-Tetracosahexaene Derivative |
| 6.4 | 0.006 | C7H12O | 112.2 | 2-Cyclohexen-1-ol, 1-methyl- |
| 7.4 | 0.003 | C7H12O | 112.2 | 2-Methylenecyclohexanol |
| 11.3 | 0.078 | C6H12O2 | 116.1 | 2-Pentanone, 4-hydroxy-4-methyl- |
| 56.6 | 0.008 | C10H10O | 146.2 | 2-Propyn-1-ol, 3-(4-methylphenyl)- |
| 61.1 | 0.015 | C10H10O2 | 162.2 | 3(2H)-Benzofuranone, 4,7-dimethyl- |
| 14.7 | 0.014 | C12H14O2 | 190.2 | 3(2H)-Furanone, dihydro-2,2-dimethyl-5-phenyl- |
| 63.5 | 0.021 | C20H28O3 | 316.4 | 3-Methoxy-D-homoestra-trien-diol |
| 83.1 | 0.894 | C19H24O2 | 284.4 | 5,7,9(11)-Androstatriene, 3-hydroxy-17-oxo- |
| 74.8 | 0.057 | C20H24O2 | 296.4 | 5,8,11,14-Eicosatetraynoic acid |
| 70.5 | 0.009 | C21H26O2 | 310.4 | 5,8,11,14-Eicosatetraynoic acid, methyl ester |
| 95.6 | 0.062 | C22H30O7 | 406.4 | 5H-Cyclopropabenzazulen-5-one Derivative |

| | | | | |
|-------|--------|----------|-------|---|
| 54.7 | 0.079 | C10H12O | 148.2 | 6-Methyl-4-indanol |
| 82.4 | 0.017 | C11H10O | 158.2 | 7-Methyl-1-naphthol |
| 7.3 | 0.009 | C7H12O | 112.2 | 7-Oxabicyclo[4.1.0]heptane, 1-methyl- |
| 90.3 | 0.025 | C14H12 | 180.2 | 9H-Fluorene, 4-methyl- |
| 69.9 | 0.037 | C14H12 | 180.2 | 9H-Fluorene, 9-methyl- |
| 61.2 | 0.019 | C11H18O4 | 214.2 | Acetic acid, 1,4-dioxa-spiro[4.6]undec-6-yl ester |
| 103.4 | 0.041 | C28H40O2 | 408.6 | Anthiaergostan-5,7,9,22-tetraen-14-ol-15-one |
| 73.5 | 0.370 | C14H10 | 178.2 | Anthracene |
| 3.2 | 0.037 | C6H6 | 78.1 | Benzene |
| 20.9 | 0.004 | C17H28 | 232.4 | Benzene, (1-methyldecyl)- |
| 25.7 | 0.001 | C11H14O | 162.2 | Benzene, 1-methyl-4-[(2-propenyloxy)methyl]- |
| 66.2 | 0.066 | C13H10O | 182.2 | Benzophenone |
| 108.6 | 90.756 | C24H38O4 | 390.5 | Bis(2-ethylhexyl) phthalate |
| 6.0 | 0.029 | C7H8 | 92.1 | Cyclobutene, 2-propenylidene- |
| 20.9 | 0.002 | C9H12 | 120.2 | Cyclohexene, 1-(1-propynyl)- |
| 8.6 | 0.004 | C13H28 | 184.3 | Decane, 2,4,6-trimethyl- |
| 6.8 | 0.004 | C13H28 | 184.3 | Decane, 2,5,9-trimethyl- |
| 9.2 | 0.002 | C11H24O | 172.3 | Ether, hexyl pentyl |
| 75.2 | 0.051 | C10H8O | 144.2 | Furan, 3-phenyl- |
| 80.9 | 1.351 | C23H48 | 324.6 | Heptadecane, 9-hexyl- |
| 84.1 | 0.170 | C36H58O6 | 586.8 | Hexadecanoic acid Derivative |
| 69.4 | 0.048 | C24H46O7 | 446.6 | Hexanoic acid Derivative |
| 71.0 | 0.103 | C13H16 | 172.2 | Naphthalene, 1,4-dihydro-2,5,8-trimethyl- |
| 94.9 | 0.021 | C14H12O | 196.2 | Naphtho[2,1-b]furan, 1,2-dimethyl- |
| 45.5 | 0.002 | C10H20O2 | 172.2 | n-Decanoic acid |
| 65.2 | 0.003 | C15H22O2 | 234.3 | Nootkaton-11,12-epoxide |
| 142.9 | 0.235 | C26H54 | 366.6 | Octadecane, 3-ethyl-5-(2-ethylbutyl)- |
| 101.3 | 0.025 | C30H50O6 | 506.6 | Olean-ene-hexol |
| 102.5 | 0.049 | C38H74O2 | 562.9 | Oleic acid, eicosyl ester |
| 50.8 | 0.015 | C7H8O2 | 124.1 | Orcinol |
| 15.2 | 0.001 | C7H14O | 114.2 | Oxirane, 2-butyl-3-methyl-, cis- |
| 25.4 | 0.004 | C7H6O2 | 122.1 | p-Benzoquinone, 2-methyl- |

| | | | | |
|-------|-------|----------|-------|--|
| 66.7 | 0.042 | C14H18 | 186.3 | Phenanthrene, 1,2,3,4,5,6,7,8-octahydro- |
| 85.1 | 0.167 | C16H14 | 206.3 | Phenanthrene, 2,7-dimethyl- |
| 99.6 | 0.191 | C15H14 | 194.2 | Phenanthrene, 9,10-dihydro-1-methyl- |
| 44.4 | 0.002 | C9H12O | 136.2 | Phenol, 3-ethyl-5-methyl- |
| 49.3 | 0.028 | C9H10O | 134.2 | Phenol, 4-(2-propenyl)- |
| 94.3 | 0.212 | C20H28O6 | 364.4 | Phorbol |
| 47.4 | 0.007 | C10H10O4 | 194.2 | Phthalic acid, monoethyl ester |
| 142.7 | 0.169 | C28H42O8 | 506.6 | Pregn-5-en-20-one Derivative |
| 163.1 | 0.019 | C20H34O4 | 338.4 | Tetrahydroaraucarolone |
| 6.0 | 0.015 | C7H8 | 92.1 | Toluene |
| 40.5 | 0.004 | C9H18O | 142.2 | trans-2,3-Epoxy-nonane |
| 95.2 | 0.152 | C18H16 | 232.3 | Triphenylene, 1,2,3,4-tetrahydro- |

Mid VM Coal – Pan

| Ret Time | Relative % | Formula | MW | Name |
|----------|------------|----------|-------|---|
| 4.2 | 0.418 | C6H10O2 | 114.1 | 2,3-Dioxabicyclo[2.2.1]heptane, 1-methyl- |
| 12.4 | 0.696 | C16H20 | 212.3 | 2,6-Diisopropylnaphthalene |
| 7.8 | 6.746 | C9H18O | 142.2 | 2-Nonanone |
| 13.1 | 0.220 | C27H46O2 | 402.6 | Cholestan-22(26)-isoepoxy-3 β -ol |
| 6.0 | 24.786 | C8H16 | 112.2 | Cyclohexane, 1,3-dimethyl-, cis- |
| 59.5 | 0.041 | C13H28 | 184.3 | Decane, 2,4,6-trimethyl- |
| 83.9 | 0.355 | C16H32O2 | 256.4 | n-Hexadecanoic acid |
| 5.5 | 0.253 | C8H16O | 128.2 | Pentane, 1-(2-propenyloxy)- |
| 75.9 | 0.141 | C15H14 | 194.2 | Phenanthrene, 9,10-dihydro-1-methyl- |
| 81.6 | 0.047 | C16H16 | 208.3 | 1,2,5,6-Tetramethylacenaphthylene |
| 18.3 | 0.100 | C20H30O4 | 334.4 | 1,2-Benzenedicarboxylic acid, butyl octyl ester |
| 88.5 | 0.040 | C34H70 | 490.8 | 15-Methyltrtriacontane |
| 69.4 | 0.050 | C7H12O3 | 144.2 | 1-Hydroxycyclohexanecarboxylic acid |
| 5.3 | 0.062 | C7H10O3 | 142.1 | 2,2,6-Trimethyl-4H-1,3-dioxin-4-one |
| 4.3 | 0.111 | C6H10O2 | 114.1 | 2,3-Dioxabicyclo[2.2.1]heptane, 1-methyl- |
| 22.1 | 0.232 | C36H46O8 | 606.7 | Tetradecapentaenoic acid Derivative |
| 14.0 | 2.538 | C16H20 | 212.3 | 2,6-Diisopropylnaphthalene |
| 3.9 | 0.082 | C7H14O | 114.2 | 2-Hexanone, 4-methyl- |

| | | | | |
|-------|-------|----------|-------|--|
| 12.1 | 0.385 | C9H18O | 142.2 | 2-Nonanone |
| 78.5 | 0.089 | C19H40 | 268.5 | 3,3-Diethylpentadecane |
| 24.6 | 0.222 | C25H36O7 | 448.5 | 4,13,20-Tri-O-methylphorbol 12-acetate |
| 80.9 | 0.071 | C22H46 | 310.5 | 5-Ethyl-5-methylnonadecane |
| 21.6 | 0.267 | C21H44 | 296.5 | 7,7-Diethylheptadecane |
| 138.1 | 1.175 | C19H34O6 | 358.4 | Heptanoic acid Derivative |
| 106.2 | 0.080 | C15H12 | 192.2 | 8,9-Dihydrocyclopenta[def]phenanthrene |
| 15.4 | 0.321 | C15H14 | 194.2 | 9H-Fluorene, 2,3-dimethyl- |
| 13.3 | 0.504 | C14H12 | 180.2 | 9H-Fluorene, 4-methyl- |
| 13.4 | 1.016 | C14H12 | 180.2 | 9H-Fluorene, 9-methyl- |
| 14.7 | 0.418 | C14H10 | 178.2 | 9H-Fluorene, 9-methylene- |
| 16.8 | 2.190 | C15H12 | 192.2 | Anthracene, 2-methyl- |
| 3.2 | 1.328 | C6H6 | 78.1 | Benzene |
| 77.7 | 0.110 | C15H14O | 210.2 | Benzene, 1-methoxy-3-(2-phenylethenyl)- |
| 12.0 | 0.692 | C13H10O | 182.2 | Benzophenone |
| 144.9 | 2.812 | C24H38O4 | 390.5 | Bis(2-ethylhexyl) phthalate |
| 21.3 | 0.140 | C28H54 | 390.7 | Cyclohexane, 1,1'-(2-tridecyl-1,3-propanediyl)bis- |
| 8.9 | 0.773 | C9H18 | 126.2 | Cyclohexane, 1,1,2-trimethyl- |
| 7.1 | 1.546 | C9H18 | 126.2 | Cyclohexane, 1,1,3-trimethyl- |
| 6.3 | 2.684 | C8H16 | 112.2 | Cyclohexane, 1,3-dimethyl-, cis- |
| 9.3 | 0.107 | C9H18 | 126.2 | Cyclohexane, 1-ethyl-2-methyl-, cis- |
| 10.4 | 1.890 | C9H18 | 126.2 | Cyclohexane, 1-ethyl-2-methyl-, cis- |
| 9.6 | 1.040 | C9H18 | 126.2 | Cyclohexane, 1-ethyl-4-methyl-, cis- |
| 10.1 | 0.505 | C16H32 | 224.4 | Cyclohexane, decyl- |
| 9.2 | 0.754 | C9H18 | 126.2 | Cyclopentane, 2-ethyl-1,1-dimethyl- |
| 17.2 | 0.097 | C11H22 | 154.3 | Cyclopropane, 1-butyl-2-(2-methylpropyl)- |
| 7.3 | 0.890 | C13H28 | 184.3 | Decane, 2,5,6-trimethyl- |
| 10.5 | 0.837 | C13H28 | 184.3 | Decane, 2,5,9-trimethyl- |
| 164.6 | 0.101 | C22H18 | 282.3 | Dibenz[a,h]anthracene, 5,6,12,13-tetrahydro- |
| 110.3 | 0.086 | C16H22O4 | 278.3 | Dibutyl phthalate |
| 13.7 | 0.208 | C16H34 | 226.4 | Dodecane, 2-methyl-6-propyl- |
| 17.1 | 0.324 | C14H26O | 210.3 | E-11,13-Tetradecadien-1-ol |

| | | | | |
|-------|--------|----------|-------|---|
| 83.4 | 0.117 | C17H32O2 | 252.4 | E-2-Methyl-3-tetradecen-1-ol acetate |
| 6.8 | 0.040 | C11H22O2 | 186.3 | Formic acid, decyl ester |
| 140.8 | 0.089 | C22H46 | 310.5 | Heneicosane, 3-methyl- |
| 13.9 | 1.715 | C10H22 | 142.3 | Heptane, 4-propyl- |
| 77.4 | 0.057 | C17H34O2 | 270.4 | i-Propyl 12-methyl-tridecanoate |
| 60.1 | 0.088 | C13H14 | 170.2 | Naphthalene, 1,6,7-trimethyl- |
| 18.0 | 0.481 | C16H12 | 204.2 | Naphthalene, 2-phenyl- |
| 18.5 | 0.163 | C16H32O2 | 256.4 | n-Hexadecanoic acid |
| 9.7 | 1.212 | C9H20 | 128.2 | Nonane |
| 84.3 | 0.099 | C19H40 | 268.5 | Octadecane, 6-methyl- |
| 6.9 | 0.069 | C14H28 | 196.3 | Octane, 2-cyclohexyl- |
| 8.6 | 0.410 | C9H20 | 128.2 | Octane, 4-methyl- |
| 4.9 | 0.053 | C8H16O | 128.2 | Pentane, 1-(2-propenyloxy)- |
| 18.8 | 1.641 | C16H14 | 206.3 | Phenanthrene, 2,7-dimethyl- |
| 15.9 | 3.731 | C15H14 | 194.2 | Phenanthrene, 9,10-dihydro-1-methyl- |
| 94.3 | 0.179 | C20H28O6 | 364.4 | Phorbol |
| 97.1 | 0.054 | C28H32O3 | 416.5 | Pregna-5,8(9),16-triene-3 β -ol-20-one benzoate |
| 10.0 | 1.071 | C9H16 | 124.2 | Propylidencyclohexane |
| 157.2 | 0.176 | C27H40O4 | 428.5 | Spirost-8-en-11-one Derivative |
| 5.7 | 27.977 | C7H8 | 92.1 | Toluene |

Mid VM - Cup

| Ret Time | Relative % | Formula | MW | Name |
|----------|------------|----------|-------|---------------------------------------|
| 77.7 | 0.219 | C16H18 | 210.3 | 1,1'-Biphenyl, 3,4-diethyl- |
| 75.3 | 0.053 | C20H40 | 280.5 | Hexadecene Derivative |
| 56.0 | 0.036 | C10H12O | 148.2 | 6-Methyl-4-indanol |
| 10.0 | 0.041 | C13H28 | 184.3 | Decane, 2,5,6-trimethyl- |
| 60.4 | 0.079 | C13H14 | 170.2 | Naphthalene, 2,3,6-trimethyl- |
| 84.0 | 0.545 | C16H32O2 | 256.4 | n-Hexadecanoic acid |
| 92.6 | 0.123 | C26H54 | 366.6 | Octadecane, 3-ethyl-5-(2-ethylbutyl)- |
| 49.0 | 0.016 | C12H22O2 | 198.3 | o-tert-Butyl cyclohexyl acetate 1 |
| 86.2 | 0.174 | C16H14 | 206.3 | Phenanthrene, 2,7-dimethyl- |
| 38.1 | 0.031 | C10H12O2 | 164.2 | Phenol, 3,4-dimethyl-, acetate |

| | | | | |
|------|-------|----------|-------|---|
| 14.7 | 0.044 | C11H18O2 | 182.2 | Hydroxymethyl-methoxy-trans-bicyclononene |
| 76.5 | 0.324 | C16H18 | 210.3 | 1,1'-Biphenyl, 3,4-diethyl- |
| 81.4 | 0.129 | C16H16 | 208.3 | 1,2,5,6-Tetramethylacenaphthylene |
| 29.6 | 0.023 | C10H14O2 | 166.2 | 1,2-Butanediol, 1-phenyl- |
| 25.9 | 0.024 | C8H16O3 | 160.2 | 1,3-Dioxolane-2-butanol, 2-methyl- |
| 74.8 | 0.057 | C17H20 | 224.3 | Tetramethyl-phenylbicycloheptadiene |
| 73.0 | 0.098 | C15H16 | 196.3 | Dimethylphenyltricycloheptene |
| 39.0 | 0.092 | C10H22O2 | 174.3 | 1,7-Octanediol, 3,7-dimethyl |
| 75.2 | 0.053 | C15H32O | 228.4 | 1-Dodecanol, 3,7,11-trimethyl- |
| 79.3 | 1.224 | C15H12 | 192.2 | 1H-Cyclopropa[l]phenanthrene,1a,9b-dihydro- |
| 45.6 | 0.063 | C11H10 | 142.2 | 1H-Indene, 1-ethylidene- |
| 82.9 | 0.264 | C16H30O2 | 254.4 | 2(3H)-Furanone, 5-dodecyldihydro- |
| 67.1 | 0.089 | C16H18O | 226.3 | Naphthalenone Derivative |
| 5.1 | 0.050 | C7H10O3 | 142.1 | 2,2,6-Trimethyl-4H-1,3-dioxin-4-one |
| 64.7 | 0.047 | C14H14 | 182.2 | 2,2'-Dimethylbiphenyl |
| 70.4 | 0.178 | C16H26O3 | 266.3 | 2,5-Furandione, 3-dodecyl- |
| 97.4 | 0.301 | C30H48 | 408.6 | Tetracosahexaene Derivative |
| 25.7 | 0.048 | C15H30O2 | 242.4 | 2-Acetoxytridecane |
| 5.0 | 0.021 | C9H18O2 | 158.2 | 2-Hexanone, 4-hydroxy-3-propyl- |
| 35.5 | 0.156 | C9H16O | 140.2 | 2-Methyl-4-octenal |
| 39.3 | 0.354 | C6H12O2 | 116.1 | 2-Pentanone, 4-hydroxy-4-methyl- |
| 60.1 | 0.080 | C13H14 | 170.2 | 3-(2-Methyl-propenyl)-1H-indene |
| 78.6 | 0.140 | C19H40 | 268.5 | 3,3-Diethylpentadecane |
| 67.9 | 0.050 | C17H36 | 240.4 | 3,3-Diethyltridecane |
| 77.7 | 0.211 | C16H18 | 210.3 | 3,5,3',5'-Tetramethylbiphenyl |
| 35.9 | 0.072 | C9H16O2 | 156.2 | 3-Hexen-1-ol, 2,5-dimethyl-, formate,(Z)- |
| 5.5 | 0.047 | C6H10O | 98.1 | 4-Penten-2-one, 4-methyl- |
| 82.9 | 0.562 | C19H24O2 | 284.4 | 5,7,9(11)-Androstatriene, 3-hydroxy-17-oxo |
| 40.1 | 0.056 | C12H26 | 170.3 | 5-Ethyldecane |
| 8.2 | 0.023 | C8H14O | 126.2 | 6,6-Dimethyl-cyclohex-2-en-1-ol |
| 73.3 | 0.207 | C17H26O5 | 310.3 | Pyran Derivative |
| 66.7 | 0.035 | C13H10O | 182.2 | 6H-Dibenzo[b,d]-pyran |

| | | | | |
|-------|--------|----------|-------|---|
| 56.0 | 0.030 | C10H12O | 148.2 | 6-Methyl-4-indanol |
| 88.2 | 0.236 | C21H44 | 296.5 | 7,7-Diethylheptadecane |
| 39.1 | 0.045 | C10H20O | 156.2 | 7-Octen-2-ol, 2,6-dimethyl- |
| 74.0 | 0.044 | C20H18O2 | 290.3 | 9,10-Ethanoanthracene, 9,10-dihydro-11,12-diacetyl- |
| 69.6 | 0.030 | C14H12 | 180.2 | 9H-Fluorene, 4-methyl- |
| 69.9 | 0.335 | C14H12 | 180.2 | 9H-Fluorene, 9-methyl- |
| 73.5 | 0.271 | C14H10 | 178.2 | 9H-Fluorene, 9-methylene- |
| 95.3 | 0.059 | C19H16O2 | 276.3 | Acetic acid, α -(1-naphthyl)benzyl ester |
| 103.3 | 0.678 | C28H40O2 | 408.6 | Anthiaergostan-5,7,9,22-tetraen-14-ol-15-one |
| 73.5 | 0.319 | C14H10 | 178.2 | Anthracene |
| 79.5 | 0.512 | C15H12 | 192.2 | Anthracene, 1-methyl- |
| 84.6 | 0.028 | C16H14 | 206.3 | Anthracene, 2-ethyl- |
| 80.0 | 1.286 | C15H12 | 192.2 | Anthracene, 2-methyl |
| 91.8 | 0.527 | C17H24O6 | 324.3 | Azulenofuranone Derivative |
| 3.2 | 0.223 | C6H6 | 78.1 | Benzene |
| 63.8 | 0.041 | C13H12 | 168.2 | Benzene, [1-(2,4-cyclopentadien-1-ylidene)ethyl]- |
| 71.1 | 0.193 | C18H20 | 236.3 | Benzene, 1,1'-(3,3-dimethyl-1-butenylidene)bis- |
| 66.2 | 1.176 | C13H10O | 182.2 | Benzophenone |
| 73.7 | 0.899 | C14H12O2 | 212.2 | Benzyl Benzoate |
| 18.3 | 0.080 | C10H18O | 154.2 | Bicycloheptanol Derivative |
| 108.9 | 50.009 | C24H38O4 | 390.5 | Bis(2-ethylhexyl) phthalate |
| 23.9 | 0.023 | C19H30O3 | 306.4 | Carbonic acid, dodecyl phenyl ester |
| 67.6 | 0.197 | C14H18O | 202.3 | Cinnamaldehyde, α -pentyl- |
| 50.1 | 0.039 | C11H20O | 168.2 | cis-4-methoxy thujane |
| 40.5 | 0.081 | C10H20O | 156.2 | Cyclodecanol |
| 9.7 | 0.577 | C9H18 | 126.2 | Cyclohexane, 1,1,3-trimethyl- |
| 7.1 | 0.253 | C8H16 | 112.2 | Cyclohexane, 1,2-dimethyl-, trans- |
| 9.3 | 0.176 | C9H18 | 126.2 | Cyclohexane, 1,3,5-trimethyl- |
| 6.2 | 0.282 | C8H16 | 112.2 | Cyclohexane, 1,3-dimethyl-, cis- |
| 6.2 | 0.156 | C8H16 | 112.2 | Cyclohexane, 1,4-dimethyl-, trans- |
| 14.1 | 1.657 | C9H18 | 126.2 | Cyclohexane, 1-ethyl-2-methyl-, cis- |
| 9.4 | 0.389 | C8H16 | 112.2 | Cyclohexane, ethyl- |

| | | | | |
|------|-------|-----------|-------|--|
| 33.9 | 0.025 | C12H22O2 | 198.3 | Cyclohexanol Derivative |
| 17.9 | 0.022 | C8H14O | 126.2 | Cyclohexanone, 2,3-dimethyl- |
| 13.1 | 0.088 | C9H18 | 126.2 | Cyclopentane, 2-ethyl-1,1-dimethyl- |
| 68.2 | 0.028 | C13H22O3 | 226.3 | Cyclopentaneacetic acid Derivative |
| 98.9 | 0.065 | C25H38O10 | 498.5 | Cyclopentanepropanoic acid Derivative |
| 6.9 | 0.045 | C8H16 | 112.2 | Cyclopropane, pentyl- |
| 10.1 | 0.249 | C13H28 | 184.3 | Decane, 2,5,6-trimethyl- |
| 18.9 | 0.021 | C13H28 | 184.3 | Decane, 2,6,7-trimethyl- |
| 47.0 | 0.041 | C13H28 | 184.3 | Decane, 6-ethyl-2-methyl- |
| 74.5 | 0.112 | C26H54 | 366.6 | Docosane, 11-butyl- |
| 78.8 | 0.129 | C25H50O3 | 398.6 | Docosyl ethyl carbonate |
| 10.8 | 0.018 | C14H26O | 210.3 | E-11,13-Tetradecadien-1-ol |
| 71.6 | 0.272 | C16H34O2 | 258.4 | Ethanol, 2-(tetradecyloxy)- |
| 73.9 | 0.046 | C17H26O | 246.4 | Ethanone Derivative |
| 66.6 | 0.035 | C21H16O3 | 316.3 | Ethanone, 2-(benzoyloxy)-1-[1,1'-biphenyl]-4-yl- |
| 8.4 | 0.023 | C11H24O | 172.3 | Ether, hexyl pentyl |
| 63.2 | 0.202 | C13H10 | 166.2 | Fluorene |
| 58.1 | 0.083 | C11H22O2 | 186.3 | Formic acid, decyl ester |
| 39.7 | 0.018 | C15H22O3 | 250.3 | Gemfibrozil |
| 65.3 | 0.128 | C18H38 | 244.4 | Heptadecane, 8-methyl- |
| 67.9 | 0.204 | C23H48 | 324.6 | Heptadecane, 9-hexyl- |
| 17.8 | 0.108 | C13H26 | 182.3 | Heptylcyclohexane |
| 79.2 | 0.055 | C18H36O2 | 284.4 | i-Propyl 12-methyltetradecanoate |
| 77.4 | 0.059 | C17H34O2 | 270.4 | Isopropyl myristate |
| 69.4 | 0.466 | C13H16O2 | 204.2 | Methanone, (1-hydroxycyclohexyl)phenyl- |
| 90.9 | 0.236 | C33H46O10 | 602.6 | Methyl urinate Derivative |
| 53.7 | 0.077 | C12H12 | 156.2 | Naphthalene, 1,4-dimethyl- |
| 53.7 | 0.099 | C12H12 | 156.2 | Naphthalene, 1,5-dimethyl- |
| 58.9 | 0.029 | C13H14 | 170.2 | Naphthalene, 1,6,7-trimethyl- |
| 61.5 | 0.373 | C13H14 | 170.2 | Naphthalene, 2,3,6-trimethyl |
| 46.7 | 0.018 | C11H10 | 142.2 | Naphthalene, 2-methyl- |
| 83.1 | 0.299 | C16H12 | 204.2 | Naphthalene, 2-phenyl- |

| | | | | |
|------|--------|----------|-------|---|
| 71.8 | 0.438 | C14H12O | 196.2 | Naphtho[2,1-b]furan, 1,2-dimethyl- |
| 81.3 | 0.146 | C18H20 | 236.3 | Naphtho[3,4:2,3]bornene |
| 84.1 | 0.633 | C16H32O2 | 256.4 | n-Hexadecanoic acid |
| 15.7 | 2.818 | C9H20 | 128.2 | Nonane |
| 97.1 | 0.220 | C26H54 | 366.6 | Octadecane, 3-ethyl-5-(2-ethylbutyl)- |
| 32.7 | 0.044 | C19H40 | 268.5 | Octadecane, 6-methyl- |
| 90.2 | 0.156 | C19H38O3 | 314.5 | Octadecanoic acid, 4-hydroxy-, methyl ester |
| 9.5 | 0.640 | C14H28 | 196.3 | Octane, 2-cyclohexyl- |
| 12.6 | 0.283 | C9H20 | 128.2 | Octane, 4-methyl- |
| 46.3 | 0.162 | C12H22O2 | 198.3 | o-tert-Butyl cyclohexyl acetate 1 |
| 4.2 | 0.023 | C7H14O | 114.2 | Oxirane, 2-methyl-2-(1-methylpropyl)- |
| 55.6 | 0.022 | C12H14O3 | 206.2 | Oxiranecarboxylic acid Derivative |
| 84.7 | 1.924 | C16H14 | 206.3 | Phenanthrene, 2,7-dimethyl- |
| 80.7 | 0.175 | C15H12 | 192.2 | Phenanthrene, 4-methyl- |
| 75.6 | 1.180 | C15H14 | 194.2 | Phenanthrene, 9,10-dihydro-1-methyl |
| 44.4 | 0.024 | C9H12O | 120.2 | Phenol, 3-ethyl-5-methyl- |
| 47.9 | 0.126 | C9H10O | 134.2 | Phenol, 4-(2-propenyl)- |
| 91.9 | 1.151 | C20H28O6 | 364.4 | Phorbol |
| 33.4 | 0.036 | C9H14O | 138.2 | Phorone |
| 99.4 | 0.291 | C18H14 | 230.3 | Pyrene, 1,3-dimethyl- |
| 53.5 | 0.129 | C14H30 | 198.4 | Tetradecane |
| 59.5 | 0.048 | C17H36 | 240.4 | Tetradecane, 2,6,10-trimethyl- |
| 74.2 | 0.179 | C14H28O2 | 228.3 | Tetradecanoic acid |
| 5.9 | 18.018 | C7H8 | 92.1 | Toluene |
| 40.5 | 0.050 | C13H26O | 198.3 | Tridecanal |
| 58.0 | 0.082 | C14H22O | 206.3 | α Isomethyl ionone |
| 73.9 | 0.036 | C15H18O3 | 246.3 | α -Santonin |

Low VM – Pan

| Ret Time | Relative % | Formula | MW | Name |
|----------|------------|---------|-------|-----------------------|
| 12.4 | 0.553 | C9H18O | 142.2 | 5-Methyl-5-octen-1-ol |
| 17.0 | 0.248 | C16H32 | 224.4 | Cyclohexane, decyl- |
| 83.0 | 0.236 | C16H34O | 242.4 | 1-Decanol, 2-hexyl- |

| | | | | |
|-------|--------|----------|-------|--|
| 72.8 | 0.622 | C22H44O2 | 340.5 | 1-Heneicosyl formate |
| 14.4 | 0.515 | C16H32 | 224.4 | 1-Nonylcycloheptane |
| 108.4 | 2.458 | C30H52O | 428.7 | Cyclohexanol Derivative |
| 6.4 | 5.552 | C7H12O | 112.2 | 2-Cyclohexen-1-ol, 1-methyl- |
| 8.6 | 0.704 | C9H18O | 142.2 | 2-Nonanone |
| 14.7 | 0.494 | C12H14O2 | 174.2 | 3(2H)-Furanone, dihydro-2,2-dimethyl-5-phenyl- |
| 4.1 | 0.771 | C6H12O2 | 116.1 | 3-Hexene-2,5-diol |
| 88.2 | 0.304 | C21H44 | 296.5 | 7,7-Diethylheptadecane |
| 7.1 | 1.642 | C7H12O | 112.2 | 7-Oxabicyclo[4.1.0]heptane, 1-methyl- |
| 73.5 | 0.361 | C14H10 | 178.2 | 9H-Fluorene, 9-methylene- |
| 79.3 | 0.386 | C15H12 | 192.2 | Anthracene, 2-methyl- |
| 3.2 | 0.984 | C6H6 | 78.1 | Benzene |
| 66.2 | 0.287 | C13H10O | 182.2 | Benzophenone |
| 13.0 | 0.952 | C9H18 | 126.2 | Cyclohexane, 1,1,2-trimethyl- |
| 10.0 | 1.775 | C9H18 | 126.2 | Cyclohexane, 1,1,3-trimethyl- |
| 10.5 | 2.791 | C9H18 | 126.2 | Cyclohexane, 1-ethyl-2-methyl-, cis- |
| 16.2 | 0.277 | C9H18 | 126.2 | Cyclohexane, 1-ethyl-4-methyl-, cis- |
| 17.9 | 0.882 | C16H32 | 224.4 | Cyclohexane, decyl- |
| 13.2 | 0.668 | C9H18 | 126.2 | Cyclopentane, 2-ethyl-1,1-dimethyl- |
| 15.9 | 9.815 | C13H28 | 184.3 | Decane, 2,4,6-trimethyl- |
| 97.1 | 0.182 | C26H32O6 | 440.5 | D-Homo-nor-oxacholadiene-trione Derivative |
| 18.4 | 0.343 | C14H26O | 210.3 | E-11,13-Tetradecadien-1-ol |
| 18.8 | 0.334 | C19H40 | 268.5 | Heptadecane, 2,6-dimethyl- |
| 9.7 | 2.616 | C14H28 | 196.3 | Octane, 2-cyclohexyl- |
| 16.8 | 0.800 | C9H16 | 124.2 | Propylidencyclohexane |
| 6.0 | 44.792 | C7H8 | 92.1 | Toluene |

Low VM – Cup

| Ret Time | Relative % | MW | Formula | Name |
|----------|------------|-----|----------|---|
| 7.3 | 0.0378 | 112 | C8H16 | Cyclohexane, 1,2-dimethyl-, trans- |
| 12.0 | 0.0364 | 128 | C9H20 | Hexane, 2,3,5-trimethyl- |
| 77.4 | 0.0166 | 270 | C17H34O2 | i-Propyl 12-methyl-tridecanoate |
| 84.0 | 0.0857 | 652 | C38H68O8 | l-(+)-Ascorbic acid 2,6-dihexadecanoate |

| | | | | |
|-------|--------|-----|-----------|---|
| 54.9 | 0.0047 | 156 | C12H12 | Naphthalene, 1,4-dimethyl- |
| 71.8 | 0.0184 | 196 | C14H12O | Naphtho[2,1-b]furan, 1,2-dimethyl- |
| 101.0 | 0.0308 | 354 | C22H42O3 | n-Butyl ricinoleate |
| 47.6 | 0.0075 | 198 | C12H22O2 | o-tert-Butyl cyclohexyl acetate 2 |
| 55.6 | 0.0150 | 206 | C12H14O3 | Oxiranecarboxylic acid Derivative |
| 76.0 | 0.0992 | 194 | C15H14 | Phenanthrene, 9,10-dihydro-1-methyl- |
| 101.4 | 0.0258 | 334 | C20H30O4 | Prostaglandin A2 |
| 58.0 | 0.3196 | 206 | C14H22O | α Isomethyl ionone |
| 18.3 | 0.0067 | 136 | C10H16 | (1R)-2,6,6-Trimethylbicyclo[3.1.1]hept-2-ene |
| 93.2 | 0.0559 | 282 | C22H18 | 1,1'-Binaphthalene, 3,3'-dimethyl- |
| 83.7 | 0.0254 | 334 | C20H30O4 | 1,2-Benzenedicarboxylic acid, butyl octyl ester |
| 29.5 | 0.0287 | 166 | C10H14O2 | 1,2-Butanediol, 1-phenyl- |
| 13.7 | 0.0627 | 154 | C9H14O2 | 1,3-Cyclohexanedione, 5-isopropyl- |
| 14.8 | 0.0393 | 106 | C8H10 | 1,3-Cyclopentadiene, 5-(1-methylethylidene)- |
| 74.8 | 0.0078 | 224 | C17H20 | Tetramethyl-phenylbicyclohepta-diene |
| 88.5 | 0.0106 | 326 | C18H30O5 | 12- β -(3'-Hydroxypropyl)deoxoartemisinin |
| 6.6 | 0.0388 | 156 | C9H16O2 | 1-Allyl-cyclohexane-1,2-diol |
| 58.0 | 0.5660 | 186 | C12H26O | 1-Dodecanol |
| 14.2 | 0.2010 | 126 | C9H18 | 1-Ethyl-4-methylcyclohexane |
| 89.8 | 0.0289 | 396 | C27H56O | 1-Heptacosanol |
| 69.5 | 0.1045 | 242 | C16H34O | 1-Hexadecanol |
| 63.2 | 0.0122 | 166 | C13H10 | 1H-Phenalene |
| 14.4 | 0.0671 | 224 | C16H32 | 1-Nonylcycloheptane |
| 99.7 | 0.0188 | 616 | C33H44O11 | Pyranuronate Derivative |
| 60.4 | 0.0579 | 206 | C14H22O | Penten-3-one Derivative |
| 98.9 | 0.1043 | 318 | C21H34O2 | Phenanthrenecarboxylic acid Derivative |
| 5.2 | 0.0211 | 142 | C7H10O3 | 2,2,6-Trimethyl-4H-1,3-dioxin-4-one |
| 23.5 | 0.0052 | 120 | C9H12 | 2,3-Heptadien-5-yne, 2,4-dimethyl- |
| 95.6 | 0.1961 | 606 | C36H46O8 | 2,4,6,8,10-Tetradecapentaenoic acid Derivative |
| 57.2 | 0.0060 | 220 | C14H20O2 | 2,5-di-tert-Butyl-1,4-benzoquinone |
| 99.2 | 0.0771 | 408 | C30H48 | Tetracosahexaene Derivative |
| 102.6 | 0.1357 | 458 | C30H50O3 | 20.Xi.-Lanosta-7,9(11)-diene-3 β ,18,20-triol |

| | | | | |
|-------|---------|-----|----------|---|
| 25.7 | 0.0306 | 256 | C16H32O2 | 2-Acetoxytetradecane |
| 14.0 | 0.0150 | 140 | C9H16O | 2-Cyclohexen-1-ol, 3,5,5-trimethyl- |
| 70.4 | 0.0348 | 266 | C16H26O3 | 2-Dodecen-1-yl(-)succinic anhydride |
| 71.3 | 0.0075 | 242 | C16H34O | 2-Hexadecanol |
| 5.1 | 0.0076 | 158 | C9H18O2 | 2-Hexanone, 4-hydroxy-3-propyl- |
| 35.9 | 0.0224 | 140 | C9H16O | 2-Methyl-4-octenal |
| 11.9 | 0.0925 | 142 | C9H18O | 2-Nonanone |
| 39.2 | 0.1922 | 116 | C6H12O2 | 2-Pentanone, 4-hydroxy-4-methyl- |
| 68.7 | 0.0073 | 202 | C14H18O | 2-Phenyl-2,4-octadienol |
| 78.5 | 0.0940 | 268 | C19H40 | 3,3-Diethylpentadecane |
| 67.9 | 0.0334 | 240 | C17H36 | 3,3-Diethyltridecane |
| 83.4 | 0.0534 | 282 | C20H42 | 3-Ethyl-3-methylheptadecane |
| 36.1 | 0.1384 | 156 | C9H16O2 | 3-Hexen-1-ol, 2,5-dimethyl-, formate,(Z)- |
| 40.1 | 0.0353 | 170 | C12H26 | 5-Ethyldecane |
| 108.8 | 28.5361 | 166 | C8H6O4 | 5-Formylsalicylic acid |
| 8.4 | 0.0103 | 126 | C8H14O | 6,6-Dimethyl-cyclohex-2-en-1-ol |
| 56.0 | 0.0051 | 148 | C10H12O | 6-Methyl-4-indanol |
| 88.2 | 0.0718 | 296 | C21H44 | 7,7-Diethylheptadecane |
| 32.7 | 0.1016 | 238 | C16H30O | 7-Hexadecenal, (Z)- |
| 7.1 | 0.1406 | 112 | C7H12O | 7-Oxabicyclo[4.1.0]heptane, 1-methyl- |
| 69.9 | 0.0289 | 180 | C14H12 | 9H-Fluorene, 2-methyl- |
| 69.9 | 0.0358 | 180 | C14H12 | 9H-Fluorene, 9-methyl- |
| 73.5 | 0.0420 | 178 | C14H10 | 9H-Fluorene, 9-methylene- |
| 73.5 | 0.0925 | 180 | C14H11 | Anthracene |
| 79.3 | 0.2787 | 192 | C15H12 | Anthracene, 2-methyl- |
| 3.2 | 0.2933 | 78 | C6H6 | Benzene |
| 20.9 | 0.0077 | 162 | C11H14O | Benzene, 1-methyl-4-[(2-propenyloxy)methyl]- |
| 48.1 | 0.0123 | 192 | C12H16O2 | Benzeneethanol, α,α -dimethyl-, acetate |
| 60.8 | 0.0193 | 204 | C14H20O | Benzenepropanal, 3-(1,1-dimethylethyl)- α -methyl- |
| 66.2 | 0.1833 | 182 | C13H10O | Benzophenone |
| 73.7 | 0.7129 | 212 | C14H12O2 | Benzyl Benzoate |
| 19.8 | 0.0091 | 152 | C11H20 | Bicyclo[4.1.0]heptane, 7-butyl- |

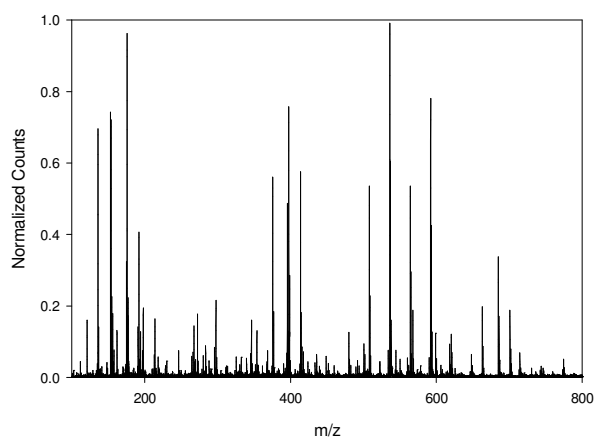
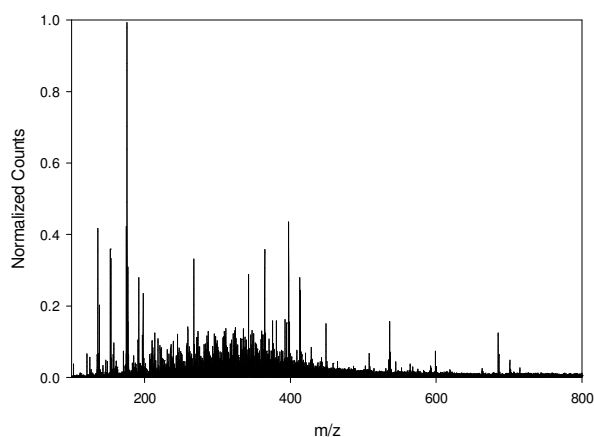
| | | | | |
|-------|---------|-----|-----------|--|
| 108.9 | 26.4666 | 390 | C24H38O4 | Bis(2-ethylhexyl) phthalate |
| 67.6 | 0.1400 | 202 | C14H18O | Cinnamaldehyde, α -pentyl- |
| 40.5 | 0.0123 | 156 | C10H20O | Cyclodecanol |
| 13.0 | 0.1020 | 126 | C9H18 | Cyclohexane, 1,1,2-trimethyl- |
| 9.9 | 0.1888 | 126 | C9H18 | Cyclohexane, 1,1,3-trimethyl- |
| 13.0 | 0.0267 | 126 | C9H18 | Cyclohexane, 1,2,3-trimethyl-, (1 α ,2 β ,3 α)- |
| 13.7 | 0.0524 | 126 | C9H18 | Cyclohexane, 1,2,4-trimethyl- |
| 9.5 | 0.0626 | 126 | C9H18 | Cyclohexane, 1,3,5-trimethyl- |
| 14.0 | 0.0120 | 378 | C27H54 | Cyclohexane, 1,3,5-trimethyl-2-octadecyl- |
| 6.3 | 0.1109 | 122 | C8H16 | Cyclohexane, 1,3-dimethyl-, cis- |
| 6.3 | 0.1203 | 112 | C8H16 | Cyclohexane, 1,4-dimethyl-, trans- |
| 9.9 | 0.3099 | 168 | C12H24 | Cyclohexane Derivative |
| 10.1 | 0.0041 | 364 | C26H52 | Cyclohexane, 1,4-dimethyl-2-octadecyl- |
| 10.4 | 0.5418 | 126 | C9H18 | Cyclohexane, 1-ethyl-2-methyl-, cis- |
| 14.4 | 0.0687 | 126 | C9H19 | Cyclohexane, 1-ethyl-4-methyl-, cis- |
| 18.0 | 0.0684 | 224 | C16H32 | Cyclohexane, decyl- |
| 17.9 | 0.1136 | 126 | C9H18 | Cyclohexane, propyl- |
| 26.5 | 0.0240 | 154 | C10H18O | Cyclohexanol Derivative |
| 51.3 | 0.0517 | 198 | C12H22O2 | Cyclohexanol, 4-(1,1-dimethylethyl)-, acetate, trans- |
| 13.2 | 0.2117 | 126 | C9H18 | Cyclopentane, 2-ethyl-1,1-dimethyl- |
| 68.2 | 0.0452 | 226 | C13H22O3 | Cyclopentaneacetic acid Derivative |
| 8.6 | 0.0140 | 184 | C13H28 | Decane, 2,4,6-trimethyl- |
| 24.6 | 0.3165 | 184 | C13H28 | Decane, 2,5,6-trimethyl- |
| 10.2 | 0.0618 | 184 | C13H28 | Decane, 2,5,9-trimethyl- |
| 10.2 | 0.0174 | 184 | C13H28 | Decane, 2,6,6-trimethyl- |
| 22.1 | 0.0387 | 184 | C13H28 | Decane, 2,6,7-trimethyl- |
| 10.2 | 0.0254 | 184 | C13H28 | Decane, 2,6,8-trimethyl- |
| 74.3 | 0.0061 | 764 | C41H64O13 | Digitoxin |
| 73.5 | 0.0435 | 178 | C14H10 | Diphenylacetylene |
| 26.5 | 0.0189 | 136 | C10H16 | D-Limonene |
| 78.8 | 0.1049 | 398 | C25H50O3 | Docosyl ethyl carbonate |
| 18.4 | 0.0218 | 210 | C14H26O | E-11,13-Tetradecadien-1-ol |

| | | | | |
|-------|---------|-----|-----------|---|
| 71.5 | 0.2167 | 230 | C14H30O2 | Ethanol, 2-(dodecyloxy)- |
| 73.9 | 0.1205 | 246 | C17H26O | Ethanone Derivative |
| 89.0 | 0.0308 | 202 | C16H10 | Fluoranthene |
| 63.2 | 0.0152 | 166 | C13H10 | Fluorene |
| 42.0 | 0.0051 | 180 | C12H20O | Geranyl vinyl ether |
| 74.4 | 0.0143 | 268 | C19H40 | Heptadecane, 2,3-dimethyl- |
| 40.1 | 0.0542 | 296 | C21H44 | Heptadecane, 2,6,10,14-tetramethyl- |
| 18.8 | 0.0597 | 268 | C19H40 | Heptadecane, 2,6-dimethyl- |
| 21.3 | 0.0111 | 156 | C10H20O | Heptane, 1-(2-propenyloxy)- |
| 19.4 | 0.0056 | 142 | C10H22 | Heptane, 4-propyl- |
| 16.9 | 0.0228 | 182 | C13H26 | Heptylcyclohexane |
| 11.9 | 0.0359 | 128 | C9H20 | Hexane, 2,3,5-trimethyl- |
| 82.9 | 0.0536 | 268 | C17H32O2 | i-Propyl 9-tetradecenoate |
| 69.4 | 0.0140 | 204 | C13H16O2 | Methanone, (1-hydroxycyclohexyl)phenyl- |
| 55.2 | 0.0040 | 168 | C11H20O | Methyl 4,6-decadienyl ether |
| 53.7 | 0.0307 | 156 | C12H12 | Naphthalene, 1,5-dimethyl- |
| 58.9 | 0.0063 | 170 | C13H14 | Naphthalene, 1,6,7-trimethyl- |
| 61.3 | 0.0053 | 170 | C13H14 | Naphthalene, 2,3,6-trimethyl- |
| 52.8 | 0.0251 | 156 | C12H12 | Naphthalene, 2,7-dimethyl- |
| 45.6 | 0.0179 | 142 | C11H10 | Naphthalene, 2-methyl- |
| 83.1 | 0.0236 | 204 | C16H12 | Naphthalene, 2-phenyl- |
| 72.5 | 0.0121 | 196 | C14H12O | Naphtho[2,1-b]furan, 1,2-dimethyl- |
| 87.5 | 0.0312 | 998 | C69H138O2 | Nonahexacontanoic acid |
| 15.9 | 0.9584 | 128 | C9H20 | Nonane |
| 92.6 | 19.6082 | 366 | C26H54 | Octadecane, 3-ethyl-5-(2-ethylbutyl)- |
| 71.0 | 0.0308 | 268 | C19H40 | Octadecane, 6-methyl- |
| 67.5 | 0.0984 | 216 | C15H20O | Octanal, 2-(phenylmethylene)- |
| 9.7 | 0.1334 | 196 | C14H28 | Octane, 2-cyclohexyl- |
| 12.8 | 0.0630 | 128 | C9H20 | Octane, 2-methyl- |
| 13.3 | 0.1585 | 128 | C9H20 | Octane, 3-methyl- |
| 113.2 | 1.7746 | 562 | C38H74O2 | Oleic acid, eicosyl ester |
| 46.3 | 0.2396 | 198 | C12H22O2 | o-tert-Butyl cyclohexyl acetate 1 |

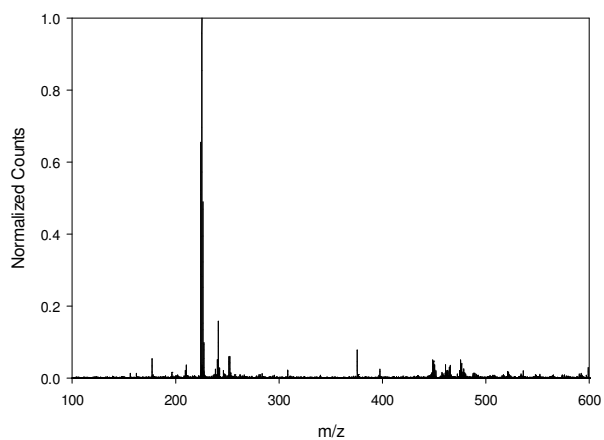
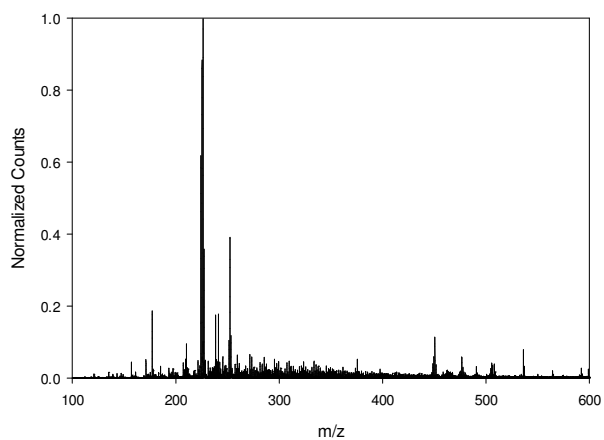
| | | | | |
|------|---------|-----|----------|--------------------------------------|
| 5.1 | 0.0446 | 100 | C6H12O | Oxirane, 2-methyl-2-(1-methylethyl)- |
| 55.4 | 0.0173 | 206 | C12H14O3 | Oxiranecarboxylic acid Derivative |
| 16.8 | 0.0536 | 124 | C9H16 | Pentalene, octahydro-2-methyl- |
| 4.7 | 0.0929 | 128 | C8H16O | Pentane, 1-(2-propenyloxy)- |
| 85.0 | 0.1529 | 206 | C16H14 | Phenanthrene, 2,7-dimethyl- |
| 80.7 | 0.0272 | 192 | C15H12 | Phenanthrene, 4-methyl- |
| 75.6 | 0.1113 | 194 | C15H14 | Phenanthrene, 9,10-dihydro-1-methyl- |
| 36.4 | 0.0140 | 164 | C10H12O2 | Phenol, 2,5-dimethyl-, acetate |
| 47.9 | 0.0091 | 134 | C9H10O | Phenol, 4-(2-propenyl)- |
| 93.4 | 0.1083 | 364 | C20H28O6 | Phorbol |
| 16.8 | 0.0942 | 124 | C9H16 | Propylidencyclohexane |
| 21.5 | 0.0067 | 604 | C43H88 | Tetracontane, 3,5,24-trimethyl- |
| 53.4 | 0.1744 | 198 | C14H30 | Tetradecane |
| 62.2 | 0.0323 | 240 | C17H36 | Tetradecane, 2,6,10-trimethyl- |
| 74.1 | 0.0291 | 228 | C14H28O2 | Tetradecanoic acid |
| 97.1 | 0.0461 | 518 | C31H50O6 | Tetradecanoic acid Derivative |
| 17.4 | 0.0168 | 156 | C10H20O | Tetrahydrofuran, 2-methyl-5-pentyl- |
| 5.9 | 11.7427 | 92 | C7H8 | Toluene |
| 22.6 | 0.0067 | 224 | C16H32 | Trans-1-methyl-2-nonyl-cyclohexane |
| 40.5 | 0.0164 | 198 | C13H26O | Tridecanal |

MALDI-TOF spectra of coal tar with various matrices

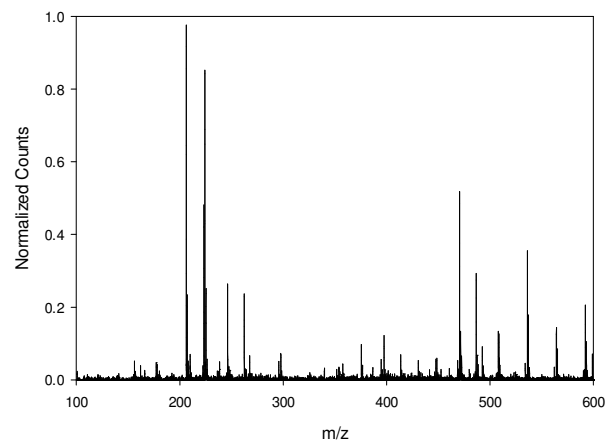
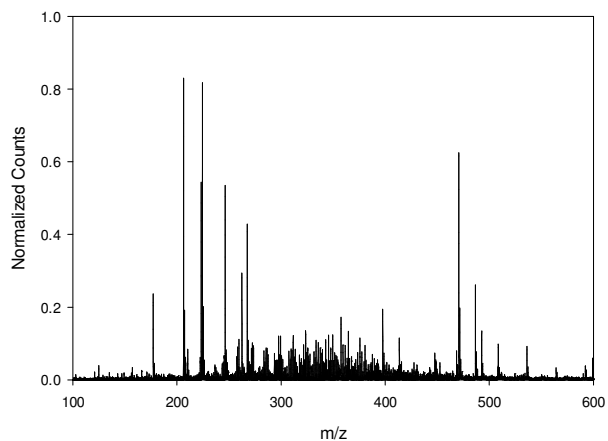
High VM Coal Tar and 2,5-dihydroxybenzoic acid (DHB)



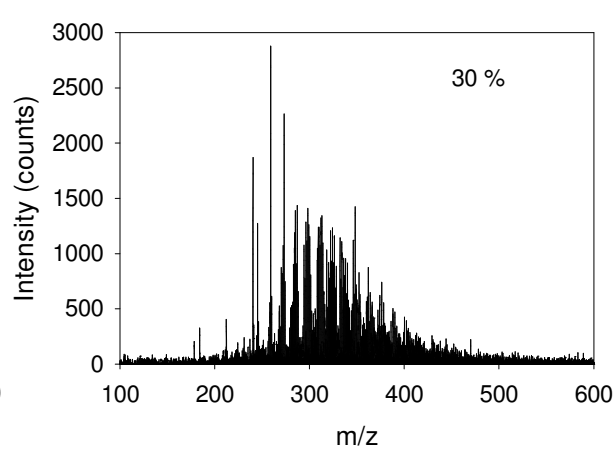
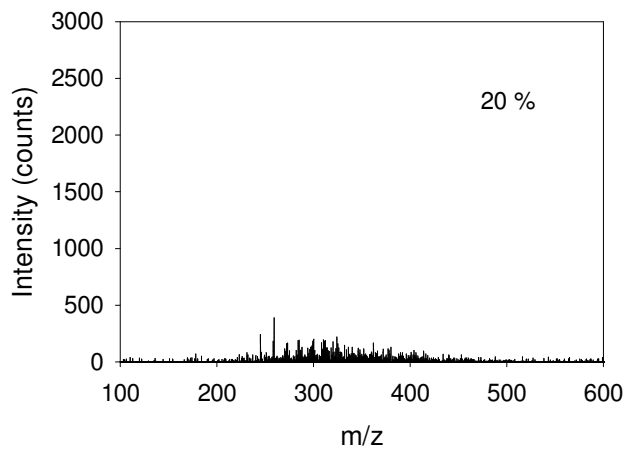
High VM Coal Tar and Dithranol

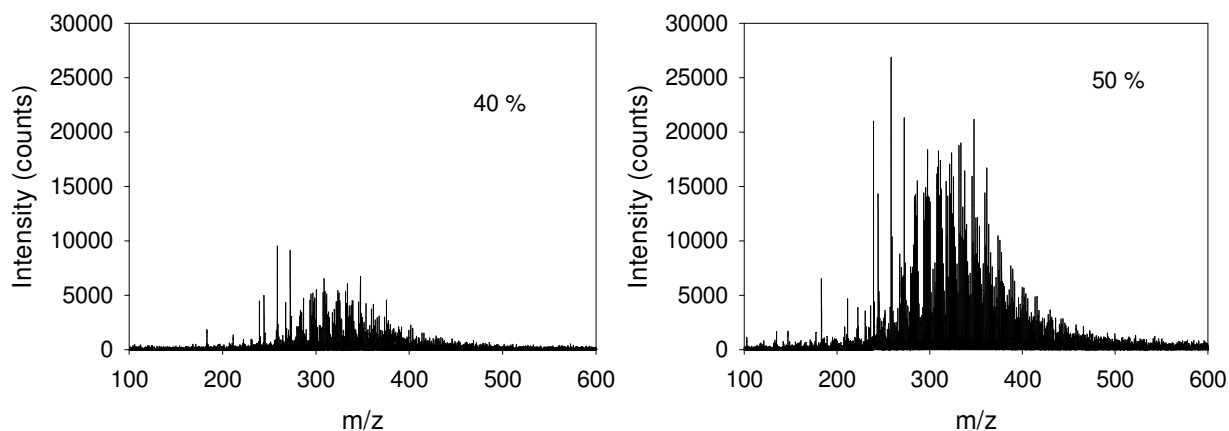


High VM Coal Tar and Sinapinic Acid

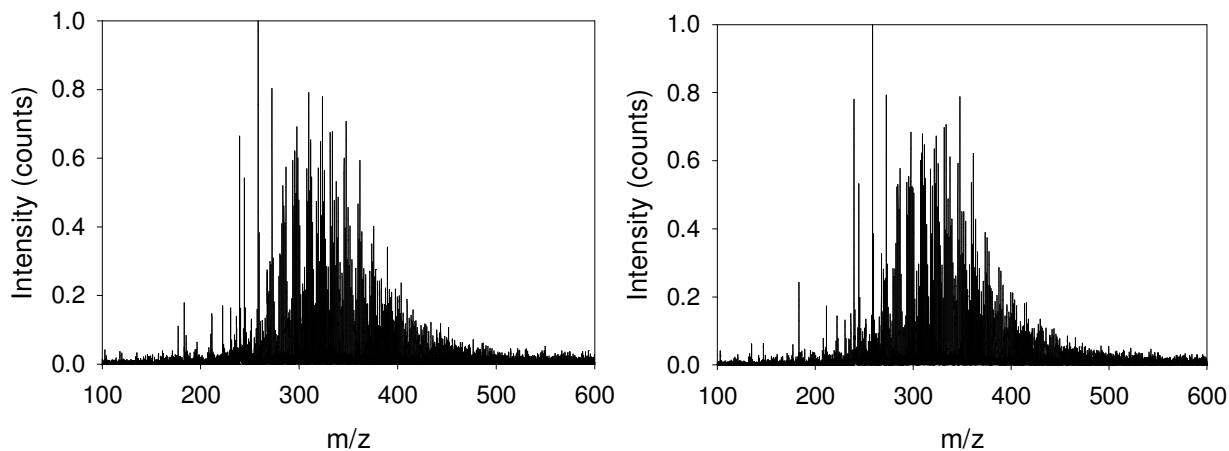


LDI-TOF spectra of coal tar using various degrees of laser power (No matrix)





Repeated LDI-TOF scans of High VM coal tar (two 0.5 μL drops on target desorbed using 50% laser power)



Example Calculation for Exercising the Measured Mass Closure

The time-resolved gas and tar evolution profiles were determined by the methods illustrated in Section 3.3.1. The evolution profiles of respective product species were fit by the Gaussian technique described in Section 3.3.4. The respective volatile product evolution profiles for pecan shell pyrolysis are provided in Figure 64 of Section 11.2.

As alluded to in Equation 3 of Section 3.3.1, the rate of solid consumption, r_{solid} , in mg min^{-1} can be calculated. The rates in terms of percent of initial mass ($\% \text{ min}^{-1}$) may be obtained by normalizing the rates with an initial mass of the sample. Calculating and normalizing r_{solid} from the time-resolved data results in the “Predicted DTG” profile shown in Figure 65. The mass loss profile or “Predicted TG” can be calculated from the rate of mass loss ($\% \text{ min}^{-1}$) at every time point and the initial condition of 100% mass.

$$m_1 = 100 - r_{solid,t=0}\Delta t$$

$$m_n = m_{n-1} - r_{solid,n-1}\Delta t$$

where m_1 is the mass (%) at the first time step, $r_{\text{solid},t=0}$ is the rate of solid consumption at time zero ($\% \text{ min}^{-1}$) and Δt is the time step interval (min).

Lastly, the O/C and H/C ratio of the solid chemical composition can be determined from the collective volatile product evolution profiles. This is performed using the chemical identification of the volatile products obtained by μGC and GC-MS shown throughout this document. From these measurements, the total carbon, hydrogen, and oxygen transferred from the solid to vapor phase can be calculated. Similarly to the calculation for mass loss, an iterative time step method can be used if the initial carbon, hydrogen and oxygen compositions are known. The initial conditions for carbon, hydrogen, and oxygen compositions are found in Table 3. An example for the case of carbon in pecan shells is shown below

$$C_1 = 52 - (r_{\text{carbon in gas},t=0}\Delta t + r_{\text{carbon in tar},t=0}\Delta t)$$

$$C_n = C_{n-1} - (r_{\text{carbon in gas},n}\Delta t + r_{\text{carbon in tar},n}\Delta t)$$

where C_1 is the carbon composition (%) in the solid at the first time step, $r_{\text{carbon in gas},t=0}$ is the summation of rates for the gaseous carbon atoms at time zero ($\% \text{ min}^{-1}$), $r_{\text{carbon in tar},t=0}$ is the rate of tar produced multiplied by the average tar carbon composition at time zero ($\% \text{ min}^{-1}$) and Δt is the time step interval (min). After each atomic composition is calculated then the H/C and O/C ratio are calculated simply by dividing one by the other.

Empirical correlations evaluated to estimate HHV from ultimate/proximate analysis results

All equations below were obtained from Channiwala and Parikh (2002) and Kieseler et al. (2013).

$$(1) \text{ HHV (MJ/kg)} = 0.3491 \cdot C + 1.1783 \cdot H + 0.1005 \cdot S - 0.103 \cdot O - 0.0151 \cdot N - 0.0211 \cdot A$$

$$(2) \text{ HHV (MJ/kg)} = 0.3391 \cdot (C - 0.75 \cdot O/2) + 1.444 \cdot (H - 0.125 \cdot O/2) + 0.1047 \cdot S$$

Original source: Sumegi, L. A formula for calculation of the calorific value of coal from chemical analysis. Magyar Mernok Epiteszeqylet Kozlonye. 1939, 73, 345-6.

$$(3) \text{ HHV (MJ/kg)} = 0.3383 \cdot C + 1.443 \cdot (H - O/8)$$

$$(4) \text{ HHV (MJ/kg)} = 0.3406 \cdot C + 1.4324 \cdot H - 0.1532 \cdot O + 0.1047 \cdot S$$

Original source: Strache, H.; Lant, R. Kohlenchemie. Leipzig: Akademische Verlagsgesellschaft, 1924. P. 476.

$$(5) \text{ HHV (MJ/kg)} = 0.3391 \cdot (C - 3/8 \cdot O) + 0.2386 \cdot 3/8 \cdot O + 1.444 \cdot (H - O/16) + 0.1047 \cdot S$$

Original source: Steuer, W. Allgemeine Formel zur Berechnung des Heizwertes von festen fossilen Brennstoffen aus der Elementaranalyse. Brennstoff-Chem 1926, 7, 344-7.

$$(6) \text{ HHV (MJ/kg)} = (0.373 - 0.00026 \cdot C) \cdot C + 1.444 \cdot (H - O/10) + 0.1047 \cdot S$$

Original source: Vondracek, R. Brennstoff-Chem 1927, 8, 22-3.

$$(7) \text{ HHV (MJ/kg)} = 0.3391 \cdot \text{C} + 1.4337 \cdot \text{H} + 0.0931 \cdot \text{S} - 0.1273 \cdot \text{O}$$

Original source: D'Huart, K. The development of formulas for determining the heating value of solid fuels. *Die Wärme* 1930, 53, 313-7.

$$(8) \text{ HHV (MJ/kg)} = (0.0152 \cdot \text{H} + 0.9875) \cdot (\text{C}/3 + \text{H} - (\text{O} - \text{S})/8)$$

Original source: Grummel, E. S.; Davis, I. A. A new method of calculating the calorific value of a fuel from its ultimate analysis *Fuel*. 1922, 12, 199-203.

$$(9) \text{ HHV (MJ/kg)} = 0.3403 \cdot \text{C} + 1.2432 \cdot \text{H} + 0.0628 \cdot \text{H}_2 + 0.1909 \cdot \text{S} - 0.0984 \cdot \text{O}$$

Original source: Gumz, W.; Hardt, L. *Kurzes Handbuch der Brennstoff—und Feuerungstechnik*, Springer-Verlag, Berlin, 1962.

$$(10) \text{ HHV (MJ/kg)} = 0.3361 \cdot \text{C} + 1.419 \cdot \text{H} - (0.1532 - 0.0007 \cdot \text{O} \cdot 100) \cdot \text{O} + 0.0942 \cdot \text{S}$$

Original source: Mott, R. A.; Spooner, C. E. The calorific value of carbon in coal: the Dulong relationship. *Fuel*. 1940, 226-31.

$$(11) \text{ HHV (MJ/kg)} = 0.3517 \cdot \text{C} + 1.1626 \cdot \text{H} + 0.1047 \cdot \text{S} - 0.111 \cdot \text{O}$$

Original source: Boie, W. Fuel technology calculations. *Energietechnik*. 1953, 3, 309.

An additional empirical correlation based on the proximate analysis was employed to calculate HHV of PS500. For solid fuel (charcoal), following equation provides HHV with a reasonable correlation ($R^2 = 0.94$) to the values measured using bomb calorimeter (Cordero et al., 2001):

$$\text{HHV (MJ kg}^{-1}\text{)} = 0.3543 (\% \text{ fixed C}) + 0.1708 (\% \text{ VM})$$

Bibliography

1. Ahmad, M. Rajapaksha, A. U. Lim, J. E. Zhang, M. Bolan, N. Mohan, D. Vithanage, M. Lee, S. S. Ok, Y. S. "Biochar as a sorbent for contaminant management in soil and water: A review" *Chemosphere*. 99. 2014. 19-33.
2. Mohan, D. Sarswat, A. Ok, Y. S. Pittman Jr., C. U. "Organic and inorganic contaminants removal from water with biochar, a renewable, low cost and sustainable adsorbent – A critical review" *Bioresource Technology*. 160. 2014. 191-202.
3. Woolf, D. et al. Sustainable biochar to mitigate global climate change. *Nat. Commun.* 1:56 doi: 10.1038 / ncomms1053 (2010).
4. "Biochars multifunctional role as a novel technology in the agricultural, environmental, and industrial sectors" *Chemosphere*. 142. 2016. 1-3.
5. Novak, J. Sigua, G. Watts, D. Cantrell, K. Shumaker, P. Szogi, A. Johnson, M. G. Spokas, K. "Biochars impact on water infiltration and water quality through a compacted subsoil layer" *Chemosphere*. 142. 2016. 160-167.
6. Bruun, E. W.; Ambus, P.; Egsgaard, H.; Hauggaard-Nielsen, H. Effects of slow and fast pyrolysis biochar on soil C and N turnover dynamics. *Soil Biology & Biochemistry*. 2012. 46. 73-79.

7. Bruun, S.; Clauson-Kaas, S.; Bobul'ská, L.; Thomsen, I. K. Carbon dioxide emissions from biochar in soil: Role of clay, microorganisms and carbonates. *Eur. J. Soil Sci.* 2014, 65, 52–59.
8. Antal Jr. M.J.; Croiset, E.; Dai, X.; DeAlmeida, C.; Mok, W.S.-L.; Norberg, N.; Richard, J.-R.; Al Majthoub, M. High-Yield Biomass Charcoal. *Energy & Fuels.* 1996. 10. 652-658.
9. Antal Jr., M. J. Allen, S. G. Dai, X. Shimizu, B. Tam, M. S. Gronli, M. "Attainment of the theoretical yield of carbon from biomass" *Ind. Eng. Chem. Res.* 2000. 39. 4024-4031
10. Wang, L.; Trninc, M.; Skreiberg, O.; Gronli, M.; Considine, R.; Antal Jr., M. J. Is Elevated Pressure Required To Achieve a High Fixed-Carbon Yield of Charcoal from Biomass? Part 1: Round-Robin Results for Three Different Corncob Materials. *Energy Fuels.* 2011. 25. 3251-3565.
11. Wesenbeeck, S. V.; Higashi, C.; Legarra, M.; Wang, L.; Antal Jr., M. J. Biomass Pyrolysis in Sealed Vessels. Fixed-Carbon Yields from Avicel Cellulose That Realize the Theoretical Limit. *Energy Fuels.* 30. 2016. 480-491.
12. Dewan M. A. R., Zhang G., Ostrovski O. Carbotermal Reduction of Titania in Different Gas Atmospheres. *Metallurgical and Materials Transactions B.* 62. (2009).
13. Antal Jr., M.J.; Mok, W.S.L.; Varhegyi, G.; Szekely, T.; Review of Methods for Improving the Yield of Charcoal from Biomass. *Energy & Fuels.* 4 (3). 1990.
14. Diez, M. A. Alvarez, R. Barriocanal, C. "Coal for metallurgical coke production: prediction of coke quality and future requirements for cokemaking" *International Journal of Coal Geology.* 50. 2002. 389-412.
15. Mok, W.S.L.; Antal Jr., M.J.; Szabo, P.; Varhegyi, G.; Zelei, B. Formation of Charcoal from Biomass in Sealed Reactor. *Ind. Eng. Chem. Res.* 1992. 31 (4). 1162-1166.
16. Antal Jr., M. J. Gronli, M. "The Art, Science and Technology of Charcoal Production" *Ind. Eng. Chem. Res.* 42. 2003. 1619-1640.
17. Ringer M., Putsche V., Scahill J. "Large-Scale Pyrolysis Oil Production: A Technology Assessment and Economic Analysis". National Renewable Energy Laboratory. (2006).
18. Lin W., Feng Y. Zhang X. "Numerical study of volatiles production, fluid flow and heat transfer in coke ovens" *Applied Thermal Engineering.* 81. 2015. 353-358.
19. Suncoke Energy Website. <http://www.suncoke.com/English/Home/default.aspx>. 01 Oct. 2016.
20. Montiano, M.G. Fernandez, A.M. Diaz-Faes, E. Barriocanal, C. "Tar from biomass/coal-containing briquettes. Evaluation of PAHs" *Fuel.* 154. 2015. 261-267.
21. Kozielska, B. Konieczynski, Jan "Polycyclic aromatic hydrocarbons in particulate matter emitted from coke oven battery" *Fuel.* 144. 2015. 327-334.
22. Benhabib, K. Faure, P. Sardin, M. Simonnot, M. "Characteristics of a solid coal tar sampled from contaminated soil and of the organic transferred into water" *Fuel.* 89. 2010. 352-359.
23. Nomura, S. "Behavior of coal chlorine in cokemaking process" *International Journal of Coal Geology.* 83. 2010. 423-429.
24. Nomura, S. "Behavior of chlorine during co-carbonization of coal and chloride compounds in cokemaking process" *International Journal of Coal Geology.* 130. 2014. 27-32.
25. Sharobem, T., "Mitigation of High Temperature Corrosion in Waste-to-Energy Power Plants" Columbia University. 2016.

26. Kumar, R. Chakraborty, S. Pal, P. "Membrane-integrated physic-chemical treatment of coke-oven wastewater: transport modeling and economic evaluation" *Environ Sci Pollut Res.* 22. 2015. 6010-6023.
27. Isaacson C.W., M. Kleber, J. A. Field "Quantitative Analysis of Fullerene Nanomaterials in Environmental Systems: A Critical Review". *Environ Sci Technol.* 2009 Sep 1; 43(17): 6463–6474.
28. Rantitsch, G. Bhattacharyya, A. Schenk, J. Lunsdorf, N.K. "Assessing the quality of metallurgical coke by Raman spectroscopy" *International Journal of Coal Geology.* 130. 2014. 1-7.
29. Best P. E, P. R. Solomon, M. A. Serio, E. M. Suuberg, W. R. Mott Jr. and R. Basilakis. "The Relationship Between Char Reactivity and Physical and Structural Features". *ACS Div. Fuel Chem. Prepr.* 32 (4), 138-146, (1987)
30. Senneca O., Russo P., Salatino P., Masi S. "The relevance of thermal annealing to the evolution of coal char gasification reactivity" *Carbon.* 35. 1997. 141-151.
31. Pahalagedara L., Sharma H. N., Kuo C., Dharmarathna S., Joshi A., Suib S. L., Mhadeshwar A. B. "Structure and Oxidation Activity Correlations for Carbon Blacks and Diesel Soot". *Energy and Fuels.* (2012).
32. Stein S. E. "Thermal Reactions and Properties of Polycyclic Aromatic Hydrocarbons". *Acc Chem Res.* 1991. 24. 350-356
33. Wang, L.; Skreiberg, O.; Gronli, M.; Specht, G.P.; Antal Jr., M.J. Is Elevated Pressure Required to Achieve a High Fixed-Carbon Yield of Charcoal from Biomass? Part 2: The Importance of Particle Size. *Energy Fuels.* 2013. 27 (4). 2146-2156.
34. Vassilev, S. V. Baxter, D. Anderson, L. K. Vassileva, C. G. "An overview of the chemical composition of biomass" *Fuel.* 89. 2010. 913-933.
35. Van Krevelen, D. W. *Coal--typology, Physics, Chemistry, Constitution.* Amsterdam: Elsevier, (1993). Print.
36. Ranzi, Cuoci, Faravelli, Frassoldati, Migliavacca, Pierucci, Sommariva, "Chemical Kinetics of Biomass Pyrolysis, *Energy and Fuels*", 2008
37. Yang B., Z. Dai, S. Ding, C.E. Wyman "Enzymatic hydrolysis of cellulosic biomass". *Biofuels.* 2011. 2 (4). 421-450.
38. Mettler, M.S. Vlachos, D. G. Dauenhauer, P. J. "Top ten fundamental challenges of biomass pyrolysis for biofuels" *Energy Environ. Sci.* 5. 2012. 7797.
39. Uchimiya, M. Stone, A. T. "Reversible redox chemistry of quinones: Impact on biogeochemical cycles" *Chemosphere.* 77. 2009. 451-458.
40. Yang H., Yan R., Chen H., Lee D. H., Zheng C. "Characteristics of hemicellulose, cellulose and lignin pyrolysis" *Fuel.* 86. 2007. 1781-1788.
41. Patuzzi F., Ciuta S., Castaldi M. J., Baratieri M. "Intraparticle gas sampling during wood particle pyrolysis: Methodology assessment by means of thermofluidynamic modeling" *Journal of Analytical and Applied Pyrolysis.* 113. 2015. 638-645.
42. Scheirs J., Camino G., Tumiatti W. "Overview of water evolution during the thermal degradation of cellulose" *European Polymer Journal.* 37. 2007. 933-942.
43. Arseneau, D. F. "Competitive Reactions in the Thermal Decomposition of Cellulose" *Canadian Journal of Chemistry.* 49. 1971. 632-638.
44. Worasuwanarak N., T. Sonobe, W. Tanthapanichakoon "Pyrolysis behaviors of rice straw, rice husk, and corncob by TG-MS technique". *J.Anal. Appl. Pyrolysis.* 78. 2007. 265-271.

45. Jones, K.; Ramakrishnan, G.; Uchimiya, M.; Orlov, A.; Castaldi, M. J.; Leblanc, J.; Hiradate, S., Fate of higher-mass elements and surface functional groups during the pyrolysis of waste pecan shell. *Energ. Fuel* 2015, 29, 8095-8101.
46. Ciuta S., Patuzzi F., Baratieri M., Castaldi M. J. "Biomass energy behavior study during pyrolysis process by intraparticle gas sampling" *Journal of Analytical and Applied Pyrolysis*. 108. 2014. 316-322.
47. Gomez, C. Velo, E. Barontini, F. Cozzani, V. "Influence of Secondary Reactions on the Heat of Pyrolysis of Biomass" *Ind. Eng. Chem. Res.* 2009. 48. 10222-10233.
48. Park W. C., Atreya A., Baum H. R. "Experimental and theoretical investigation of heat and mass transfer process during wood pyrolysis" *Combustion and Flame*. 157. 2010. 481-494.
49. Bahng, M. K.; Donohoe, B. S.; Nimlos, M. R., Application of an fourier transform-infrared imaging tool for measuring temperature or reaction profiles in pyrolyzed wood. *Energ. Fuel* 2011, 25, 370-378.
50. Uchimiya, M. Orlov, A. Ramakrishnan, G. Sistani, K. "In situ and ex situ spectroscopic monitoring of biochar's surface functional groups" *Journal of Analytical and Applied Pyrolysis*. 102. 2013. 53-59.
51. Keiluweit, M. Nico, P. S. Johnson, M. G. Kleber, M. Dynamic molecular structure of plant biomass-derived black carbon (Biochar). *Environ. Sci. Technol.* 2010, 44, 1247-1253.
52. Lin, Y. C.; Cho, J.; Tompsett, G. A.; Westmoreland, P. R.; Huber, G. W. Kinetics and mechanism of cellulose pyrolysis. *J. Phys. Chem. C* 2009, 113, 20097-20107.
53. Di Blasi, C., Pyrolytic behavior and products of some wood varieties, *Combustion and Flame* 124 (1-2) (2001) 165-177.
54. Niksa S. "Predicting the rapid devolatilization of diverse forms of biomass with bio-FLASHCHAIN" *Proceedings of the Combustion Institute*. 28. 2000. 2727-2733.
55. Pan W., Richards G. N. "Influence of Metal Ions on Volatile Products of Pyrolysis of Wood" *Journal of Analytical and Pyrolysis*. 16. 1989. 117-126.
56. Gavalas G. R., Cheong P. H., Jain R. "Model of Coal Pyrolysis. 1. Qualitative Development" *Ind. Eng. Chem. Fundam.* 20. 1981. 113-122.
57. Gavalas, George R. *Coal Pyrolysis*. Amsterdam: Elsevier Scientific Pub., 1982.
58. Marzec, A. Towards an understanding of the coal structure: a review. *Fuel Processing Technology*, 2002, 77-78, 25-32.
59. Niksa S. "FLASHCHAIN Theory for Rapid Coal Devolatilization Kinetics. 7. Predicting the Release of Oxygen Species from Various Coals" *Energy and Fuels*. 10. 1996. 173-187.
60. Omais, B. Charon, N. Courtiade, M. Ponthus, J. Thiebaut, D. "A novel analytical approach for oxygen speciation in coal-derived liquids" *Fuel*. 104. 2013. 805-812.
61. Niksa S. "FLASHCHAIN Theory for Rapid Coal Devolatilization Kinetics. 6. Predicting the Evolution of Fuel Nitrogen from Various Coals" *Energy and Fuels*. 9. 1995. 467-478.
62. Deshpande G. V., Solomon P. R., Serio M. A. "Crosslinking Reactions in Coal Pyrolysis". *Advanced Fuel Research Inc.*
63. Solomon P. R., Hamblen D. G., Carangelo R. M., Serio M. A., Deshpande G. V. "General Model of Coal Devolatilization" *Energy and Fuels*. 2. 1988. 405-422.
64. Poutsma M. L. "Free-radical thermolysis and hydrogenolysis of model hydrocarbons relevant to processing of coal". *Energy and Fuels*. 4. 1990. 113-131.

65. Yokono, T.; Obara, T.; Iyama, S.; Sanada, Y. "Hydrogen donor and acceptor ability of coal and pitch – factors governing mesophase development from low rank coal during carbonization" *Carbon*. 22 (6). 1984. 623-624.
66. Savage P. E. "Mechanisms and kinetics models for hydrocarbon pyrolysis". *J Anal App Pyro*. 2000. 54. 109-126.0
67. Chatterjee, K.; Balkrishna, B.; Stock, L. M.; Zabransky, R., F. *Energy Fuels* 1989, 3, 427.
68. Oh, "Softening Coal Pyrolysis", Ph. D dissertation, MIT
69. Yu, J., Lucas, J.A., Wall, T.A., *Prog. In Energy and Comb. Science*, 2007 33, p. 135-170.
70. Niksa S. "FLASHCHAIN Theory for Rapid Coal Devolatilization Kinetics. 4. Predicting Ultimate Yields from Ultimate Analysis Alone" *Energy and Fuels*. 8. 1991. 659-670.
71. Serio, M. A.; Peters W. A.; Howard J. B. *Kinetics of Vapor-Phase Secondary Reactions of Prompt Coal Pyrolysis Tars*. *Ind. Eng. Chem. Res.* (1987). 26. 1831-1838.
72. Chen, J.C. Niksa, S. "Coal devolatilization during rapid transient heating. 1. Primary Devolatilization" *Energy & Fuels*. 6. 3. 1992. 254-264.
73. Da Silva, J.M. Machado, M.E. Maciel, G.P.S. Molin, D.D. Caramao, E.B. "Speciation of nitrogen-containing compounds in an unfractionated coal tar sample by comprehensive two-dimensional gas chromatography coupled to time-of-flight mass spectrometry" *Journal of Chromatography A*. 1373. 2014. 159-168.
74. Niksa S. "FLASHCHAIN Theory for Rapid Coal Devolatilization Kinetics. 5. Interpreting Rate of Devolatilization for Various Coal Types and Operating Conditions" *Energy and Fuels*. 8. 1994. 671-679.
75. Mochizuki, Y. Ono, Y. Uebo, K. Tsubouchi, N. "The fate of sulfur in coal during carbonization and its effect on coal fluidity" *International Journal of Coal Geology*. 120. 2013. 50-56.
76. Niksa S. "FLASHCHAIN Theory for Rapid Coal Devolatilization Kinetics. 3. Modeling the Behavior of Various Coals" *Energy and Fuels*. 5. 1991. 673-683.
77. Willems P. A., G. F. Froment "Kinetic Modeling of the Thermal Cracking of Hydrocarbons 1. Calculation of Frequency Factors" *Ind. Eng. Chem. Res.* 1988. 27. 1959-1966.
78. Sundaram M. K., Froment G. F. "Modeling of Thermal Cracking Kinetics. 3. Radical Mechanisms for the Pyrolysis of Simple Paraffins, Olefins and Their Mixtures" *Ind. Eng. Chem. Fundam.* 17. 1978. 174-182.
79. Reyniers G. C., G. F. Froment, F. D. Kopinke, G. Zimmermann "Coke Formation in the Thermal Cracking of Hydrocarbons. 4. Modeling of Coke Formation in Naphtha Cracking" *Ind. Eng. Chem. Res.* 1994. 33. 2584-2590.
80. Kopinke F. D., G. Zimmermann, S. Nowak "On the Mechanism of Coke Formation in Steam Cracking-Conclusion from Results Obtained by Tracer Experiments" *Carbon*. 1988. 26. 117-124.
81. Kopinke F. D., G. Zimmermann, G. C. Reyniers, G. F. Froment "Relative Rate of Coke Formation from Hydrocarbons in Steam Cracking of Naphtha. 2. Paraffins, Naphthenes, Mono-, Di-, and Cycloolefins and Acetylenes" *Ind. Eng. Chem. Res.* 1993. 32. 56-61.
82. Chen, J.C. Castagnoli, C. Niksa, S. "Coal devolatilization during Rapid Transient Heating. 2. Secondary Pyrolysis" *Energy & Fuels*. 1992. 6. 264-271
83. Pather, T. S., Al-Masry, W. A.; The Influence of bed depth on secondary reactions during slow pyrolysis of coal, *Journal of Analytical and Applied Pyrolysis*, 37 (1996), 83-94.

84. Niksa S. "FLASHCHAIN Theory for Rapid Coal Devolatilization Kinetics. 2. Impact of Operating Conditions" *Energy and Fuels*. 5. 1991. 665-673.
85. Peters, W. Bertling, H. "Kinetics of the Rapid Degasification of Coals". Division of Fuel Chemistry. American Chemical Society. Aug 30 – Sept 4 1964. Chicago, IL.
86. Anthony, D. B.; Howard, J. B. Coal devolatilization and hydrogasification. *AIChE J*. 1976, 22, 625.
87. Lin, W.; Feng, Y.; Zhang, X. Numerical study of volatiles production, fluid flow and heat transfer in coke ovens. *Applied Thermal Engineering*. 2015. 81. 353-358.
88. Niksa S., Kerstein A. R. "FLASHCHAIN Theory for Rapid Coal Devolatilization Kinetics. 1. Formulation" *Energy and Fuels*. 5. 1991. 647-665.
89. Neeft J. A. P., Knoef H. A. M., Zielke U., Sjöström K., Hasler P., Simell P. A., Dorrington M.A., Thomas L., Abatzoglou N., Deutch S., Greil C., Buffinga G.J., Brage C., Suomalainen M. "Guideline for Sampling and Analysis of Tar and Particles in Biomass Producer Gases". Energy Project ERK6-CT1999-20002. Version 3.3
90. Miljevic, Branka and Modini, Robin L. and Bottle, Steven and Ristovski, Zoran "On the efficiency of impingers with fritted nozzle tip for collection of ultrafine particles." *Atmospheric Environment*, 43(6). pp. 1372-1376.
91. Friedl, A. Padouvas, E. Rotter, H. Varmuza, K. "Prediction of heating values of biomass fuel from elemental composition" *Analytica Chimica Acta*. 544. 2005. 191-198.
92. Kieseler, S. Neubauer, Y. Zobel, N. "Ultimate and proximate correlations for estimating the higher heating value of hydrothermal solids" *Energy and Fuels*. 27. 2013. 908-918.
93. Green, D. W.; Perry, R. H., *Perry's Chemical Engineering Handbook*, 8th edition. McGraw-Hill Publishing: Columbus, OH, 2008.0
94. Suuberg, E. M., Approximate solution technique for nonisothermal, gaussian distributed activation energy models. *Combust. Flame* 1983, 50, 243-245.
95. Straka, P.; Endrysova, J. "Using DRIFT Spectrometry with PLS Method for Determination of Oxygen Functionalities in Heterogeneous Materials" *Chem. Papers*. 1999. 53 (5). 283-287.
96. Suuberg, E. M.; Peters, W. A.; Howard, J. B. Product composition and kinetics of lignite pyrolysis. *Ind. Eng. Chem. Process Des. Dev.* 1978, 17, 34-46.
97. Fraas, A. P.; Furgerson, R. L.; Falkenberry, H. L U.S. Patent 08, 835, 419, 2006.
98. Fan, X.; Wei, X-Y.; Zong, Z-M. Application of gas chromatography/mass spectrometry in studies on separation and identification of organic species in coals. *Fuel*. 2013, 109, 28-32.
99. Zhu, J-L.; Fan, X.; Wei, X-Y.; Wang, S-Z.; Zhu, T-G.; Zhou, C-C.; Zhao, Y-P.; Wang, R-Y.; Lu, Y.; Chen, L.; You, C-C. Molecular characterization of heteroatomic compounds in high-temperature coal tar using three mass spectrometers. *Fuel Processing Technology*. 2015, 138, 65-73.
100. Wu, Z.; Rodgers, R. P.; Marshall, A. G. ESI FT-ICR mass spectral analysis of coal liquefaction products. *Fuel*. 2005, 84, 1790-1797.
101. Li, P.; Zong, Z-M.; Li, Z-K.; Wang, Y-G. Liu, F-J.; Wei, X-Y. Characterization of basic heteroatoms-containing organic compounds in liquefaction residue from Shenmu-Fugu subbituminous coal by positive-ion electrospray ionization Fourier transform ion cyclotron resonance mass spectrometry. *Fuel Processing Technology*. 2015, 132, 91-98.

102. Herod, A. A.; Bartle, K. D.; Kandiyoti, R. Characterization of heavy hydrocarbons by chromatographic and mass spectrometric methods: An review. *Energy and Fuels*. 2007, 21, 2176-2203.
103. Herod, A. A. "Limitations of mass spectrometric methods for characterization of polydisperse materials" *Rapid Communications in Mass Spectrometry*. 2010, 24, 2507-2519.
104. Millan, M. Morgan, T.J. Behrouzi, M. Karaca, F. Galmes, C. Herod, A.A. Kandiyoti, R. The high-mass component ($>m/z$ 10 000) of coal tar pitch by matrix-assisted laser desorption/ionization mass spectrometry and size-exclusion chromatography. *Rapid Communications in Mass Spectrometry*. 2005, 19, 1867-1873.
105. Johnson, B.R. Bartle, K.D. Domin, M. Herod, A.A. Kandiyoti, R. Absolute calibration of size exclusion chromatography for coal derivatives through MALDI-m.s. *Fuel*. 1998, 77, 933-945.
106. Herod, A.A. Lazaro, M.-J Domin, M. Islas, C.A. Kandiyoti, R. Molecular mass distributions and structural characterization of coal derived liquids. *Fuel*. 2000, 79, 323-337.
107. Lazaro, M.-J. Herod, A.A. Cocksedge, M. Domin, M. Kandiyoti, R. Molecular mass determinations in coal-derived liquids by MALDI mass spectroscopy and size-exclusion chromatography. *Fuel*. 1997, 76, 1225-1233.
108. Solomon, P.R.; Serio, M.A.; Despande, G.V.; Kroo, E. Cross-linking reactions during coal conversion. *Energy and Fuels*. 1990, 4 (1), 42-54.
109. You, C-Y; Fan, X.; Zhen, A-L; Wei, X-Y; Zhao, Y-P; Cao, J-P; Zhao, W; Zhou, C-C; Zhu, J-L; Chen, L.; Wang, S-L Molecular characterizatics of a Chinese coal analyzed using mass spectrometry with various ionization modes. *Fuel*. 2015, 155, 122-127.
110. Kong, J.; Wei, X-Y.; Yan, H-L.; Li, Z-K.; Zhao, M-X.; Li, Y.; Zong, Z-M. Analysis of extractable basic nitrogen compounds in Buliangou subbituminous coal by positive-ion ESI FT-ICR MS. *Fuel*. 2015, 159, 385-391.
111. Schulten, H.R.; Marzec, A. Time- and Temperature-resolved field ionization mass spectrometry of coals and their extracts. *Fuel*, 1986, 65 (6), 855-860.
112. Herod, A.A.; Zhang, S.-F.; Carter, D.M.; Domin, M. Cocksedge, M.J.; Parker, J.E.; Johnson, C.A.F.; John, P.; Smith, G.P.; Johnson, B.R.; Bartle, K.D.; Kandiyoti, R. Matrix-assisted Laser Desorption/Ionization Mass Spectrometry of Pitch Fractions Separated by Planar Chromatography. *Rapid Communications in Mass Spectrometry*. 10, 1996, 171-177.
113. Herod, A. A.; Shearman, J.; Lazaro, M.-J.; Johnson, B. R.; Bartle, K. D.; Kandiyoti, R. *Energy Fuels* 1998, 12, 174.
114. Karaca, F.; Islas, C. A.; Millan, M.; Behrouzi, M.; Morgan, T. J.; Herod, A. A.; Kandiyoti, R. The calibration of size exclusion chromatography columns: Molecular mass distributions of heavy hydrocarbon liquids. *Energy Fuels* 2004, 18, 778-788.
115. Hamilton, J. F.; Lewis, A. C.; Millan, M.; Bartle, K. D.; Herod, A. A.; Kandiyoti, R. Comprehensive Two-dimensional Gas chromatography coupled to time-of-flight mass spectroscopy of coal liquids produced during a coal liquefaction process. *Energy and Fuels*. 2007, 21, 286-294.

116. Devi, T.G.; Kannan, M. P. and Abduraheem; V. P., "Jump in the air gasification rate of potassium-doped cellulosic chars," *Fuel Processing Technology*, vol. 91, pp. 1826–1831, Dec 2010.
117. Bautista, J.R.; Russel, W.B.; Saville, D.A. Time-resolved pyrolysis product distributions of softening coals. *Ind. Eng. Chem. Fundam.* 1986, 25 (4), 536-544.
118. Van Krevelen, D.W.; Huntjens, F.J.; Dormans, H.N.M. Chemical structure and properties of coal: XVI. Plastic behavior on heating. *Fuel.* 1956, 35, 462-475.
119. Van Krevelen, D.W.; Dormans, H.N.M.; Huntjens, F.J. *Fuel.* 1959, 38, 165-182.
120. Frenklach, M. Reaction mechanism of soot formation in flames. *Physical Chemistry Chemical Physics.* 2002, 4, 2028-2037.
121. Howard, J.B. Essenhigh, R.H., *I&EC Process Design and Development*, 1967 6, pp.74-84. Print.
122. Komnitsas, K.; Zaharaki, D.; Bartzas, G.; Kaliakatsou, G.; Kritikaki, A., Efficiency of pecan shells and sawdust biochar on Pb and Cu adsorption. *Desalin. Water Treat.* 2014, 1-10.
123. Gómez, C. J.; Várhegyi, G.; Puigjaner, L., Slow pyrolysis of woody residues and an herbaceous biomass crop: A kinetic study. *Ind. Eng. Chem. Res.* 2005, 44, 6650-6660.
124. Chen, T.; Zhang, J.; Wu, J., Kinetic and energy production analysis of pyrolysis of lignocellulosic biomass using a three-parallel Gaussian reaction model. *Bioresour. Technol.* 2016, 211, 502-508.
125. Cramer, B., Methane generation from coal during open system pyrolysis investigated by isotope specific, Gaussian distributed reaction kinetics. *Org. Geochem.* 2004, 35, 379-392.
126. Pauling, L., *General Chemistry*. W.H. Freeman: CA, 1970.
127. De Caprariis, B.; De Filippis, P.; Herce, C.; Verdone, N., Double-gaussian distributed activation energy model for coal devolatilization. *Energ. Fuel* 2012, 26, 6153-6159.
128. Uchimiya, M., Influence of pH, ionic strength, and multidentate ligand on the interaction of CdII with biochars. *ACS Sustainable Chem. Eng.* 2014, 2, 2019-2027.
129. El-Hendawry, A-N. A. Variation in the FTIR spectra of a biomass under impregnation, carbonization and oxidation condition. *Journal of Analytical and Applied Pyrolysis*, 75, 2006, 159-166.
130. Ducouso, M., Weiss-Hortala, E., Nzihou, A., Castaldi, M. J. Reactivity enhancement of gasification biochars for catalytic applications. *Fuel*, 159, 2015, 491-499.
131. Uchimiya, M.; Hiradate, S.; Antal, M. J. Dissolved phosphorus speciation of flash carbonization, slow pyrolysis, and fast pyrolysis biochars. *ACS Sustainable Chem. Eng.* 2015, 3, 1642–1649.
132. Paulsen, A. D.; Hough, B. R.; Williams, C. L.; Teixeira, A. R.; Schwartz, D. T.; Pfaendtner, J.; Dauenhauer, P. J., Fast pyrolysis of wood for biofuels: Spatiotemporally resolved diffuse reflectance insitu spectroscopy of particles. *ChemSusChem* 2014, 7, 765-776.
133. Fasina, O.; Littlefield, B., TG-FTIR analysis of pecan shells thermal decomposition. *Fuel Process. Technol.* 2012, 102, 61-66.
134. Allen, R. M.; Laird, D. A., Quantitative prediction of biochar soil amendments by near-infrared reflectance spectroscopy. *Soil Sci. Soc. Am. J.* 2013, 77, 1784-1794.

135. T. G. Devi, M. P. Kannan, and V. P. Abduraheem, "Jump in the air gasification rate of potassium-doped cellulosic chars," *Fuel Processing Technology*, vol. 91, pp. 1826–1831, Dec 2010.
136. Baker, "The relationship between particle motion on a graphite surface and Tammann temperature," *Journal of Catalysis*, vol. 78, no. 2, pp. 473–476, 1982.
137. Klinghoffer, N. "Utilization of char from biomass gasification in catalytic applications" PhD Dissertation. Columbia University. 2013.
138. Shaikhutdinov, Sh. K. Avdeeva, L. B. Novgorodov, B. N. Zaikovskii, V. I. Kochubey, D. I. "Nickel catalysts supported on carbon nanofibers: structure and activity in methane decomposition" *Catalysis Letters*. 47. 1997. 35-42.
139. Fenelonov, V. B. Derevyankin, A. Yu. Okkel, L. G. Avdeeva, L. B. Zaikovskii, V. I. Moroz, E. M. Salanov, A. N. Rudina, N. A. Likholobov, V. A. Shaikhutdinov, Sh. K. "Structure and texture of filamentous carbons produced by methane decomposition on Ni and Ni-Cu Catalysts" *Carbon*. 35. 8. 1197. 1129-1140.
140. Ermakova, M. A. Ermakov, D. Yu. Kuvshinov, G. G. "Effective catalysts for direct cracking of methane to produce hydrogen and filamentous carbon Part I. Nickel catalyst" *Applied Catalysis A: General*. 201. 2000. 61-70.
141. Snoeck, J. W. Froment, G. F. Fowles, M. "Steam/CO₂ Reforming of Methane. Carbon filament formation by the Boudouard reaction and gasification by CO₂, by H₂, and by steam: kinetic study" *Ind. Eng. Chem. Res.* 41. 2002. 4252-4265.
142. Zaitseva, N. A. Goidin, V. V. Molchanov, V. V. Chesnokov, V. V. Buyanov, R. A. Utkin, V. A. "Catalysts based on filamentous carbon in the hydrogenation of aromatic compounds" *Kinetic and Catalysis*. 52. 5. 2011. 770-773.
143. Helveg, S. Lopez-Cartes, C. Sehested, J. Hansen, P. L. Clausen, B. S. Rostrup-Nielsen, J. R. Abild-Pedersen, F. Norskov, J. K. "Atomic-scale imaging of carbon nanofibre growth" *Nature*. 427. 2004. 426-429.
144. Dufour A., Ouartassi B., Bounaceur R., Zoulalian A. "Modelling intra-particle phenomena of biomass pyrolysis" *Chemical Engineering Research and Design*. 89. 2011. 2136-2146.